Phase Transitions: Applications to Physics Beyond the Standard Model

by

Nikita Blinov

Mathematical Physics, BSc, University of Alberta, Edmonton, 2010

A THESIS SUBMITTED IN PARTIAL FULFILLMENT
OF THE REQUIREMENTS FOR THE DEGREE OF

Doctor of Philosophy

in

THE FACULTY OF GRADUATE AND POSTDOCTORAL STUDIES
(Physics)

The University Of British Columbia
(Vancouver)

August 2015

Abstract

Despite their phenomenological successes, the Standard Models (SMs) of particle physics and cosmology remain incomplete. Several theoretical and observational problems cannot be explained within this framework, including the hierarchy problem, dark matter (DM), and the baryon asymmetry of the Universe. The objective of this thesis is to investigate phenomenological and theoretical aspects of the solutions to these issues. We consider two kinds of phase transitions that can occur in the early or late Universe in extensions of the SM, that can be either responsible for dark matter and/or baryon asymmetry production or may be used to constrain possible models of new physics.

In the first part we analyze string theory-inspired models where the Universe transitions from matter- to radiation-dominated evolution just before Big Bang Nucleosynthesis through out-of-equilibrium decays of a scalar modulus field. We employ these decays to produce DM and for baryogenesis. We study the phenomenology of these scenarios and its implications for high-scale physics.

The second part of this thesis is dedicated to thermodynamic and quantum phase transitions in the early and late Universe, respectively. In the former case, we investigate the dynamics of the electroweak phase transition when the electroweak symmetry is broken down to electromagnetism in the Inert Doublet Model, a simple extension of the SM that can account for DM. Such transitions can generate the baryon asymmetry in a process called electroweak baryogenesis. Some extensions of the SM also predict similar transitions through quantum tunnelling that break the colour and electromagnetic symmetries, indicating that our ground state is unstable. We use these arguments to put new constraints on the Minimal Supersymmetric Standard Model.

Preface

Parts II and III of this thesis are based on published and unpublished work in collaboration with other authors. Parts I and IV (as well as certain sections in Parts II, III) are original expository materials.

A version of Chapter 3 has appeared in N. Blinov, J. Kozaczuk, A. Menon, and D. E. Morrissey, *Confronting the moduli-induced lightest-superpartner problem*, *Phys.Rev.* **D91** (2015), no. 3 035026, [arXiv:1409.1222]. This thesis contains an expanded introduction in Sections 3.1, 3.1.1 and 3.1.2. I participated in the construction of models in Sections 3.3, 3.4. I was also responsible for the majority of analytic and numerical calculations in Sections 3.2, 3.3, 3.4 and 3.5, as well as their composition. David Morrissey was the supervisory author on this work and contributed analytic results to these and other sections. Jonathan Kozaczuk provided various indirect detection constraints in Sections 3.3 and 3.4. Arjun Menon cross-checked the results of Sec. 3.2. All authors contributed to the composition of the manuscript.

A longer version of Chapter 4 appeared in N. Blinov, D. E. Morrissey, K. Sigurdson, and S. Tulin, *Dark Matter Antibaryons from a Supersymmetric Hidden Sector*, *Phys.Rev.* **D86** (2012) 095021, [arXiv:1206.3304]. I performed the calculations in Section 4.3, and contributed to Section 4.5. Sean Tulin was responsible for Section 4.5.1, while David Morrissey wrote Sections 4.4 and 4.5.3. David Morrissey and Kris Sigurdson were the supervisory authors in this work. All authors contributed to the composition and editing of the manuscript; the appendix that appears in the published work has been excluded from this thesis, because I did not write it.

Chapter 6 is based on N. Blinov and D. E. Morrissey, *Vacuum Stability and the MSSM Higgs Mass*, *JHEP* **1403** (2014) 106, [arXiv:1310.4174]. I contributed the majority of the numerical results in Section 6.3.3 and Appendix B as well as the proof in Appendix A. David Morrissey was the supervising author and contributed Section 6.5. We jointly composed and edited the manuscript.

Chapter 7 is based on work in N. Blinov, S. Profumo, and T. Stefaniak, *The Electroweak Phase Transition in the Inert Doublet Model*, *JCAP* **2015** (2015), no. 07 028, [arXiv:1504.05949]. Here I contributed most of the analytic and numerical results in Sections 7.3 and 7.5. Tim Stefaniak was responsible for checking collider constraints for models of Section 7.5. Stefano Profumo was the supervising author and wrote Section 7.4. I composed the manuscript; all authors were involved in editing it.

Table of Contents

List of Tables

List of Figures

Glossary

ADM asymmetric dark matter

AMSB Anomaly Mediated Supersymmetry Breaking

BBN Big Bang Nucleosynthesis

CC charged current

CKM Cabibbo-Kobayashi-Maskawa

CMB Cosmic Microwave Background

DM dark matter

EDM electric dipole moment

EOM equation of motion

EW electroweak

EWBG electroweak baryogenesis

EWPT electroweak phase transition

EWSB electroweak symmetry breaking

FRW Friedmann-Robertson-Walker

GR General Relativity

GUT Grand Unification

HS hidden sector

IDM Inert Higgs Doublet Model

IND induced nucleon decay

LHC Large Hadron Collider

LSP lightest supersymmetric particle

MSSM Minimal Supersymmetric Standard Model

NGB Nambu-Goldstone boson

OR O'Raifeartaigh

QCD Quantum Chromodynamics

SM Standard Model

SSB spontaneous symmetry breaking

SUGRA supergravity

UV ultraviolet

vev vacuum expectation value

WIMP weakly interacting massive particle

WZ Wess-Zumino

Acknowledgements

This thesis is the culmination of five years of work which would not have been possible without the help and support of many people. First I would like to thank the faculty, post-docs, students and staff at TRIUMF, UBC and UC Santa Cruz. I am especially grateful to Peter Winslow and Jonathan Kozaczuk with whom I had many illuminating discussions about field theory, the Universe and everything.

All research presented in this thesis is the product of a collective effort. I am indebted to my collaborators Sean Tulin, Kris Sigurdson, Jonathan Kozaczuk, Carlos Tamarit, Stefano Profumo, Tim Stefaniak and Arjun Menon for their guidance and patience for my many questions.

I am grateful to my doctoral committee, Jeremy Heyl, Alison Lister, David Morrissey and Kris Sigurdson, for carefully reading this manuscript and for providing feedback throughout the program.

Most importantly, I would like to thank David Morrissey for being the best advisor a student can imagine. His mentorship, support and encouragement have been invaluable. Thank you for sharing your passion for physics and for always keeping your door open.

I am fortunate to able to thank many friends in Vancouver, Edmonton and abroad. Thank you for regularly pulling me away from theory back into the real world.

Finally, I could not have completed this work without the incredible support from my family in Canada and Russia.

Thank you, all of you.

Посвящается маме и папе, за бесконечную помощь и любовь

и Даше Зинченко, потому что она очень просила

Part I

Standard Models and Their Extensions

Chapter 1

Introduction

The Standard Model (SM) of particle physics has proven to be an extremely successful theory of strong and electroweak interactions. The Higgs boson, responsible for the breaking of the electroweak (EW) symmetry, has finally been observed at the Large Hadron Collider (LHC) [12, 13], confirming a 50 year old theoretical prediction by Higgs [14], Englert and Brout [15] and Guralnik, Hagen and Kibble [16].[1] All SM parameters have been measured. On the cosmological frontier, the Planck experiment has observed the Cosmic Microwave Background (CMB) with unprecedented precision, with the resulting data in near-perfect agreement with the Standard Model of cosmology [17], confirming our understanding of the physical processes that occurred over 13 billion years ago.

These are just some of the latest successes of the Standard Models in a long history of correct predictions that included new *fundamental* particles like the electroweak gauge bosons and the top quark, and baryon acoustic oscillations and the CMB power spectrum. There are, however, several strong indications of the existence of physical phenomena unexplained by the SMs. Before describing these shortcomings and thereby motivating the following chapters, we discuss the structure of the SM in Sec. 1.1. The essential aspects of the Standard Model of cosmology are described in Sec. 1.2. In Sec. 1.3 we outline some of the central issues that the models of new physics we consider attempt to address. These include the hierarchy problem, the nature of dark matter and the creation of the baryon asymmetry of the Universe.

In this thesis we use the following conventions. For the spacetime metric we use the "mostly minus" version with $\eta_{\mu\nu} = \text{diag}(1, -1, -1, -1)$ in flat space. Unless stated otherwise, formulae are given in natural units with $\hbar = c = 1$, so all dimensionful quantities are measured in units of energy (typically GeV).

[1] For reasons of brevity we will refer to the Higgs-Englert-Brout-Guralnik-Hagen-Kibble boson as the Higgs boson as is commonly done.

1.1 The Standard Model of Particle Physics

1.1.1 Symmetries and Interactions

The fundamental interactions among known particles are well described by gauge field theories. The SM is a gauge field theoretic description of the strong, weak and electromagnetic forces. All interactions are completely determined by symmetries and particle content of the theory. The gauge symmetry of the SM is $SU(3)_C \times SU(2)_L \times U(1)_Y$. The first factor, $SU(3)_C$ describes Quantum Chromodynamics (QCD) - interactions of quarks and gluons, which at low energies manifest themselves in the existence of colour-neutral hadrons, such as protons and neutrons and their binding into nuclei. The remaining factor $SU(2)_L \times U(1)_Y$ is the electroweak theory: a unification of the weak and electromagnetic interactions, notably responsible for β radioactivity of certain nuclei and the existence of atoms.

Gauge symmetry is an invariance of a theory under local (i.e., spacetime dependent) transformations. The implementation of such symmetries requires the existence of a vector gauge field in the adjoint representation of the corresponding group. In QCD this is the gluon A^a_μ, where a is the adjoint $SU(3)_C$ index running from 1 to 8. The weak triplet W^a_μ ($a = 1, 2, 3$) and the hypercharge B_μ are the gauge bosons of $SU(2)_L$ and $U(1)_Y$, respectively. After electroweak symmetry breaking (EWSB) W^a_μ and B_μ mix to give the mass eigenstates: $W^\pm$ and Z bosons, and the photon γ, as discussed in Sec. 1.1.3.

The fermion content of the SM consists of three generations of quarks (particles with $SU(3)_C$ charge) and leptons (those with only $SU(2)_L \times U(1)_Y$ charges). All stable matter is made of the first generation fermions (written in $SU(2)_L$ space)

$$
\begin{aligned}
Q &= \begin{pmatrix} u \\ d \end{pmatrix}_L : (\mathbf{3}, \mathbf{2}, +1/6) \\
L &= \begin{pmatrix} \nu \\ e \end{pmatrix}_L : (\mathbf{1}, \mathbf{2}, -1/2) \\
u^c_R &: (\mathbf{3}, \mathbf{1}, -2/3) \\
d^c_R &: (\mathbf{3}, \mathbf{1}, +1/3) \\
e^c_R &: (\mathbf{1}, \mathbf{1}, +1),
\end{aligned}
$$

where the $SU(3)_C \times SU(2)_L \times U(1)_Y$ charges are given in parentheses on the right hand side. The two heavier generations have identical structure. The fermions above are two-component Weyl fields; two component spinors are reviewed in Ref. [18]. The physical propagating states are four-component Dirac fermions.[2] For example the electron field is (now written in Dirac

[2] Whether the neutrinos are Dirac or Majorana is still unknown.

space)

$$e = \begin{pmatrix} e_L \\ e_R \end{pmatrix},$$

where $e_R = (e_R^c)^\dagger$. Thus, the SM is a chiral gauge theory, with left- and right-handed fermions transforming in different representations of the gauge group. The physical consequence of this structure is violation of parity P in physical processes, such as β decay [19]. General chiral theories suffer from anomalies – violations of the gauge symmetries arising from quantum corrections. However, the charges of the SM fermions are such that every possible gauge anomaly cancels [20].

The final ingredient of the SM is the Higgs boson. The chiral nature of the SM prohibits gauge-invariant mass terms for the gauge bosons and fermions. Gauge invariance can be preserved if the masses are generated dynamically through spontaneous symmetry breaking (SSB), when a new scalar field, charged under $SU(2)_L \times U(1)_Y$ acquires a vacuum expectation value (vev). *A priori*, boson and fermion mass generation are independent. The SM is economical in that it uses the same Higgs boson H with charges $(\mathbf{1}, \mathbf{2}, 1/2)$ to give masses to all SM states simultaneously. Note that there is no right-handed ν in the SM, so ν_L remain massless. This is in conflict with neutrino flavour oscillation observations. We do not include R-type neutrinos since the origin of the ν mass is still unknown. The field content of the SM is summarized in Tab. 1.1.

The interactions of the SM is are given by the most general renormalizable Lagrangian consistent with symmetries and field content of the model. Poincaré invariance allows the Lagrangian to be written as *space* integral of a density $\mathscr{L}$ which is constructed from Lorentz invariant objects evaluated at the same spacetime point (as required by causality and locality); the action is then the full *spacetime* integral of $\mathscr{L}$. Lorentz invariance is implemented by ensuring there are no uncontracted vector or spinor indices. General gauge transformations of a field ψ in the fundamental representation take the form

$$\psi \to e^{it^a \alpha^a(x)} \psi, \tag{1.1}$$

where $\alpha^a(x)$ is a spacetime-dependent gauge parameter and t^a are the Lie group generators. Spacetime derivatives of ψ do not transform in a simple way when α^a is a function of x. It is therefore useful to define the covariant derivative

$$D_\mu \psi = \left(\partial_\mu + i g_s t_C^a A_\mu^a + i g t_L^a W_\mu^a + i g' Y B_\mu\right) \psi, \tag{1.2}$$

which has a simple transformation rule

$$D_\mu \psi \to e^{it^a \alpha^a(x)} D_\mu \psi, \tag{1.3}$$

when the gauge fields transform as discussed below. Above, g_s, g and g' are the strong, weak and hypercharge gauge couplings, respectively. It is now easy to write down gauge invariant kinetic terms for the SM fermions and the Higgs field:

$$\mathscr{L}_{\rm kin} \supset \sum_i i\bar{\psi}_i \bar{\sigma}^\mu D_\mu \psi_i + (D_\mu H)^\dagger (D^\mu H)\,. \tag{1.4}$$

Note that gauge invariance completely fixes the interactions of the matter (and Higgs) fields with the gauge bosons. Gauge invariance also allows for the following renormalizable Higgs self-interactions:

$$\mathscr{L}_{\rm Higgs} = -V_{\rm Higgs} = -\mu^2|H|^2 - \lambda|H|^4. \tag{1.5}$$

To ensure Eq. (1.3) holds, gauge fields must transform under an infinitesimal gauge transformation as

$$A^a_\mu \to A^a_\mu + f^{abc}\alpha^b(x)A^c_\mu - \frac{1}{g}\partial_\mu \alpha^a(x), \tag{1.6}$$

where g is the gauge coupling and f^{abc} are the group structure constants satisfying

$$[t^a, t^b] = i f^{abc} t^c. \tag{1.7}$$

The structure constants vanish for an Abelian group. One can construct a gauge invariant field strength tensor $F^a_{\mu\nu}$ from the vector fields:

$$F^a_{\mu\nu} = \partial_\mu A^a_\nu - \partial_\nu A^a_\mu + i f^{abc} A^b_\mu A^c_\nu, \tag{1.8}$$

where A^a_μ stands for any of the three SM gauge fields. The non-vanishing Lorentz invariant combinations are then

$$\mathscr{L}_{\rm kin} \supset -\frac{1}{4}G^a_{\mu\nu}G^{a\,\mu\nu} - \frac{1}{4}W^a_{\mu\nu}W^{a\,\mu\nu} - \frac{1}{4}B_{\mu\nu}B^{\mu\nu} \tag{1.9}$$

$$- \frac{\theta_{\rm QCD}}{32\pi^2}G^a_{\mu\nu}\widetilde{G}^{a\,\mu\nu} - \frac{\theta_{\rm EW}}{32\pi^2}W^a_{\mu\nu}\widetilde{W}^{a\,\mu\nu} - \frac{\theta_B}{32\pi^2}B_{\mu\nu}\widetilde{B}^{\mu\nu}, \tag{1.10}$$

where $G^a_{\mu\nu}$, $W^a_{\mu\nu}$ and $B_{\mu\nu}$ are the field strengths associated with $SU(3)_C$, $SU(2)_L$ and $U(1)_Y$, respectively. In the second line $\widetilde{F}^a_{\mu\nu} = \epsilon_{\mu\nu\sigma\rho}F^{a\,\sigma\rho}/2$ is the dual field strength. One can show that $F\widetilde{F}$ terms are in fact total derivatives. These contribute a surface term (at spacetime infinity) that vanishes, unless the vacuum gauge field configuration has a non-trivial winding. Such configurations can exist for non-Abelian gauge theories. In particular, the $SU(3)_C$ term gives rise to the strong CP problem [21]. The electroweak vacuum angle $\theta_{\rm EW}$ can be removed from the Lagrangian using appropriate global B (baryon number) and L (lepton number) transformations [22].

Gauge Eigenstates	$SU(3)_C$	$SU(2)_L$	$U(1)_Y$
A^a_μ	**8**	**1**	0
W^a_μ	**1**	**3**	0
B^a_μ	**1**	**1**	0
Q	**3**	**2**	$+1/6$
L	**1**	**2**	$-1/2$
u^c_R	**3**	**1**	$-2/3$
d^c_R	**3**	**1**	$+1/3$
e^c_R	**1**	**1**	$+1$
H	**1**	**2**	$+1/2$

Table 1.1: Field content of the Standard Model in the gauge eigenbasis. Only one generation of fermions is shown; the other two families have identical gauge charges.

Next, we have the Yukawa interactions

$$\mathscr{L}_{\text{Yukawa}} = H\epsilon Q Y_u u^c_R - H^\dagger Q Y_d d^c_R - H^\dagger L Y_e e^c_R + \text{h.c.}, \tag{1.11}$$

where ϵ is the two component Levi-Civita symbol with $\epsilon^{12} = +1$ and Y_i are general complex 3×3 matrices in family space. The complete SM Lagrangian at the classical level then takes the form

$$\mathscr{L}_{\text{SM}} = \mathscr{L}_{\text{kin}} + \mathscr{L}_{\text{Higgs}} + \mathscr{L}_{\text{Yukawa}}. \tag{1.12}$$

1.1.2 Gauge Fixing and Ghosts

Evaluating physical quantities in the quantum theory requires the computation of time ordered products of fields using path integrals like [23, 24]

$$\langle 0|Tf(x_1, x_2, \dots)|0\rangle = \frac{\int [\mathscr{D}A] f(x_1, x_2, \dots) \exp(iS[A])}{\int [\mathscr{D}A] \exp(iS[A])}, \tag{1.13}$$

where $f(x_1, x_2, \dots)$ is a gauge invariant product of fields inserted at positions x_i. In writing the above we have suppressed dependence of the path integrals on fields other than the gauge field A. Gauge symmetry of the theory is a redundancy in the number of degrees of freedom specified by A. Thus, the unrestricted integration over A counts contributions from physically equivalent gauge configurations multiple times. This overcounting factorizes in the numerator and denominator of Eq. (1.13) and therefore cancels in the ratio.

A second related issue arises when we try to evaluate these path integrals in perturbation theory where we need to compute the propagator of A, which is the inverse of the quadratic part

of the equation of motion operator. For example, for an Abelian gauge field with a canonical kinetic term $-F_{\mu\nu}F^{\mu\nu}/4$, the momentum space propagator $D^{\nu\rho}$ is the Green's function defined by

$$(-k^2 g_{\mu\nu} + k_\mu k_\nu) D^{\nu\rho} = i\delta^\rho_\mu. \tag{1.14}$$

The operator on the left hand side is not invertible, since it annihilates any tensor proportional to $k^\nu k^\rho$, which corresponds to the unphysical longitudinal polarizations of A. These zero modes are responsible for the infinite factors in the path integrals mentioned above. The inversion can be performed and the propagator constructed if the integration is restricted to field configurations that are not related to each other by gauge transformations, i.e., if we explicitly *fix* the gauge. A particular gauge is specified by a functional F that satisfies

$$F[A^g_\mu] = 0. \tag{1.15}$$

The superscript g emphasizes that this relation is satisfied only for a unique choice of gauge transformation. This condition can be enforced in the path integral by employing the Faddeev-Popov trick [23]. After manipulation, the Lagrangian density is modified by

$$\Delta\mathscr{L} = -\frac{1}{2\xi}\left(F[A]\right)^2 + \bar{\eta}(x) M(x,y)\eta(y), \tag{1.16}$$

where

$$M(x,y)\eta(y) = \int d^4y \frac{\delta F[A^\theta_\mu(x)]}{\delta\theta(y)}\bigg|_{\theta=0} \eta(y), \tag{1.17}$$

and θ is an infinitesimal gauge transformation parameter. The auxiliary fields $\bar{\eta}$ and η are Grassmanian (anti-commuting) scalar fields, called ghosts, that are integrated over in the path integral. They are required for the cancellation of unphysical gauge field degrees of freedom in perturbative computations at one- and higher loop orders. The parameter ξ is real and parametrizes the family of gauges specified by F. The first term in the gauge fixing Lagrangian of Eq. (1.16) contains pieces quadratic in A that modify the operator in Eq. (1.14), allowing it to be inverted.

In unbroken gauge theories such as QCD it is often useful to work in a Lorentz covariant gauge, with a popular choice being

$$F[A] = \partial_\mu A^\mu. \tag{1.18}$$

With this gauge fixing Eq. (1.14) becomes

$$(-k^2 g_{\mu\nu} + (1 - \frac{1}{\xi}) k_\mu k_\nu) D^{\nu\rho} = i\delta^\rho_\mu, \tag{1.19}$$

which can be solved for $D^{\nu\rho}$, because the operator on the left hand side is now invertible. Different forms of F lead to different forms of the vector propagator.

There exists a more convenient choice of the gauge fixing functional for spontaneously broken theories. With SSB, the Higgs kinetic terms in Eq. (1.4) give rise to a mixing between the gauge bosons and Goldstone bosons via bilinear terms like

$$\mathscr{L}_{\text{kin}} \supset igA^a_\mu(\partial^\mu H^\dagger t^a \langle H\rangle - \langle H^\dagger\rangle t^a \partial^\mu H), \tag{1.20}$$

where $\langle H\rangle$ is the Higgs field vev. To avoid mass matrix diagonalization, the mixing can be removed by choosing

$$F^a[A] = \partial^\mu A^a_\mu - i\xi g(H^\dagger t^a \langle H\rangle - \langle H^\dagger\rangle t^a H). \tag{1.21}$$

This family of gauges is known as the R_ξ gauges. The full SM Lagrangian which contains gauge fixing for the entire $SU(3)_C \times SU(2)_L \times U(1)_Y$ and the corresponding ghost terms is presented in, e.g., [23, 25].

1.1.3 Spontaneous Symmetry Breaking and the Physical Spectrum

The $SU(2)_L \times U(1)_Y$ symmetry forbids mass terms for EW gauge bosons and SM fermions. To match observations the SM generates masses dynamically through spontaneous symmetry breaking. The order parameter of the symmetry is the expectation value of the Higgs field; a general vev can always be chosen (using a global $SU(2)_L \times U(1)_Y$ rotation) to be

$$\langle H\rangle = \begin{pmatrix} 0 \\ v/\sqrt{2} \end{pmatrix} \tag{1.22}$$

with v real and positive. At tree-level this pattern of symmetry breaking arises when we take $\mu^2 < 0$ in V_{Higgs} (see Eq. (1.5)). From the Higgs kinetic terms in Eq. (1.4) we obtain mass terms for the $SU(2)_L \times U(1)_Y$ gauge bosons. The mass matrix in the (W^1, W^2, W^3, B) basis is [26]

$$M^2_{\text{gb}} = \frac{1}{4}v^2 \begin{pmatrix} g^2 & 0 & 0 & 0 \\ 0 & g^2 & 0 & 0 \\ 0 & 0 & g^2 & -gg' \\ 0 & 0 & -gg' & g'^2 \end{pmatrix}. \tag{1.23}$$

The upper left 2×2 block has two degenerate eigenvalues that correspond to mass of the charged W bosons

$$W^\pm = \frac{1}{\sqrt{2}}(W^1 \mp iW^2) \tag{1.24}$$

with the value

$$m_W^2 = \frac{1}{4} g^2 v^2. \tag{1.25}$$

The (canonically normalized) combination

$$Z = c_W W^3 - s_W B \tag{1.26}$$

receives the mass

$$m_Z^2 = \frac{1}{4}(g^2 + g'^2) v^2, \tag{1.27}$$

where c_W (s_W) are the cosine (sine) of the Weinberg angle, defined by

$$c_W^2 = \cos^2 \theta_W = \frac{g^2}{g^2 + g'^2}. \tag{1.28}$$

The orthogonal combination

$$A = s_W W^3 + c_W B \tag{1.29}$$

remains massless and is identified with the photon. Thus the full SM gauge symmetry $SU(3)_C \times SU(2)_L \times U(1)_Y$ is broken down to $SU(3)_C \times U(1)_{\rm em}$. From the kinetic terms of Eq. (1.4) it follows that A couples to matter with electromagnetic charge

$$Q = t_L^3 + Y \tag{1.30}$$

in units of $e = g s_W = g' c_W$. The measured masses of the W and Z bosons are $80.385 \pm 0.015\,\text{GeV}$ and $91.1876 \pm 0.0021\,\text{GeV}$ [27]. Together with the Higgs vev, $v \approx 246\,\text{GeV}$, these numbers set the fundamental mass scale of the SM. In the following chapters we will refer to masses and energies of order $\mathcal{O}(100\,\text{GeV})$ as electroweak scales.

As emphasized above, fermion mass generation is *a priori* unrelated to that of the gauge bosons. The SM is economical in that it uses the same Higgs field for both tasks. The fermion mass matrices can be read off from Eq. (1.11) by substituting the Higgs vev, Eq. (1.22), for H:

$$\mathscr{L}_{\rm Yukawa} = -\frac{v}{\sqrt{2}} u_L Y_u u_R^c - \frac{v}{\sqrt{2}} d_L Y_d d_R^c - \frac{v}{\sqrt{2}} e_L Y_e e_R^c + \text{h.c.} \tag{1.31}$$

Note the absence of a mass term for the neutrinos due to lack of a right handed ν. The complex Yukawa matrices Y_i can be diagonalized using two unitary transformations, U and V, corresponding to separate rotations of the L and R type fermions in family space, respectively,

$$f'_L = U_f f_L, \quad f'_R = V_f f_R, \tag{1.32}$$

such that

$$M_f = \frac{v}{\sqrt{2}} U_f^T Y_f V_f \tag{1.33}$$

is diagonal. All gauge interactions, except the quark charged current (CC) terms, are invariant under these rotations; dropping the primes, the CC interactions can be written as

$$\mathscr{L}_{cc} = -\frac{g}{\sqrt{2}} W_\mu^+ \left(\bar{u}_L \bar{\sigma}^\mu V_{\rm CKM} d_L + \bar{\nu}_L \bar{\sigma}^\mu e_L\right) + \text{h.c.}, \tag{1.34}$$

where $V_{\rm CKM} = U_u^\dagger U_d$ is the unitary Cabibbo-Kobayashi-Maskawa (CKM) matrix. Note that there is no equivalent matrix in the lepton sector because the neutrinos are massless in the SM. There are 4 physical parameters in the CKM matrix, including 1 phase [26]. The existence of this complex phase implies that $\mathscr{L}_{cc}$ is not invariant under CP.

The SM and relevant field-theoretic details are described in, e.g., Refs. [20, 23, 25, 26, 28–32]. The historical development of the electroweak theory and chromodynamics is discussed in Refs. [33–35].

1.2 The Standard Model of Cosmology

1.2.1 The Expanding Universe

On cosmological scales the Universe appears approximately isotropic and homogeneous. The most convincing evidence for this is the CMB, which is isotropic to a few parts in 10^{-5} [36]. Any general-relativistic description of our Universe should therefore possess these features. The most general metric satisfying isotropy and homogeneity is the Friedmann-Robertson-Walker (FRW) metric, with [36, 37]

$$ds^2 = dt^2 - a(t)^2 \left(\frac{dr^2}{1-kr^2} + r^2 d\Omega^2\right), \tag{1.35}$$

where $k = -1, 0, +1$ corresponds to constant negative, zero or positive spacial curvature; $d\Omega^2 = d\theta^2 + \sin^2\phi d\phi^2$ is the usual metric on a sphere. Various observations, including the latest results from Planck [38, 39] suggest that the Universe is, to a very good approximation, flat with $k = 0$. Then the physical (proper) distance to an object at radial coordinate r is given by $a(t)r$. The function $a(t)$ is therefore called the scale factor. The present-day scale factor, $a(t_0)$, is usually taken to be 1. When discussing astrophysical observables it is common to use the redshift z instead of a:

$$z(t) = \frac{a(t_0)}{a(t)} - 1, \tag{1.36}$$

where t_0 is the current time. This is a useful quantity since a photon emitted at time t with wavelength λ is observed at time t_0 to have wavelength $(1 + z(t))\lambda$.

The Einstein equations determine the evolution of the metric in the presence of an energy density distribution [37]

$$R_{\mu\nu} = 8\pi G \left(T_{\mu\nu} - \frac{1}{2} g_{\mu\nu} T \right), \tag{1.37}$$

where $R_{\mu\nu}$ is the Ricci tensor (computed from the metric), $T_{\mu\nu}$ is the energy-momentum tensor (the source for the gravitational field), $T = T^{\mu}_{\mu}$, and G is Newton's constant. We will model energy densities as perfect fluids, that is, continuous distributions that are isotropic in their rest frame. The state of such fluid is specified by energy density ρ and isotropic pressure p. The energy momentum tensor for a perfect fluid can be written as [37]

$$T^{\mu\nu} = (\rho + p) U^{\mu} U^{\nu} + p g^{\mu\nu}, \tag{1.38}$$

where U^{μ} is the fluid 4−velocity. In its rest frame, we have $U^{\mu} = (1, 0, 0, 0)$.

For an FRW metric Eq. (1.37) reduces to the two Friedmann equations [37]

$$\frac{\ddot{a}}{a} = -\frac{4\pi G}{3} \rho - \frac{k}{\rho + 3p}, \tag{1.39}$$

and

$$H^2 \equiv \left(\frac{\dot{a}}{a} \right)^2 = \frac{8\pi G}{3} \rho - \frac{k}{a^2}, \tag{1.40}$$

where the Hubble parameter H determines the rate of expansion of the Universe. The current value of the expansion rate, H_0, is often written in terms of a dimensionless number h as $H_0 = 100h$ km sec^{-1} Mpc^{-1}, with $h = 0.673 \pm 0.0012$ [27]. Equation (1.40) is frequently written in dimensionless form as

$$1 = \Omega + \Omega_k, \tag{1.41}$$

with

$$\Omega = \frac{\rho}{\rho_c}, \ \Omega_k = -\frac{k}{a^2 H^2}, \tag{1.42}$$

where the critical density ρ_c is

$$\rho_c = \frac{3H^2}{8\pi G}. \tag{1.43}$$

If the sum of the fluid densities in the Universe is equal to the critical density, the spatial curvature k must vanish. The density parameters Ω are often used to specify the energy

density composition of the Universe.

Another useful relationship is the covariant continuity (or energy-momentum conservation) equation

$$\partial_t \rho + 3H(\rho + p) = 0, \tag{1.44}$$

which follows from the diffeomorphism/coordinate invariance of the matter action

$$S_M = \int d^4x \sqrt{-g} \mathscr{L}_M, \tag{1.45}$$

where g is the determinant of the metric and $\mathscr{L}_M$ is the matter Lagrangian density. For the SM, $\mathscr{L}_M$ is given in Eq. (1.12). Note that the factor $\sqrt{-g}$ gives the *minimal* coupling of matter to gravity. We will make use of this coupling when discussing moduli in Chapters 3 and 4.

The fluids relevant to cosmology obey equations of state of the form

$$p = w\rho, \tag{1.46}$$

with $w = 0, 1/3, -1$ for matter/dust (non-relativistic particles), radiation (relativistic species) and vacuum energy, respectively. In each case the continuity equation, Eq. (1.44), can be solved to yield

$$\rho \propto a^{-3(1+w)}. \tag{1.47}$$

For example dust ($w = 0$) energy density dilutes as a^{-3}, corresponding to the growth of the comoving volume with a^3. If the total energy density ρ is dominated by one fluid, the Friedmann equation, Eq. (1.40), can be solved for the time dependence of the scale factor. For a spatially flat Universe ($k = 0$) we find

$$a \propto \begin{cases} t^{\frac{2}{3(1+w)}} & w \neq -1 \\ \exp(Kt) & w = -1, \end{cases} \tag{1.48}$$

where K is a constant and we only wrote down the expanding solutions. Thus, the change in the rate of expansion depends on the composition of the energy density of the Universe.

Using the above results we can can decompose the total density parameter Ω, defined in Eq. (1.42), into components

$$\Omega = \Omega_r + \Omega_m + \Omega_\Lambda, \tag{1.49}$$

where the three contributions correspond to radiation ($w = 1/3$), matter ($w = 0$) and vacuum energy ($w = -1$). All present measurements are consistent with $\Omega \approx 1$ and $\Omega_k = 0$, so throughout this work we will assume that the Universe is spatially flat with $k = 0$ [27].

1.2.2 Thermodynamics

We will often be interested in the present day abundances of particles that interacted with the hot plasma of the early Universe. The thermodynamic properties of an ensemble of particles are contained in the phase space distribution functions $f_i(p,T)$ where i labels particle species, p is the momentum and T is the temperature. From these distributions we can compute number and energy densities, and pressure [40, 41]:

$$n_i = g_i \int \frac{d^3p}{(2\pi)^3} f_i(p,T), \tag{1.50}$$

$$\rho_i = g_i \int \frac{d^3p}{(2\pi)^3} f_i(p,T) E_i(p), \tag{1.51}$$

$$p_i = g_i \int \frac{d^3p}{(2\pi)^3} f_i(p,T) \frac{p^2}{3E_i} \tag{1.52}$$

where $E_i^2 = p^2 + m_i^2$ and g_i is the number of internal degrees of freedom. In kinetic equilibrium and at zero chemical potential the distributions have the Bose-Einstein or Fermi-Dirac form:

$$f_i(p,T) = \frac{1}{\exp(E_i(p)/T) \pm 1}, \tag{1.53}$$

where $+$ is for fermions and $-$ is for bosons. At a given temperature T it is useful to partition the plasma into relativistic ($T \gg m_i$) and non-relativistic ($T \ll m_i$) components. Assuming kinetic equilibrium, Eqs. (1.50), (1.51), (1.52) can be evaluated in these limits analytically. In the relativistic limit

$$n_i = g_i \frac{\zeta(3)}{\pi^2} T^3 \begin{cases} 1 & \text{bosons} \\ \frac{3}{4} & \text{fermions} \end{cases}, \tag{1.54}$$

$$\rho_i = g_i \frac{\pi^2}{30} T^4 \begin{cases} 1 & \text{bosons} \\ \frac{7}{8} & \text{fermions} \end{cases}, \tag{1.55}$$

$$p_i = \rho_i/3. \tag{1.56}$$

In the non-relativistic limit both distributions reduce to

$$n_i = g_i \left(\frac{m_i T}{2\pi}\right)^{3/2} \exp(-m_i/T), \tag{1.57}$$

$$\rho_i = m_i n_i, \tag{1.58}$$

$$p_i = n_i T. \tag{1.59}$$

Note that the energy density and pressure of relativistic species are parametrically larger than those of non-relativistic states. This means that the total energy density and total pressure of the heat bath are well approximated by the relativistic contributions alone. Summing over all

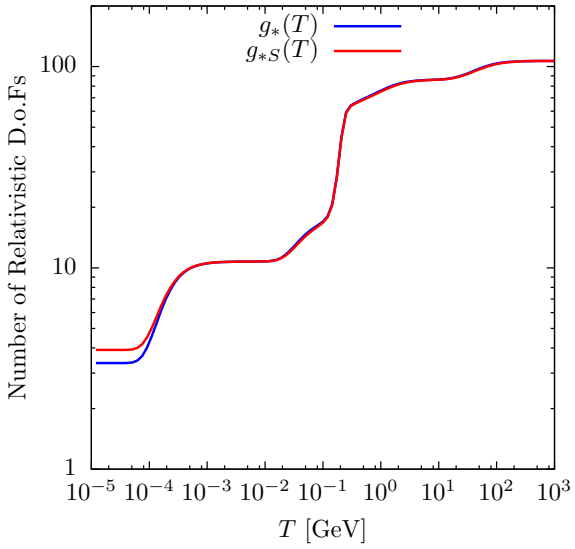

Figure 1.1: Number of energy and entropy relativistic degrees of freedom, g_* and g_{*S}, respectively, for the Standard Model as a function of temperature. The large drop in the number of degrees of freedom at $T \sim 200\,\mathrm{MeV}$ corresponds to the QCD phase transition when quarks and gluons became confined in hadrons.

relativistic species we find the total radiation density and pressure:

$$\rho_R = \frac{\pi^2}{30} g_*(T) T^4 \tag{1.60}$$

$$p_R \approx \rho_R/3, \tag{1.61}$$

where g_* counts the number of relativistic degrees of freedom at temperature T

$$\begin{aligned} g_*(T) &= \frac{15}{\pi^4} \sum_i g_i \left(\frac{T_i}{T}\right)^4 \int_{x_i}^{\infty} \frac{(u^2 - x_i^2)^{1/2} u^2}{\exp(u) \pm 1} du \\ &\approx \sum_{i=\text{bosons}} g_i \left(\frac{T_i}{T}\right)^4 + \frac{7}{8} \sum_{i=\text{fermions}} g_i \left(\frac{T_i}{T}\right)^4, \end{aligned} \tag{1.62}$$

where $x_i = m_i/T_i$, T_i is the temperature of species i, and T is the photon temperature; the last equality follows for $x_i \ll 1$ and the observation that non-relativistic species do not contribute significantly to ρ_R.[3] The integral in Eq. (1.62) smoothly removes non-relativistic species from the summation. This function for the SM fields is shown in Fig. 1.1 as the solid blue curve. The large decrease in g_* at $T \sim 200\,\mathrm{MeV}$ corresponds to the QCD phase transition when free quarks and gluons condensed into hadrons.

We can use the above results to derive the evolution of radiation and entropy density in the

[3]The function g_* for pressure is numerically different from g_* defined above due to different integrands in Eq. (1.51) and (1.52). $p_R = \rho_R/3$ exactly only when $x_i = 0$.

expanding Universe. In the absence of energy injection, the First Law of thermodynamics

$$dU + PdV = 0, \tag{1.63}$$

with total energy U and pressure P, as applied to the radiation bath gives

$$a^3 d\rho_R + (\rho_R + p_R) da^3 = 0. \tag{1.64}$$

Using Eq. (1.61) we can write this as

$$\dot{\rho}_R + 4H\rho_R = 0. \tag{1.65}$$

In equilibrium, entropy S is conserved:

$$0 = dS = d(sV) = \frac{d(\rho V) + pdV}{T}, \tag{1.66}$$

where we used the fundamental thermodynamic relation, $TdS = dU + pdV$, in the second step and defined the entropy density s as [36]

$$s = \sum_i \frac{\rho_i + p_i}{T_i}. \tag{1.67}$$

As for the energy, the entropy density is dominated by relativistic species. Using the definitions of Eq. (1.51) and (1.52) we can rewrite this as

$$s = \frac{2\pi^2}{45} g_{*S}(T) T^3, \tag{1.68}$$

where

$$\begin{aligned} g_{*S}(T) &= \frac{45}{4\pi^4} \sum_i g_i \left(\frac{T_i}{T}\right)^3 \int_{x_i}^{\infty} \frac{(u^2 - x_i^2)^{1/2} u^2}{\exp(u) \pm 1} du \\ &\approx \sum_{i=\text{bosons}} g_i \left(\frac{T_i}{T}\right)^3 + \frac{7}{8} \sum_{i=\text{fermions}} g_i \left(\frac{T_i}{T}\right)^3, \end{aligned} \tag{1.69}$$

When all species have the same temperature $g_{*S} \approx g_*$; however, when a relativistic species decouples from the bath and $T_i \neq T$, $g_{*S} \neq g_*$. This can be seen in Fig. 1.1 at low temperatures, where g_{*S} is shown as the solid red curve. The difference is due to the decoupling of neutrinos at $T \sim 1\,\text{MeV}$ and the subsequent e^+e^- annihilation for $T \lesssim 2m_e$ (when they become non-relativistic). The annihilations deposit energy into the photon bath, but not into the neutrinos (since they are decoupled), leading to $T/T_\nu = (11/4)^{1/3}$ at late times [36, 40].

When a massive species decouples from the plasma, its comoving number $N = na^3$ is (approximately) conserved until present day, unless it decays. Such relics will play key roles

in Chapters 3 and 4 where we consider dark matter and baryon production. At high enough temperatures, a particle χ is kept in *chemical* equilibrium with the thermal bath through interactions like $\chi\bar{\chi} \leftrightarrow X\bar{X}$, where X is part of the plasma. For example for $T \gtrsim 1\,\mathrm{GeV}$, χ could be a quark and X a gluon. If equilibrium persists sufficiently long, and χ is stable, it becomes non-relativistic as the Universe cools and since $n_\chi \propto \exp(-m/T)$, its density will become negligible. However, if the interactions that keep χ in equilibrium are not fast enough to keep up with the expansion of the Universe, the number density will become frozen-in. This happens approximately when the interaction rate

$$\Gamma = \langle \sigma v \rangle n_\chi \tag{1.70}$$

falls below the Hubble expansion rate H, where $\langle \sigma v \rangle$ is the thermally averaged interaction rate (defined below). This freeze-out mechanism is quantitatively described by the Boltzmann equation. In its most fundamental form the Boltzmann equation describes the time evolution of the particle phase space density $f(p)$

$$L[f] = C[f], \tag{1.71}$$

where $L = d/dt$ is the Liouville operator, given by [40–42]

$$L = \frac{\partial}{\partial t} - H\frac{|\mathbf{p}|^2}{E}\frac{\partial}{\partial E}, \tag{1.72}$$

for a spatially homogeneous distribution in the FRW spacetime and $C[f]$ is the collision term that encodes particle interactions. By integrating over phase space, one obtains a time evolution equation for number densities,

$$\dot{n}_i + 3Hn_i = g_i \int C[f_j]\frac{d^3p}{(2\pi)^3 E_i} \tag{1.73}$$

The general collision term C is a complicated expression that depends on matrix elements for the forward and reverse reactions, as well as the phase space densities of all of the interacting particles. We will be primarily interested in decays and $2 \to 2$ scattering reactions. Several assumptions can be used to simplify $C[f]$:

1. Kinetic and thermal equilibrium is attained immediately by the annihilation products X and $\bar{X}$, implying that their interactions with the plasma must be relatively strong. This will be the case when X is a SM state.

2. Maxwell-Boltzmann statistics is valid, which is a good assumption for non-degenerate gases with $T \lesssim 3m$ [42].

Under these assumptions, the collision term for a reaction of the type $12 \to 34$ reduces to

$$g_1 \int C[f_j] \frac{d^3p}{(2\pi)^3 E_1} = -\langle \sigma v \rangle (n_1 n_2 - n_1^{\rm eq} n_2^{\rm eq}), \tag{1.74}$$

where

$$\langle \sigma v \rangle_{12\to 34} = \frac{\int \sigma v_{\rm M\o l} e^{-E_1/T} e^{-E_2/T} d^3p_1 d^3p_2}{\int e^{-E_1/T} e^{-E_2/T} d^3p_1 d^3p_2}, \tag{1.75}$$

$$v_{\rm M\o l} = \frac{\sqrt{(p_1 \cdot p_2)^2 - m_1^2 m_2^2}}{E_1 E_2}, \tag{1.76}$$

and $n^{\rm eq}$ is given by Eq. (1.57). The cross section σ for $12 \to 34$ is computed using the usual Feynman rules. For many cases of interest decoupling of a particle from the plasma occurs when it is already non-relativistic, in which case Eq. (1.75) admits a simple expansion in $m/T \gg 1$ [42].

We can now write down the simplest Boltzmann equation for a single self-conjugate species χ annihilating into SM particles:

$$\dot{n}_\chi + 3Hn_\chi = -\langle \sigma v \rangle \left(n_\chi^2 - (n_\chi^{\rm eq})^2 \right). \tag{1.77}$$

The solution of this equation for $m_\chi = 100\,{\rm GeV}$ and $\sigma \sim 10^{-11}\,{\rm GeV}^{-2}$ is shown in Fig. 1.2. Note that at early times the comoving number density $N = n_\chi a^3$ tracks the equilibrium, until the $\chi\chi$ annihilations freeze-out. This occurs at $x_f = m_\chi/T_{\rm fo} \sim 20$, so χ decouples when it is already non-relativistic. In this simple scenario it is possible to analytically estimate both the freeze-out point x_f and the final abundance of Ω_χ. The freeze-out temperature can be found using the decoupling condition, Eq. (1.70) [40, 43]:

$$x_f = \ln \left(\sqrt{\frac{45}{4\pi^5}} \frac{g_\chi}{\sqrt{g_*}} m_\chi M_{\rm Pl} \langle \sigma v \rangle \right) - \frac{1}{2} \ln x_f, \tag{1.78}$$

where $M_{\rm Pl} = 2.435 \times 10^{18}\,{\rm GeV}$ is the reduced Planck mass. In particular, note that x_f is only logarithmically sensitive to m_χ and $\langle \sigma v \rangle$, so $x_f \sim 20$ is generic for weak-scale masses and cross-sections. The approximate abundance can be obtained by matching the early-time solution (which tracks $n_\chi^{\rm eq}$) with the late-time solution (where $n_\chi^{\rm eq}$ can be neglected) [40], with the result

$$\Omega_\chi = \frac{m_\chi n_\chi}{\rho_c} = h^{-2} \left(\frac{2 \times 10^{-10}\,{\rm GeV}^{-2}}{\langle \sigma v \rangle} \right) \left(\frac{x_f}{20} \right) \left(\frac{g_*(T_{\rm fo})}{85} \right)^{-1/2}. \tag{1.79}$$

Note that the abundance is inversely proportional to the annihilation cross-section: the more effective $\chi\chi$ annihilations are, the smaller the final abundance.

The above results hold for a single particle with a cross section constant with T. In realistic

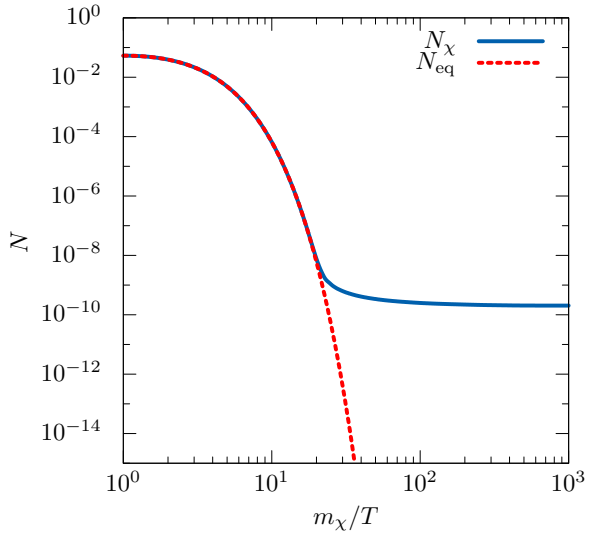

Figure 1.2: Comoving number density $N = n_\chi a^3$ (solid line) of a self-conjugate particle χ as a function of m_χ/T. The equilibrium number density is shown as a dashed line. Freeze-out occurs at $m_\chi/T \sim 20$.

models, there can be other states present in the plasma that interact with the long-lived particle of interest. The annihilation rate can have important features as a function of T, such as resonances when intermediate states go on shell. These and other effects can significantly modify the final abundance [43].

1.2.3 The First 400 000 Years

Having discussed thermodynamics in an expanding Universe, we can begin to reconstruct the thermal history of the Universe. Here we highlight some of the key events. We start at $t \sim 10^{-43}$ s, corresponding to temperatures $T \sim 10^{18}\,\text{GeV}$, where a theory of quantum gravity is required even for a qualitative description. Shortly after this, inflation or another mechanism operates to solve the horizon and flatness problems [44]. The evolution down to $T \sim 10^3\,\text{GeV}$ has not been probed experimentally, but many models of baryogenesis and neutrino mass generation operate above this energy [45, 46]. As we cool further and cross the TeV threshold at $t \sim 10^{-13}$ s, we enter the realm of energies that *have* been probed experimentally. At $T \sim 100\,\text{GeV}$ ($t \sim 10^{-11}$ s), the Universe undergoes the electroweak phase transition (EWPT) where $SU(2)_L \times U(1)_Y$ is broken down to $U(1)_{\rm em}$. The QCD chiral phase transition at $T \sim 200\,\text{MeV}$ ($t \sim 10^{-5}$ s) occurs when quarks and gluons condensed into hadrons. Neutrinos decouple at $T \sim 1\,\text{MeV}$ ($t \sim 1$ s), fixing the neutron to proton ratio. Big Bang Nucleosynthesis begins shortly after at $T \sim 0.1\,\text{MeV}$ ($t \sim 10^2$ s) when the primordial plasma is cool enough to not disassociate the majority of newly formed nuclei. The matter density becomes comparable to radiation density at $T = 1$ eV ($t = 10^4$ years), initiating structure formation. Finally, baryons recombine with

electrons at $T \sim 0.1$ eV ($t \sim 4 \times 10^5$ years), making the Universe transparent to photons. The free-streaming photons from that era make up the CMB.

The above history is the canonical account of early Universe cosmology. In particular, it assumes that the Universe remains radiation-dominated until matter-radiation equality at $T = 1$ eV. As we will discuss in Chapters 4 and 3, this idea is experimentally grounded only for $T \lesssim 5\,\mathrm{MeV}$. There we will consider modifications to this radiation-dominated scenario.

1.3 Outstanding Problems

Despite their innumerable successes, the Standards Models are incomplete. Below we list some of the major motivations for new physics. In the following, chapters we consider models that attempt to explain one or more of the following: the hierarchy problem, the baryon asymmetry of the Universe and dark matter. These are discussed in detail in Sections 1.3.1, 1.3.2 and 1.3.3, respectively. This is far from an exhaustive list. Other important issues in particle physics include the origins of neutrino masses and the flavour structure of the SM, the strong CP and the cosmological constant problems [47]. The latter, in particular, indicates that something fundamental is missing in our understanding of gravity and particle physics.

1.3.1 Hierarchy Problem and Naturalness

The Higgs boson mass was measured to be ~ 125 GeV [6]. In order to relate this observation to other parameters in the theory, we must compute quantum corrections shown in Fig. 1.3, which contain ultraviolet (UV) divergent integrals over spacetime, that must be regulated. For example, a fermion with mass M_f, N_c colours and Yukawa coupling $yh\bar{f}f/\sqrt{2}$ shifts the mass by

$$m_h^2 = m_0^2 - \frac{y^2 N_c}{8\pi^2}\Lambda^2 + \ldots, \tag{1.80}$$

where the loop integral corresponding to the left diagram in Fig. 1.3 has been regulated using the momentum cutoff Λ; the ellipsis stands for terms that are at most logarithmically divergent as $\Lambda \to \infty$. The SM is a valid effective field theory for energies below Λ. If Λ is much bigger than the electroweak scale ~ 100 GeV, then to get $m_h = 125$ GeV we must tune the tree-level parameter m_0^2 very precisely to cancel the large contribution from new physics at scale Λ. We expect new degrees of freedom to exist at several possible scales associated with, e.g., neutrino mass generation, unification, or, at the very least, quantum gravity. Taking $\Lambda \sim M_{\rm Pl}$, we find that m_0^2 has to be chosen with a precision of *one part in* 10^{32}. This is called the fine-tuning or naturalness problem. Equivalently, it is a statement about the enormous hierarchy in energy scales between gravitational and electroweak physics. In absence of symmetry, one would naturally expect $m_h \sim M_{\rm Pl}$ and similar strengths of weak and gravitational interactions.

The disturbing precision of the required cancellation has been a strong motivation for the development of models where the quadratic divergence in Λ is absent and m_h is natural. The

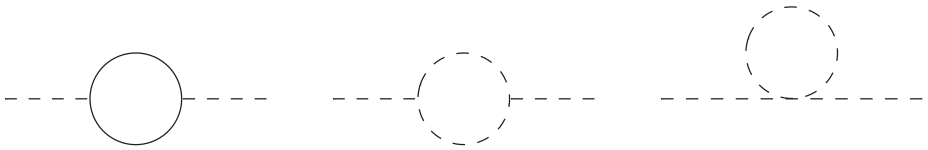

Figure 1.3: Possible contributions to the Higgs mass parameter from fermions (left graph) and scalars (middle and right graphs). The momentum integrals associated with these graphs are UV divergent and give rise to the fine-tuning problem.

solutions can be divided into several categories. First, we may introduce a symmetry that regulates the size of these large quantum corrections. For example, suppose that in addition to the new fermion, there exist a pair of complex coloured scalars $\phi_{L,R}$ of mass M_s that couple to the Higgs boson via

$$\mathscr{L} \supset -\frac{\lambda}{2}(v+h)^2(|\phi_L|^2 + |\phi_R|^2). \tag{1.81}$$

The corresponding quantum corrections are computed from the middle and right graphs of Fig. 1.3; only the right diagram is quadratically divergent with the result

$$m_h^2 = m_0^2 + \frac{\lambda N_c}{8\pi^2}\Lambda^2 + \dots \tag{1.82}$$

In particular, if $\lambda = y^2$ the Λ^2 contributions to the Higgs self-energy cancel exactly with that coming from the fermion, and no fine tuning would be required to have m_h at the electroweak scale. The cancellation of quadratic divergences does not depend on the mass difference $M_f - M_s$; the logarithmic divergences (not written) cancel if $M_f = M_s$. This is exactly what happens in supersymmetry, which we discuss in Ch. 2. Shift symmetries $h \to h + \alpha$ can also forbid large quantum corrections, resulting in technically natural m_h. Such symmetries are associated with Nambu-Golsdstone bosons (NGBs) of spontaneously broken global symmetries. Since NGBs are massless and the Higgs is not, the symmetry must be broken explicitly in analogy to pion mass generation and the breaking of the chiral $SU(2)$ by non-degenerate quark masses. The class of models where the Higgs boson is a pseudo-NGB are known as Little Higgs theories [48]. In both cases, naturalness demands the existence of new states that couple strongly to the Higgs with masses close to the electroweak scale. Other explanations include compositeness of the Higgs [49] and extra dimensions [50, 51]

It is also possible that the Higgs mass is *not* natural and fine-tuning is required for life to exist. However, such anthropic arguments are less convincing for the case of Higgs mass (as opposed to the cosmological constant), since one can get a habitable Universe even when $m_h \sim M_{\rm Pl}$ [52]. Anthropic reasoning often emerges in the context of the string theory landscape [53].

1.3.2 Baryon Asymmetry of the Universe

Relativistic field theory requires the existence of antimatter. Each anti-particle has opposite gauge charges but otherwise identical properties to the corresponding particle [45]. It is then puzzling why the local Universe seems to be composed of entirely of matter and not anti-matter. It is conceivable that the Universe is actually baryon-symmetric – domains of matter are spatially separated from domains of antimatter. However, pair annihilation at interfaces of such regions would produce unacceptably high gamma ray fluxes, unless the regions are separated by distances greater than 10 Mpc (roughly the size of the Virgo cluster) [40]. Still, annihilation is inevitable, unless the domains are separated by enormous voids. These voids would appear as inhomogeneities in the CMB [45, 54].

Ignoring the above difficulties, suppose the Universe *is* baryon-symmetric. At high temperatures baryons are kept in equilibrium with the plasma by pair annihilations with $\langle \sigma v \rangle \sim m_\pi^{-2} = 5 \times 10^{-5}\,\mathrm{GeV}^2$. These interactions freeze-out via the mechanism discussed in Sec. 1.2.2 when $T_{\mathrm{fo}} \approx 20\,\mathrm{MeV}$ (from Eq. (1.70)), resulting in baryon abundance that is 9 orders of magnitude too small [40]. This means that either some mechanism separated baryons from antibaryons before the annihilations depleted the abundance, or, there was a slight excess of matter over antimatter, such that only the asymmetry remained at late times. In the former case, the mass of baryons contained within the horizon at that time was a fraction of a solar mass, so the mechanism that separates cluster-sized masses of baryons and antibaryons would have to violate causality [40]. Thus, in this work we consider only the latter possibility.

The observed baryon to photon ratio, $\eta = n_B/n_\gamma = 6.19 \times 10^{-10}$ suggests that at temperatures above 1 GeV the excess of quarks over antiquarks was tiny: about one more quark per every thirty million antiquarks [40]. This asymmetry can be an initial condition or it can be generated dynamically. The initial condition hypothesis is impossible to test, so we consider theories of dynamical baryogenesis instead. Sakharov outlined the general conditions necessary to generate this asymmetry in the early Universe [55]:

1. Baryon number must be violated in order to generate $B \neq 0$ from a symmetric initial state.

2. C (charge conjugation invariance) and CP (charge-parity conjugation invariance) must be violated to produce more baryons than antibaryons. Given a process $i(\{\mathbf{s}_i\},\{\mathbf{p}_i\}) \to f(\{\mathbf{s}_f\},\{\mathbf{p}_f\})$ that produces baryon number, its charge conjugate $\bar{i} \to \bar{f}$ yields opposite baryon number.[4] If the rates are equal, there is no net asymmetry produced. Since local Lorentz invariant theories conserve CPT, CP invariance is equivalent to time-reversal invariance T. If the rate for the T-conjugate process $f(\{-\mathbf{s}_f\},\{-\mathbf{p}_f\}) \to i(\{-\mathbf{s}_i\},\{-\mathbf{p}_f\})$ is equal to $i(\{\mathbf{s}_i\},\{\mathbf{p}_i\}) \to f(\{\mathbf{s}_f\},\{\mathbf{p}_f\})$, no net asymmetry is produced.

3. There must be a departure from thermal equilibrium, since the rates for $i \to f$ and $f \to i$ are equal in equilibrium.

[4] $\{\mathbf{s}_{i,f}\}$ and $\{\mathbf{p}_{i,f}\}$ represent the sets of spins and momenta in the initial or final state.

The SM has all of the above ingredients: non-perturbative $SU(2)_L$ processes can provide $B \neq 0$, while the single phase in the CKM matrix violates C and CP. The departure from thermal equilibrium is achieved if the electroweak phase transition is first order: bubbles of phase with non-vanishing Higgs vev nucleate within the plasma, expand and collide until $SU(2)_L \times U(1)_Y$ is broken everywhere. This process is described in more detail in Sec. 7.1. In the SM, the EW phase transition proceeds in that way only if the Higgs boson is light, i.e., $m_h \leq 70$ GeV [56], in conflict with the observed value of ~ 125 GeV. Thus this mechanism does not work in the SM alone and new physics is required.

In this work we focus on the third requirement, the departure from equilibrium. We consider two different ways to achieve this. In Ch. 4, we investigate a scenario with an out-of-equilibrium decay of a new heavy particle. In Ch. 7, we augment the SM with extra matter to ensure that the EW phase transition *is* first order and therefore suitable for baryogenesis.

1.3.3 Dark Matter

Observations of radial velocities of galaxies in the Coma cluster provided the first hint for the existence of dark matter [57–59]. Later, measurements of orbital speeds of visible objects inside galaxies (i.e., galactic rotation curves) indicated that the galactic mass distribution must extend beyond luminous matter [60].[5] Consider a visible object on a stable orbit around a galaxy. Assuming Newtonian gravity is valid, the orbital speed for a body at distance r from the galactic center is

$$v = \sqrt{\frac{GM(r)}{r}}, \tag{1.83}$$

where $M(r)$ is the mass enclosed by the trajectory. In particular, if only luminous matter contributes to M, beyond the visible part of the galaxy M is constant, so the orbital speed must decrease as $v \propto r^{-1/2}$. However observations of many galaxies indicate that the speed does not decrease at all, but flattens out, implying that $M \propto r$ in this region. This suggests the existence of a spherical dark matter halo that extends beyond luminous matter, with density falling as $\rho \propto r^{-2}$. This gives rise to the idea that galaxies are embedded in halos of non-luminous, dark matter (DM) [61]. Since the initial measurements on cluster scales, the DM hypothesis has received support from an array of observations over a wide range of distance scales, from sub-galactic to cosmological. For example, gravitational lensing of galaxies and clusters is sensitive to the total amount of matter in the lens [62]. These measurements unequivocally show that the amount of matter in these objects is much larger than what is visible. The possibility that this missing matter is in the form of massive compact halo objects (MACHOs) is excluded by microlensing surveys of nearby satellite galaxies [62].

An even more stringent limit on the baryonic contribution to total matter abundance in

[5] These measurements are usually done using the 21 cm line from Hydrogen hyperfine splitting and optical surface photometry [61].

the Universe comes from Big Bang Nucleosynthesis (BBN). Nucleosynthesis is the earliest epoch in the history of the Universe that is probed observationally, corresponding to times on the order of 1 second after the Big Bang. Standard BBN has been very successful in predicting the present-day abundances of the light elements such as helium, deuterium and lithium [63].[6] Nucleosynthesis predictions are very sensitive to the nucleon to photon ratio η with the equilibrium abundance of element with atomic number A proportional to η^{A-1} [40]. As a result, the observed light element abundances constrain the baryonic contribution to total matter density to be [27]

$$\Omega_b \sim m_b n_\gamma \eta / \rho_c \lesssim 0.053. \tag{1.84}$$

This upper bound on baryonic matter in nucleons combined with total matter density measurements from dynamical (i.e., rotation curves) means and lensing imply that most of the matter content of the Universe is in the form of DM. Note that, if there exist exotic quark "nugget" bound states with a sufficiently strong binding, they will not participate in in BBN and DM *can* be of baryonic origin – see Ref. [66] for a review of this possibility.

The most precise determination of DM abundance in the Universe comes from fits to cosmological data from the expansion of Universe, galaxy clustering, CMB power spectra and other measurements. The CMB power spectrum, in particular, is sensitive both to the total amount of matter and its baryonic fraction. For temperatures above about 1 eV, the primordial plasma is ionized and the baryon fluid is coupled to the photon fluid via electromagnetic interactions (for a review of CMB physics, see, e.g., Refs. [27, 67]).[7] This coupled fluid oscillates in the gravitational potential established by DM over/under-densities, leading to temperature anisotropies on top of a nearly perfect black body spectrum. The CMB power spectrum of these anisotropies has been subject of intense experimental study, culminating with the Planck mission, which provided the most precise measurements of the temperature power spectrum to date.[8] Fitting the standard cosmological model to the latest Planck data yields a baryon abundance [17] of

$$\Omega_b = 0.049 \pm 0.002 \tag{1.85}$$

and total matter abundance of

$$\Omega_m = 0.315 \pm 0.013. \tag{1.86}$$

This incredibly precise measurement of the matter density on *cosmological* scales again requires

[6] At present, the prediction for ^{7}Li is inconsistent with the CMB measurement of η. This is known as the Lithium problem [64]. Possible solutions can include astro- and nuclear physics effects, as well physics beyond the Standard Model [65].

[7] In the astrophysics community "baryon" refers to all SM particles, including baryons and leptons [68].

[8] Planck is able to detect angular variations of $\sim 0.1^\circ$ on the sky. Ground based telescopes can attain even higher resolution.

a large component of non-baryonic DM.

Finally, DM is necessary for the formation of large scale structure consistent with what is observed today in galactic surveys [69]. The growth of the initial density perturbations in the primordial plasma occurs at different rates in the matter and radiation-dominated phases. Gravitational collapse is more efficient during matter domination, which does not occur early enough with only baryonic matter to reproduce the observed matter power spectrum [62]. If matter has a significant non-baryonic component that is not strongly coupled to photons, then the matter dominated epoch can begin earlier. The DM hypothesis thus provides an excellent fit to the matter power spectrum from cosmological scales down to ~ 0.1 Mpc (see, e.g., [70]).

The validity of the cold (i.e., non-relativistic), non-interacting DM fluid on small scales ($\lesssim 10$ kpc, corresponding to small galaxies and inner regions of larger ones) has been less certain, as several apparent conflicts between astrophysical observations and many-body simulations emerged. These difficulties are reviewed in Ref. [71, 72] and are called "core vs cusp", "missing satellites" and "too big to fail" problems. The first of these is the statement that DM-only many-body simulations predict a DM density profile with a cusp near the galactic center, which provides a poor fit to the inner regions of real galactic rotation curves. Moreover, these simulations produce many more small satellite galaxies (dwarves) than observed in the vicinity of the Milky Way. This is the missing satellites problem. Some of these missing DM halos are so massive that it is puzzling that they have failed to form stars. These issues are facets of the same problem: *DM-only* simulations predict more substructure than what is observed. This has motivated modifications of the standard cold DM paradigm that included warm (semi-relativistic) and self-interacting DM. The former allows DM to stream out of gravitational wells, washing out structure of sizes smaller than the free-streaming length; self-interacting DM results in a hotter halo core that prevents the formation of cusps [68]. However, as emphasized above, the simulations that lead to these small scale structure anomalies have not included baryonic physics. These effects include gas outflows, energy feedback from stars and supernovae and can significantly alter galactic evolution and the form of the resulting DM distribution through gravitational interactions [68].

Having discussed the successes and difficulties of the dark matter framework, it is important to note that it is *not* the only logical possibility to explain the above *purely gravitational* observations. In principle, this can also be done by modifying general relativity. In practice, this is difficult because of the vast range of length scales spanned by these observations (see [73] for an example of problems faced by modified gravity). Hence in this thesis we assume that DM is a new particle or a set of particles. With this in mind, DM must be long-lived, massive, non-relativistic during structure formation and interact only weakly with photons. The SM of particle physics lacks such a particle and we must look beyond the SM for suitable candidates.

Even with the above requirements, the nature of DM is difficult to determine from cosmological data alone, with DM masses in viable models spanning ~ 31 orders of magnitude from $10^{-15}\,\mathrm{GeV}$ for axion DM to $10^{16}\,\mathrm{GeV}$ for "WIMPzillas", with interaction strengths varying

across an even wider range [74]. We will focus on a well-motivated class of DM candidates with masses in the range $1 - 1000\,\mathrm{GeV}$ and weak-scale couplings to ordinary matter. This is the domain of the weakly interacting massive particle (WIMP). Stable particles in this mass range frequently arise in extensions of the SM that address other issues, such as the hierarchy problem. Perhaps the best studied examples of WIMPs are the neutralinos of supersymmetric theories [75], where DM production occurs through the thermal freeze-out process described in Sec. 1.2.2.

Much of the experimental effort in the search for DM is focused on WIMPs. The experiments fall into three broad categories. Direct detection searches for collisions of DM particles in the halo with nuclei in ultra-sensitive detectors. The present status and future prospects for these experiments are reviewed in Ref. [76]. There have been many observed event excesses in the last few years, but they have not been corroborated by competing groups. The second class of experiments searches for energetic DM annihilation products from astrophysical sources, such as the Galactic Center and dwarf galaxies. The products can be cosmic rays, diffuse or line-like gamma rays or neutrinos. Both indirect and direct detection are subject to many astrophysical uncertainties, such as DM substructure and poorly understood backgrounds [77, 78]. Finally, there are accelerator based methods that seek to *produce* DM and associated particles in the laboratory, as opposed to detecting relic DM. Since DM is stable and is expected to be weakly interacting, it escapes the detector giving a "missing energy" signal. Searches for such signals give a complementary probe of the "dark sector", since astrophysical uncertainties are absent. For a brief review of recent work in this direction see Ref. [79].

Chapter 2

Aspects of Supersymmetry

2.1 Introduction

The search for solutions to problems in particle physics and cosmology described in the previous chapter has lead to the development of a wide variety models for physics beyond the standard models. Supersymmetry (SUSY) has emerged as one of the most fruitful of these ideas, providing a powerful framework for tackling problems of naturalness, dark matter, baryogenesis, and gauge coupling unification [80]. Aside from these phenomenological benefits, SUSY enables effective study of field theories in non-perturbative regimes through its dualities and non-renormalization theorems (for a detailed introduction, see, e.g., Ref. [81]). For example, it is possible to prove confinement in some theories with extended SUSY [82]. Finally, SUSY provides a connection to most consistent formulations of string theory, which require supersymmetry, at least at string scales.

All possible symmetries of the scattering (S) matrix have been analyzed in the "no-go" theorem of Coleman and Mandula [83]. The Coleman-Mandula theorem states that the full symmetry group of the S-matrix is necessarily the direct product of the Poincaré spacetime symmetry and any internal symmetries. This means that it is not possible to augment spacetime symmetries with, e.g., gauge symmetries. That is, the generators of the new symmetries must be Poincaré scalars, carrying no spacetime indices. Otherwise, the S-matrix would be trivial and no interactions would occur. The theorem assumes bosonic generators (those that obey commutation relations) for the symmetry groups, leaving the possibility of anti-commuting (fermionic) generators.[1] In this sense, SUSY is the *unique* extension of the usual Poincaré symmetry that incorporates fermionic generators into the group algebra [84]. Qualitatively, the action of the SUSY generators Q on states of definite statistics is [80]

$$Q|\text{boson}\rangle = |\text{fermion}\rangle, \quad Q|\text{fermion}\rangle = |\text{boson}\rangle. \tag{2.1}$$

[1] Another assumption is the existence of a mass gap between the vacuum and first excited state, which does not occur in conformal field theories (CFTs). However, CFTs do not contain particle-like excitations and, therefore, are not appropriate for the description of particle physics near electroweak scales.

In order for the above to make sense, Q must carry a fermionic (i.e., a spacetime) index. Supersymmetry adds to the standard Poincaré algebra of translations, boosts and rotations, the following relations[2] [81, 85]

$$\{Q^A_\alpha, Q^B_\beta\} = \{Q^\dagger_{\dot\alpha\, A}, Q^\dagger_{\dot\beta\, B}\} = 0, \tag{2.2}$$

$$[P_\mu, Q^A_\alpha] = [P_\mu, Q^\dagger_{\dot\alpha\, A}] = 0, \tag{2.3}$$

$$\{Q^A_\alpha, Q^\dagger_{\dot\alpha\, B}\} = -2\sigma^\mu_{\alpha\dot\alpha} P_\mu \delta^A_B. \tag{2.4}$$

Here α and $\dot\alpha$ are two-component spinor indices; $A,\ B = 1, \ldots, \mathcal{N}$ label different generators; P_μ is the energy momentum operator (generator of spacetime translations); $\sigma^\mu = (1, \sigma^i)$ where σ^i are the Pauli matrices. Theories with $\mathcal{N} > 1$ are called extended supersymmetry. In these theories fermions arise in vector pairs – one can always write down gauge invariant mass terms. This is unlike the SM, which is a chiral theory. Thus $\mathcal{N} = 1$ SUSY is considered to be more applicable for extending the SM [81]. In the following, we work only with $\mathcal{N} = 1$, so we can drop the labels A and B.

Chapters 3, 4 and 6 make extensive use of supersymmetric model building. Therefore this chapter is devoted to the introduction of some of the relevant techniques. The outline of this chapter is as follows. In Sec. 2.2 we describe the superspace formalism for writing down supersymmetric theories. In Sec. 2.3 we introduce the minimal supersymmetric extension of the SM and discuss some benefits of SUSY. We discuss supersymmetry breaking in Sec. 2.4 and review current status of experimental searches in Sec. 2.5.

2.2 Superspace

In the following chapters we will frequently need to construct supersymmetric models. In this section we outline the formalism of superspace, which efficiently encodes interactions of supersymmetric theories.

Poincaré invariance is guaranteed if we construct the action S from the unrestricted spacetime integral over a Lorentz scalar Lagrangian density $\mathscr{L}$:

$$S = \int d^4x \mathscr{L}. \tag{2.5}$$

Similarly, it is useful to implement supersymmetric invariance using an integral over a "superspace", where SUSY transformations are represented simply as translations. As with the Lorentz group, it is useful to work with irreducible representations of the symmetry algebra. Superspace facilitates this as well, by allowing us to write a supermultiplet (which contains bosonic and fermionic degrees of freedom) as a single superfield. To achieve this, superspace is parametrized by the spacetime coordinate x^μ (mass dimension -1) and Grassman number (anti-commuting) spinors θ^α and $\bar\theta_{\dot\alpha}$ (mass dimension -1/2). A general function on superspace

[2] Here we show only a subset of the entire supersymmetry algebra. The complete set can be found in Ref. [85].

can be expanded in a Taylor series that terminates due to the anti-commuting nature of θ and $\bar{\theta}$. For example, a general Lorentz scalar superfield is given by [86]:

$$T = a + \theta\xi + \theta^2 b + \bar{\theta}\bar{\chi} + \bar{\theta}\bar{\sigma}^\mu\theta v_\mu + \theta^2\bar{\theta}\bar{\zeta} + \bar{\theta}^2 c + \bar{\theta}^2\theta\eta + \theta^4 d, \tag{2.6}$$

where Greek (Roman) letters denote fermions (bosons). Note that there are 8 complex bosonic and 8 complex fermionic degrees of freedom. The superspace translations by an infinitesimal spinor ϵ^α

$$\begin{aligned} \theta^\alpha &\to \theta^\alpha + \epsilon^\alpha, \\ \bar{\theta}_{\dot{\alpha}} &\to \bar{\theta}_{\dot{\alpha}} + \bar{\epsilon}_{\dot{\alpha}}, \\ x^\mu &\to x^\mu + \Delta^\mu, \end{aligned} \tag{2.7}$$

with $\Delta^\mu = i\epsilon\sigma^\mu\bar{\theta} + i\bar{\epsilon}\bar{\sigma}^\mu\theta$, generate the required supersymmetric transformations that mix bosons with fermions. The corresponding generators are

$$Q_\alpha = i\frac{\partial}{\partial\theta^\alpha} - (\sigma^\mu\bar{\theta})_\alpha\partial_\mu,\ \overline{Q}^{\dot{\alpha}} = i\frac{\partial}{\partial\bar{\theta}_{\dot{\alpha}}} - (\bar{\sigma}^\mu\theta)^{\dot{\alpha}}\partial_\mu. \tag{2.8}$$

An infinitesimal transformation is then[3]

$$\delta_\epsilon T = T(x + \Delta, \theta + \epsilon, \bar{\theta} + \bar{\epsilon}) - T(x, \theta, \bar{\theta}) = -i(\epsilon Q + \epsilon\overline{Q})T, \tag{2.9}$$

from which one can derive explicit transformation laws for all components of T. For example, the lowest and highest components of the superfield T transform as [86]

$$\begin{aligned} a &\to a + \xi\epsilon + \bar{\chi}\bar{\epsilon}, \\ d &\to d + \frac{i}{2}\partial_\mu(\bar{\zeta}\bar{\sigma}^\mu\epsilon + \eta\sigma^\mu\bar{\epsilon}). \end{aligned} \tag{2.10}$$

Note that the highest component of any superfield transforms by a total spacetime derivative. Therefore any action of the form

$$S = \int d^4x T|_{\theta^4} + \text{h.c.} = \int d^4x \int d^4\theta T + \text{h.c.} \tag{2.11}$$

is invariant under supersymmetry transformations. In the last step we wrote the highest component of T as an integral over the Grassmannian coordinates. Differentiation and integration with Grassmannian numbers are reviewed in Refs. [80, 86].

The general superfield of Eq. (2.6) is a reducible representation of SUSY, meaning that there are objects with fewer degrees of freedom that have simple supersymmetric transformation properties [81, 86]. Irreducible representations are obtained by imposing restrictions on T. The

[3]Different authors use various normalizations for the SUSY transformations; see, e.g., Ref. [80].

first relevant case is the chiral superfield Φ, defined by

$$\bar{D}\Phi = 0, \tag{2.12}$$

where we introduced the SUSY covariant derivatives

$$D_\alpha = \frac{\partial}{\partial\theta^\alpha} - i(\sigma^\mu\bar{\theta})_\alpha\partial_\mu,\ \bar{D}^{\dot{\alpha}} = \frac{\partial}{\partial\bar{\theta}_{\dot{\alpha}}} - i(\bar{\sigma}^\mu\theta)^{\dot{\alpha}}\partial_\mu. \tag{2.13}$$

These operators obey

$$\{D_\alpha, D_\beta\} = 0,\ \{D_\alpha, \bar{D}_{\dot{\beta}}\} = 2i\sigma^\mu_{\alpha\dot{\beta}}\partial_\mu. \tag{2.14}$$

The most general solution of Eq. (2.12) is conveniently written in terms of a new coordinate $y^\mu = x^\mu + i\bar{\theta}\bar{\sigma}^\mu\theta$ (in which $\bar{D}^{\dot{\alpha}} = \partial/\partial\bar{\theta}^{\dot{\alpha}}$):

$$\Phi = \phi(y) + \sqrt{2}\theta\psi(y) + \theta^2 F(y). \tag{2.15}$$

The above expression can be related to the components of the general superfield, Eq. (2.6), by expanding y. The chiral supermultiplet contains a complex scalar ϕ, a Weyl fermion ψ and a complex scalar auxiliary field F. If ϕ has canonical mass dimension 1 (in 4D), then ψ and F have dimensions 3/2 and 2, respectively. The only dependence on $\bar{\theta}$ enters through y^μ. To construct realistic theories (i.e., those with interactions), we take products of chiral superfields Φ_i like $\Phi_i\Phi_j$ and $\Phi_i\Phi_j\Phi_k$; these superfields are also chiral, because the SUSY covariant derivatives defined in Eq. (2.13) obey the Leibniz (product) rule. Moreover, by writing the supercharges Q and $\overline{Q}$ from Eq. (2.8) in terms of y, one can easily show that

$$\begin{aligned}
\delta_\epsilon\phi &= \sqrt{2}\epsilon\psi, \\
\delta_\epsilon\psi_\alpha &= -i\sqrt{2}(\sigma^\mu\epsilon^\dagger)_\alpha\partial_\mu\phi + \sqrt{2}\epsilon_\alpha F, \\
\delta_\epsilon F &= -i\sqrt{2}\bar{\epsilon}\bar{\sigma}^\mu\partial_\mu\psi.
\end{aligned} \tag{2.16}$$

Note that the highest component of a chiral superfield transforms by a total derivative, so the supersymmetry-invariant action can also include terms of the form

$$S \supset \int d^4x \int d^2\theta W(\Phi) + \text{h.c.}, \tag{2.17}$$

where W is a holomorphic function of chiral superfields called the superpotential. The superpotential must have mass dimension 3, so the most general renormalizable expression for W is

$$W = \frac{1}{2}m_{ij}^2\Phi_i\Phi_j + \frac{1}{3}\lambda_{ijk}\Phi_i\Phi_j\Phi_k. \tag{2.18}$$

Interactions of the component fields can be derived from W by noting that [85]

$$\Phi_i \Phi_j|_{\theta\theta} = \phi_i F_j + \phi_j F_i - \psi_i \psi_j \tag{2.19}$$

$$\Phi_i \Phi_j \Phi_k|_{\theta\theta} = F_i \phi_j \phi_k - \psi_i \psi_j \phi_k + \text{permutations}, \tag{2.20}$$

where the fields on the right hand side are functions of y only.

Finally, the canonically normalized kinetic terms are contained in

$$S \supset \int d^4\theta \Phi^\dagger \Phi = \partial_\mu \phi \partial^\mu \phi + i\bar{\psi}\bar{\sigma}^\mu \partial_\mu \psi + F^\dagger F. \tag{2.21}$$

Note that F does not have a kinetic term. In fact, its equation of motion is an algebraic (as opposed to a differential) equation that can be used to eliminate F from the Lagrangian:

$$F_i^\dagger = -\left.\frac{\delta W}{\delta \Phi_i}\right|_{\Phi_i = \phi_i}. \tag{2.22}$$

Thus F is said to be an auxiliary field.

To implement gauge symmetries we require invariance of the action under local phase rotations of the (matter) chiral superfields

$$\Phi \to e^{iq\Omega}\Phi, \tag{2.23}$$

where q is the charge of Φ under an Abelian gauge symmetry. In order for the transformed field to remain a chiral superfield, the transformation parameter, Ω, must also be a chiral superfield, which follows from the definition in Eq. (2.12). Since Ω is a complex quantity, we absorb the factor i into its definition. The kinetic terms of Eq. (2.21) are not invariant under this transformation since

$$\Phi^\dagger \Phi \to \Phi^\dagger e^{q(\Omega^\dagger + \Omega)} \Phi. \tag{2.24}$$

As in non-supersymmetric field theory, we must introduce a compensating gauge field V and include it into the kinetic terms, which gives rise to gauge interactions. The appropriate form for the new gauge invariant kinetic energy is

$$\int d^4\theta \Phi^\dagger e^{2qV} \Phi, \tag{2.25}$$

where V is real

$$V = V^\dagger, \tag{2.26}$$

and transforms as

$$V \to V - \frac{1}{2}(\Omega + \Omega^\dagger) \tag{2.27}$$

under a gauge transformation. The above transformation is much more general than a standard gauge transformation. This freedom can be exploited to eliminate components of V. When writing interactions in terms of component fields it is extremely helpful to use the Wess-Zumino (WZ) gauge [85], in which

$$V = A_\mu \bar{\theta}\bar{\sigma}^\mu\theta + \bar{\theta}\bar{\theta}\theta\lambda + \theta\theta\bar{\theta}\bar{\lambda} + \frac{1}{2}\theta\theta\bar{\theta}\bar{\theta}D \tag{2.28}$$

$$V^2 = \frac{1}{2}A^\mu A_\mu \theta\theta\bar{\theta}\bar{\theta} \tag{2.29}$$

$$V^3 = 0. \tag{2.30}$$

Thus, the physical degrees of freedom of a vector superfield consist of a vector A_μ, Weyl fermion λ and an auxiliary scalar field D. Even after this simplifying gauge choice, there remains freedom to perform the standard gauge transformations, under which

$$A_\mu \to A_\mu + \partial_\mu \alpha(x), \tag{2.31}$$

while λ and D remain unchanged; here α corresponds to the imaginary part of the scalar component of Ω, which follows from Eq. (2.27) [86]. In the WZ gauge, the gauge invariant kinetic term of Eq. (2.25) gives

$$\int d^4\theta \Phi^\dagger e^{2qV}\Phi = (D_\mu\phi)^\dagger D^\mu\phi + i\bar{\psi}\bar{\sigma}^\mu D_\mu\psi + F^\dagger F - \sqrt{2}q(\phi^\dagger\psi\lambda + \text{h.c.}) + q\phi^\dagger\phi D, \tag{2.32}$$

where $D_\mu = \partial_\mu - iqA_\mu$ is the covariant derivative. Finally, the gauge kinetic terms are constructed from

$$W_\alpha(y,\theta) = -\frac{1}{4}\bar{D}^2 D_\alpha V = \lambda_\alpha + D\theta_\alpha + \frac{i}{2}F_{\mu\nu}(\sigma^\mu\bar{\sigma}^\nu\theta)_\alpha + i(\sigma^\mu\partial_\mu\lambda)_\alpha\theta\theta, \tag{2.33}$$

which is a chiral superfield. Gauge invariance of W_α is easily proven using commutation relations of D_α and $\bar{D}_{\dot{\beta}}$ in Eq. (2.14). Canonically normalized kinetic terms for the vector A and gaugino λ come from

$$\int d^2\theta \left(\frac{1}{4} - \frac{i\theta_{\text{CP}}}{32\pi^2}\right) W^\alpha W_\alpha + \text{h.c.} = -\frac{1}{4}F_{\mu\nu}F^{\mu\nu} + i\bar{\lambda}\bar{\sigma}^\mu\partial_\mu\lambda + \frac{\theta_{\text{CP}}}{32\pi^2}F_{\mu\nu}\widetilde{F}^{\mu\nu} + \frac{1}{2}D^2. \tag{2.34}$$

Note that D is an auxiliary field with no proper kinetic terms. Its equations of motion can be solved algebraically:

$$D = -\phi_i^\dagger q_i \phi_i \tag{2.35}$$

The $\theta_{\rm CP}$ term for an Abelian theory is a total derivative and can be dropped. The above discussion can be generalized to non-Abelian gauge symmetries [80, 85, 86].

To summarize, the Lagrangian density of a renormalizable supersymmetric Abelian gauge theory can be written as

$$\mathscr{L} = \int d^4\theta \Phi_i^\dagger e^{2q_i V} \Phi^i + \int d^2\theta \left(\frac{1}{4} W^\alpha W_\alpha + W(\Phi) + \text{h.c.} \right). \tag{2.36}$$

The interactions of the component fields can be read off from Eqs. (2.20), (2.32), and (2.34). However, this form slightly obfuscates the scalar potential V of the model. A more useful representation of the scalar potential is obtained by fixing the auxiliary fields F_i and D using their equations of motion (Eqs. (2.22) and (2.35)), which gives

$$V = F_i^\dagger F^i + \frac{1}{2} D^2 = \left| \frac{\delta W}{\delta \Phi_i} \right|^2 + \frac{1}{2} g^2 \left| \sum_i \phi_i^\dagger q_i \phi^i \right|^2 \tag{2.37}$$

where in $\delta W / \delta \Phi_i$ is taken to be a function of the scalar components of chiral superfields Φ_j only. For a non-Abelian gauge theory, the charge q_i is replaced by the group generator T^a appropriate for the representation of Φ_i.

2.3 The Minimal Supersymmetric Standard Model

It is now easy to specify the simplest realistic supersymmetric theory: the Minimal Supersymmetric Standard Model (MSSM). All SM matter fields are promoted to chiral superfields, while gauge bosons become real gauge superfields. The superpotential of the model is

$$W = u_R^c Y_u Q H_u - d_R^c Y_d Q H_d - e_R^c Y_e L H_d + \mu H_u H_d, \tag{2.38}$$

and the superfields have the same gauge charges as their analogues in the SM (see Sec. 1.1.1). One immediate novel feature is that we need two Higgs doublets H_d (hypercharge $Y = -1/2$) and H_u ($Y = +1/2$) to write this superpotential. [4] In the SM, we were able to couple both up and down type fermions to the same doublet by using the conjugate field $H^\dagger$. Since W is a holomorphic function, complex conjugates do not appear – another Higgs doublet with opposite hypercharge is required.[5]

Unlike the Yukawa interactions of Eq. (1.11), this superpotential is not the most general renormalizable functional of the chiral superfields consistent with gauge symmetries. For example, one can also write down the gauge invariant operators [80]

$$W_{\Delta B=1} = \frac{1}{2} \lambda''^{ijk} u_{Ri}^c d_{Rj}^c d_{Rk}^c, \quad W_{\Delta L=1} = \frac{1}{2} \lambda^{ijk} L_i L_j e_{Rk}^c + \lambda'^{ijk} L_i Q_j d_{Rk}^c + \mu'^i L_i H_u, \tag{2.39}$$

[4] The doublets are sometimes called H_1 and H_2 instead of H_d and H_u, respectively.

[5] Another doublet is also needed for anomaly cancellation since they introduce chiral fermions [80].

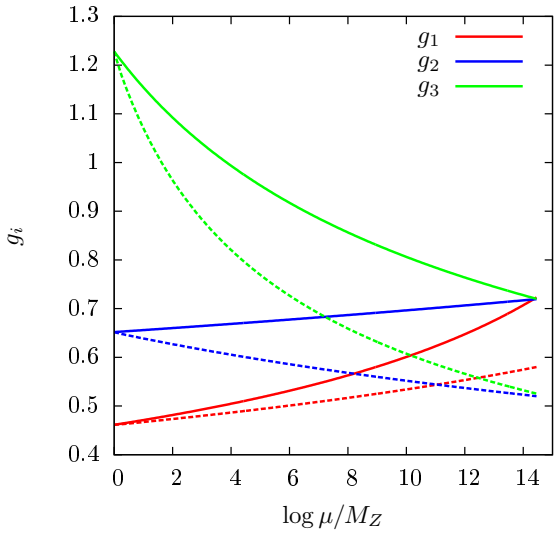

Figure 2.1: Renormalization group evolution of the gauge couplings in the SM (dashed lines) and the MSSM (solid lines). In the MSSM gauge couplings appear to unify at around $\mu \approx 2 \times 10^{16}$ GeV.

which violate baryon and lepton numbers by one unit. For non-zero values of, e.g., λ'' and λ, these interactions lead to a large proton decay rate. Such dangerous terms can be forbidden by R-parity, a new type of discrete $\mathbb{Z}_2$ symmetry with SM fields having charge $+1$ and their superpartners having charge -1. In the superspace language, each superfield has the charge of its lowest component. So, for example, the quark and lepton superfields are odd under R-parity, while the Higgs and gauge multiplets are even. Thus terms in Eq. (2.39) are forbidden.

The physical content of R-parity is that superpartners are always produced in pairs and that the lightest supersymmetric particle (LSP) is stable. If it is electrically neutral, it can be a good dark matter candidate [75]. As was alluded to in the previous sections, the MSSM has several other enticing features. First, in the supersymmetric limit, quadratically-divergent quantum corrections to the physical Higgs boson mass cancel exactly among superpartners via the mechanism described in Sec. 1.3.1. Second, the matter content in the MSSM is more consistent with gauge coupling unification at the scale of $\sim 2 \times 10^{16}$ GeV, the so-called Grand Unification (GUT) scale. The running of gauge coupling in the SM and MSSM is shown in Fig. 2.1 by dashed and solid lines, respectively. The common value of the couplings at GUT scale suggests that the SM gauge group descends from a simple gauge group such as $SU(5)$ with a single gauge coupling [27].

The spectrum of the MSSM consists of SM particles and their superpartners, along with the extended Higgs sector. Electroweak symmetry breaking occurs when the two Higgs doublets H_d and H_u acquire expectation values v_d and v_u; these are usually specified using the SM vev $v = v_d^2 + v_u^2 = 246.22\,\text{GeV}$ and $\tan\beta = v_u/v_d$. Symmetry breaking mixes the components of

gauge-eigenstate superfields; the resulting particle content of the MSSM is shown in Tab. 2.1. In addition to the SM-like Higgs, there are CP odd neutral and charged scalars. Each SM fermion (4 degrees of freedom on-shell) has a pair of complex scalar superpartner "sfermions". The gluon has a strongly-interacting Majorana fermion partner - the gluino. Electroweak gauge boson superpartners (gauginos) mix with Higgs superpartners (the Higgsinos) to create spin 1/2 neutralinos and charginos. In this table and below, we use the convention for R-type sfermions that $\tilde{f}_R^c = \tilde{f}_R^\dagger$. The details of electroweak symmetry breaking and MSSM mass spectrum computation can be found in, e.g., Refs. [80, 81, 87] and (partially) in the following chapters.

Despite its attractive theoretical features, the exactly-supersymmetric MSSM is already ruled out since it requires near degeneracy between SM states and their superpartners. This can be seen through the "supertrace" [80, 88]

$$\mathrm{Str}(m^2) = \sum_s (-1)^{2s}(2s+1)\mathrm{Tr}(m_s^2) = 0, \tag{2.40}$$

where the sum is over particles of spin s. This relation is valid for renormalizable theories, even if supersymmetry is broken spontaneously at tree-level. For example, the contribution of first generation quark superfields decouples, yielding [86]

$$\mathrm{Str}(m^2) = m_{\tilde{u}_R}^2 + m_{\tilde{u}_L}^2 + m_{\tilde{d}_R}^2 + m_{\tilde{d}_L}^2 - 2(m_u^2 + m_d^2) = 0, \tag{2.41}$$

which implies that the first generation squarks are at the MeV scale! Since the supertrace relationship holds for renormalizable interactions, SUSY cannot be broken spontaneously *in the MSSM sector*. We conclude that if supersymmetry has anything to do with nature, it must be broken in a "hidden" sector, such that physics looks explicitly non-supersymmetric in the MSSM, or "visible" sector. Supersymmetry-breaking effects must be communicated from the hidden to the visible sector via quantum (loop) effects and non-renormalizable interactions.

Before discussing the possible mechanisms of supersymmetry breaking and its communication to the visible sector, we note that in the MSSM, renormalizable SUSY breaking effects can be parametrized by [80]

$$\begin{aligned}
\mathscr{L}_{\text{soft}} = &-\left(M_3 \tilde{g}^a \tilde{g}^a + M_2 \widetilde{W}^a \widetilde{W}^a + M_1 \widetilde{B}\widetilde{B} + \text{h.c.}\right) \\
&-\left(\tilde{u}_R^\dagger A_u \widetilde{Q} H_u - \tilde{d}_R^\dagger A_d \widetilde{Q} H_d - \tilde{e}_R^\dagger A_e \widetilde{L} H_d + \text{h.c.}\right) \\
&- \widetilde{Q}^\dagger m_Q^2 \widetilde{Q} - \widetilde{L}^\dagger m_L^2 \widetilde{L} - \tilde{u}_R^\dagger m_{\tilde{u}}^2 \tilde{u}_R - \tilde{d}_R^\dagger m_{\tilde{d}}^2 \tilde{d}_R - \tilde{e}_R^\dagger m_{\tilde{e}}^2 \tilde{e}_R \\
&- m_{H_u}^2 |H_u|^2 - m_{H_d}^2 |H_d|^2 - (b H_u H_d + \text{h.c.}),
\end{aligned} \tag{2.42}$$

which is the most general SUSY-breaking Lagrangian with only positive mass dimension (soft) operators. Taking operators with positive dimension ensures that we do not introduce any new quadratic divergences (which SUSY was designed to cure in the first place). Using dimensional analysis, it is easy to see that any 2 point function corrections arising from these couplings will

Name	Gauge Eigenstates	Mass Eigenstates	$SU(3)_C$	$U(1)_{\rm em}$	R
Neutral Higgs	$H_u^0,\ H_d^0$	$h,\ H,\ A$	**1**	0	+1
Charged Higgs	$H_u^\pm,\ H_d^\pm$	$H^\pm$	**1**	±1	+1
up squarks	$\tilde{u}_{L,R},\ \tilde{c}_{L,R},\ \tilde{t}_{L,R}$	$\tilde{u}_{1,2},\ \tilde{c}_{1,2}, \tilde{t}_{1,2}$	**3**	+2/3	-1
down squarks	$\tilde{d}_{L,R},\ \tilde{s}_{L,R},\ \tilde{b}_{L,R}$	$\tilde{d}_{1,2},\ \tilde{s}_{1,2}, \tilde{b}_{1,2}$	**3**	-1/3	-1
sleptons	$\tilde{e}_{L,R},\ \tilde{\mu}_{L,R},\ \tilde{\tau}_{L,R}$	$\tilde{e}_{1,2},\ \tilde{\mu}_{1,2},\ \tilde{\tau}_{1,2}$	**1**	-1	-1
sneutrinos	$\tilde{\nu}_e,\ \tilde{\nu}_\mu,\ \tilde{\nu}_\tau$	same	**1**	0	-1
gluino	$\tilde{g}$	same	**8**	0	-1
neutralinos	$\widetilde{H}_u^0,\ \widetilde{H}_d^0,\ \widetilde{W}^3,\ \widetilde{B}$	$\widetilde{N}_i,\ i=1,2,3,4$	**1**	0	-1
charginos	$\widetilde{H}_u^\pm,\ \widetilde{H}_d^\pm,\ \widetilde{W}^\pm$	$\widetilde{C}_i,\ i=1,2$	**1**	±1	-1

Table 2.1: Particle content in the MSSM before and after electroweak symmetry breaking, along with colour, electromagnetic charge and R-parity assignments.

have magnitude $\sim m_{\rm soft}^2$, where $m_{\rm soft}$ is the generic scale of couplings appearing in Eq. (2.42). With these terms included the SM particles and their superpartners are no longer degenerate. As a result the cancellation of the leading quadratic divergence is not exact; fortunately, the remainder is proportional to $m_{\rm soft}^2$, instead of Λ^2 as in Sec. 1.3.1. Thus, the hierarchy between the EW and gravitational scales is reduced, assuming $m_{\rm soft} \ll M_{\rm Pl}$.

In Eq. (2.42) the couplings m_i^2, A_i are real and complex matrices in family space, respectively. In total, there are more than 100 new parameters beyond those found in the SM [80, 89]. Therefore, studying the full parameter of the MSSM with generic soft breaking terms is intractable. Moreover, arbitrary choices for these parameters generally suffer from phenomenological problems, such as flavour mixing and CP violation, which are severely constrained by, e.g., bounds on rare decays such as $\mu \to e\gamma$ and $K - \overline{K}$ oscillation measurements [80]. This is known as the SUSY flavour problem. This motivates the search for a mechanism of supersymmetry breaking, that can generate Eq. (2.42) and predict the various couplings in terms of (hopefully) a small number of fundamental parameters. The proliferation of parameters can also be seen as being advantageous, since there are many new possible CP-violating sources, which is important for baryogenesis, as discussed in Sec. 1.3.2.

2.4 Supersymmetry Breaking and Supergravity

2.4.1 Global Supersymmetry Breaking

In the previous section we determined that if supersymmetry is realized in nature, it cannot be an exact symmetry, since we do not observe any superpartners mass-degenerate with known particles. In this section we discuss how to break supersymmetry spontaneously and how these effects are communicated to the visible sector in realistic theories.

If supersymmetry is broken spontaneously, the vacuum $|0\rangle$ is not invariant under SUSY

transformations, that is

$$Q_\alpha|0\rangle \neq 0,\ Q_{\dot\alpha}|0\rangle \neq 0. \tag{2.43}$$

Our first goal is to determine whether a given model breaks SUSY. Using the supersymmetry algebra, Eq. (2.4), we can express the Hamiltonian as

$$H = \frac{1}{4}\left(Q_1 Q_1^\dagger + Q_1^\dagger Q_1 + Q_2 Q_2^\dagger + Q_2^\dagger Q_2\right), \tag{2.44}$$

so Eq. (2.43) implies

$$\langle 0|H|0\rangle > 0 \tag{2.45}$$

when supersymmetry is spontaneously broken. Since kinetic terms cannot have an expectation value in a homogeneous vacuum, we conclude that the potential alone must have an expectation value. The SUSY potential (see Eq. (2.37)) is positive definite, so $\langle V\rangle > 0$ implies either

$$F^i \neq 0 \quad (F\text{-term breaking}), \tag{2.46}$$

for some i or

$$D^a \neq 0 \quad (D\text{-term breaking}). \tag{2.47}$$

There is an alternative way to see that these are the conditions required for spontaneous SUSY breaking, that will be useful when discussing supergravity. If the vacuum state is not invariant, that is Eq. (2.43) is satisfied, we have

$$\langle 0|\delta_\epsilon T|0\rangle \neq 0, \tag{2.48}$$

for some superfield T (either chiral or vector), where $\delta_\epsilon T$ is defined in Eq. (2.9). Let us specialize to the case where T is a chiral superfield. Looking at the transformation of the component fields, Eq. (2.16), we see that only $\delta_\epsilon\psi$ can have a non-zero expectation value without breaking Lorentz invariance[6] when

$$\sqrt{2}\epsilon_\alpha F \neq 0. \tag{2.49}$$

Thus we recover the condition for F-term SUSY breaking. The same analysis can be repeated with a vector superfield to re-derive D-term breaking.

A simple renormalizable example of F-term breaking is the O'Raifeartaigh (OR) model [80,

[6]It is also possible to do this using a non-zero expectation value of a fermion bilinear [90].

81, 91] with the superpotential

$$W_{OR} = -k^2\Phi_1 + m\Phi_2\Phi_3 + \frac{y}{2}\Phi_1\Phi_3^2. \tag{2.50}$$

The corresponding F-terms are

$$F_1 = -k^2 + \frac{y}{2}(\phi_3^*)^2 \tag{2.51}$$

$$F_2 = m\phi_3^* \tag{2.52}$$

$$F_3 = m\phi_2^* + y\phi_1^*\phi_2^*. \tag{2.53}$$

In particular, we cannot simultaneously have $F_1 = 0$ and $F_2 = 0$, so $\langle V \rangle > 0$ and SUSY is spontaneously broken. For example, in the vacuum where all scalar VEVs vanish, $V = |F_1|^2 = k^4 > 0$, as required by (2.45). To confirm that SUSY is broken, we can evaluate the spectrum of the model, which consists of 6 real scalars with squared masses (assuming real m and k^2)

$$0,\ 0,\ m^2,\ m^2,\ m^2 \pm yk^2 \tag{2.54}$$

and 3 Weyl fermions with mass squared

$$0,\ m^2,\ m^2, \tag{2.55}$$

which demonstrates the mass splitting among spin 0 and spin 1/2 partners. Note that this spectrum satisfies the supertrace relationship, Eq. (2.40). While the vanishing scalar masses are lifted by quantum corrections [81], the massless fermion remains massless at all orders in perturbation theory. The appearance of a massless *fermion*, the Goldstino, is a general feature of spontaneous supersymmetry breaking, and is completely analogous to the appearance of a Nambu-Goldstone *boson* in a theory with spontaneously broken continuous symmetry. The difference in statistics is due to the fermionic nature of the SUSY generators. The existence of a Goldstino in a general theory can also be seen from the fact that the linear combination [80, 86]

$$\eta = F^i\psi_i + \frac{1}{\sqrt{2}}D^a\lambda^a \tag{2.56}$$

is an eigenvector of the fermion mass matrix with eigenvalue 0.

The OR model relies on the existence of an explicit dimensionful parameter in the superpotential, which some find unsatisfying, since the scale of SUSY breaking $\sqrt{F_1} = k$ is effectively put in by hand. This motivated the search for dynamical, non-perturbative mechanisms that generate this scale from dimensionless parameters. For a recent review of such mechanisms see, e.g., Refs. [92–94]. Quantitative discussion of non-perturbative processes is only made possible by the existence of dualities (weakly coupled descriptions of strongly coupled physics) and holomorphy of the superpotential (which severely restricts the couplings that can appear in the

action) [95].

2.4.2 Super-Higgs Mechanism and Supergravity

Phenomenological difficulties associated with a massless fermion aside, we will usually think of SUSY descending from a string theoretic framework, where SUSY is realized as a *local* symmetry [96]. In local supersymmetry, or supergravity (SUGRA), the Goldstino is not part of the physical spectrum, but rather is absorbed as an extra polarization state of a "gauge fermion" associated with SUGRA, the spin 3/2 gravitino (superpartner of the spin 2 graviton). In the process, the gravitino becomes massive. This super-Higgs mechanism is analogous to spontaneous breaking of (bosonic) SM gauge group $SU(2)_L \times U(1)_Y$ when W and Z bosons acquire masses. Note that the gravitino mass, $m_{3/2}$, must vanish in the supersymmetric limit, as well as in the limit where gravity is completely decoupled ($M_{\rm Pl} \to \infty$). For F-term breaking, this suggests that the gravitino mass must scale as [80]

$$m_{3/2} \sim \frac{F}{M_{\rm Pl}}. \tag{2.57}$$

The above relation can be made more precise. While the construction of the full SUGRA-invariant action [90] is beyond the scope of this work, we will display some useful results. First, because gravity is non-renormalizable, we cannot restrict ourselves to renormalizable "kinetic" and superpotential terms. In the global SUSY limit, this means we must consider Lagrangian densities of the form

$$\mathscr{L} = \int d^4\theta K(\Phi_i^\dagger e^{2qV}, \Phi_j) + \int d^2\theta \left(\frac{1}{4} f_{ab}(\Phi) W^a W^b + W(\Phi) + \text{h.c.} \right), \tag{2.58}$$

where K, f_{ab} are arbitrary functions called the Kähler potential and gauge kinetic function [97]; note that f_{ab} must be a chiral superfield for the above to be SUSY invariant; here a and b are adjoint group indices. The SUGRA potential can be expressed entirely in terms of a Kähler function G

$$G = \frac{1}{M_{\rm Pl}^2} K + \ln\left(\frac{|W|^2}{M_{\rm Pl}^6} \right) \tag{2.59}$$

and the gauge kinetic function f_{ab} as [90]

$$V = M_{\rm Pl}^4 e^G \left(G^{i\bar{j}} G_i G_{\bar{j}} - 3 \right) + \frac{g^2}{2} M_{\rm Pl}^4 (\text{Re} f_{ab}^{-1}) G_i T_{ij}^a \phi_j G_k T_{kl}^b \phi_l, \tag{2.60}$$

where

$$G_i = \frac{\partial G}{\partial \phi_i}, \quad G_{\bar{\imath}} = \frac{\partial G}{\partial \phi_i^*}, \quad G_{i\bar{\jmath}} = \frac{\partial G}{\partial \phi_i \partial \phi_j^*}, \tag{2.61}$$

and $G^{i\bar{j}}$ is the matrix inverse of $G_{i\bar{j}}$. Equation (2.60) is the generalization of Eq. (2.37) to local supersymmetry; the first and second terms correspond to F and D contributions in global SUSY. Note that the potential of Eq. (2.60) is no longer positive-indefinite, so the global SUSY-breaking criterion, Eq. (2.45), is no longer appropriate. We can still employ the alternative condition, Eq. (2.48), from which it follows that either [90, 98]

$$G^{i\bar{j}}G_{\bar{j}} \neq 0, \tag{2.62}$$

or

$$\mathrm{Re} f_{ab}^{-1} G_i T_{ij}^b \phi_j \neq 0. \tag{2.63}$$

These conditions generalize F- and D-term breaking, respectively, to supergravity. Both cases require that there exists an i such that $G_i \neq 0$. For example, for the canonical choice of the Kähler potential

$$K = \Phi_i^\dagger \Phi_i, \tag{2.64}$$

we have $G_{\bar{j}} = \phi_j / M_{\rm Pl}^2 + (W^\dagger)^{-1}(\partial_j W)^\dagger$, $G^{i\bar{j}} = \delta_{ij} M_{\rm Pl}^2$, so Eq. (2.62) simplifies to

$$M_{\rm Pl}^2 \frac{\delta W}{\delta \Phi_i}\bigg|_{\Phi_i = \phi_j} + \phi_i^* W \neq 0. \tag{2.65}$$

Note that in the limit $M_{\rm Pl} \to \infty$ we recover the global SUSY F-term breaking condition, Eq. (2.46) (via the equation of motion, Eq. (2.22)).

We can now describe how the gravitino obtains its mass. After SUSY breaking, the SUGRA Lagrangian density contains a mixing term between the gravitino Ψ_μ and the Goldstino $\Psi = (\eta,\ \eta^\dagger)^T$[7]

$$\frac{i}{2} M_{\rm Pl} e^{G/2} \overline{\Psi}_{L\mu} \gamma^\mu \Psi_L + \text{h.c.}, \tag{2.66}$$

where G is the expectation of Eq. (2.59) in the SUSY breaking vacuum. Just like in the case of bosonic local symmetries, there exists a "unitary" gauge (here a local SUSY transformation) that removes this mixing, leaving behind only the physical propagating state – the massive gravitino [90]. The gravitino mass parameter can be read off from the remaining mass term

$$\frac{i}{2} M_{\rm Pl} e^{G/2} \overline{\Psi}_\mu \sigma^{\mu\nu} \Psi_\nu, \tag{2.67}$$

[7]Here we have momentarily switched to 4 component notation because the Rarita-Schwinger equation, the equation of motion for a spin 3/2 field, is most easily specified using Dirac spinors [99].

so

$$m_{3/2} = e^{G/2} M_{\rm Pl} = e^{K/2M_{\rm Pl}^2} \frac{|W|}{M_{\rm Pl}^2}. \tag{2.68}$$

This result can be simplified, if, in addition to canonical kinetic terms, we also assume a vanishing cosmological constant [86]

$$m_{3/2} \approx \frac{F_{\rm tot}}{\sqrt{3} M_{\rm Pl}}, \tag{2.69}$$

where

$$|F_{\rm tot}|^2 = \left| \frac{\delta W}{\delta \Phi_i}\bigg|_{\Phi_i = \phi_j} + \frac{\phi_i^* W}{M_{\rm Pl}^2} \right|^2 \tag{2.70}$$

parametrizes the total amount of supersymmetry breaking from non-vanishing F-terms. The gravitino mass is often used as a proxy for the scale of supersymmetry breaking.

2.4.3 Models of Supersymmetry Breaking

In Sec. 2.3 we determined that phenomenologically viable models of SUSY must be softly broken. We parametrized this breaking by a generic Lagrangian with many new parameters. We noted that arbitrary choices of these parameters lead to phenomenological problems. We now seek to relate these parameters to a fundamental theory of spontaneous SUSY breaking.

Suppose that SUSY is broken in a hidden sector (HS) by a collection of non-MSSM fields that couple weakly to the MSSM via some messenger fields. There are three well-studied classes of SUSY breaking mechanisms, which differ in the nature of the messengers.

Even in the absence of any coupling between the SUSY-breaking and visible sectors, gravity can mediate these effects to the MSSM. We will see that this scenario yields

$$m_{\rm soft} \sim m_{3/2} \quad \text{(gravity mediation)}. \tag{2.71}$$

Note that this implies (via Eq. (2.57)) that the scale of SUSY breaking must be

$$F \sim m_{\rm soft} M_{\rm Pl} \sim (10^{11}\,{\rm GeV})^2, \tag{2.72}$$

where we assumed that $m_{\rm soft} \sim 1\,{\rm TeV}$.

We demonstrate the appearance of soft SUSY breaking terms in the visible sector using a simple example. Suppose the SUSY-breaking sector has superpotential $W_H(Z_r)$, a function of HS fields Z_r. Furthermore, assume there is no explicit coupling between Z_r and visible sector fields Φ_i, so the full superpotential takes the form

$$W = W_V(\Phi_i) + W_H(Z_r), \tag{2.73}$$

where W_V is the superpotential in the visible sector. Taking the minimal Kähler function and using Eq. (2.60) yields the potential

$$V = e^{K/M_{\rm Pl}^2}\left(\left|\frac{\phi_i^* W}{M_{\rm Pl}^2} + \frac{\partial W_V}{\partial \phi_i}\right|^2 + \left|\frac{z_r^* W}{M_{\rm Pl}^2} + \frac{\partial W_H}{\partial z_r}\right|^2 - 3\frac{|W|^2}{M_{\rm Pl}^2}\right). \tag{2.74}$$

Note that even though we started with no explicit coupling between the visible and hidden sectors, the supergravity potential automatically generates mixings between the two. When the HS fields acquire SUSY-breaking expectation values parametrized as [97]

$$W_H = \mu M_{\rm Pl}^2, \quad z_r = a_r M_{\rm Pl}, \quad \frac{\partial W_H}{\partial z_r} = c_r \mu M_{\rm Pl}, \tag{2.75}$$

and one finds the gravitino mass (using Eq. (2.68))

$$m_{3/2} = e^{|a_r|^2/2}\mu. \tag{2.76}$$

Here μ has dimensions of energy, while a_r and c_r are dimensionless. These substitutions allow one to expand Eq. (2.74) in $m_{3/2}/M_{\rm Pl} \ll 1$:

$$V \approx \left|\frac{\partial \widehat{W}_V}{\partial \phi_i}\right|^2 + m_{3/2}^2|\phi_i|^2 + \left(m_{3/2}\left[|a_r|^2 + c_r a_r^* - 3\right]\widehat{W}_V + m_{3/2}\phi_i\frac{\partial \widehat{W}_V}{\partial \phi_i} + \text{h.c.}\right), \tag{2.77}$$

where $\widehat{W}_V = \exp(|a_r|^2/2)W_V$. The first term matches the global SUSY F-term contribution (see Eq. (2.37)). The following terms are soft SUSY-breaking parameters, including a universal mass for all visible scalars, bi- and tri-linear interactions, all set by the scale $m_{3/2}$. These operators match onto the general soft SUSY-breaking Lagrangian of Eq. (2.42). At this point we are only missing the gaugino mass terms, which arise from the term

$$\frac{1}{4}M_{\rm Pl}e^{G/2}\frac{\partial f_{ab}^*}{\partial z^{*\bar{j}}}G^{\bar{j}k}G_k\lambda^a\lambda^b, \tag{2.78}$$

in the SUGRA Lagrangian [90]. Note that this requires a non-minimal gauge kinetic function f_{ab}; assuming these effects are generated by SUGRA interactions, this term yields a gaugino mass $m_{1/2} \sim m_{3/2}$. The scenario just described is called minimal supergravity (mSUGRA) or constrained MSSM (cMSSM) and has the virtue of having very few parameters. Moreover, the universal scalar mass suppresses dangerous flavour and CP-violating effects that plague generic SUSY-breaking parameters. For these reasons, much experimental and phenomenological effort has been spent on constraining and excluding mSUGRA [80], despite the fact that the extremely strong assumptions (namely the form of the Kähler potential and the superpotential) are not well-motivated theoretically. For more general choices of K and W, scalar masses are no longer universal, and once again flavour observables become a problem.

One way to avoid flavour problems is to ensure that SUSY-breaking is communicated to

the MSSM in a way that does not mix different generations. This can be achieved using messengers (new chiral superfields) that are charged under $SU(3)_C \times SU(2)_L \times U(1)_Y$. Since gauge interactions do not violate flavour at tree-level, we expect the resulting soft terms to be phenomenologically viable. This mechanism is known as gauge mediation. Consider a pair of chiral superfields Φ and $\bar{\Phi}$ that are charged under $SU(3)_C \times SU(2)_L \times U(1)_Y$ and that couple directly to a field X whose vev breaks SUSY:

$$W \supset X\bar{\Phi}\Phi, \tag{2.79}$$

where $X = M + \theta^2 F$. The SUSY breaking vev F splits the masses of the messenger scalars and fermions, but these effects are communicated to the MSSM only indirectly via loops of messenger and gauge fields. For example, the gaugino mass arises at one loop, while soft scalar mass squared parameters appear at two loops from diagrams like those shown in Fig. 2.2. Thus, we expect the leading contributions to gaugino and scalar masses to be [100]

$$M_{\tilde{g}} \sim \frac{g^2}{16\pi^2}\frac{F}{M}, \quad m_{\tilde{f}}^2 \sim \left(\frac{g^2}{16\pi^2}\frac{F}{M}\right)^2. \tag{2.80}$$

In either case, the messengers couple to MSSM through gauge interactions and the resulting soft parameters are flavour diagonal, alleviating the SUSY flavour problem. Interestingly, in order to obtain the precise leading order (in F/M^2) predictions for the soft parameters, one does not need to evaluate diagrams like those in Fig. 2.2 explicitly. Instead, these results are completely determined by the beta functions and anomalous dimensions of the theory [101]. Due to the non-renormalization of the superpotential [81], X dependence may only enter in the Kähler potential and gauge kinetic function, i.e., via renormalizations of matter and gauge kinetic terms, respectively. The former is related to anomalous dimensions, while the latter to beta functions of gauge couplings. One can then use the reality of the Kähler potential and the holomorphy of the gauge kinetic function to determine their dependence on X and thereby extract the soft parameters which arise from terms like

$$\int d^4\theta \left(\frac{X^\dagger X}{M^2}\right) Q^\dagger Q, \tag{2.81}$$

and

$$\int d^2\theta \left(\frac{X}{M}\right) W^a W^a + \text{h.c.} \tag{2.82}$$

in the Lagrangian. For example, for the gaugino masses this procedure gives

$$M_a = \frac{N g_a^2}{16\pi^2}\frac{F}{M}, \tag{2.83}$$

where N is the number of messenger fields and where a labels the gauge group. The scalar soft

masses and cubic A-terms are found to depend only on beta function coefficients and group theoretic invariants [80].

From Eqs. (2.57) and (2.80) it is clear that

$$m_{\rm soft} \sim \frac{g^2}{16\pi^2}\left(\frac{M_{\rm Pl}}{M}\right) m_{3/2} \quad \text{(gauge mediation)}, \tag{2.84}$$

so $m_{\rm soft} \gg m_{3/2}$ unless $M \sim M_{\rm Pl}$. In the latter limit, however, gravitational effects become important and the flavour problem is reintroduced. Thus, in gauge mediation, the gravitino is usually the LSP and it is much lighter than the rest of superpartners. This has several interesting collider (e.g., displaced vertices) and cosmological implications due to its weak (gravitational strength) interactions [80, 100].

Our last example of theories of SUSY breaking is motivated by extra-dimensional constructions. When discussing gravity mediation we mentioned that, in general, because gravitational interactions are flavour blind, there is a severe flavour problem due to inter-generational mixing of SM superpartners. This is because the Kähler potential that gives rise canonical kinetic terms, Eq. (2.64), is not radiatively stable; [8] in the presence of gravitational interactions at high scales one expects [81]

$$K = \left(\delta_{ij} + \frac{c_{ij} X^\dagger X}{M_{\rm Pl}^2}\right) \Phi_i^\dagger \Phi_j, \tag{2.85}$$

where X is the chiral superfield with the SUSY-breaking vev. The coefficients c_{ij} are not diagonal and $\mathcal{O}(1)$; such terms arise from integrating out heavy string states that do not necessarily respect flavour symmetries [102]. These undesirable terms can be suppressed if the SUSY-breaking sector is physically sequestered from the visible sector in an extra dimension.

The above scenario is implemented as follows [102]. The MSSM and SUSY-breaking sectors are embedded into different 3-branes, a distance R apart in an extra dimension. It is then natural to have a "separable" superpotential of the form given in Eq. (2.73). Moreover, if supergravity (and heavy string) states are the only degrees of freedom allowed to propagate in the bulk of the extra dimension, the effects of SUSY-breaking on the MSSM brane will be suppressed by

$$e^{-M_5 R}, \tag{2.86}$$

where M_5 is the higher-dimensional Planck scale. Thus, if the size of the extra dimension is such that $M_5 R \gg 1$, the undesirable flavour violating effects will be suppressed.

In the above limit, the leading order effects arise due to anomalous global symmetries of the classical SUGRA action [103]. In the derivation of the low-energy effective theory for SUGRA with canonically normalized gravitational kinetic terms, one is forced to make a certain set field

[8] The superpotential is not renormalized in perturbation theory, so the special form of Eq. (2.73) *is* radiatively stable.

redefinitions. While the classical action is invariant under these, the path integral measure is not, and as a result, new terms in the effective action are generated at one loop, similar to the more familiar chiral anomalies of quantum field theory. The resulting terms in the action depend on auxiliary fields of the supergravity multiplet. Since the supergravity multiplet couples to the SUSY-breaking sector, these auxiliary fields can inherit a SUSY-breaking vev and give rise to soft terms. This scenario is called Anomaly Mediated Supersymmetry Breaking (AMSB) and the resulting soft terms have magnitude

$$m_{\text{soft}} \sim \frac{g^2}{16\pi^2}\frac{F}{M_{\text{Pl}}} \sim \frac{g^2}{16\pi^2} m_{3/2} \quad \text{(anomaly mediation)}. \tag{2.87}$$

An efficient way to derive these effects is to use the super-conformal compensator formalism [100, 102]. The soft parameters are completely determined in terms of gauge beta functions and anomalous dimensions. For example, gaugino masses are given by [81]

$$M_a = \frac{b_a g_a^2}{16\pi^2}\frac{F}{M_{\text{Pl}}}, \tag{2.88}$$

where a labels the gauge group and b_a is the corresponding β function coefficient. The sfermion masses depend on the anomalous dimension matrix γ_j^i [80]

$$(m_{\tilde{f}}^2)_j^i = \frac{1}{2}\mu\frac{d\gamma_j^i}{d\mu}\frac{F^2}{M_{\text{Pl}}^2}. \tag{2.89}$$

Note that while Eq. (2.89) contains non-flavour diagonal contributions, they are proportional to MSSM Yukawa couplings and therefore do not introduce significant flavour violation beyond what is already present in the SM. While AMSB is very predictive (all masses are determined in terms of a single parameter F/M_{Pl}^2), it is not a complete model, since Eq. (2.89) can give rise to tachyonic sfermion masses. For example, for the the right-handed selectron we have [80]

$$m_{\tilde{e}_R}^2 = -\frac{99 g_1^4}{3200\pi^2}\frac{F^2}{M_{\text{Pl}}^2}. \tag{2.90}$$

This is a general problem for matter that is charged under a gauge group that is not asymptotically free. Thus, in general AMSB requires additional dynamics to be a viable theory of supersymmetry breaking and the resulting spectrum of superpartners depends on the nature of these modifications.

There is additional motivation to consider AMSB contributions to soft masses. In the absence of extra-dimensional sequestering between the MSSM and the SUSY-breaking sectors, normal supergravity contributions to the soft *scalar* masses are important, since there is no symmetry that can forbid terms like Eq. (2.81), since $X^\dagger X$ is invariant under all symmetries. In contrast, gaugino mass terms of the form of Eq. (2.82) require the SUSY-breaking field X to be a gauge singlet, which can be difficult to realize, especially in theories with dynamical

Figure 2.2: Example contributions to soft SUSY-breaking parameters from heavy messenger loops (bold lines) to MSSM gauginos (left) and sfermions (right) in gauge mediation.

supersymmetry breaking [102]. Thus, it is natural for these terms to be forbidden, and as a result, the leading contributions to gaugino masses come from anomaly mediation. This gives rise to split spectra, with light gauginos (since Eq. (2.88) is loop suppressed relative to $F/M_{\rm Pl}$) and heavy scalars with $m_{\tilde{f}} \sim F/M_{\rm Pl}$. This class of models will be the subject of Chapter 3.

The above discussion of SUSY breaking scenarios is far from an exhaustive list. Each case described above suffers from drawbacks: the flavour problem in gravity mediation, potentially dangerous gravitino cosmology in gauge mediation and tachyonic slepton masses in anomaly mediation. Thus, fully satisfactory mechanisms of SUSY breaking often require further dynamics beyond the basic scenarios.

2.5 Status of Experimental Searches for Supersymmetry

The most important states in the MSSM spectrum for maintaining naturalness (i.e., small fine-tuning of the Higgs mass parameter) are the stop and the gluino. The stop cancels the quadratic divergence in the Higgs self-energy associated with the top, while the gluino has indirect effects through large radiative corrections to the squark masses [80]. As a result, these states are two of the primary targets for direct searches for SUSY at colliders. With no signals reported, the most stringent constraints (as of March 2015) come from the ATLAS and CMS experiments at the LHC based on 20 fb^{-1} of data.[9] Typical production mechanisms of squarks and gluinos at the LHC are shown in Fig. 2.3. Note that in R-parity conserving SUSY, the superpartners are produced in pairs. Once produced, squarks undergo a cascade of decays that eventually terminates with the LSP, here taken to be the lightest neutralino $\widetilde{N}_1$. The neutralino escapes the detector, resulting in "missing" momentum transverse to the beam direction. The precise limits on stop masses depend on the spectrum of a given model (especially the mass of the LSP); for generic values of $m_{\widetilde{N}_1}$, ATLAS and CMS exclude $m_{\tilde{t}} \lesssim 700\,\text{GeV}$ (see, e.g., Refs. [104, 105]). [10] The production cross section for gluinos and first generation squarks is greater than for stops, resulting in bounds that reach $m_{\tilde{g}} \sim 1400\,\text{GeV}$ and $m_{\tilde{q}} \sim 1500\,\text{GeV}$ [105–107]. Dominant production of sleptons and "electroweakinos" (charginos and neutralinos) occurs through electroweak interactions and has correspondingly smaller rates, compared to the QCD production of gluinos and squarks [80]. The resulting bounds probe LSP masses of

[9] The LHC is the culmination of the energy frontier searches for SUSY. For a brief summary of earlier results from LEP and Tevatron see Ref. [80].

[10] Near certain degenerate regimes, e.g., $m_{\tilde{t}_1} = m_t + m_{\widetilde{N}_1}$, the bounds can be significantly weaker.

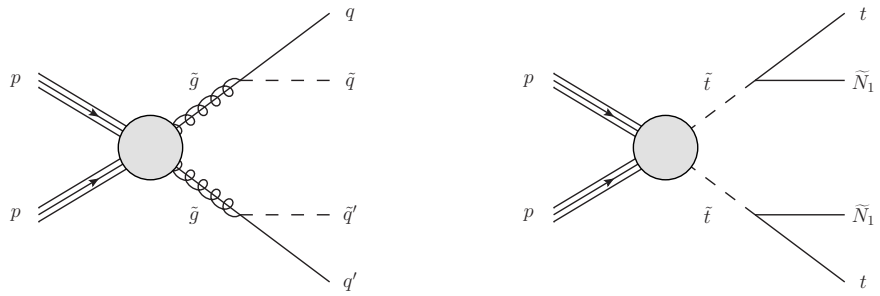

Figure 2.3: Typical LHC production mechanisms for gluinos and squarks (left) and stops (right).

$\sim 350\,\text{GeV}$, lightest chargino masses of $\sim 700\,\text{GeV}$ and slepton masses of $\sim 300\,\text{GeV}$ [108, 109].

Supersymmetric particles can also have indirect effects on measurements of processes that are already present in the SM. For example, various Higgs production and decay rates are modified in the MSSM. Neither ATLAS nor CMS observe statistically significant deviations from SM predictions [27]. This can be interpreted as a lower limit on the mass of additional MSSM states, such that their effects on Higgs rates are suppressed. Alternatively, this result can be seen as an "alignment" limit of the theory, where MSSM Higgs boson interactions effectively reduce to those of the SM, without the need for heavy MSSM states [110]. However, even if the tree-level couplings of the lightest MSSM Higgs are the same as in the SM, the rates for loop induced processes, namely $h \leftrightarrow gg,\ Z\gamma,\ \gamma\gamma$ can still be modified by $\mathcal{O}(10\%)$ in the presence of light stops, staus ($\lesssim 350\,\text{GeV}$) and charginos ($\lesssim 250\,\text{GeV}$) (see, e.g., Refs. [111, 112]). With 3000 fb^{-1} of data, the LHC will be able to probe Higgs couplings to gluons, photons and Z boson with a precision of about $\lesssim 5\%$ [113]. The complementarity between direct searches for superpartners and precise measurements of Higgs boson properties is discussed in detail in Ref. [114].

Flavour physics experiments can also be extremely sensitive indirect probes of supersymmetric states [115, 116]. For example, the process $B_s \to \mu^+\mu^-$ has been recently seen at LHCb, with the observed rate in agreement with the SM prediction [117]. However, the SM rate is so small (due to loop, CKM and helicity suppressions – see the left graph of Fig. 2.4) that *generic*, TeV scale, new physics contributions would give a larger result. Agreement of the measured rate with SM therefore places strong constraints on the scale of new physics. In particular, in the MSSM additional contributions to this amplitude arise from the exchange of new scalars as shown in the right graph of Fig. 2.4. However, within the MSSM with a particular flavour structure for the soft terms, these constraints are important only in the large $\tan\beta$ regime, rendering them very model dependent [116].

A variety of other low energy precision probes of SUSY are available [118]. Some of the most important tests are measurements of electric dipole moments (EDMs), which are sensitive to CP violation (crucial for baryogenesis) and flavour structure in the MSSM. One of the strongest

Figure 2.4: Representative contributions to $B_s \to \mu^+\mu^-$ in the SM (left) and the MSSM (right).

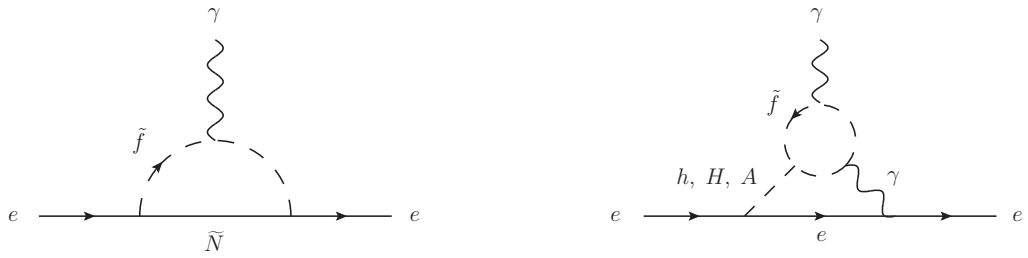

Figure 2.5: Representative contributions to electron EDM in the MSSM at one (left) and two (right) loops.

limits to date has been recently obtained by ACME [119] for the electron EDM. The exact limit on superpartner masses depends on which loop order the EDM contributions occur at; as shown in Fig. 2.5 there are both one and two loop diagrams contributing to fermion EDMs. In the absence of cancellations among different phases (i.e., tuning), the ACME result translates into a lower bound on m_{soft} of 1 to 3 TeV [119].

Finally, models with DM candidates can be probed on the cosmological frontier with direct and indirect detection. These were described in Sec. 1.3.3 and will be discussed in more detail in Chapters 3 and 4. Complementarity between direct and indirect detection and LHC searches is discussed in Ref. [120].

Part II

Moduli Decays

Chapter 3

Moduli Induced Lightest Superpartner Problem

3.1 Introduction

String theory is the only known consistent framework that can incorporate both the Standard Model of particle physics and General Relativity (GR) in a theory that is free of ultraviolet divergences. Instead of point particles, the fundamental degrees of freedom are strings, whose finite size regulates UV behaviour. Consistency suggests the existence of extra dimensions (10 or 11 in total), while low energy observations indicate that we live in a $3 + 1$ dimensional world. The extra dimensions must then be small and nearly unobservable. Compactification leads to a landscape of $\sim 10^{500}$ vacua [53], each differing by the shape of the extra dimensions. Each vacuum corresponds to vastly different physics at low energy, with distinct particle and symmetry content. The lack of a unique vacuum, or at least an easily identifiable class of physical vacua, has been a major criticism of string theory. At the same time, this landscape may provide an anthropic explanation for problems such as the smallness of the cosmological constant.

While difficult to test at every day energies or even at the LHC, viable string vacua have generic features that are important at energies far below the Planck scale. First, many string models enjoy spacetime supersymmetry.[1] Nature at low energies is not supersymmetric. However, if the scale of supersymmetry breaking is not too high, superpartners can be observed directly at colliders or as cosmological relics from the early Universe.

The second feature is the presence of moduli – light (compared to $M_{\rm Pl}$) scalar fields with only higher-dimensional couplings to other light species. In string theory, each vacuum is labelled by a set of continuous parameters which determine the size and shape of the compactified dimensions [121–124]. These parameters are expectation values of the moduli. While the couplings of moduli to matter are model dependent, they are always non-renormalizable, i.e.,

[1] Exceptions exist but these often have tachyons in the spectrum [53].

they are suppressed by a heavy scale Λ. For moduli originating from compactification, $\Lambda \sim M_{\rm Pl} = 2.435 \times 10^{18}\,\text{GeV}$. Such a coupling is too weak to be probed directly at present, but it can have significant implications for the cosmological history of the Universe, the mass spectrum of the supersymmetric partners of the SM, and the density of dark matter today [123, 125, 126].

In Sections 3.1.1 and 3.1.2 we justify two key moduli properties that we will repeatedly make use of. These properties are

1. Interactions of moduli with matter occur through higher-dimensional operators suppressed by a heavy scale,

2. The mass of the lightest modulus is typically on the order of $m_{3/2}$, the supersymmetry breaking scale.

The latter point is closely connected to supergravity and supersymmetry breaking which is discussed in detail in Sec. 2.4.

A modulus field can alter the standard cosmology if it is significantly displaced from the minimum of its potential in the early Universe, as can occur following primordial inflation [127]. The modulus will be trapped by Hubble damping until $H \sim m_\varphi$, at which point it will begin to oscillate. The energy density of these oscillations dilutes in the same way as non-relativistic matter, and can easily come to dominate the expansion of the Universe.[2] This will continue until the modulus decays at time $t \sim \Gamma_\varphi^{-1}$, transferring the remaining oscillation energy into radiation. At this point, called *reheating*, the radiation temperature is approximately [133]

$$T_{\rm RH} \;\sim\; (5\,\text{MeV}) \left(\frac{M_{\rm Pl}}{\Lambda}\right) \left(\frac{m_\varphi}{100\ \text{TeV}}\right)^{3/2}, \tag{3.1}$$

where Λ is the heavy mass scale characterizing the coupling of the modulus to light matter. To avoid disrupting primordial nucleosynthesis, the reheating temperature should be greater than about $T_{\rm RH} \gtrsim 5\,\text{MeV}$ [134], and this places a lower bound on the modulus mass.

Acceptable reheating from string moduli therefore suggests $m_\varphi \sim m_{3/2} \gtrsim 100$ TeV. This has important implications for the masses of the SM superpartner fields. Surveying the most popular mechanisms of supersymmetry breaking mediation described in Sec. 2.4.3, the typical size of the superpartner masses is

$$m_{\rm soft} \sim \begin{cases} m_{3/2} & \text{gravity mediation} \\ \left(\frac{LM_{\rm Pl}}{M}\right) m_{3/2} & \text{gauge mediation} \\ L m_{3/2} & \text{anomaly mediation} \end{cases} \tag{3.2}$$

where $L \sim g^2/(16\pi^2)$ is a typical loop factor and $M \ll M_{\rm Pl}/L$ is the mass of the gauge messengers. Of these mechanisms, only anomaly mediation (AMSB) allows for superpartners that are light enough to be directly observable at the LHC [102, 135]. Contributions to the

[2] Such an early matter-dominated phase might also leave an observable signal in gravitational waves at multiple frequencies [128] or modify cosmological observables [129–132].

soft terms of similar size can also be generated by the moduli themselves [136, 137], or other sources [138–141]. However, for these AMSB and AMSB-like contributions to be dominant, the gravity-mediated contributions must be suppressed [102], which is non-trivial for the scalar soft masses [142–146]. An interesting intermediate scenario is mini-split supersymmetry where the dominant scalar soft masses come from direct gravity mediation with $m_{\rm soft} \sim m_{3/2}$, while the gaugino soft masses are AMSB-like [147–152].

Moduli reheating can also modify dark matter production [133, 153–156]. A standard weakly-interacting massive particle (WIMP) χ will undergo thermal freeze-out at temperatures near $T_{\rm fo} \sim m_\chi/20$ as shown in Sec. 1.2.2. If this is larger than the reheating temperature, the WIMP density will be strongly diluted by the entropy generated from moduli decays. On the other hand, DM can be created *non-thermally* as moduli decay products. A compelling picture of non-thermal dark matter arises very naturally for string-like moduli and an AMSB-like superpartner mass spectrum [133]. The lightest (viable) superpartner (LSP) in this case tends to be a wino-like neutralino. These annihilate too efficiently to give the observed relic density through thermal freeze-out [157–159]. However, with moduli domination and reheating, the wino LSP can be created non-thermally in moduli decays, and the correct DM density is obtained for $M_2 \sim 200$ GeV and $m_\varphi \sim 3000$ TeV.

This scenario works precisely because the wino annihilation cross section is larger than what is needed for thermal freeze-out. Unfortunately, such enhanced annihilation rates are strongly constrained by gamma-ray observations of the galactic centre by Fermi and HESS, and the non-thermal wino is ruled out even for very conservative assumptions about the DM profile in the inner galaxy (e.g., cored isothermal) [158, 159]. A wino-like LSP can be consistent with these bounds if it is only a subleading component of the total DM density. Using the AMSB relation for M_2 in terms of $m_{3/2}$, this forces $m_\varphi/m_{3/2} \gtrsim 100$, significantly greater than the generic expectation [159]. The problem is even worse for other neutralino LSP species, since these annihilate less efficiently and an even larger value of $m_\varphi \gg m_{3/2}$ is needed to obtain an acceptable relic density. Furthermore, $m_\varphi > 2m_{3/2}$ also allows the modulus field to decay to pairs of gravitinos. The width for this decay is typically similar to the total width to SM superpartners [160–163]. For $m_\varphi \gg m_{3/2} > 30$ TeV, the gravitinos produced this way will decay to particle-superpartner pairs before nucleosynthesis but after the modulus decays, and recreate the same LSP density problem that forced $m_\varphi \gg m_{3/2}$ in the first place.

These results suggest a degree of tension between reheating by string-motivated moduli (with $m_\varphi \sim m_{3/2}$ and $\Lambda \sim M_{\rm Pl}$) and the existence of a stable TeV-scale LSP in the minimal supersymmetric standard model (MSSM). This tension can be resolved if all relevant moduli have properties that are slightly different from the naïve expectation; for example $m_\varphi \gg m_{3/2}$ and ${\rm BR}(\varphi \to \psi_{3/2}\psi_{3/2}) \ll 1$ [163, 164], an enhanced modulus decay rate with $m_\varphi \sim m_{3/2}$ and $\Lambda < M_{\rm Pl}$ [165], or a suppressed modulus branching fraction into superpartners [166]. Given the challenges and uncertainties associated with moduli stabilization in string theory, we focus on what seem to be more generic moduli and we investigate a second approach: extensions of the

MSSM that contain new LSP candidates with smaller relic densities or that are more difficult to detect than their MSSM counterparts.

In this chapter we investigate extensions of the MSSM containing additional hidden gauge sectors as a way to avoid the moduli-induced LSP problem of the MSSM. Such gauge extensions arise frequently in grand-unified theories [167] and string compactifications [168, 169]. We assume that the dominant mediation of supersymmetry breaking to gauginos is proportional to the corresponding gauge coupling, as in anomaly or gauge mediation, allowing the hidden sector gauginos to be lighter than those of the MSSM if the former have a smaller coupling constant [170–172]. We also focus on the case of a single light modulus field with $m_\varphi \sim m_{3/2}$ and $\Lambda \sim M_{\rm Pl}$, although similar results are expected to hold for multiple moduli or for reheating by gravitino decays.

This chapter is organized as follows. In Sec. 3.1.1 we review the origin of moduli from compactification and highlight their properties. We discuss moduli masses in Sec. 3.1.2. In Sec. 3.1.3 we review moduli cosmology and the resulting non-thermal production of LSPs. Next, in Sec. 3.2 we examine in more detail the tension between moduli reheating and a stable MSSM LSP. In the subsequent three sections we present three extensions of the MSSM containing new LSP candidates and examine their abundances and signals following moduli reheating. The first extension, discussed in Sec. 3.3, comprises a minimal supersymmetric $U(1)_x$ hidden sector. We find that this setup allows for a hidden sector LSP with a relic density lower than that of the wino and which is small enough to evade the current bounds from indirect detection. In Sec. 3.4 we extend the $U(1)_x$ hidden sector to include an asymmetric dark matter candidate and find that it is able to saturate the entire observed DM relic density while avoiding constraints from indirect detection. In Sec. 3.5 we investigate a pure non-Abelian hidden sector, and show that the corresponding gaugino LSP can provide an acceptable relic density and avoid constraints from indirect detection, although it is also very strongly constrained by its effect on structure formation and the cosmic microwave background. Finally, Sec. 3.6 is reserved for our conclusions. This chapter is based on work published in Ref. [1] in collaboration with Jonathan Kozaczuk, Arjun Menon and David Morrissey.

3.1.1 Moduli from Compactification

As a toy example of a modulus field associated with compactification, consider (non-supersymmetric) $5D$ gravity - the Kaluza-Klein model, which attempted to unify GR with electromagnetism [173, 174]. The Einstein-Hilbert action in $5D$ is

$$S_5 = -\frac{1}{2} M_5^3 \int_{S_1 \times \mathbb{R}^{1,3}} d^5x \sqrt{-G} R_5[G], \tag{3.3}$$

where we parametrize the $5D$ metric as [51, 96]

$$G_{MN} = \begin{pmatrix} \varphi^{-1/3}(g_{\mu\nu} - \varphi A_\mu A_\nu) & -\varphi^{2/3} A_\nu \\ -\varphi^{2/3} A_\mu & -\varphi^{2/3} \end{pmatrix}. \tag{3.4}$$

Here M_5 is the $5D$ Planck mass, G is the determinant of the metric, R_5 is the $5D$ Ricci scalar and $M, N = 1, \ldots 5$, and $\mu, \nu = 1, \ldots, 4$. The fields in Eq. (3.4) are functions of x_μ only, and are constant over the fifth dimension x_5. This means we are considering only the zero modes in the Kaluza-Klein expansion; higher modes receive masses on the order of the compactification scale and can be integrated out of the low-energy dynamics. Using this metric parametrization we can rewrite S_5 as an effective $4D$ action

$$S_5 = -\frac{1}{2}(2\pi R M_5^3) \int d^4x \sqrt{-g} \left(R_4[g] + \frac{1}{4}\varphi F_{\mu\nu} F^{\mu\nu} - \frac{1}{6}\varphi^{-2} \partial_\mu \varphi \partial^\mu \varphi, \right) \tag{3.5}$$

where R is the radius of the compactified extra dimension, R_4 is the $4D$ Ricci scalar (a functional of $g_{\mu\nu}$ only), $F_{\mu\nu} = \partial_\mu A_\nu - \partial_\nu A_\mu$. We can now identify $2\pi R M_5^3 = M_{\rm Pl}^2$. Finally, using the field redefinitions $\varphi \to \exp(-\sqrt{6}\varphi/M_{\rm Pl})$ and $F \to M_{\rm Pl} F/\sqrt{2}$, we get canonical kinetic terms for φ and F

$$S_5 = -\frac{1}{2} M_{\rm Pl}^2 \int d^4x \sqrt{-g} R_4[g] + \int d^4x \sqrt{-g} \left(-\frac{1}{4} F_{\mu\nu} F^{\mu\nu} e^{-\sqrt{6}\varphi/M_{\rm Pl}} + \frac{1}{2} \partial_\mu \varphi \partial^\mu \varphi \right). \tag{3.6}$$

The scalar φ is the desired modulus. Note that its interactions with the vector field F are non-renormalizable and are suppressed by the heavy scale $M_{\rm Pl}$.

The compactified action of Eq. (3.6) illustrates the second important property of moduli: there is no tree-level potential for φ. Without additional dynamics these fields remain massless. Because different values of the fields correspond to physically distinct vacua, in a quantum theory one wants to stabilize moduli at particular values. Moreover, at low energies these new massless degrees of freedom can be inconsistent with precise tests of gravitational interactions (see Ref. [58] and references therein). Moduli stabilization is therefore necessary. It is usually achieved through the inclusion of background fluxes (gauge fields) and/or gaugino condensation [175, 176]. In the next section, we argue that the lightest modulus mass is often on the order of supersymmetry breaking scale, independently of the stabilization mechanism.

The above example is a simple illustration of a much more complicated process. In realistic string theory compactifications, there are six (or seven) compact dimensions curled up into a (possibly) complex manifold. As a result, there can be $\mathcal{O}(100)$ moduli, all of which must be stabilized [175].

3.1.2 Moduli Masses

Moduli stabilization can be divided into two categories. In supersymmetric stabilization, the modulus φ acquires a mass without relying on SUSY breaking, such that $m_\varphi \gg m_{3/2}$ is possible.

However, once the potential is tuned to reproduce the small cosmological constant, one finds that the mass of the lightest modulus is parametrically related to $m_{3/2}$ [177], as we argue below. Even if this is not true and $m_\varphi \gg m_{3/2}$, moduli decay to gravitinos which generally cause similar cosmological problems. This point is discussed in more detail in Sec. 3.1.6. The second case corresponds to the modulus acquiring a mass $m_\varphi \sim m_{3/2}$ from SUSY breaking effects.

Moduli masses can be easily related to $m_{3/2}$ for the simple (i.e., somewhat unrealistic) case of the canonical Kähler potential of Eq. (2.64). Assuming the moduli superfields Φ_i have no superpotential, the SUGRA potential, Eq. (2.60), for these fields reads [154]

$$V \supset M_{\rm Pl}^2 e^G |\varphi_i|^2 = m_{3/2}^2 |\varphi_i|^2, \tag{3.7}$$

where G the expectation value of the Kähler function defined in Eq. (2.59); we have used Eq. (2.68) in the last step to rewrite this term after SUSY breaking. This shows that the modulus mass is on the order of the SUSY-breaking scale. Note that the precise relationship depends on the form of the Kähler potential and the possible existence of non-perturbative contributions to the superpotential (see, e.g., Ref. [178] for examples). Alternative, more rigorous derivations of the $m_\varphi \sim m_{3/2}$ relationship for more general models can be found in Refs. [123, 124].

The above result relied on the absence of a modulus potential at the supersymmetric level and a canonical Kähler function. Non-perturbative effects from instantons and fermion condensation can give rise to a modulus superpotential of the form [179]

$$W = W_0 - \Lambda^3 e^{-b\Phi/M_{\rm Pl}}, \tag{3.8}$$

where the parameters W_0, Λ and b can be determined in string theory [177]. It is usually assumed that $|W_0| \ll \Lambda^3 \sim M_{\rm Pl}^3$, while $b \leq 2\pi$ and depends on the nature of the non-perturbative effects. Moreover, moduli generally have logarithmic Kähler functions like

$$K = -3\ln(\Phi + \Phi^\dagger), \tag{3.9}$$

with the functional form related to the volume of the compact dimensions parametrized by Φ [177]. The resulting scalar potential gives rise to a supersymmetric anti-de Sitter (AdS) vacuum with a negative cosmological constant and the modulus stabilized with an expectation value $\langle\varphi\rangle \sim b^{-1} M_{\rm Pl} \ln(\Lambda^3/W_0)$. The energy density of this vacuum is $V_{\rm AdS} \sim -W_0^2/M_{\rm Pl}^2$, while the mass of the fluctuations is $m_\varphi \sim \exp(G/2)\langle\varphi\rangle$. Our vacuum is observed to be de Sitter (dS), with a small positive cosmological constant, so a realistic theory must *uplift* the AdS minimum to yield a positive vacuum energy density. This can be achieved through supersymmetry breaking, which gives a positive contribution to the energy density, as was shown explicitly for the O'Raifeartaigh model in Sec. 2.4; the contribution of the SUSY breaking sector to the vacuum energy was found to be $V_{OR} \sim \kappa^4$, where κ^2 determines the scale of

the F-term vev. The requirement of a tiny positive cosmological constant then forces $\kappa \sim (W_0/M_{\rm Pl})^{1/2}$. This relates the scales of SUSY breaking and moduli stabilization, such that the modulus mass is now given by $m_\varphi \sim m_{3/2}\ln(\Lambda^3/W_0)$. Note that the modulus mass is enhanced only logarithmically relative to $m_{3/2}$. More complicated superpotentials can give rise to a larger hierarchy between m_φ and $m_{3/2}$, but this typically requires additional tuning of parameters [177].

Once the modulus develops a non-trivial potential, it can significantly modify the cosmological evolution of the Universe, as we discuss in the following sections.

3.1.3 Moduli Reheating

A modulus field φ is very likely to develop a large initial displacement from the minimum of its potential before or during the course of primordial inflation [127, 180]. Hubble damping will trap the modulus until $H \sim m_\varphi$, at which point it will start to oscillate coherently. This is shown in the left plot of Fig. 3.1, where we take an initial displacement of $\mathcal{O}(M_{\rm Pl})$ and $m_\varphi = 100\,\text{TeV}$. For even moderate initial displacements, the energy density in these oscillations will eventually dominate over radiation, as shown in the right plot of Fig. 3.1. The time evolution of the average modulus oscillation energy density for $H < m_\varphi$ is given by [40]

$$\dot{\rho}_\varphi + 3H\rho_\varphi + \Gamma_\varphi \rho_\varphi = 0, \tag{3.10}$$

where Γ_φ is the modulus decay rate. For a modulus field with $M_{\rm Pl}$-suppressed couplings

$$\Gamma_\varphi = \frac{c}{4\pi}\frac{m_\varphi^3}{M_{\rm Pl}^2}, \tag{3.11}$$

where c is a model-dependent number with a typical range of $10^{-3} < c < 100$ [159].[3] As the modulus oscillates, it decays to radiation with the radiation density becoming dominant once more when $H \sim \Gamma_\varphi$.

Thermodynamics in the early Universe was described in Sec. 1.2.2. Moduli decays inject energy into the plasma, which can be accounted for by straightforward modifications of the equations in that section. For example, the evolution of the radiation density ρ_R follows from the First Law of thermodynamics as in Eq. (1.65):

$$\frac{d\rho_R}{dt} + 3H(\rho_R + p_R) = \Gamma_\varphi \rho_\varphi, \tag{3.12}$$

where p_R is the radiation pressure. The right hand side is the rate of energy injection into the bath, of which moduli decays are assumed to be the dominant source. Contributions from DM annihilation can also be included, but these do not make much difference when the DM is

[3] Values of c much larger than this can be interpreted as corresponding to a suppression scale $\Lambda < M_{\rm Pl}$.

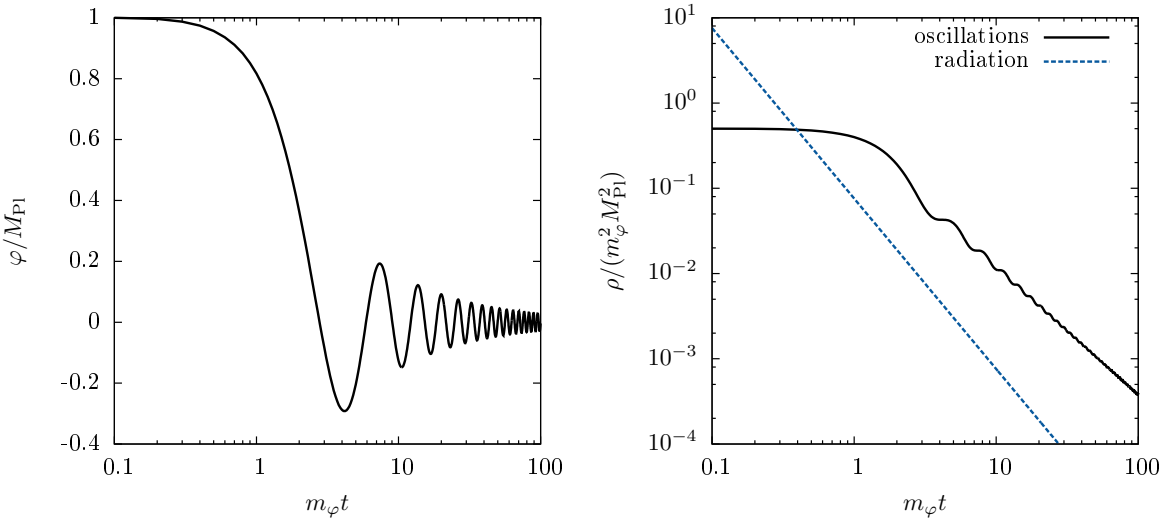

Figure 3.1: (Left) Solution of the modulus equation of motion for an initial displacement of $M_{\rm Pl}$ and modulus mass $m_\varphi = 100\,\text{TeV}$. (Right) Evolution of the energy density in the modulus oscillations (solid) and radiation (dashed). Because the oscillation energy density dilutes slower with the expansion of the Universe, it will eventually dominate the energy density in radiation.

lighter than the modulus field. The radiation density is used to define the temperature through

$$\rho_R = \frac{\pi^2}{30} g_*(T) T^4, \tag{3.13}$$

where $g_*(T)$ is the effective number of relativistic degrees of freedom [181]. Reheating is said to occur when radiation becomes the dominant energy component of the Universe, corresponding to $H(T_{\rm RH}) \simeq \Gamma_\varphi$. Following Ref. [133], we define the reheating temperature $T_{\rm RH}$ to be:

$$\begin{aligned} T_{\rm RH} &= \left(\frac{90}{\pi^2 g_*(T_{\rm RH})}\right)^{1/4} \sqrt{\Gamma_\varphi M_{\rm Pl}} \\ &\simeq (5.6\text{ MeV})\, c^{1/2} \left(\frac{10.75}{g_*}\right)^{1/4} \left(\frac{m_\varphi}{100\text{ TeV}}\right)^{3/2}. \end{aligned} \tag{3.14}$$

Here $M_{\rm Pl} \simeq 2.4 \times 10^{18}\,\text{GeV}$ is the reduced Planck mass. The reheating temperature $T_{\rm RH}$ should exceed 5 MeV to preserve the predictions of primordial nucleosynthesis [134].[4] For $c = 1$ this implies that $m_\varphi \gtrsim 100$ TeV.

[4] We have adjusted for our slightly different definition of $T_{\rm RH}$ relative to Ref. [134] in the quoted bound.

3.1.4 Non-Thermal Dark Matter

Moduli decays can also produce stable massive particles, such as a self-conjugate dark matter candidate χ [133]. This is described by

$$\frac{dn_\chi}{dt} + 3Hn_\chi = \frac{\mathcal{N}_\chi \Gamma_\varphi}{m_\varphi}\rho_\varphi - \langle\sigma v\rangle(n_\chi^2 - n_{\rm eq}^2), \tag{3.15}$$

where $\langle\sigma v\rangle$ is the thermally averaged annihilation cross-section, $n_{\rm eq} = gTm_\chi^2 K_2(m_\chi/T)/2\pi^2$ is the equilibrium number density, with g being the number of internal degrees of freedom and $\mathcal{N}_\chi$ is the average number of χ particles produced per modulus decay.[5] Values of $\mathcal{N}_\chi \sim 1$ are usually expected when χ is the LSP [178, 183]. Together, Eqs. (3.10, 3.12, 3.15) and the Friedmann equation form a closed set of equations for the system.

The general solution of these equations interpolates between three distinct limits [133, 153, 155]. For reheating temperatures above the thermal freeze out temperature $T_{\rm fo}$ of χ, the final χ density approaches the thermal value. When $T_{\rm RH} < T_{\rm fo}$, annihilation may or may not be significant depending on $\langle\sigma v\rangle$ and $\mathcal{N}_\chi$. Smaller values imply negligible χ annihilation after reheating and a final relic density of about [155]

$$\begin{aligned}\Omega_\chi h^2 &\simeq \frac{3}{4}\mathcal{N}_\chi \left(\frac{m_\chi}{m_\varphi}\right) T_{\rm RH}\left(\frac{s_0}{\rho_c/h^2}\right) \\ &\simeq (1100)\,\mathcal{N}_\chi \left(\frac{m_\chi}{100\ {\rm GeV}}\right)\left(\frac{T_{\rm RH}}{5\ {\rm MeV}}\right)\left(\frac{100\,{\rm TeV}}{m_\varphi}\right),\end{aligned} \tag{3.16}$$

where s_0 is the entropy density today and ρ_c/h^2 is the critical density. Larger values of $\mathcal{N}_\chi$ or $\langle\sigma v\rangle$ lead to significant annihilation among the χ during the reheating process, giving a relic density of [154, 155]

$$\begin{aligned}\Omega_\chi h^2 &\simeq \frac{m_\chi \Gamma_\varphi}{\langle\sigma v\rangle s_{\rm RH}}\left(\frac{s_0}{\rho_c/h^2}\right) \\ &\simeq (0.2)\left(\frac{m_\chi/20}{T_{\rm RH}}\right)\left(\frac{3\times 10^{-26}{\rm cm}^3/{\rm s}}{\langle\sigma v\rangle}\right)\left(\frac{10.75}{g_*}\right)^{1/2} \\ &\simeq (200)\,c^{-1/2}\left(\frac{m_\chi}{100\ {\rm GeV}}\right)\left(\frac{3\times 10^{-26}{\rm cm}^3/{\rm s}}{\langle\sigma v\rangle}\right)\left(\frac{100\ {\rm TeV}}{m_\varphi}\right)^{3/2}\left(\frac{10.75}{g_*}\right)^{1/4}.\end{aligned} \tag{3.17}$$

We emphasize that the expressions of Eqs. (3.16,3.17) are only approximations valid to within a factor of order unity. In what follows we solve this system numerically using the methods of Refs. [184, 185]. For $T_{\rm RH} < T_{\rm fo}$ and $\mathcal{N}_\chi$ not too small, the reannihilation scenario is usually the relevant one [155].

[5] This includes χ produced in direct decays, as well as rescattering [182] and decay cascades.

3.1.5 Scaling Relations

It is instructive to look at how the relation of Eq. (3.17) scales with the relevant couplings and masses [170]. Motivated by the MSSM wino in anomaly mediation, we will assume that the dark matter mass scales with a coupling g_χ according to

$$m_\chi = r_\chi \frac{g_\chi^2}{(4\pi)^2} m_{3/2}, \tag{3.18}$$

for some parameter r_χ. We will assume further that the dark matter annihilation cross section scales with the coupling as well,

$$\langle \sigma v \rangle = \frac{k_\chi}{4\pi} \frac{g_\chi^4}{m_\chi^2}, \tag{3.19}$$

for some parameter k_χ. For an AMSB-like wino, the r and k parameters are [133]

$$r_2 \simeq 1, \tag{3.20}$$

$$k_2 \simeq 2 \frac{[1-(m_W/M_2)^2]^{3/2}}{[2-(m_W/M_2)^2]^2} \rightarrow 1/2, \tag{3.21}$$

with $g_\chi = g_2 \simeq 0.65$, and the last expression neglects coannihilation with charginos, which can be suppressed at low reheating temperatures [155].

With these assumptions, the thermal χ abundance is

$$\Omega_\chi^{\rm th} h^2 \simeq (5.5 \times 10^{-3}) \frac{r_\chi^2}{k_\chi} \left(\frac{m_\chi/T_{\rm fo}}{20}\right) \left(\frac{m_{3/2}}{100\ {\rm TeV}}\right)^2 \left(\frac{106.75}{g_*}\right)^{1/2} \tag{3.22}$$

independent of the specific mass or coupling. This is no longer true of non-thermal DM produced by moduli decays, where the mass dependence is different. Rewriting Eq. (3.17) subject to the assumptions of Eqs. (3.18,3.19), we obtain

$$\Omega_\chi h^2 \simeq 15\, c^{-1/2} \left(\frac{r_\chi^3/k_\chi}{r_2^3/k_2}\right) \left(\frac{g_\chi}{g_2}\right)^2 \left(\frac{m_{3/2}}{m_\varphi}\right)^3 \left(\frac{m_\varphi}{100\ {\rm TeV}}\right)^{3/2} \left(\frac{10.75}{g_*}\right)^{1/4}. \tag{3.23}$$

This result shows that reducing the coupling or the modulus mass suppresses the non-thermal relic density. It also makes clear that $m_\varphi > m_{3/2}$ is needed to obtain an acceptable wino abundance within the reannihilation regime.

3.1.6 Gravitino Production and Decay

Our previous discussion of moduli reheating did not take gravitinos into account. Moduli can also decay to gravitinos if $m_\varphi > 2m_{3/2}$, and the corresponding branching ratio $\mathrm{BR}_{3/2}$ is expected to be on the order of unity unless some additional structure is present [160–163]. For $m_\varphi \sim 2m_{3/2}$, the gravitinos will decay at about the same time as the moduli and our previous

results for the moduli-only case are expected to apply here as well. On the other hand, if $m_\varphi \gg m_{3/2}$ and $\mathrm{BR}_{3/2}$ is not too small, the gravitinos produced by decaying moduli are likely to come to dominate the energy density of the Universe before they themselves decay. We examine this possibility here, and show that our results for moduli decay can be applied to this scenario as well after a simple reinterpretation of parameters.

If the gravitino is not the LSP, it will decay to lighter particle-superpartner pairs with

$$\Gamma_{3/2} \;=\; \frac{d}{4\pi}\frac{m_{3/2}^3}{M_{\rm Pl}^2}, \tag{3.24}$$

where $d = 193/96$ if all MSSM final states are open and $d = (1+3+8)/8 = 3/2$ if only gaugino modes are available [186]. These decays will not appreciably disrupt BBN for $m_{3/2} \gtrsim 30$ TeV, but they can produce a significant amount of LSP dark matter.

For $m_\varphi \gg m_{3/2}$, the modulus will decay much earlier than the gravitino (unless $c \ll d$). The gravitinos produced by moduli decays at time $t_i \simeq \Gamma_\varphi^{-1}$ will be initially relativistic with $p/m_{3/2} = m_\varphi/2m_{3/2}$. Their momentum will redshift with the expansion of the Universe, and they will become non-relativistic at time

$$t_{\rm nr} \simeq \frac{d}{4c}\left(\frac{m_{3/2}}{m_\varphi}\right)\Gamma_{3/2}^{-1}, \tag{3.25}$$

where we have assumed that the Universe is radiation-dominated after moduli reheating. Thus, the gravitinos produced in moduli decays become non-relativistic long before they decay for $m_{3/2}/m_\varphi \ll 1$ (and $c \sim d$). While $t_{\rm nr} < t < \Gamma_{3/2}^{-1}$, the gravitinos will behave like matter. The quantity $m_{3/2}n_{3/2}$ begins to exceed the (non-gravitino) radiation density at time

$$t \simeq \frac{d}{c}\left(\frac{1-\mathrm{BR}_{3/2}}{\mathrm{BR}_{3/2}}\right)^2\left(\frac{m_{3/2}}{m_\varphi}\right)^3\Gamma_{3/2}^{-1} \tag{3.26}$$

Again, this is much earlier than the gravitino decay time for $m_{3/2}/m_\varphi \ll 1$ unless $\mathrm{BR}_{3/2}$ or c/d is suppressed.[6]

The scenario that emerges for $m_{3/2} \ll m_\varphi$, $c \sim d$, and $\mathrm{BR}_{3/2} \sim 1$ is very similar to a second stage of moduli reheating: the gravitinos produced in moduli decays become non-relativistic and come to dominate the energy density of the Universe until they decay at time $t \simeq \Gamma_{3/2}^{-1}$, at which point they reheat the Universe again. Dark matter will also be created by the gravitino decays, with at least one LSP produced per decay (assuming R-parity conservation). The large gravitino density from moduli decays can interfere with nucleosynthesis or produce too much dark matter, and is sometimes called the moduli-induced gravitino problem [160–163].

We will not discuss gravitinos much for the remainder of this chapter. Instead, we will focus mainly on the case of $m_\varphi \sim m_{3/2}$, where the presence of gravitinos does not appreciably change our results [155]. However, our findings can also be applied to scenarios with $m_\varphi \gg m_{3/2}$, $c \sim d$,

[6] We have assumed radiation domination here, but a similar result holds for matter domination.

and $\mathrm{BR}_{3/2} \sim 1$ with the moduli decays reinterpreted as gravitino decays (i.e., $m_\varphi \to m_{3/2}$, $c \to d$, $\mathcal{N}_\chi \to 1$).

3.2 Moduli Reheating and the MSSM

The discussion of Sec. 3.1.3 shows that the LSP relic density is enhanced in the moduli-decay scenario relative to thermal freeze out unless the fraction of decays producing LSPs $\mathcal{N}_\chi$ is very small. In Ref. [159], this observation was used to put a very strong constraint on wino-like LSPs produced by moduli decays. In this section we apply these results to more general MSSM neutralino LSPs, and we argue that the MSSM has a *moduli-induced LSP problem* for $m_\varphi \sim m_{3/2}$, $c \sim 1$, and $\mathcal{N}_\chi$ not too small. See also Refs. [187, 188] for related analyses.

Consider first a wino-like LSP with an AMSB-like mass. Direct searches at the LHC imply that the mass must lie above $m_{\chi_1^0} \gtrsim 270$ GeV if it is nearly pure wino [189], although smaller masses down to the LEP limit $m_{\chi_1^\pm} \gtrsim 104$ GeV are possible if it has moderate mixing with a Higgsino [190]. Examining Eq. (3.23), the moduli-induced wino relic density (in the reannihilation regime) tends to be larger than the observed DM density, and indirect detection places an even stronger bound of $\Omega_\chi h^2 \lesssim 0.05$ [159]. Fixing $m_\chi = 270$ GeV, a relic density of this size can be obtained with the very optimistic combination of parameter values $c = 100$, $m_\varphi = 2m_{3/2}$, and $r_\chi/r_2 \lesssim 0.3$. Such a reduction in r_χ/r_2 can arise from supersymmetry-breaking threshold corrections [191, 192] or moduli-induced effects [136, 137], but requires a significant accidental cancellation relative to the already-small AMSB value of r_2 [159].

A small effective value of $r_\chi < r_2$ could also arise from $|\mu| \ll |M_2|$ and a corresponding Higgsino-like LSP. The reduction in the relic density in this case is countered by a smaller annihilation cross section: for $\mu \gg m_W$, heavy scalars, and neglecting coannihilation we have $g_\chi \simeq g_2$, $r_\chi = (\mu/M_2)$, and $k_\chi \simeq (3 + 2t_W^2 + t_W^4)/128 \simeq 0.03$ [157] (where $t_W \equiv \tan\theta_W$, with θ_W the Weinberg angle). To investigate this possibility in more detail, we set $m_\varphi/m_{3/2} = 1$, 10, 100 and $c = 1$, and compute the moduli-induced LSP relic density for various values of μ/M_2 and $m_{3/2}$. In doing so, we fix M_2 to its AMSB value with $c = 1$ and $m_\varphi = m_{3/2}$, and we compute the annihilation cross section in `DarkSUSY` [193, 194]. For the other MSSM parameters, we set $\tan\beta = 10$, $m_A = 1000$ GeV, $\tilde{m} = 2000$ GeV for all scalars, and we fix A_t such that $m_h = 126 \pm 1$ GeV.

Fixing $m_\varphi/m_{3/2} = 1$, 10 we find no Higgsino-like points with $\Omega_\chi h^2 \leq 0.12$, i.e., for values which would appear to be generically expected from string theory.[7] Smaller relic densities are found for $m_\varphi/m_{3/2} = 100$, and the results of our scan for this ratio are shown in Fig. 3.2. The LSP relic density is smaller than the total DM density to the left and below the solid black line, while the grey dashed contours show the LSP mass. To the right of the red line, the reheating temperature lies above the freeze-out temperature and the resulting density is thermal. The coloured dashed contours correspond to bounds from indirect detection for different DM density

[7] We also fail to find any such points for $c = 100$ and $m_\varphi = 2m_{3/2}$.

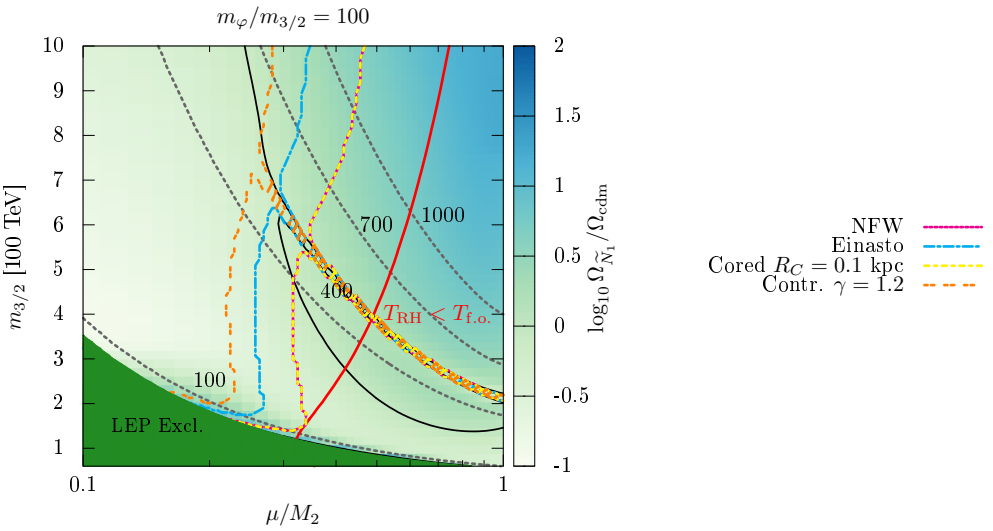

Figure 3.2: Relic density and constraints from indirect detection (ID) for a mixed Higgsino-wino LSP produced by moduli reheating as a function of μ/M_2 and $m_{3/2}$. The modulus parameters are taken to be $m_\varphi/m_{3/2} = 100$, $c = 1$, and $\mathcal{N}_\chi = 1$. Contours of the LSP mass in GeV are given by the dashed grey lines. The solid black contours show where $\Omega_{\chi_1^0} = \Omega_{\rm cdm}$. The solid red line shows where $T_{\rm RH} = T_{\rm fo}$: to the left of it we have $T_{\rm RH} > T_{\rm fo}$; to the right $T_{\rm RH} < T_{\rm fo}$ and the production is non-thermal. The remaining lines correspond to bounds from ID for different galactic DM distributions, and the area below and to the right of these lines is excluded.

profiles, excluding everything below and to the right of them.[8] This figure also shows a funnel region with very low relic density along the $m_{\chi_1^0} = 500\,\text{GeV}$ contour corresponding to an s-channel A^0 pseudoscalar resonance.

In general, for $m_\varphi \sim m_{3/2}$, we find that a Higgsino-like LSP also tends to produce too much dark matter when it is created in moduli reheating. As for the wino, this can be avoided for larger values of $m_\varphi/m_{3/2}$, as demonstrated by Fig. 3.2, although one must still ensure that the very heavy modulus does not decay significantly to gravitinos.

These results can be extended to an arbitrary MSSM neutralino LSP. In general, mixing with a bino will further suppress the annihilation cross section, leading to an overproduction of dark matter for $m_\varphi \sim m_{3/2}$. The only loophole we can see is a very strong enhancement of the annihilation from a resonance or coannihilation [43]. This requires a very close mass degeneracy either between $2m_\chi$ and the mass of the resonant state, or between m_χ and the coannihilating state, with coannihilation further suppressed at low reheating temperatures. The only other viable LSP candidates in the MSSM are the sneutrinos. These annihilate about as efficiently as a Higgsino-like LSP [195], and therefore also tend to be overproduced. The MSSM sneutrinos also have a very large scattering cross section with nuclei, and bounds from direct detection

[8] The details of our indirect detection analysis will be presented in the next section.

permit them to be only a small fraction of the total DM density [196].

Having expanded slightly on the findings of Ref. [159], we conclude that a neutral MSSM LSP is typically overproduced in moduli reheating unless $m_\varphi \gg m_{3/2}$ (with tiny $\mathrm{BR}_{3/2}$), $\mathcal{N}_\chi \ll 1$, or the decay coefficient $c \gg 100$ is very large. None of these features appears to be generic in string compactifications. We call this the *moduli-induced MSSM LSP problem*. For this reason, we turn next to extensions of the MSSM with more general LSP candidates that can potentially avoid this problem.

3.3 Variation #1: Hidden $U(1)$

The first extension of the MSSM that we consider consists of a hidden $U(1)_x$ vector multiplet X and a pair of hidden chiral multiplets H and H' with charges $x_{H,H'} = \pm 1$. Motivated by the scaling relation of Eq. (3.23), we take the characteristic gauge coupling and mass scale of the hidden sector to be significantly less than electroweak, along the lines of Refs. [197–199]. The LSP of the extended theory will therefore be the lightest hidden neutralino. We also assume that the only low-energy interaction between the hidden and visible sectors is gauge kinetic mixing. Among other things, this allows the lightest MSSM superpartner to decay to the hidden sector. In this section we the investigate the contribution of the hidden LSP to the dark matter density following moduli reheating as well as the corresponding bounds from indirect and direct detection.

3.3.1 Setup and Spectrum

The hidden superpotential is taken to be

$$W_{\mathrm{HS}} = -\mu' H H', \tag{3.27}$$

and the soft supersymmetry breaking terms are

$$-\mathscr{L}_{\mathrm{soft}} \supset m_H^2 |H|^2 + m_{H'}^2 |H'|^2 + \left(-b' H H' + \frac{1}{2} M_x \widetilde{X} \widetilde{X} + \text{ h.c.} \right). \tag{3.28}$$

The only interaction with the MSSM comes from supersymmetric gauge kinetic mixing in the form

$$\mathscr{L} \supset \int d^2\theta \, \frac{\epsilon}{2} X^\alpha B_\alpha, \tag{3.29}$$

where X and B are the $U(1)_x$ and $U(1)_Y$ field strength superfields, respectively.

We assume that the gaugino mass is given by its AMSB value [198]

$$M_x = b_x \frac{g_x^2}{(4\pi)^2} m_{3/2}, \tag{3.30}$$

where $b_x = 2$ and g_x is the $U(1)_x$ gauge coupling. Since pure AMSB does not provide a viable scalar spectrum in the MSSM, we do not impose AMSB values on the scalar soft terms in the hidden sector. However, we do assume that they (and μ') are of similar magnitude to their AMSB values, on the order of $(g_x^2/16\pi^2)m_{3/2}$. This could arise if the dynamics that leads to a viable MSSM spectrum also operates in the hidden sector and that its effects are proportional to the corresponding gauge coupling.

For a range of values of μ' and the soft terms, the scalar components of H and H' will develop vacuum expectation values,

$$\langle H \rangle = \eta \sin\zeta, \ \langle H' \rangle = \eta \cos\zeta. \tag{3.31}$$

Correspondingly, the hidden vector boson X_μ receives a mass

$$m_x = \sqrt{2} g_x \eta. \tag{3.32}$$

The scalar mass eigenstates after $U(1)_x$ breaking consist of two CP-even states $h^x_{1,2}$ (with h^x_1 the lighter of the two) and the CP-odd state A^x. The fermionic mass eigenstates are mixtures of the hidden Higgsinos and the $U(1)_x$ gaugino, and we label them in order of increasing mass as $\chi^x_{1,2,3}$. Full mass matrices for all these states can be found in Refs. [200, 201].

3.3.2 Decays to and from the Hidden Sector

Kinetic mixing allows the lightest MSSM neutralino to decay to the hidden sector. It can also induce some of the hidden states to decay back to the SM. We discuss the relevant decay modes here.

The MSSM neutralinos connect to the hidden sector through the bino. For AMSB gaugino masses, the bino soft mass is significantly heavier than that of the wino, and the lightest neutralino χ^0_1 tends to be nearly pure wino. Even so, it will have a small bino admixture given by the mass mixing matrix element $\mathbf{N}_{11}$. In the wino limit, it can be approximated by [157]

$$|\mathbf{N}_{11}| = \frac{c_W s_W m_Z^2 (M_2 + \sin 2\beta\mu)}{(M_1 - M_2)(\mu^2 - M_2^2)}. \tag{3.33}$$

With this mixing, the lightest MSSM neutralino will decay to the hidden sector through the channels $\chi^0_1 \to \chi^x_k + S^x$, where χ^x_k are the hidden neutralinos and $S^x = h^x_{1,2}, \ A^x, X_\mu$ are the hidden bosons, with total width [200]

$$\begin{aligned} \Gamma_{\chi^0_1} &= \frac{\epsilon^2 g_x^2 |\mathbf{N}_{11}|^2}{4\pi} m_{\chi^0_1} \\ &= (1.3 \times 10^{-16} \text{ sec})^{-1} |\mathbf{N}_{11}|^2 \left(\frac{\epsilon}{10^{-4}}\right)^2 \left(\frac{g_x}{0.1}\right)^2 \left(\frac{m_{\chi^0_1}}{100 \text{ GeV}}\right). \end{aligned} \tag{3.34}$$

The corresponding χ^0_1 lifetime should be less than about $\tau \lesssim 0.1\,\text{s}$ to avoid disrupting nucle-

osynthesis. This occurs readily for MSSM gaugino masses below the TeV scale and ϵ not too small.

In the hidden sector, the χ_1^x neutralino will be stable while the other states will ultimately decay to it or to the SM. To ensure that χ_1^x is able to annihilate efficiently, it should also be heavier than the vector X^μ. This implies that the hidden vector will decay to the SM through kinetic mixing, or via $X \to h_1^x A^x$. For $m_x > 2m_e$, the vector decay width to the SM is

$$\Gamma(X \to \mathrm{SM} + \mathrm{SM}) = R' \frac{\alpha \epsilon^2 m_x}{3}, \tag{3.35}$$

where R' is a constant on the order of unity that depends on the number of available final states. This decay is much faster than $\tau = 0.1\,\mathrm{s}$ for $\epsilon \gtrsim 4 \times 10^{-10}$ and $m_x \gtrsim 2m_\mu$.

Of the remaining hidden states, the longest-lived is typically the lightest CP-even scalar h_1^x. The structure of the hidden sector mirrors that of the MSSM, and this scalar is always lighter than the vector at tree level. Loop corrections are not expected to change this at weak coupling. As a result, the h_1^x decays exclusively to the SM through mixing with the MSSM Higgs scalars (via a Higgs portal coupling induced by gauge kinetic mixing) or through a vector loop [200]. This decay is typically faster than $\tau = 0.1\,\mathrm{s}$ for $\epsilon \gtrsim 2 \times 10^{-4}$ and $m_{h_1^x} \gtrsim 2m_\mu$ [201].

Light hidden sectors of this variety are strongly constrained by fixed-target and precision experiments [202, 203]. For dominant vector decays to the SM, the strongest limits for $m_x > 2m_\mu$ come from the recent BaBar dark photon search [204], and limit $\epsilon \lesssim 5 \times 10^{-4}$. As the vector mass approaches $m_x = 20$ MeV, fixed-target searches become relevant and constrain the mixing ϵ to extremely small values [202, 203]. In this analysis, we will typically choose $m_x > 20$ MeV and $\epsilon \sim 10^{-4}$ so that the hidden sector is consistent with existing searches.

3.3.3 Hidden Dark Matter from Moduli

Moduli decays are expected to produce both visible and hidden particles and reheat both sectors. The superpartners created by moduli decays will all eventually cascade down to the hidden neutralino LSP. Kinetic mixing can allow the hidden LSP to thermalize by scattering elastically with the SM background through the exchange of X vector bosons. The rate of kinetic equilibration depends on the typical energy at which the LSP is created, the reheating temperature, and the mass and couplings in the hidden sector [155]. For optimistic parameter values we find that it is faster than the Hubble rate for $T_{\mathrm{RH}} \gtrsim 5$ MeV, and we will assume here that such thermalization occurs.

If the net rate of superpartner production in moduli decays is unsuppressed and the χ_1^x annihilation cross section is moderate, the χ_1^x LSPs will undergo additional annihilation to produce a final relic density as described in Eq. (3.17). The relevant annihilation modes of the LSP are $\chi_1^x \chi_1^x \to h_1^x h_1^x,\ X h_1^x,\ XX$. Computing the corresponding annihilation rates using the method of Ref. [42] near $T \sim T_{\mathrm{RH}}$, we find that the XX final state typically dominates provided it is open, as we will assume here. Using these rates, we compute the relic abundance of χ_1^x by

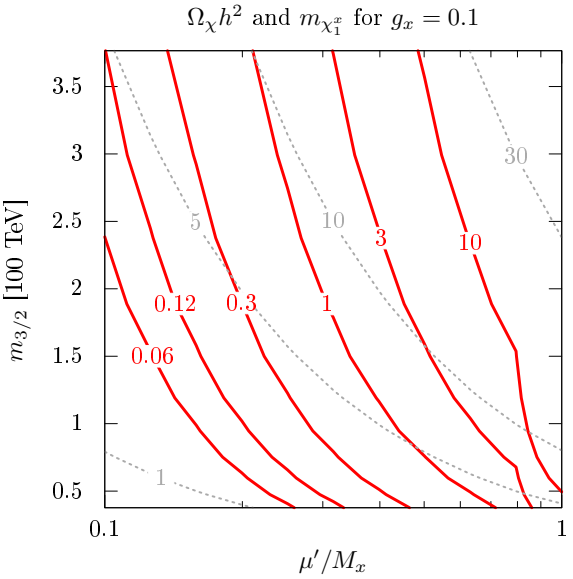

Figure 3.3: Contours of the hidden neutralino χ_1^x mass in GeV (dashed grey) and moduli-generated relic abundance $\Omega_\chi h^2$ (solid red) as a function of of μ'/M_x and $m_{3/2}$. The moduli parameters are taken to be $m_\varphi = m_{3/2}$, $c = 1$, and $\mathcal{N}_\chi = 1$, with the hidden-sector parameters as described in the text.

numerically solving the system of equations presented in Sec. 3.1.3. In doing so, the decays of the MSSM LSP and all hidden states are treated as being prompt.

Before presenting our numerical results, it is instructive to examine the parametric dependence of the approximate solution of Eq. (3.17). Writing

$$\mu' = \xi\, M_x, \tag{3.36}$$

and focusing on a hidden Higgsino-like LSP with $\xi \leq 1$, we obtain $g_\chi = g_x$ and $r_\chi = 2\xi$ in Eq. (3.23). Thus, smaller values of ξ and g_x are expected to produce decreased χ_1^x relic abundances.

The results of a full numerical analysis are illustrated in Fig. 3.3, where we show the contours of the final χ_1^x abundance (solid red) and DM mass (dashed grey) in the $\xi - m_{3/2}$ plane for $m_\varphi = m_{3/2}$, $c = 1$, and $\mathcal{N}_\chi = 1$. The range of $m_{3/2}$ considered corresponds to $M_2 \in [100, 1000]$ GeV, and the hidden sector parameters are taken to be $g_x = 0.1$, $\tan\zeta = 10$, and $m_x = 0.2$ GeV, $m_{A^x} = 10$ GeV. The shape of the abundance contours in Fig. 3.3 is in agreement with the scaling predicted by Eq. (3.23). We also see that $\xi = \mu'/M_x < 1$ is typically needed to avoid creating too much dark matter, and this implies some degree of fine tuning for hidden-sector symmetry breaking. Larger values of ξ are allowed when the moduli decay parameter c is greater than unity, since this leads to a higher reheating temperature and more efficient reannihilation.

3.3.4 Constraints from Indirect Detection

While this extension of the MSSM can yield an acceptable hidden neutralino relic density from moduli reheating, it is also constrained by indirect detection (ID) searches for DM.[9] The pair annihilation of hidden neutralinos can produce continuum photons at tree level from cascades induced by $\chi_1^x \chi_1^x \to XX$ with $X \to f\bar{f}$, as well as photon lines at loop level through kinetic mixing with the photon and the Z. These signals have been searched for by a number of gamma-ray telescopes, and limits have been placed on the corresponding gamma-ray fluxes. We examine here the constraints on the χ_1^x state from observations of the galactic centre (GC) gamma ray continuum by the Fermi Large Area Telescope (Fermi-LAT) [205], as well as from observations of the diffuse photon flux by the INTEGRAL [206], COMPTEL [207], EGRET [208, 209], and Fermi [210] experiments. For the GeV-scale dark matter masses we are considering, these observations are expected to give the strongest constraints [211, 212].[10] We also study bounds from the effects of DM annihilation during recombination on the cosmic microwave background (CMB) [213, 214].

The continuum photon flux from χ_1^x pair annihilation into hidden vectors is given by

$$\frac{d\Phi_\gamma}{dE_\gamma} = \frac{\langle \sigma v \rangle_{\chi\chi \to XX}}{8\pi m_\chi^2} \frac{dN_\gamma^{\rm tot}}{dE_\gamma} \times \int dl \; \rho^2(l), \tag{3.37}$$

where $\langle \sigma v \rangle_{\chi\chi \to XX}$ is the thermally averaged annihilation rate at present, $\rho(l)$ is the dark matter density along the line of sight l, and $dN_\gamma^{\rm tot}/dE_\gamma$ is the total differential photon yield per annihilation, defined as

$$\frac{dN_\gamma^{\rm tot}}{dE_\gamma} \equiv \sum_f {\rm BR}_f \frac{dN_\gamma^f}{dE_\gamma} \tag{3.38}$$

where ${\rm BR}_f$ is the branching fraction of the XX state into the final state f.

In our calculations, we use the results of Refs. [215, 216] to estimate the partial yields dN_γ^f/dE_γ by interpolating between the results for the values of m_χ and m_χ/m_x listed in these studies. For the dark matter density profile, we consider four distributions that span the range of reasonable possibilities: Navarro-Frenk-White (NFW) [217], Einasto [218, 219], con-

[9] Constraints from direct detection are not relevant; the χ_1^x LSP is a Majorana fermion, and scatters off nuclei mainly through a suppressed Higgs mixing coupling [201].

[10] We have also examined constraints from monochromatic photon line searches and found the continuum constraints significantly more stringent for the small values of ϵ allowed by fixed target experiments.

tracted [211], and cored NFW [211]. These take the forms

$$\rho(r) \propto \begin{cases} \left[\frac{r}{R_s}\left(1+\frac{r}{R_s}\right)^2\right]^{-1} & \text{(NFW)} \\ e^{-2/\alpha\left[\left(\frac{r}{R_s}\right)^{\alpha}-1\right]} & \text{(Einasto)} \\ \left[\left(\frac{r}{R_s}\right)^{\gamma}\left(1+\frac{r}{R_s}\right)^{3-\gamma}\right]^{-1} & \text{(contracted)} \\ \left[\frac{r_c+(r-r_c)\,\Theta(r-r_c)}{R_s}\left(1+\frac{r_c+(r-r_c)\,\Theta(r-r_c)}{R_s}\right)^2\right]^{-1} & \text{(cored)} \end{cases} . \tag{3.39}$$

Here, r is the radial distance from the GC and Θ is a step function. Following Refs. [159, 211], we fix the scale radius to be $R_s = 20\,\text{kpc}$ and the Einasto parameter $\alpha = 0.17$. For the contracted profile we set $\gamma = 1.4$ and for the cored profile we set the core radius to be $r_c = 1\,\text{kpc}$, as in Ref. [211]. In all four cases, we fix the overall normalization such that $\rho(r = 8.5\,\text{kpc}) = 0.3\ \text{GeV/cm}^3$.

Using these halo profiles, we are able to compute the gamma-ray fluxes from hidden dark matter created in moduli decays and compare them to limits derived from observations of the GC and the diffuse gamma-ray background. For the GC signal, we use the limits on $\langle\sigma v\rangle/m_\chi^2 \int_{E_{\rm min}}^{E_{\rm max}} dE_\gamma\, dN_\gamma^{\rm tot}/dE_\gamma$ computed in Ref. [211] in several energy bins $[E_{{\rm min},i}, E_{{\rm max},i}]$ and each of the four DM profiles described above. For the diffuse gamma ray background, we use the flux limits compiled and computed in Ref. [212].

In addition to measurements of cosmic gamma rays, observations of the CMB also provide a significant limit on DM annihilation [213, 214]. The energy released by dark matter annihilation around the time of recombination will distort the last scattering surface, and hence affect the CMB anisotropies. The limit derived from this effect is [220–222]

$$f\frac{\Omega_\chi^2}{\Omega_{\rm cdm}^2}\langle\sigma v\rangle_{\rm CMB} \leq (2.42\times 10^{-27}\,\text{cm}^3/\text{s})\left(\frac{m_\chi}{\text{GeV}}\right), \tag{3.40}$$

where $\langle\sigma v\rangle_{\rm CMB}$ is the thermally averaged cross section during recombination and f is a constant efficiency factor parametrizing the fraction of energy transferred to the photon-baryon fluid, which can typically range from $f \approx 0.2{-}1.0$ [222]. We will vary f across this range to illustrate its effect on the resulting constraint.

These observations put very strong constraints on hidden dark matter when it is produced in moduli decays. The corresponding ID and CMB bounds are shown in Fig. 3.4 in the $m_{3/2}-g_x$ plane. We fix the moduli parameters to $m_\varphi = m_{3/2}$ and $c = 1$ in the left panel and $m_\varphi = 2m_{3/2}$ and $c = 10$ in the right. The relevant hidden-sector parameters are taken to be $\xi = 0.1$ and $m_x = m_\chi/2$. The solid red line shows where $\Omega_\chi = \Omega_{\rm cdm}$, with the region above and to the right of the line producing too much dark matter. The green shaded regions show the exclusion from Fermi observations of the GC assuming the Einasto DM profile of Eq. (3.39) rescaled by the expected dark matter fraction $(\Omega_\chi/\Omega_{\rm cdm})^2$, while the blue shaded regions show the exclusion

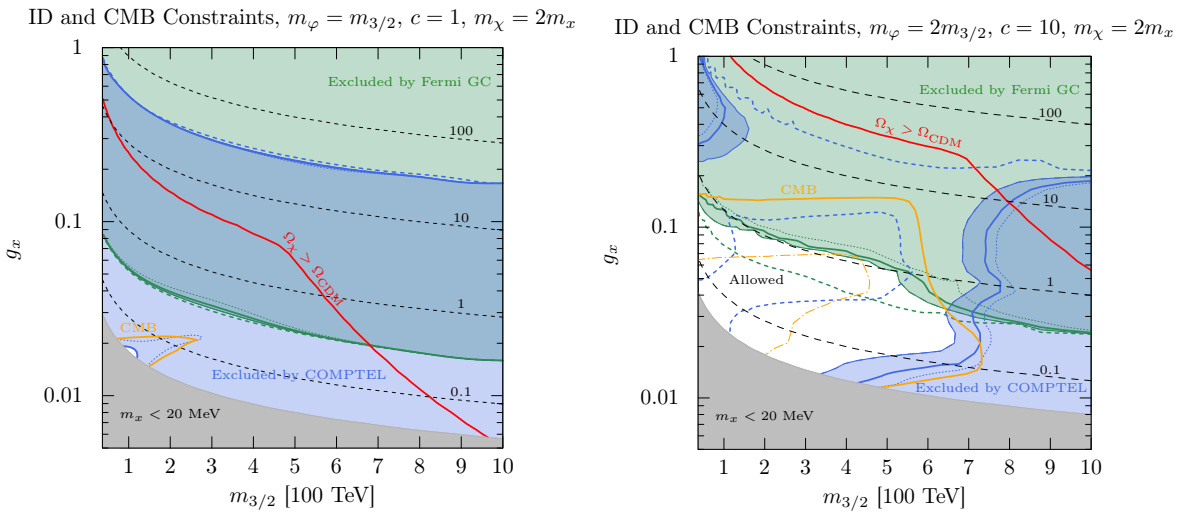

Figure 3.4: Constraints from indirect detection on hidden $U(1)_x$ neutralino DM produced by moduli decays for $m_x = m_\chi/2$, $\xi = 0.1$, as well as ($c{=}1$, $m_\varphi{=}m_{3/2}$) (left), and ($c = 10$, $m_\varphi = 2m_{3/2}$) (right). The green shaded region is excluded by Fermi GC observations and the blue shaded region is excluded by COMPTEL. Both exclusions assume an Einasto galactic DM profile. The thick solid and thin dotted contours correspond to the exclusions assuming the NFW and cored profiles, respectively. The green and blue dashed lines show the boundaries of the stronger exclusion obtained assuming a contracted profile with $\gamma = 1.4$. Above and to the right of the solid red line, the hidden LSP density is larger than the observed DM density. The solid and dash-dotted orange lines shows the exclusion from deviations in the CMB for $f = 0.2$ and $f = 1$, respectively, with the excluded areas above and to the right of the lines. Note that the entire $c = 1$ parameter space is excluded by the CMB constraint for $f = 1$. The gray shaded region at the bottom has a hidden vector mass $m_x < 20$ MeV that is excluded by fixed-target experiments.

from COMPTEL under the same conditions. Exclusions for other profiles are also shown by the parallel contours.[11] We have also considered the corresponding constraints from INTEGRAL, EGRET, and Fermi diffuse gamma ray observations, but these do not exclude any additional parameter space and so are not included in Fig. 3.4 for clarity. Limits from CMB distortions are shown by the solid and dash-dotted orange lines, for $f = 0.2$ and 1 respectively, with the excluded region above and to the right of the contours. The dashed black lines are contours of the hidden LSP χ mass in GeV, with the region where $m_x = m_\chi/2 < 20$ MeV excluded by fixed target experiments [202].

For generic moduli parameters, $c = 1$ and $m_\varphi = m_{3/2}$, we find that constraints from indirect detection and CMB observations nearly completely rule out this scenario even with optimistic choices for the DM halo properties and CMB energy injection efficiency. However, for $c = 10$

[11] The thick green and blue dashed lines show the boundaries of the regions excluded for a more aggressive contracted profile with $\gamma = 1.4$. For clarity, we do not shade the interior of these. The thick solid and thin dotted contours correspond to the NFW and cored profiles, respectively.

and $m_\varphi = 2m_{3/2}$, the hidden neutralino relic density can become sufficiently small to evade the strong limits from ID and the CMB, despite the relatively large χ_1^x annihilation cross section. In this case, a second more abundant contribution to the total dark matter abundance would be needed. Note as well that the remaining allowed region corresponds to sub-GeV hidden sector masses that could potentially be probed in current and planned precision searches [203].

3.3.5 Summary

With optimistic but reasonable choices for the moduli parameters, a light hidden sector neutralino LSP produced in moduli reheating can be consistent with current DM searches. Even so, the scenario is tightly constrained by indirect detection and CMB measurements. The challenge here is precisely the same as in the MSSM: to avoid overproducing the neutralino LSP during moduli reheating, the annihilation rate must be large relative to the standard thermal value $\langle \sigma v \rangle \sim 3 \times 10^{-26}\,\mathrm{cm}^3/\mathrm{s}$, and such an enhanced rate is strongly constrained by indirect DM searches. To avoid these bounds while not creating too much dark matter, the annihilation rate must be large enough that the LSP relic abundance is only a small fraction of the total DM density.

The $U(1)_x$ hidden sector does slightly better than the MSSM in this regard for two reasons. First, the hidden gauge coupling can be taken small (as can $\xi = \mu'/M_x$), which helps to reduce the LSP relic abundance as suggested by Eq. (3.23). And second, the hidden LSP can be much lighter than an MSSM wino or Higgsino, leading to smaller photon yields below the primary sensitivity of Fermi-LAT. The strongest constraints for such light masses come from COMPTEL, which are less stringent than those from Fermi. Since the large late-time hidden neutralino annihilation rate is the primary hindrance to realizing this set-up, one might consider analogous scenarios in which the CMB and indirect detection signatures are suppressed; we address this possibility in the following section.

Before moving on, let us also comment on the spectrum in the hidden sector. To avoid a large fine tuning, the hidden scalar soft terms must be relatively small, on the same order or less than the hidden gaugino mass. Given the large values of $m_{3/2}$ considered, the scalar soft masses must be sequestered from supersymmetry breaking. They must also receive new contributions beyond minimal AMSB, and the b' bilinear soft term must not be too much larger than $(\mu')^2$. All three features require non-trivial additional structure in the underlying mechanisms of supersymmetry breaking or mediation [223, 224].

3.4 Variation #2: Asymmetric Hidden $U(1)$

As a second extension of the MSSM, we investigate a theory of hidden asymmetric dark matter (ADM) [225–228]. In the ADM framework, the DM particle has a distinct antiparticle, and its abundance is set mainly by a particle-antiparticle asymmetry in analogy to baryons, and this tends to suppress indirect detection signals from late-time annihilation if very little anti-DM is present [5, 229–231]. The ADM theory we consider is nearly identical to the hidden $U(1)_x$

theory studied in Sec. 3.3, but with an additional pair of vector-like hidden chiral superfields Y and Y^c with $U(1)_x$ charges $x_Y = \pm 1$. We assume that a small asymmetry in the Y density is generated during moduli reheating, in addition to the much larger symmetric density, and we compute the resulting relic densities and experimental signals.

3.4.1 Mass Spectrum and Decays

The superpotential in the hidden sector is the same as that considered in Sec. 3.3 up to a new mass term for the Y and Y^c multiplets,

$$W \supset -\mu_Y Y Y^c. \tag{3.41}$$

We also include the new soft supersymmetry breaking terms

$$-\mathscr{L}_{\text{soft}} \supset m_{\widetilde{Y}}^2 |\widetilde{Y}|^2 + m_{\widetilde{Y}^c}^2 |\widetilde{Y}^c|^2 - (b_Y \widetilde{Y}\widetilde{Y}^c + \text{h.c.}). \tag{3.42}$$

As in Sec. 3.3, we fix the hidden gaugino mass to its AMSB value with $b_x = 2(1+1)$, accounting for the new superfields. We also do not impose minimal AMSB values for the scalar soft terms, but take them (as well as μ' and μ_Y) to be of similar size to the gaugino soft mass. Finally, we arrange parameters so that the hidden Higgs scalars develop expectation values and spontaneously break the $U(1)_x$.

The mass spectrum of the hidden sector follows the minimal model considered in Sec. 3.3, but now a new Dirac fermion Ψ of mass $m_\Psi = \mu_Y$ and two complex scalars $\Phi_{1,2}$. The scalar mass matrix in the $(\widetilde{Y},\, \widetilde{Y}^{c*})$ basis is

$$\mathcal{M}_{\widetilde{Y}}^2 = \begin{pmatrix} |\mu_Y|^2 + m_{\widetilde{Y}}^2 - \tilde{\delta}_D & b_Y^* \\ b_Y & |\mu_Y|^2 + m_{\widetilde{Y}^c}^2 + \tilde{\delta}_D, \end{pmatrix}, \tag{3.43}$$

where $\tilde{\delta}_D = g_x^2 \eta^2 \cos 2\zeta + x_Y \epsilon g_x g' v^2 \cos 2\beta/2$. Taking $m_{\widetilde{Y}}^2 = m_{\widetilde{Y}^c}^2$ for convenience, the mass eigenvalues are

$$m_{1,2}^2 = |\mu_Y|^2 + m_{\widetilde{Y}}^2 \mp \sqrt{\tilde{\delta}_D^2 + |b_Y|^2}. \tag{3.44}$$

In what follows we will refer to the lighter scalar Φ_1 as Φ.

This theory preserves both the usual R-parity as well as a non-anomalous global $U(1)$ flavour symmetry among the Y and Y^c multiplets, and can support multiple stable states. The number of stable particles depends on the mass spectrum. To allow for dominantly asymmetric dark matter, we will focus on spectra with $m_{\chi_1^x} > m_\Psi + m_\Phi$ such that the decay $\chi_1^x \to \Psi + \Phi^*$ is possible, and the only stable hidden states are Ψ and Φ. If this channel is not kinematically allowed, the χ_1^x neutralino will also be stable and can induce overly large gamma ray signals as in the previous section. We also choose soft masses such that $m_x < m_\Phi$, m_Ψ to allow both states to annihilate efficiently into hidden vectors. With this mass ordering, the lightest hidden

states will be the vector X^μ and the hidden Higgs h_1^x. Both will decay to the SM in the same way as in the minimal model of Sec. 3.3. The lightest MSSM neutralino will also continue to decay to the hidden sector through gauge kinetic mixing, now with additional decay modes $\chi_1^0 \to \Psi\Phi_{1,2}$. As before, the net χ_1^0 lifetime is expected to be short relative to the cosmological timescales of interest.

3.4.2 Moduli Reheating and Asymmetric Dark Matter

The Ψ and Φ states will both act as ADM if they are created in the moduli reheating process slightly more often than their antiparticles. The production of the asymmetry can be accommodated within a set of Boltzmann equations similar to Eq. (3.15) as follows:

$$\begin{aligned} \frac{dn_\Psi}{dt} + 3Hn_\Psi &= (1+\kappa/2)\frac{\mathcal{N}_\Psi \Gamma_\varphi}{m_\varphi}\rho_\varphi - \langle\sigma v\rangle_\Psi \left(n_\Psi n_{\overline{\Psi}} - (n_\Psi^{\rm eq})^2\right) \\ &- \langle\sigma v\rangle_{\rm trans}(n_\Psi^2 - \nu^2 n_\Phi^2) \end{aligned} \tag{3.45}$$

$$\begin{aligned} \frac{dn_\Phi}{dt} + 3Hn_\Phi &= (1+\kappa/2)\frac{\mathcal{N}_\Phi \Gamma_\varphi}{m_\varphi}\rho_\varphi - \langle\sigma v\rangle_\Phi \left(n_\Phi n_{\Phi^*} - (n_\Phi^{\rm eq})^2\right) \\ &- \langle\sigma v\rangle_{\rm trans}(\nu^2 n_\Phi^2 - n_\Psi^2), \end{aligned} \tag{3.46}$$

with a similar set of equations for the anti-DM $\overline{\Psi}$ and Φ^*, but with $\kappa \to -\kappa$. Here, $\mathcal{N}_\Psi$ and $\mathcal{N}_\Phi$ are the mean number of Ψ and Φ produced per modulus decay. This includes particles created directly in moduli decays, rescattering, and from the cascade decays of other states. The thermally-averaged cross sections $\langle\sigma v\rangle_{\Psi,\Phi}$ describe the $\Psi\overline{\Psi}$ and $\Phi\Phi^*$ annihilation, while $\langle\sigma v\rangle_{\rm trans}$ in each equation corresponds to the transfer reaction $\Psi\Psi \leftrightarrow \Phi\Phi$ mediated by $U(1)_x$ gaugino exchange with $\nu = 2\left(m_\Psi/m_\Phi\right)^2 K_2(m_\Psi/T)/K_2(m_\Phi/T)$.

Asymmetry generation in this scenario is parametrized by the constant κ. It could arise directly from moduli decays or from the interactions of intermediate moduli decay products along the lines of one of the mechanisms of Refs. [232–238]. Indeed, this theory can be viewed as a simplified realization of the supersymmetric hylogenesis model studied in Ref. [2]. Relative to that work, we undertake a more detailed investigation of the relic density resulting from different choices for the moduli parameters, and we do not attempt to link the DM asymmetry to the baryon asymmetry.

The annihilation cross section $\langle\sigma v\rangle_\Psi$ is dominated by the $\Psi\overline{\Psi} \to XX$ channel to hidden vector bosons and is given by

$$\langle\sigma v\rangle_\Psi = \frac{1}{16\pi}\frac{g_x^4}{m_\Psi^2}\left(1 - \frac{m_x^2}{m_\Psi^2}\right)^{3/2}\left(1 - \frac{m_x^2}{2m_\Psi^2}\right)^{-2} \tag{3.47}$$

$$\simeq (1.5\times 10^{-24}\,{\rm cm}^2/{\rm s})\left(\frac{g_x}{0.05}\right)^4\left(\frac{1\,{\rm GeV}}{m_\Psi}\right)^2. \tag{3.48}$$

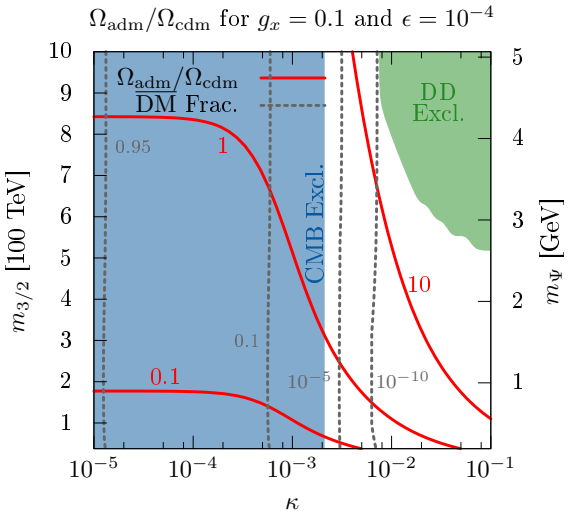

Figure 3.5: Abundance of Ψ and Φ in the $\kappa - m_{3/2}$ plane. The right y axis shows the Ψ mass $m_\Psi = \mu_Y$. Solid red contours show the fraction of the measured abundance made up by Ψ and Φ and their anti-particles. The dashed grey lines show the fractional asymmetry between DM and anti-DM. The blue region is excluded by the CMB bound and the green by direct detection.

The scalar annihilation rate is similar. For the transfer reaction, we have

$$\langle \sigma v \rangle_{\rm trans} \approx \frac{g_x^4}{8\pi} \sqrt{1 - \frac{m_\Phi^2}{m_\Psi^2}} \left| \sum_{k=1}^{3} \frac{(A_k^{*2} - B_k^2) m_{\chi_k^x}}{m_{\chi_k^x}^2 + m_\Psi^2 - m_\Phi^2} \right|^2 , \tag{3.49}$$

where $A_k = \mathbf{Z}_{11}^* \mathbf{P}_{k3}$ and $B_k = \mathbf{Z}_{12} \mathbf{P}_{k3}$ with $\mathbf{P}_{k3}$ the HS gaugino content of χ_k^x and $\mathbf{Z}_{ij}$ is a unitary matrix that diagonalizes the scalar mass matrix of Eq. (3.43). Note that the transfer reaction can be suppressed relative to annihilation for $m_{\chi_1^x} > m_\Psi + m_\Phi$.

3.4.3 Relic Densities and Constraints

To investigate the relic densities of Ψ and Φ in this theory following moduli reheating and the corresponding constraints upon them, we set all the dimensionful hidden parameters to be fixed ratios of the $U(1)_x$ gaugino soft mass $M_x = 4 g_x^2 m_{3/2}/(4\pi)^2$:

$$m_{A^x} = 10\mu' = 50\mu_Y = 100 m_x = 250 b_Y^{1/2} = 250 m_{\widetilde{Y}} = M_x. \tag{3.50}$$

With these choices, the mass spectrum for $g_x = 0.1$ and $m_{3/2} = 200$ TeV is

$$m_\Psi = 1\,\text{GeV},\ m_\Phi = 0.97\,\text{GeV},\ m_{\chi_1^x} = 5.1\,\text{GeV},\ m_x = 0.51\,\text{GeV},\ m_{h_1^x} = 0.5\,\text{GeV}.$$

This mass ordering coincides with the spectrum described in in Sec. 3.4.1.

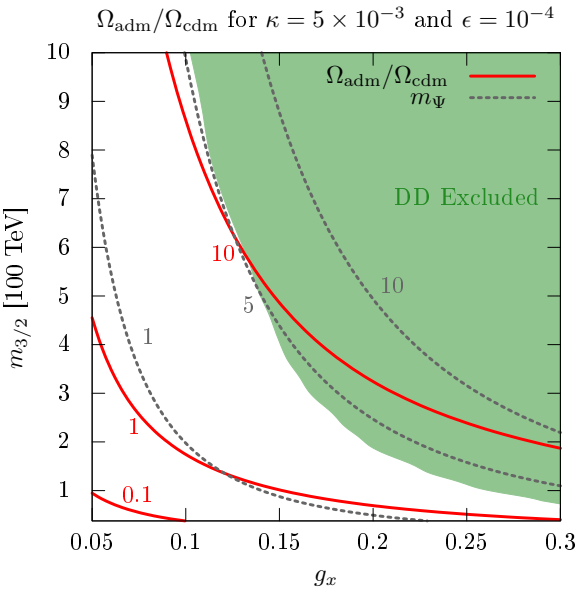

Figure 3.6: Abundance of Ψ and Φ in the $g_x - m_{3/2}$ plane. Solid red contours show the fraction of the measured abundance made up by Ψ and Φ and their anti-particles. The dashed grey lines show the Ψ mass in GeV. The green region is excluded by direct detection.

In Fig. 3.5 we show the dark matter abundance $\Omega_{\rm adm} = \rho_{\rm adm}/\rho_c$ of Ψ and Φ (and their antiparticles) relative to the observed abundance $\Omega_{\rm cdm}$ in the $\kappa - m_{3/2}$ plane for $g_x = 0.1$, $\epsilon = 10^{-4}$, $m_\varphi = m_{3/2}$, and $c = 1$. Contours of $\Omega_{\rm adm}/\Omega_{\rm cdm} = 0.1$, 1, 10 are given by solid red lines. The grey dashed lines in this figure correspond to the net residual anti-DM abundance $R_\Psi + R_\Phi$, where $R_\Psi = \Omega_{\overline{\Psi}}/\Omega_\Psi$ and similarly for Φ. Not surprisingly, larger values of the production asymmetry parameter κ lead to smaller residual anti-DM abundances. In this figure we also show in blue the region of parameters that is excluded by CMB observations, as well as the region excluded by direct detection in green. These constraints will be discussed in more detail below.

The ADM abundance in the $g_x - m_{3/2}$ plane is shown in Fig. 3.6 for $\kappa = 5\times10^{-3}$, $\epsilon = 10^{-4}$, $m_\varphi = m_{3/2}$, and $c = 1$. Again, contours of $\Omega_{\rm adm}/\Omega_{\rm cdm} = 0.1$, 1, 10 are given by solid red lines. We also plot contours of the Ψ mass with dashed grey lines. As before, the shaded green region is excluded by direct detection searches.

The region excluded by CMB observations in Fig. 3.5 (shaded blue) coincides with larger values of the residual anti-DM abundances $R_\Psi + R_\Phi$. These residual abundances provide an annihilation mode that injects energy into the cosmological plasma during the CMB era [5], as discussed in Sec. 3.3.4. Accounting for exclusively asymmetric annihilation and the multiple DM species, the result of Eq. (3.40) translates into

$$2f \sum_{i=\Psi,\Phi} \left(\frac{\Omega_i + \Omega_{\bar{i}}}{\Omega_{\rm cdm}}\right)^2 \frac{R_i}{(1+R_i)^2} \frac{\langle\sigma v\rangle_i}{m_i} \;<\; \frac{2.42\times10^{-27}\ {\rm cm}^3/{\rm s}}{\rm GeV}. \tag{3.51}$$

The CMB exclusion shown in Fig. 3.5 uses $f = 1$, but other values in the range $f = 0.2$–1.0 yield similar results. The boundary of the excluded region is also nearly vertical and independent of $m_{3/2}$. This can be understood in terms of an approximate cancellation of factors of $m_{3/2} = m_\varphi$ in the combination $\Omega^2_{\rm adm}\langle\sigma v\rangle/m$, while R_i is determined primarily by κ. In addition to the limits from the CMB, we have also computed the bounds from indirect detection as described in Sec. 3.3. These searches yield exclusions very similar to that from the CMB and are omitted from Fig. 3.5.

Direct detection searches also place a significant constraint on this ADM scenario. Kinetic mixing of the hidden $U(1)_x$ with hypercharge links the hidden vector to charged matter with an effective coupling proportional to $-e\epsilon\, c_W$. In the present case, the dark matter consists of Dirac fermions and complex scalars charged under $U(1)_x$, and this allows a vectorial coupling of these states to the X gauge boson. Together, these two features induce a vector-vector effective operator (for $m_x \gtrsim 20$ MeV) connecting the DM states to the proton that gives rise to spin-independent (SI) scattering on nuclei. The Ψ-proton scattering cross section is

$$\sigma_p = \frac{\epsilon^2 c_W^2 e^2 g_x^2 \mu_n^2}{\pi m_x^4}. \tag{3.52}$$

A similar expression applies to the scalar Φ. This gives rise to an effective SI cross section per nucleon (in terms of which experimental limits are typically quoted) of

$$\begin{aligned} \tilde{\sigma}_n &= (Z^2/A^2)\sigma_p \\ &\simeq 2\times 10^{-38}\ \mathrm{cm}^2 \left(\frac{2Z}{A}\right)^2 \left(\frac{\epsilon}{10^{-3}}\right)^2 \left(\frac{g_x}{0.1}\right)^2 \left(\frac{\mu_n}{1\ \mathrm{GeV}}\right)^2 \left(\frac{1\ \mathrm{GeV}}{m_x}\right)^4. \end{aligned} \tag{3.53}$$

Comparing this result to the exclusions of low-mass DM from LUX [8], XENON10 S2 only analysis [9], CDMSLite [10] and CRESST-Si [11], we obtain the green exclusion regions shown in Figures 3.5 and 3.6.

3.4.4 Summary

This hidden $U(1)_x$ extension of the MSSM can account for the entire relic dark matter abundance in the aftermath of moduli reheating while being consistent with existing constraints from direct and indirect detection. Even though the DM annihilation cross section is much larger than the standard thermal value, a strong DM-anti-DM asymmetry allows for a significant total density while suppressing DM annihilation signals at late times. Limits from direct detection searches can also be evaded for light DM masses below the sensitivity of current experiments.

To achieve a strong DM asymmetry, a relatively large asymmetry parameter $\kappa \gtrsim 10^{-3}$ is needed. We have not specified the dynamics that gives rise to the asymmetry in moduli reheating, but more complete theories of asymmetry generation suggest that values this large can be challenging to obtain [2, 233–235]. Furthermore, as in the symmetric hidden sector theory considered previously, the spectrum required for this mechanism to work requires scalar

sequestering and scalar soft masses of the right size.

3.5 Variation #3: Hidden $SU(N)$

The third extension of the MSSM that we consider consists of a pure supersymmetric $SU(N)_x$ gauge theory together with heavy connector matter multiplets charged under both $SU(N)_x$ and the MSSM gauge groups.[12] In contrast to the two previous extensions, we do not have to make any strong assumptions about the scalar soft mass parameters for the theory to produce an acceptable LSP relic density. In particular, this extension can work in the context of a *mini-split* spectrum where the scalar superpartners are much heavier than the gauginos [147–152].

3.5.1 $SU(N)_x$ Mass Spectrum and Confinement

The hidden states below the TeV scale consist of the $SU(N)_x$ gluon and gluino. The hidden gluino soft mass is

$$M_x = r_x \frac{g_x^2}{(4\pi)^2} m_{3/2}, \tag{3.54}$$

where $r_x = 3N$ if it is generated mainly by AMSB effects. In the discussion to follow, we will consider additional heavy matter charged under $SU(N)_x$ with large supersymmetric mass μ_F. For $\mu_F \gg m_{3/2}$, the coefficient r_x will be unchanged [135]. However, when $\mu_F \lesssim m_{3/2}$, the value of r_x can be modified by an amount of order unity that depends on the soft masses of these states [139, 192]. We consider deviations in r_x away from the AMSB value but still of the same general size.

Below the hidden gluino mass, the hidden sector is a pure $SU(N)_x$ gauge theory. It is therefore guaranteed to be asymptotically free, and the low-energy theory of hidden gluons should undergo a confining transition at some energy scale Λ_x to a theory of massive glueball (and glueballino) bound states. The one-loop estimate of the confinement scale gives

$$\Lambda_x = M_x \exp\left(-\frac{3r_x}{22N}\frac{m_{3/2}}{M_x}\right). \tag{3.55}$$

Demanding that the $SU(N)_x$ gluino be lighter than the lightest MSSM neutralino typically forces Λ_x to be very small. For example, setting $M_x < 1000$ GeV, $r_x = 3N$, and requiring that $M_x < M_2$ (with its value as in AMSB, $M_2 \simeq m_{3/2}/360$), one obtains $\Lambda_x < 10^{-61}$ GeV. Thus, we will neglect $SU(N)_x$ confinement in our analysis and treat the hidden gauge theory as weakly interacting.

[12] See also Refs. [239, 240] for previous studies of this scenario in a slightly different context.

3.5.2 Connectors to the MSSM

The lightest MSSM superpartner must be able to decay to the hidden sector for this extension to solve the MSSM moduli relic problem. Such decays can be induced by heavy matter multiplets charged under both the MSSM gauge groups and $SU(N)_x$. Following Ref. [239], we examine two type of connectors.

The first set of connectors consists of N_F pairs of chiral superfields F and F^c with charges $(1, 2, \mp 1/2; N)$ under $SU(3)_C \times SU(2)_L \times U(1)_Y \times SU(N)_x$ with a supersymmetric mass term [239]

$$W \supset \mu_F F F^c. \tag{3.56}$$

For $\mu_F \gtrsim m_{3/2}$, the heavy multiplets can be integrated out supersymmetrically to give [239]

$$\begin{aligned} -\Delta\mathscr{L} &\supset \int d^4\theta \, \frac{g_x^2 g_2^2}{(4\pi)^2} \frac{2N_F}{\mu_F^4} \, W^\dagger_{x\,\dot\alpha} W^{\dagger\,\dot\alpha} W_x^\alpha W_\alpha & (3.57) \\ &\supset \alpha_x \alpha_2 \frac{2N_F}{\mu_F^4} \left[\widetilde{G}_x^\dagger (\bar\sigma \cdot \partial) \widetilde{W} \, G_x^{\mu\nu} W_{\mu\nu} + (G_x^{\mu\nu} W_{\mu\nu})^2 \right]. & (3.58) \end{aligned}$$

Similar operators involving the $U(1)_Y$ vector multiplet will also be generated, and additional operators will also arise with the inclusion of supersymmetry breaking. The wino operator of Eq. 3.58 allows the decay $\widetilde{W}^0 \to W^0 \, G_x \, \widetilde{G}_x$, whose rate we estimate to be

$$\begin{aligned} \Gamma &\sim \frac{4(N^2-1)N_F^2}{8\pi(4\pi)^2} \, \alpha_x^2 \alpha_2^2 \, |\mathbf{N}_{12}|^2 \frac{m_{\chi_1^0}^9}{\mu_F^8} & (3.59) \\ &\simeq (7 \times 10^5 \, \mathrm{s})^{-1} (N^2-1) N_F^2 |\mathbf{N}_{12}|^2 \left(\frac{\alpha_x}{10^{-3}} \right)^2 \left(\frac{m_{\chi_1^0}}{270 \text{ GeV}} \right)^9 \left(\frac{100 \text{ TeV}}{\mu_F} \right)^8, \end{aligned}$$

where $m_{\chi_1^0}$ is the mass of the lightest MSSM neutralino, $|\mathbf{N}_{12}|$ is its wino content, and the fiducial value of $m_{\chi_1^0}$ corresponds to the AMSB value of M_2 for $m_{3/2} \simeq 100$ TeV. Note that these sample parameter values lead to decays after the onset of primordial nucleosynthesis.

The second set of connectors that we consider consists of the same N_F heavy multiplets F and F^c together with P and P^c multiplets with charges $(1, 1, 0, \bar{N})$ [239]. This allows the couplings

$$W \supset \lambda_u H_u F P + \lambda_d H_d F^c P^c + \mu_F F F^c + \mu_P P P^c. \tag{3.60}$$

Neglecting supersymmetry breaking, integrating out the heavy F and P multiplets at one-loop order generates operators such as [239]

$$\begin{aligned} -\Delta\mathscr{L} &\supset \int d^2\theta \, \frac{g_x^2 \lambda_u^2}{(4\pi)^2} \frac{2N_F}{\mu_F^2} \, W^{x\,\alpha} W_{x\,\dot\alpha} \, H_u \cdot H_d & (3.61) \\ &\supset \alpha_x \left(\frac{\lambda_u^2}{4\pi} \right) \frac{2N_F}{\mu_F^2} \left[\widetilde{G}_x \sigma_\mu \bar\sigma_\nu \widetilde{H}_d \, H_u \, G_x^{\mu\nu} + G_x^{\mu\nu} G_{x\,\mu\nu} \, H_u \cdot H_d \right]. & (3.62) \end{aligned}$$

where we have set $\mu_P = \mu_F$ and $\lambda_d = \lambda_u$ for simplicity. Additional related operators arise when supersymmetry breaking is included. The first term in Eq. 3.62 induces the decay $\chi_1^0 \to G_x \tilde{G}_x$, whose rate we estimate to be

$$\begin{aligned}\Gamma &\sim \frac{4(N^2-1)N_F^2}{8\pi}\,\alpha_x^2\left(\frac{\lambda_u^2}{4\pi}\right)^2 |\mathbf{N}_{13}|^2\,\frac{v_u^2 m_{\chi_1^0}^3}{\mu_F^4} \\ &\simeq (1\times 10^{-6}\,\mathrm{s})^{-1}(N^2-1)N_F^2|\mathbf{N}_{13}|^2\left(\frac{\alpha_x}{10^{-3}}\right)^2\left(\frac{\lambda_u}{0.75}\right)^4\left(\frac{m_{\chi_1^0}}{200\ \mathrm{GeV}}\right)^3\left(\frac{100\ \mathrm{TeV}}{\mu_F}\right)^4,\end{aligned} \tag{3.63}$$

where $|\mathbf{N}_{13}|$ describes the $\widetilde{H}_d$ content of the MSSM LSP. This decay can occur before primordial nucleosynthesis, even for very large values of $\mu_F \gtrsim 100$ TeV.

Finally, let us mention that the exotic doublets F and F^c will disrupt standard gauge unification. This can be restored by embedding these multiplets in **5** and **5** representations of $SU(5)$ and limiting the amount of new matter to maintain perturbativity up to the unification scale [239]. The latter requirement corresponds to $N \times N_F \leq 5$ for $\mu_F \sim 100$ TeV.

3.5.3 Moduli Reheating and Hidden Dark Matter

The treatment of dark matter production by moduli reheating in this scenario is slightly different from the situations studied previously. The key change is that the visible and hidden sectors are unlikely to reach kinetic equilibrium with one another after reheating for $\mu_{F,P} \gtrsim m_{3/2}$. As a result, it is necessary to keep track of the effective visible and hidden temperatures independently.

To estimate kinetic equilibration, let us focus on the wino operator of Eq. 3.58. This gives rise to $G_x\gamma \to G_x\gamma$ scattering with a net rate of $\Gamma \sim T^9/\mu_F^8$. Comparing to the Hubble rate, kinetic equilibration requires $T_{\rm eq} \gtrsim (\mu_F^8/M_{\rm Pl})^{1/7}$. On the other hand, the reheating temperature after moduli decay is on the order $T_{\rm RH} \sim (m_{3/2}^3/M_{\rm Pl})^{1/2}$. Thus, we see that $T_{\rm RH}$ is parametrically smaller than $T_{\rm eq}$ for $\mu_F \gtrsim m_{3/2}$. A similar argument applies to the Higgs interaction in the second term in Eq. 3.62.

The total modulus decay rate is the sum of partial rates into the visible and hidden sectors,

$$\Gamma_\varphi \;=\; \frac{c}{4\pi}\frac{m_\varphi^3}{M_{\rm Pl}^2} \;=\; \Gamma_v + \Gamma_x \;=\; \frac{c_x + c_v}{4\pi}\frac{m_\varphi^3}{M_{\rm Pl}^2}, \tag{3.64}$$

where c_x and c_v describe the relative hidden and visible decay fractions. Moduli decays will reheat both sectors independently, and self-interactions within each sector will lead to self-thermalization. The total radiation density is the sum of the two sectors, $\rho_R = \rho_v + \rho_x$. We will also define effective temperatures within each sector by

$$\rho_v = \frac{\pi^2}{30} g_* T^4, \tag{3.65}$$

$$\rho_x = \frac{\pi^2}{30} g_{*x} T_x^4, \tag{3.66}$$

where g_* and T refer to the visible sector, and g_{*x} and T_x to the hidden. Since the hidden and visible sectors do not equilibrate with each other after reheating, entropy will be conserved independently in both sectors.

Just after reheating, we also have

$$\rho_v = \left(\frac{c_v}{c}\right)\rho_R, \qquad \rho_x = \left(\frac{c_x}{c}\right)\rho_R. \tag{3.67}$$

Given the first equality, we now define the reheating temperature to be

$$T_{\rm RH} = \left(\frac{c_v}{c}\right)^{1/4}\left[\frac{90}{\pi^2 g_*(T_{\rm RH})}\right]^{1/4}\sqrt{\Gamma_\varphi M_{\rm Pl}}, \tag{3.68}$$

corresponding approximately to the visible radiation temperature when $H = \Gamma_\varphi$. In the same way, we also define the reheating temperature in the hidden sector to be

$$T^x_{\rm RH} = (c_x/c_v)^{1/4}(g_*/g_{*x})^{1/4}T_{\rm RH}. \tag{3.69}$$

The number density of $SU(N)_x$ gaugino dark matter evolves according to Eq. (3.15) but with two important modifications. First, the quantity $\mathcal{N}_\chi$ now corresponds to the mean number of hidden gauginos produced per modulus decay. This includes production from direct decays, decay cascades (including decays of the lightest MSSM neutralino), and re-scattering. The second key change is that the thermal average in $\langle\sigma v\rangle$ is now taken over the hidden-sector distribution with effective temperature $T_x \simeq T^x_{\rm RH}$.

The thermally-averaged $SU(N)_x$ gaugino cross section can receive a non-perturbative Sommerfeld enhancement from multiple hidden gluon exchange if the hidden confinement scale is very low, as we expect here [241, 242]. This enhancement can be written as a rescaling of the perturbative cross section,

$$\langle\sigma v\rangle = S_x\langle\sigma v\rangle_{\rm pert}. \tag{3.70}$$

The perturbative cross section can be obtained by modifying the $SU(3)_C$ gluino result [243] by the appropriate colour factor:

$$\langle\sigma v\rangle_{\rm pert} \;=\; \frac{3N^2}{16(N^2-1)}\frac{1}{4\pi}\left(\frac{g_x^4}{M_x^2}\right). \tag{3.71}$$

The Sommerfeld enhancement factor is [241–243]

$$S_x = A/(1-e^{-A}), \tag{3.72}$$

with $A = \pi\alpha_x/v$, for $v = \sqrt{1-4M_x^2/s}$. In the perturbative cross section, the characteristic momentum transfer is $\sqrt{s} \simeq 2M_x$, and α_x should be evaluated at this scale. However, the typical momentum transfer leading to the non-perturbative enhancement is $\sqrt{s} \sim 2vM_x$ [243].

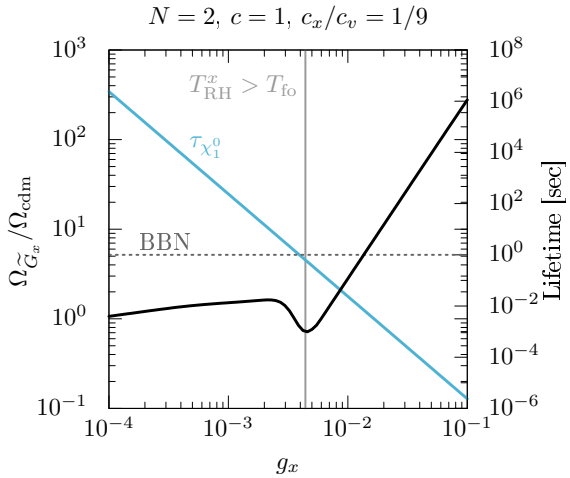

Figure 3.7: Relic abundance of the hidden gluino $\widetilde{G}_x$ (solid black) after moduli reheating as a function of the hidden gauge coupling g_x for $N = 2$, $m_\varphi = m_{3/2} = 100$ TeV, $c = 1$, $\mathcal{N}_x = 1$, and $c_x/c_v = 1/9$. The lifetime of the lightest MSSM superpartner, assumed to be a Higgsino-like neutralino, is shown in light blue for $\mu = 150$ GeV, $N_F = 3$, and $\lambda_u = 0.75$. The vertical solid grey line corresponds to $T^x_{\rm RH} \approx T_{\rm fo}$, while the dashed horizontal line shows $\tau_{\chi_1^0} = 1\,\text{s}$.

In our calculation, we estimate $v \simeq \sqrt{3T^x_{\rm RH}/2M_x}$ and take A to be

$$A \simeq \frac{\pi}{2v}\alpha_x \left[1 + \frac{11N}{6\pi}\alpha_x \ln(v)\right]^{-1}, \tag{3.73}$$

where α_x in this expression is evaluated at $2M_x$.

In Fig. 3.7 we show the relic density of hidden gluinos produced by moduli reheating as a function of g_x for $m_\varphi = m_{3/2} = 100$ TeV, $c = 1$, $\mathcal{N}_x \sim 1$, and $c_x/c_v = 1/9$. We also show in this figure the lifetime of the lightest MSSM superpartner in seconds, which we take to be a Higgsino-like neutralino with $\mu = 150$ GeV, along with $N = 2$, $\mu_F = m_{3/2}$, $N_F = 3$, and $\lambda_u = 0.75$. As expected from the estimate of Eq. (3.23), smaller values of the gauge coupling $g_x \ll g_2$ are needed to obtain an acceptable relic density.

For very small g_x, the hidden gluino mass becomes small enough that the reheating temperature exceeds the freeze-out temperature, and the final density is given by the thermal value. This corresponds to the plateau, where the abundance is only weakly dependent on the gauge coupling. At intermediate g_x, freeze-out happens in the matter dominated phase, where $\Omega_{\widetilde{G}_x} \propto M_x^{-3} \propto g_x^{-6}$ [185], resulting in the turn-over. The abundance continues to decrease until non-thermal production takes over, corresponding to the straight section for $g_x \gtrsim 4 \times 10^{-3}$. Note as well that very small values of g_x also increase the lifetime of the lightest MSSM state to $\tau > 1\,\text{s}$. This can be problematic for nucleosynthesis, and will be discussed in more detail below.

3.5.4 Hidden Gluino Bounds

We found previously that for $M_x < M_2$ and AMSB-like masses, the $SU(N)_x$ confinement scale is negligibly small relative to the Hubble scale today. This implies that the hidden gluon will be a new relativistic degree of freedom in the early Universe. A nearly massless hidden gluon will also interact significantly with the relic hidden gluinos, which has significant implications for dark matter clustering and its imprint on the CMB.

New relativistic particles are constrained by primordial nucleosynthesis and the CMB. The number of corresponding degrees of freedom is often written in terms of an effective number of additional neutrino species, $\Delta N_{\rm eff}$. If the hidden gluon is the only new light state below the reheating temperature and 5 MeV $< T_{\rm RH} < m_\mu$, we have [199]

$$\Delta N_{\rm eff} \simeq \left(\frac{4}{7}\right)(N^2-1)\left(\frac{c_x}{c_v}\right), \tag{3.74}$$

where c_x and c_v correspond to the hidden and visible branching fractions of the moduli. The current upper bound (95% c.l.) on $\Delta N_{\rm eff}$ from primordial nucleosynthesis is [244, 245]

$$\Delta N_{\rm eff} \lesssim 1.0 \quad \text{at} \quad T \sim T_{\rm BBN}. \tag{3.75}$$

This bound can be satisfied for smaller N provided $(c_x/c_v) < 1$. If we reinterpret our moduli results in terms of heavy gravitino decay, the corresponding ratio is $c_x/c_v = (N^2-1)/12$ if only gaugino modes are open and $c_x/c_v = 12(N^2-1)/193$ if all MSSM channels are available [186]. A similar limit on $N_{\rm eff}$ can be derived from the CMB [246]. However, the net effect of the hidden gluon and gluino on the CMB is more complicated than just a change in $\Delta N_{\rm eff}$, as we will discuss below.

A more significant challenge to this scenario comes from the relatively unsuppressed interactions among the hidden gluons and gluinos. Self-interactions among dark matter particles are strongly constrained by observations of elliptical galaxies and the Bullet Cluster [247–249].[13] Furthermore, we find that the relic hidden gluinos remain kinetically coupled to the hidden gluon bath until very late times. This generates a pressure in the dark gluino fluid that interferes with its gravitational collapse into bound structures. A study of this effect lies beyond the scope of this chapter, and we only attempt to describe some of the general features here.

In this scenario, moduli reheating generates a bath of thermal gluons with temperature $T_x \sim (c_x/c_v)^{1/4} T$. Arising from a non-Abelian gauge group, the gluons will interact with themselves at the rate

$$\Gamma \sim \alpha_x^2 T_x \sim (10^{-12}\text{eV})\left(\frac{c_x}{c_v}\right)^{1/4}\left(\frac{\alpha_x}{10^{-4}}\right)^2\left(\frac{T}{2.7\,\text{K}}\right). \tag{3.76}$$

[13] Dark matter interactions close to these upper bounds can help to resolve some of the puzzles of large-scale structure [240, 250–253].

This is easily larger than the Hubble rate today, $H \sim 10^{-33}\,\text{eV}$, and we expect the hidden gluon to remain in self-equilibrium at the present time. One of the key features of such non-Abelian plasmas at temperatures well above the confinement scale is that the gluon field is screened by its self-interactions [254, 255]. Correspondingly, the electric and magnetic components of the gluon develop *Debye masses* on the order of [256],

$$m_E \sim \sqrt{\alpha_x}\, T_x \tag{3.77}$$

$$m_B \sim \alpha_x T_x. \tag{3.78}$$

Relic hidden gluinos will interact with the hidden gluon bath through Compton-like scattering. This can proceed through a t-channel gluon with no suppression by the hidden gluino mass. Modifying the calculation of Refs. [257], we find that the corresponding rate of momentum transfer between a relic gluino and the gluon bath is much larger than the Hubble rate even at the present time. We also estimate that for moderate α_x and $m_\varphi \sim 100$ TeV the rate of formation of gluino-gluino bound states, which are expected to be hidden-colour singlets in the ground state [258–260], is much smaller than the Hubble rate at temperatures below the binding energy.

Together, these two results imply that the relic gluinos remain kinetically coupled to the gluon bath. The pressure induced by the gluons will drive gluinos out of overdense regions and interfere with structure formation, analogous to the photon pressure felt by baryons before recombination. This is very different from the behaviour of standard collisionless cold dark matter, and implies the hidden gluinos can only be a small fraction of the total dark matter density. This fraction, can be constrained using observations of the CMB and by galaxy surveys. A study along these lines was performed in Ref. [261], and their results suggest that the fraction $f_x = \Omega_{\widetilde{G}_x}/\Omega_{\text{cdm}}$ must be less than a few percent, depending on the temperature ratio $T_x/T \simeq (c_x/c_v)^{1/4}$.[14] Hidden gluino interactions may also modify the distribution of dark matter on galactic scales [264].

3.5.5 Summary

This supersymmetric hidden $SU(N)_x$ extension can produce a much smaller non-thermal LSP relic density than the MSSM, and has only invisible annihilation modes that are not constrained by indirect detection. However, the hidden gluino LSP remains in thermal contact with a bath of hidden gluons, and thus can only make up at most a few percent of the total dark matter density. Obtaining such small relic densities is non-trivial and leads to new challenges, as we will discuss here.

From Fig. 3.7 we see that reducing the gauge coupling g_x lowers the non-thermal hidden gluino density until $T_{\text{RH}} \sim T_{\text{fo}}$, at which point the relic abundance becomes approximately

[14] A relic population of millicharged particles will have a similar effect. This was considered in Refs. [262, 263], and a limit of $f_x \lesssim 1\%$ was obtained.

constant in g_x. At the same time, Eq. (3.63) shows that smaller values of g_x also suppress the decay rate of the lightest MSSM superpartner. If such decays happen after the onset on primordial nucleosynthesis, they can disrupt the abundances of light elements [265, 266]. The direct two-body decays $\chi_1^0 \to \widetilde{G}_x G_x$ are invisible. However, the operator of Eq. 3.62 also gives rise to the semi-visible three-body mode $\chi_1^0 \to h^0 \widetilde{G}_x G_x$ if it is kinematically allowed. The decay products of the Higgs boson will be significantly hadronic, and can modify light-element abundances. The branching fraction of this three-body mode depends on the available phase space. Taking it to be $B_h \sim 10^{-3}$ and estimating the Higgsino yield as in Sec. 3.2, we find that Higgsino lifetimes below $\tau_{\chi_1^0} \lesssim 1-100\,\mathrm{s}$ are allowed [265]. This can occur for larger values of N, N_F, or λ_u, or smaller values of μ or μ_F. Note that reducing μ_F below $m_\varphi/2$ is dangerous because it would lead to the production of stable massive F and P states which would tend to overclose the Universe.

An acceptable hidden gluino relic density with a sufficiently rapid MSSM decay can be obtained in this scenario, but only in a very restricted and optimistic region of parameters. For example, with $r_x = 3N/5$, $g_x = 0.01$, $N = 2$, $N_F = 3$, $\lambda_u = 0.75$, $c_x/c_v = 1/9$, and $m_\varphi = 2m_{3/2} = 2\mu_F = 100$ TeV, we obtain $\Omega_{\widetilde{G}_x}/\Omega_{\mathrm{cdm}} = 0.023$ and $\tau_{\chi_1^0} = 0.01\,\mathrm{s}$. Compared to the parameters used in Fig. 3.7, the greatest effect comes from the small value of r_x relative to the minimal AMSB value ($r_x = 3N$). Such a reduction could arise from threshold corrections due to the heavy multiplets [192].

3.6 Conclusions

In this work we have investigated the production of LSP dark matter in the wake of moduli oscillation and reheating. For seemingly generic string-motivated moduli parameters $m_\varphi = m_{3/2}$, $c = 1$, $\mathcal{N}_\chi \sim 1$, we have argued that the MSSM LSP is typically created with an abundance that is larger than the observed dark matter density. The exception to this is a wino-like LSP, which has been shown to be inconsistent with current bounds from indirect detection. We call this the MSSM moduli-induced LSP problem.

To address this problem, we have studied three gauge extensions of the MSSM. In the first, the MSSM is expanded to include a lighter hidden $U(1)_x$ vector multiplet with kinetic mixing with hypercharge that is spontaneously broken by a pair of chiral hidden Higgs multiplets. The kinetic mixing interaction allows the lightest MSSM superpartner to decay to the lighter hidden sector LSP. If this LSP consists primarily of the hidden Higgsinos and is sufficiently light, it will annihilate very efficiently. The resulting hidden LSP relic abundance after moduli reheating can be small enough to be consistent with current bounds from indirect detection and the CMB. In this case, a second more abundant component of the DM density is needed. The spectrum of scalar soft terms required in this theory can also be challenging to obtain for the large values of $m_{3/2} \gtrsim 100$ TeV considered.

The second extension of the MSSM that we studied has an asymmetric dark matter candidate. The underlying theory in this case was again a kinetically-mixed $U(1)_x$ vector multiplet

spontaneously broken by a pair of chiral hidden Higgs, but now with an additional pair of chiral multiplets Y and Y^c. For a range of parameters, the two stable states in this theory are the Dirac fermion Ψ and the lighter complex scalar Φ derived from Y and Y^c. If Ψ or Φ obtain a significant particle anti-particle asymmetry in the course of moduli reheating, they can account for the entire DM density. A large production asymmetry leads to a very small residual anti-DM component, which allows the asymmetric abundances of Ψ and Φ to be consistent with limits from indirect (and direct) detection. However, the production asymmetry required for this to work is relatively large, and may be difficult to obtain in a more complete theory of asymmetry generation. This theory also faces the same scalar soft term requirement as the symmetric hidden $U(1)_x$ extension.

The third extension of the MSSM consists of a pure non-Abelian $SU(N)_x$ vector multiplet at low energies. This sector can connect to the MSSM through additional heavy multiplets charged under both the visible and hidden gauge groups, allowing for decays of the lightest MSSM superpartner to the $SU(N)_x$ gluino. Acceptable hidden gluino relic densities can be obtained for smaller values of the $SU(N)_x$ gauge coupling. This implies a potential tension with primordial nucleosynthesis from late MSSM decays, and leads to a negligibly small hidden confinement scale. In contrast to the two previous extensions, light scalar superpartners are not required and this mechanism can work in the context of mini-split supersymmetry [147–152]. While this theory is not constrained by standard indirect detection searches, the coupling of the hidden gluino to a bath of hidden gluons leads to non-standard DM dynamics that require the hidden gluino density to be only a few percent of the total DM density. It is very difficult to obtain relic densities this small in this scenario.

Our main conclusion is that it is challenging to avoid producing too much LSP dark matter in the course of string-motivated moduli reheating. For seemingly generic modulus parameters, the relic density in the MSSM is either too large or at odds with limits from indirect detection. This may be a hint that the properties of moduli (in our vacuum at least) differ from the general expectations discussed above [124, 178]. Alternatively, this could be an indication of new light physics beyond the MSSM. We have considered three examples of the latter possibility in this chapter and have shown that they can produce a stable LSP abundance that is consistent with current observations and limits. Even so, these three extensions all lead to a significant complication of the MSSM and require a somewhat fortuitous conspiracy of parameters for them to succeed. A more direct solution might be the absence of a stable LSP through R-parity violation, or simply the absence of light superpartners and very large $m_\varphi \sim m_{3/2}$.

Chapter 4

Dark Matter Antibaryons from a Supersymmetric Hidden Sector

4.1 Introduction

The apparent coincidence between the densities of dark and baryonic matter, given by $\Omega_{\rm DM}/\Omega_{\rm b} \approx 5$, may be a clue that both originated through a unified mechanism. A wide variety of models have been proposed along these lines within the framework of asymmetric DM [225, 232, 267–277]; see Ref. [278] for a review. In these scenarios, DM carries a conserved global charge, and its relic abundance is determined by its initial chemical potential. Moreover, if the DM charge is related to baryon number (B), then the cosmic matter coincidence is naturally explained for $\mathcal{O}(5\text{ GeV})$ DM mass.

In this chapter, we explore model-building, cosmological, and phenomenological aspects of hylogenesis ("matter-genesis"), a unified mechanism for generating dark and baryonic matter simultaneously [232, 279]. This model is an extension of the scenario that was presented in Sec. 3.4. Hylogenesis requires new hidden sector states that are neutral under SM gauge interactions but carry non-zero B. CP-violating[1] out-of-equilibrium decays in the early Universe generate a net B asymmetry among the SM quarks and an equal-and-opposite B asymmetry among the new hidden states. The Universe has zero total baryon number, but for appropriate interaction strengths and particle masses, the respective B charges in the two sectors will never equilibrate, providing an explanation for the observed asymmetry of (visible) baryons. The stable exotic particles carrying the compensating hidden antibaryon number produce the correct abundance of dark matter. Put another way, DM consists of the missing antibaryons.

The minimal hylogenesis scenario, described in Refs. [232, 279], has the following three ingredients:

1. DM consists of two states, a complex scalar Φ and Dirac fermion Ψ, each carrying $B = -1/2$.

[1] C is charge conjugation and P is parity.

2. A Dirac fermion X, carrying $B = 1$, that transfers B between quarks and DM through the gauge invariant operators [280]

$$X\, u^c_{Ri}\, d^c_{Rj}\, d^c_{Rk}\,, \quad X\Psi\Phi \tag{4.1}$$

where i, j, k label generation (colour indices and spinor contractions are suppressed).

3. An additional $U(1)'$ gauge symmetry that is kinetically mixed with hypercharge and spontaneously broken near the GeV scale, producing a massive Z'.[2]

With these ingredients, hylogenesis proceeds in three stages, which we illustrate schematically in Fig. 4.1:

1. Equal (CP-symmetric) densities of X and $\bar{X}$ are created non-thermally, e.g., at the end of a moduli-dominated epoch when the Universe is reheated through moduli decay to a temperature $T_{\rm RH}$ in the range of 5 MeV $\lesssim T_{\rm RH} \lesssim$ 100 GeV $\ll m_X$ [133].

2. The interactions of Eq. (4.1) allow X to decay to $u_{Ri}\, d_{R_j}\, d_{Rk}$ or $\bar{\Psi}\Phi^*$, and similarly for $\bar{X}$. With at least two flavours of X, these decays can violate CP leading to slightly different partial widths for X relative to $\bar{X}$, and equal-and-opposite asymmetries for visible and hidden baryons.

3. Assuming Φ and Ψ are charged under $U(1)'$, the symmetric densities of hidden particles annihilate away almost completely, with $\Psi\bar{\Psi} \to Z'Z'$ and $\Phi\Phi^* \to Z'Z'$ occurring very efficiently in the hidden sector, followed by Z' decaying to SM states via kinetic mixing. The residual antibaryonic asymmetry of Φ and Ψ is asymmetric DM. Likewise, the symmetric density of visible baryons and antibaryons annihilates efficiently into SM radiation.

Both Ψ and Φ are stable provided $|m_\Psi - m_\Phi| < m_p + m_e$, and they account for the observed DM density for $m_\Psi + m_\Phi \approx 5m_p$, implying an allowed mass range $1.7 \lesssim m_{\Psi,\,\Phi} \lesssim 2.9$ GeV.

On the phenomenological side, hylogenesis models possess a unique experimental signature: induced nucleon decay (IND), where antibaryonic DM particles scatter inelastically on visible baryons, destroying them and producing energetic mesons. If X couples through the "neutron portal" $u_R d_R d_R$, IND produces π and η final states, while if X couples through the "hyperon portal" $u_R d_R s_R$, IND produces K final states. These signatures mimic regular nucleon decay, with effective nucleon lifetimes comparable to or shorter than existing limits; however, present nucleon decay constraints do not apply in general due to the different final state kinematics of IND. Searching for IND in nucleon decay searches, such as the Super-Kamiokande experiment [281] and future experiments [282–284], therefore offers a novel and unexplored means for discovering DM.

[2] We use different notation for hidden sector states and parameters in this chapter compared to Ch. 3, in order to more closely match with the original literature of Refs. [232, 279].

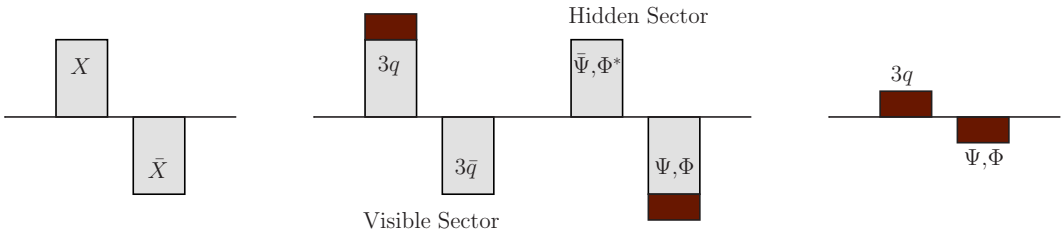

Figure 4.1: The three steps of hylogenesis.

Although the minimal hylogenesis model described above successfully generates the cosmological baryon and DM densities, two puzzles remain. Is there a natural framework to consider DM as a quasi-degenerate scalar/fermion pair? Is there a mechanism to ensure the quantum stability of the GeV-scale masses for hidden sector scalars? Supersymmetry (SUSY) can provide answers to both questions; the DM pair (Φ, Ψ) forms a supermultiplet with $B = -1/2$, and the stability of the GeV-scale hidden sector and the (Φ, Ψ) mass splitting is ensured naturally, provided SUSY breaking is suppressed in the hidden sector compared to the visible sector.

The goal of this chapter is to embed hylogenesis in a supersymmetric framework of natural electroweak and hidden symmetry breaking, and to study in detail the cosmological and phenomenological consequences. In Sec. 4.2, we present a minimal supersymmetric extension of the hylogenesis theory described above. We also address the origin of the nonrenormalizable nucleon portal operator $X\, u^c_{Ri}\, d^c_{Rj}\, d^c_{Rk}$. In Sec. 4.3, we investigate the cosmological dynamics of supersymmetric hylogenesis, showing explicitly the range of masses and parameters that can explain the correct matter densities. Section 4.4 contains a discussion of how such parameter values can arise in a natural way from various mechanisms for supersymmetry breaking. In Sec. 4.5 we investigate the phenomenology of our model, including IND signatures, collider probes, and DM direct detection. Our results are summarized in Sec. 4.6. This chapter is based on Ref. [2], completed in collaboration with David Morrissey, Kris Sigurdson and Sean Tulin; an alternative supersymmetric model based on Higgs portal mixing is also presented in the Appendix of that work.

4.2 Supersymmetric Hylogenesis Model

In this section, we present an extension of the Minimal Supersymmetric Standard Model (MSSM) that can account for the dark matter and baryon densities through a unified mechanism of hylogenesis. In order to organize our discussion, it is useful to divide our model into three sectors, given by the superpotential terms

$$W = W_{\rm MSSM} + W_{\rm HS} + W_{\rm trans}\ . \tag{4.2}$$

superfield		$U(1)'$	B	R
hidden baryons	$X_{1,2}$	0	$+1$	-1
	Y_1	0	$-1/2$	i
	Y_2	$+1$	$-1/2$	i
hidden $U(1)'$	H	$+1$	0	$+1$
	Z'	0	0	0

Table 4.1: New superfields in the hidden sector, with quantum numbers under $U(1)'$, B, and R-parity. Chiral supermultiplets $X_{1,2}, Y_{1,2}, H$ also include vector partners $X^c_{1,2}, Y^c_{1,2}, H^c$ with opposite charge assignments (not listed).

First, $W_{\rm MSSM}$ corresponds to the superpotential of the usual MSSM with weak-scale superpartners; this is the visible sector. Second, we introduce a hidden sector comprised of new states which carry B, but are uncharged under the SM gauge group, and whose interactions are described by the superpotential $W_{\rm HS}$. The third term $W_{\rm trans}$ corresponds to operators responsible for B transfer between the visible and hidden sectors. Baryon transfer operators generate equal-and-opposite B asymmetries within the two sectors, and lead to IND signatures in nucleon decay searches.

4.2.1 Hidden Sector

The hidden sector of our model consists of (i) four vector-like chiral superfields carrying nonzero B, denoted $X_{1,2}$ and $Y_{1,2}$, with charge-conjugate partners $X^c_{1,2}$ and $Y^c_{1,2}$,[3] and (ii) a $U(1)'$ gauge sector, with gauge boson Z' and gauge coupling e', spontaneously broken by a vector pair of hidden Higgs supermultiplets H, H^c. Table 4.1 summarizes these exotic fields. The superpotential is given by

$$W_{\rm HS} = \sum_{a=1,2} \zeta_a X_a Y_1^2 + \bar{\zeta}_a X_a^c (Y_1^c)^2 + \gamma Y_1 Y_2^c H + \bar{\gamma} Y_1^c Y_2 H^c + \mu_{X_a} X_a X_a^c + \mu_{Y_a} Y_a Y_a^c + \mu_H H H^c \,, \tag{4.3}$$

which includes Yukawa-type interactions with couplings $\zeta_{1,2}$, $\bar{\zeta}_{1,2}$, γ, $\bar{\gamma}$, and vector masses $\mu_{X_{1,2}}$, $\mu_{Y_{1,2}}$, μ_H. We also assume a canonical Kähler potential for these multiplets. Note as well that we have extended R-parity to a $\mathbb{Z}_4^R$ for the $Y_i^{(c)}$ multiplets. Aside from allowing the couplings listed above, this extension does not lead to any novel features in the present case, beyond those imposed by the standard R-parity.

After symmetry breaking in the hidden sector, the superfields $Y_{1,2}$ and $Y^c_{1,2}$ mix to form two Dirac fermions Ψ_a ($a = 1, 2$) and four complex scalars Φ_b ($b = 1, 2, 3, 4$) with $B = -1/2$. Among these, the lightest states Ψ_1 and Φ_1 are stable DM. The fermionic mass terms for $Y_{1,2}$

[3] Two species $X_{1,2}$ are required for CP-violating decays (see Sec. 4.3), while two species $Y_{1,2}$ are needed to couple them to the gauge-singlet X fields.

are (in two-component notation)

$$\mathscr{L}_{\rm ferm} = -\left(Y_1^c, Y_2^c\right) \mathbf{M}_Y \begin{pmatrix} Y_1 \\ Y_2 \end{pmatrix} + \text{h.c.}\,, \qquad \mathbf{M}_Y \equiv \begin{pmatrix} \mu_{Y_1} & \bar{\gamma}\eta_c \\ \gamma\eta & \mu_{Y_2} \end{pmatrix}\,. \tag{4.4}$$

where $\eta \equiv \langle H \rangle$, $\eta_c \equiv \langle H^c \rangle$ are the hidden Higgs vacuum expectation values (vevs). This mass matrix can be diagonalized by a biunitary transformation $V^T \mathbf{M}_Y U^\dagger = \text{diag}(m_{\Psi_1}, m_{\Psi_2})$. The scalar mass terms in the basis $\widetilde{Y} \equiv (\widetilde{Y}_1, \widetilde{Y}_2, \widetilde{Y}_1^{c*}, \widetilde{Y}_2^{c*})^T$ are

$$\mathscr{L}_{\rm scalar} = -\widetilde{Y}^\dagger \mathbf{M}^2_{\widetilde{Y}} \widetilde{Y}\,. \tag{4.5}$$

The 4×4 mass matrix $\mathbf{M}^2_{\widetilde{Y}}$ receives contributions from F terms from Eq. (4.3), D terms, and soft SUSY-breaking terms

$$-\mathscr{L}_{\rm soft} \supset m^2_{Y_1}|\widetilde{Y}_1|^2 + m^2_{Y_2}|\widetilde{Y}_2|^2 + m^2_{Y_1^c}|\widetilde{Y}_1^c|^2 + m^2_{Y_2^c}|\widetilde{Y}_2^c|^2 \tag{4.6}$$

$$+ \left(b_1 \widetilde{Y}_1 \widetilde{Y}_1^c + b_2 \widetilde{Y}_2 \widetilde{Y}_2^c + \gamma A_\gamma \widetilde{Y}_1 \widetilde{Y}_2^c H + \bar{\gamma} A_{\bar{\gamma}} \widetilde{Y}_1^c \widetilde{Y}_2 H^c + \text{h.c.}\right)\,, \tag{4.7}$$

We have

$$\mathbf{M}^2_{\widetilde{Y}} \equiv \begin{pmatrix} \mathbf{M}_Y^\dagger \mathbf{M}_Y - \boldsymbol{\delta} + \mathbf{m}^2_{\widetilde{Y}} & \boldsymbol{\Delta}^\dagger \\ \boldsymbol{\Delta} & \mathbf{M}_Y \mathbf{M}_Y^\dagger + \boldsymbol{\delta} + \mathbf{m}^2_{\widetilde{Y}^c} \end{pmatrix}\,, \quad \boldsymbol{\Delta} \equiv \begin{pmatrix} b_1 & \gamma A_\gamma \eta \\ \bar{\gamma} A_{\bar{\gamma}} \eta_c & b_2 \end{pmatrix}\,, \tag{4.8}$$

also defining $\mathbf{m}^2_{\widetilde{Y}} \equiv \text{diag}(m^2_{Y_1}, m^2_{Y_2})$, $\mathbf{m}^2_{\widetilde{Y}^c} \equiv \text{diag}(m^2_{Y_1^c}, m^2_{Y_2^c})$, $\boldsymbol{\delta} \equiv e'^2(\eta_c^2 - \eta^2) \times \text{diag}(0, 1)$. The scalar mass matrix can be diagonalized by a unitary transformation $Z \mathbf{M}^2_{\widetilde{Y}} Z^\dagger = \text{diag}(m^2_{\Phi_1}, m^2_{\Phi_2}, m^2_{\Phi_3}, m^2_{\Phi_4})$. Similar mass matrices arise for the X supermultiplets; for simplicity we assume that the fermion states $X_{1,2}$ and scalar states $\widetilde{X}_{1,2}$, $\widetilde{X}^c_{1,2}$ are all mass eigenstates.

The $U(1)'$ gauge sector consists of the Z' gauge boson, with mass $m^2_{Z'} = 2e'^2(\eta^2 + \eta_c^2)$, the $\widetilde{Z}'$ gaugino, and the hidden Higgsinos $\widetilde{H}, \widetilde{H}^c$. The three neutralinos have the mass matrix

$$M = \begin{pmatrix} M' & -\sqrt{2}e'\eta & \sqrt{2}e'\eta_c \\ -\sqrt{2}e'\eta & 0 & \mu_H \\ \sqrt{2}e'\eta_c & \mu_H & 0 \end{pmatrix}\,, \tag{4.9}$$

which can be brought into a diagonal form using a unitary transformation P, such that $P^\dagger M P = \text{diag}(m_{\chi_1}, m_{\chi_2}, m_{\chi_3})$. The $U(1)'$ gauge superfield mixes kinetically with the MSSM hypercharge,[4]

$$-\mathscr{L} \supset \frac{\kappa}{2} \int d^2\theta B^\alpha Z'_\alpha \; + \text{h.c.}\,, \tag{4.10}$$

where Z'_α and B_α are the $U(1)'$ and $U(1)_Y$ supersymmetric gauge field strengths, respectively,

[4]The kinetic mixing parameter in Ch. 3 was called ϵ.

with the mixing parameter $\kappa \ll 1$.

The full particle content of the hidden sector after the spontaneous breaking of $U(1)'$ consists of the following mass eigenstates: three neutralinos χ_i; three hidden Higgs scalars h, H, A; two Dirac fermions Ψ_i; four complex scalars Φ_i; and a massive gauge boson Z'. The lightest Dirac fermion Ψ_1 and complex scalar Φ_1 are stable due to their masses and B charge assignments — they make up the dark matter. All other states either annihilate or decay into Standard Model particles as described in Sec. 4.3.

Now that we have presented the ingredients for the hidden sector states, we make some remarks:

- We assume that the mass scales of the hidden sector parameters lie at the GeV scale (with the exception of the X states). For the soft terms, this can be accomplished by assuming that SUSY-breaking is suppressed in the hidden sector (see Sec. 4.4). However, the SUSY-preserving vector mass terms present a hidden μ-problem; we ignore this issue, but in principle this can be solved by introducing an additional hidden singlet analogous to the NMSSM.

- Since $X_{1,2}$ mediates baryon transfer between the visible and hidden sectors (described below), IND signatures are more favourable if the DM states (Φ_1, Ψ_1) are mostly aligned with the Y_1 supermultiplet. However, nonzero mixing with Y_2 is induced by SUSY-breaking and hidden Higgs vevs resulting in a DM-Z' coupling that is essential for annihilation of the symmetric DM density.

- We have imposed B as a global symmetry. Since gravitational effects are expected to violate global symmetries, B violation could arise through Planck-suppressed operators, potentially leading to DM particle-antiparticle oscillations that can erase the hidden baryon asymmetry [285–288]. In our SUSY framework, these effects are forbidden by the $\mathbb{Z}_4^R$ extension of R-parity. For example, the $B = -1$ operators $W \sim MY_1^2,\ Y_1Y_2H^c$ are allowed by $U(1)'$ and can lead to DM oscillations, but they are not invariant under R-parity. If $\mathbb{Z}_4^R$ descends from an anomaly-free gauge symmetry, such as $U(1)_{B-L}$ spontaneously broken by two units, it cannot be violated by gravity [289, 290] and these operators are forbidden. Thus there exists a consistent embedding of $\mathbb{Z}_4^R$ in a gauge symmetry that excludes the Majorana mass terms for $Y_{1,2}$ that could erase the hidden asymmetry by oscillations.

4.2.2 Baryon Transfer

Baryon number is transferred between the hidden and visible sectors through superpotential terms W_{trans}. The hidden baryon states $X_{1,2}$ are coupled to the operator $U_i^c D_j^c D_k^c$, where U_i^c, D_j^c are the usual $SU(2)_L$-singlet quark superfields (i, j, k label generation). We focus on the case involving light quarks ($U^c \equiv U_1^c$, $D^c \equiv D_1^c$, $S^c \equiv D_2^c$), corresponding to the "hyperon

portal" [280]:

$$W_{\rm trans} = \sum_{a=1,2} \frac{\lambda_a}{M} \epsilon_{\alpha\beta\gamma} X_a U^c_\alpha D^c_\beta S^c_\gamma \,, \tag{4.11}$$

with $SU(3)_C$ indices α, β, γ and nonrenormalizable couplings $\lambda_{1,2}/M$. Although hylogenesis is viable for any generational structure, Eq. (4.11) is the most interesting case for IND signatures. In contrast to non-SUSY hylogenesis models, the "neutron portal" coupling $X_{1,2} U^c D^c D^c$ vanishes by antisymmetry. SUSY hylogenesis therefore favours IND involving K final states, rather than π, η final states allowed in generic non-SUSY models.

The simplest possibility to generate the nonrenormalizable coupling in Eq. (4.11) is to introduce a vector-like colour triplet supermultiplet P with global charges $B = -2/3$ and $R = 1$. There are three cases to consider:[5]

$$W_{\rm trans} = \begin{cases} \lambda'_{1,2} X_{1,2} P_\alpha U^c_\alpha + \lambda'' \, \epsilon_{\alpha\beta\gamma} P^c_\alpha S^c_\beta D^c_\gamma + \mu_P P_\alpha P^c_\alpha & \text{(case I)} \\ \lambda'_{1,2} X_{1,2} P_\alpha D^c_\alpha + \lambda'' \, \epsilon_{\alpha\beta\gamma} P^c_\alpha U^c_\beta S^c_\gamma + \mu_P P_\alpha P^c_\alpha & \text{(case II)} \\ \lambda'_{1,2} X_{1,2} P_\alpha S^c_\alpha + \lambda'' \, \epsilon_{\alpha\beta\gamma} P^c_\alpha D^c_\beta U^c_\gamma + \mu_P P_\alpha P^c_\alpha & \text{(case III)} \end{cases} \tag{4.12}$$

The $SU(3)_C \times SU(2)_L \times U(1)_Y$ quantum numbers for P are $(3, 1, 2/3)$ for case I (up-type), and $(3, 1, -1/3)$ for cases II and III (down-type). In all cases P^c carries the opposite charges. The choice between the cases in Eq. (4.12) makes little difference for hylogenesis cosmology. However, the different cases affect the IND signals, manifested in the ratio of the rates of $p \to K^+$ to $n \to K^0$ channels, discussed in Sec. 4.5.

Integrating out P and P^c at the supersymmetric level generates the superpotential operator of Eq. (4.11) with $\lambda_a/M \equiv \lambda'_a \lambda''/\mu_P$ together with the (higher-order) Kähler potential term (for case I, with similar operators for cases II and III)

$$K \supset \frac{|\lambda''|^2}{|\mu_P|^2} \left[(D^{c\dagger} D^c)(S^{c\dagger} S^c) - (S^{c\dagger} D^c)(D^{c\dagger} S^c) \right] \,. \tag{4.13}$$

Including supersymmetry breaking leads to additional operators. In particular, the holomorphic soft scalar coupling $b_P \tilde{P} \tilde{P}^c$ (or a squark-gaugino loop with a gaugino mass insertion) gives rise to the four-fermion operator $X u^c_R d^c_R s^c_R$ that plays a central role in IND.

4.3 Hylogenesis Cosmology

We turn next to a study of the early Universe dynamics of our supersymmetric model of hylogenesis. To summarize the main ingredients:

- We assume that the Universe is dominated at early times by a long-lived non-relativistic state φ (e.g., an oscillating modulus field), which decays and reheats the Universe before

[5] We consider the interactions of cases II and III separately, although in general both may arise simultaneously. The simultaneous presence of both sets of couplings leads to strangeness-violating interactions that may be constrained by flavour violation constraints that we do not consider here.

the onset of Big Bang nucleosynthesis (BBN) [133].

- Nonthermal CP-symmetric densities of X_1 and $\widetilde{X}_1$ states are populated through φ decays. Depending on their specific origin, the scalar or the fermion can be created preferentially [127]. CP-violating decays of X_1 and $\widetilde{X}_1$ generate equal-and-opposite asymmetries in quarks and hidden sector baryons (Ψ, Φ), while the total baryon number is conserved.[6]

- A hidden $U(1)'$ gauge sector allows for cascade decays of heavier $B = -1/2$ states (Φ_2, Ψ_2, *etc.*) into the lightest states $\Phi \equiv \Phi_1$ and $\Psi \equiv \Psi_1$ that are DM. Both states can be stable provided the condition $|m_\Psi - m_\Phi| < m_p + m_e$ is met. Also, the symmetric DM densities annihilate efficiently through the light Z', which decays to SM states via kinetic mixing with hypercharge.

Below, we first compute the CP asymmetries for X_1 and $\widetilde{X}_1$ decays. Second, we ensure that the successful predictions of BBN are not modified by hidden sector decays into SM particles. Third, we solve the system of Boltzmann equations for hylogenesis, incorporating all of the aforementioned ingredients, to compute the baryon asymmetries. There are significant differences compared to nonsupersymmetric hylogenesis [232]; in particular, the DM masses m_Φ, m_Ψ and the ratio of Φ to Ψ states can be different, with implications for IND phenomenology.

4.3.1 CP-violating Asymmetries

Visible and hidden B asymmetries are produced by CP violation in the partial decay widths of X_1

$$X_1 \to u_R \tilde{d}_R \tilde{s}_R + d_R \tilde{s}_R \tilde{u}_R + s_R \tilde{u}_R \tilde{d}_R \,, \quad X_1 \to \bar{\Psi}_i \Phi_j^* \,, \tag{4.14}$$

due to interference between tree-level and one-loop amplitudes, shown in Fig. 4.2. The corresponding CP asymmetry is

$$\epsilon_X \equiv \frac{1}{\Gamma_{X_1}} \Big[\Gamma(X_1 \to u_R \tilde{d}_R \tilde{s}_R) - \Gamma(\bar{X}_1 \to \bar{u}_R \tilde{d}_R^* \tilde{s}_R^*) + \text{perms.} \Big] \tag{4.15a}$$

$$= \frac{3 \left[\text{Im}(\lambda_1^* \zeta_1 \zeta_2^* \lambda_2) m_{X_1} + \text{Im}(\lambda_1^* \bar{\zeta}_1^* \bar{\zeta}_2 \lambda_2) m_{X_2} \right] m_{X_1}^3}{64\pi^3 M^2 (m_{X_2}^2 - m_{X_1}^2)(|\zeta_1|^2 + |\bar{\zeta}_1|^2)} . \tag{4.15b}$$

We assume that Γ_{X_1} is dominated by the two-body decay to $\bar{\Psi}_i \Phi_j^*$ final states.[7] For $\epsilon_X > 0$, a positive net B asymmetry is generated in the visible sector. By CPT invariance, the decay rates for X_1 and $\bar{X}_1$ are equal, and so an equal-and-opposite (negative) B asymmetry is generated in the hidden sector. Additional contributions to ϵ_X from $X_1 \to u_R d_R s_R$, arising through SUSY-breaking or at one-loop, may be subleading provided squark decays are kinematically available.

[6] We neglect CP-violating decays of X_2 and $\widetilde{X}_2$, which in principle can also contribute to B asymmetries.

[7] In what follows, flavour indices i, j for hidden sector states are implicitly summed over in final states.

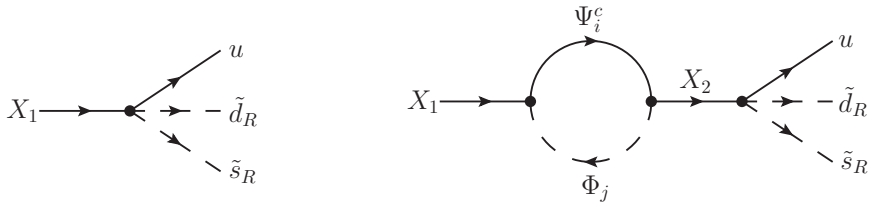

Figure 4.2: Representative diagrams contributing to $X_1 \to q_i \tilde{q}_{Rj} \tilde{q}_{Rk}$ decays which are responsible for the generation of the baryon asymmetry.

The baryon asymmetry can also be generated through the decays of the scalar component of the X_1 superfield, $\widetilde{X}_1$, via interference of supersymmetrizations of the diagrams in Fig. 4.2. In the supersymmetric limit, the CP-asymmetry due to $\widetilde{X}_1$ is equal to Eq. (4.15). However, $\widetilde{X}_1$ decay can populate preferentially Ψ or Φ, due to the different hidden sector decay rates

$$\Gamma(\widetilde{X}_1 \to \Phi_i^* \Phi_j^*) = \frac{|\bar{\zeta}_1|^2}{16\pi} m_{X_1}\,, \quad \Gamma(\widetilde{X}_1 \to \bar{\Psi}_i \bar{\Psi}_j) = \frac{|\zeta_1|^2}{16\pi} m_{X_1}. \tag{4.16}$$

For X_1 decays, the primordial ratio

$$r \equiv n_\Psi / n_\Phi \tag{4.17}$$

of charge densities $n_{\Psi,\Phi}$ is equal to unity. However, $\widetilde{X}_1$ decays can deviate from $r = 1$ for $|\zeta_1| \neq |\bar{\zeta}_1|$. As we discuss below, IND signals can be significantly enhanced if the heavier state is overpopulated compared to the lighter state (e.g., $r \gg 1$ for $m_\Psi > m_\Phi$).

The dark matter abundance is given by

$$\frac{\Omega_{\rm DM}}{\Omega_{\rm b}} = \frac{2(m_\Psi r + m_\Phi)}{m_p (1+r)}, \tag{4.18}$$

where we have neglected the contributions from the DM anti-particles. This is appropriate in the limit of completely asymmetric DM populations. The allowed DM mass window, including the uncertainty in $\Omega_{\rm DM}/\Omega_{\rm b} \approx 5$, is then

$$1.3 \text{ GeV} \leq m_\Psi,\, m_\Phi \leq 3.4 \text{ GeV}. \tag{4.19}$$

More specifically, Fig. 4.3 shows the allowed mass range for m_Ψ (blue) and m_Φ (red), for a given value of r. In the $r \to 0$ (∞) limit, only Φ (Ψ) is populated and its mass is required to be approximately $5m_p/2$ to explain the DM density; the underpopulated Ψ (Φ) state is constrained within the range of Eq. (4.19) by the stability condition $|m_\Psi - m_\Phi| < m_p + m_e$.

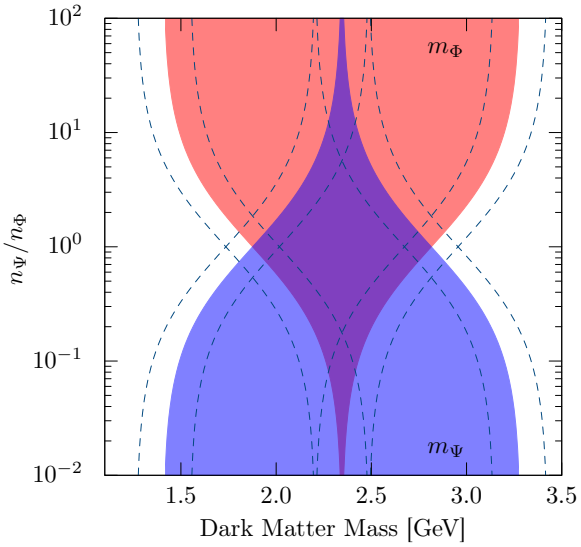

Figure 4.3: Allowed masses for the scalar Φ and fermion Ψ components of dark matter. For a fixed value of n_Ψ/n_Φ, the shaded region shows the entire mass range of Ψ (blue) and Φ (red) that reproduces $\Omega_{\rm DM}/\Omega_{\rm b} \approx 5$ and satisfies the stability requirement $|m_\Psi - m_\Phi| < m_e + m_p$. Shifting $\Omega_{\rm DM}/\Omega_{\rm b}$ by $+(-)6\%$ moves the allowed region right (left), as indicated by the dashed contours.

4.3.2 Decays and Annihilations of SUSY States

Aside from the stable DM states Φ_1 and Ψ_1, the hidden sector contains numerous states that decay, producing additional SM radiation. These decays, listed below, must occur with a lifetime shorter than about one second to avoid conflicts with BBN predictions.

- The Z' gauge boson decays to SM states via kinetic mixing with the photon, requiring $\kappa \gtrsim 10^{-11}\,(m_{Z'}/\,\text{GeV})^{-1}$ [291], while $\kappa \lesssim 10^{-3}$ is consistent with existing limits for $m_{Z'} \sim$ GeV [202, 292].[8]

- For the hidden Higgs states, the heavy CP-even state decays $H \to Z'Z'$, while the CP-odd state decays $A \to Z'h$, through $U(1)'$ gauge interactions. Since the lighter CP-even state h is necessarily lighter than the Z', it must decay to Standard Model fermions either via loop-suppressed processes [293] or via D-term mixing with the MSSM Higgs [200]. For h masses above the two-muon threshold, the mixing process dominates requiring $\kappa \gtrsim 10^{-5}$.

- The heavy dark states Φ_i $(i > 1)$ and Ψ_2 cascade down to Φ_1 and Ψ_1 by emitting Z' and h bosons.

[8] We assume a stronger condition $\kappa \gtrsim 10^{-8} g_*(m_{Z'}/\,\text{GeV})^{-1}(T_{\rm RH}/\,\text{GeV})^{3/2}$ such that the hidden and visible sectors are in kinetic equilibrium at $T < T_{\rm RH}$. [291]

- The hidden neutralinos can decay $\chi_i \to \Phi_1\bar{\Psi}_1, \Phi_1^*\Psi_1$ provided this channel is open (assumed below). If this channel is closed, then the lightest state χ_1 is stable, providing an additional DM component, and must annihilate efficiently via the t-channel process $\chi_1\chi_1 \to Z'Z'$.

In addition, the lightest supersymmetric particle within the MSSM decays to hidden states through mixing of the hidden and MSSM neutralinos induced by κ. This mixing generally has a negligible effect on the mass eigenvalues [200].

The symmetric DM densities of $\Psi_1\bar{\Psi}_1$ and $\Phi_1\Phi_1^*$ annihilate to Z' gauge bosons. In the case where DM is nearly aligned with the Y_2 multiplet, the cross sections are given by [291]

$$\langle\sigma v\rangle_{\Psi\bar{\Psi}\to Z'Z'} = \frac{e'^4}{16\pi m_\Psi^2}\sqrt{1-m_{Z'}^2/m_\Psi^2}, \quad \langle\sigma v\rangle_{\Phi\Phi^*\to Z'Z'} = \frac{e'^4}{16\pi m_\Phi^2}\sqrt{1-m_{Z'}^2/m_\Phi^2}\,. \quad (4.20)$$

To have $\langle\sigma v\rangle \gtrsim 3\times10^{-26}$ cm^3/s for efficient annihilation, we require $e' \gtrsim 0.03$ [229].

The presence of light hidden neutralinos allows for the chemical equilibration of baryon number between Φ and Ψ. The most important process is $\Phi_1\Phi_1 \leftrightarrow \Psi_1\Psi_1$ which transfers the B asymmetry from the heavier DM state to the lighter state. This effect is phenomenologically important for IND, potentially quenching the more energetic down-scattering IND processes. The transfer arises from the supersymmetrization of the hidden gauge and Yukawa interactions, which, in the mass basis, takes the form

$$\begin{aligned}\mathscr{L} \supset \Phi_i\overline{\Psi}_j \Big[&\Big(-\sqrt{2}e' Z_{i4}^* V_{j2} P_{1k} - \gamma Z_{i1}^* V_{j2} P_{2k} - \bar{\gamma} Z_{i2}^* V_{j1} P_{3k}\Big) P_L \\ &+ \Big(\sqrt{2}e' Z_{i2}^* U_{j2} P_{1k}^* - \gamma^* Z_{i4}^* U_{j1} P_{2k}^* - \bar{\gamma}^* Z_{i3}^* U_{j2}^* P_{3k}^*\Big) P_R\Big]\chi_k + \text{h.c.}\end{aligned} \quad (4.21)$$

In the limit where the dark matter is mostly aligned with the Y_2 supermultiplet, the interaction simplifies to

$$\mathscr{L} \supset \sqrt{2}e'\Phi_1\overline{\Psi}_1\,(aP_L + bP_R)\,\chi_1 + \text{ h.c.}, \quad (4.22)$$

where $a = -\sqrt{2}e'Z_{14}^*$, $b = \sqrt{2}e'Z_{12}^*$, and χ_1 is the $U(1)'$ gaugino. Note that even if the mixing due to $U(1)'$ breaking can be neglected, the scalars $\widetilde{Y}_2$ and $\widetilde{Y}_2^{c*}$ will still mix via the soft b-term. For $m_\Phi \geq m_\Psi$ the s-wave contribution to the thermalized $\Phi_1\Phi_1 \to \Psi_1\Psi_1$ cross section for this interaction takes the form

$$\begin{aligned}\langle\sigma v\rangle_{\Phi\Phi\to\Psi\Psi} = &\frac{1}{8\pi(M^2+m_\Phi^2-m_\Psi^2)^2}\sqrt{1-\frac{m_\Psi^2}{m_\Phi^2}}\times \\ &\times\Big(2m_\Phi^2\big[\,(|a|^4+|b|^4)m_\chi^2 + (|a|^2+|b|^2)(ab^*+a^*b)m_\chi m_\Psi + 2|a|^2|b|^2 m_\Psi^2\,\big] \\ &-m_\Psi^2|(a^2+b^2)m_\chi + 2abm_\Psi|^2\Big)\,.\end{aligned} \quad (4.23)$$

In our numerical calculations we use $a = b = e'$ for simplicity. In this case the transfer cross section reduces to

$$\langle \sigma v \rangle_{\Phi\Phi\to\Psi\Psi} = e'^4 \frac{(m_\chi + m_\Psi)^2}{2\pi(m_\chi^2 + m_\Phi^2 - m_\Psi^2)^2} \left(1 - \frac{m_\Psi^2}{m_\Phi^2}\right)^{3/2}. \tag{4.24}$$

The cross section for the reverse process $\Psi_1\Psi_1 \to \Phi_1\Phi_1$ is related to $\Phi_1\Phi_1 \to \Psi_1\Psi_1$ by the detailed balance condition

$$\langle \sigma v \rangle_{\Phi\Phi\to\Psi\Psi} = \left(n_\Psi^{\rm eq}/n_\Phi^{\rm eq}\right)^2 \langle \sigma v \rangle_{\Psi\Psi\to\Phi\Phi}, \tag{4.25}$$

where the equilibrium distributions $n_i^{\rm eq}$ are given in Eq. (4.34). We discuss depletion of the heavier DM state in more detail below. Before doing so, however, let us mention that the transfer process is not generic, and may be absent in other constructions. In particular, this is true of the alternate Higgs portal model presented in the Appendix of Ref. [2].

4.3.3 Boltzmann Equations

The generation of the visible and hidden B asymmetries during reheating is described by a system of Boltzmann equations:

$$\dot\rho_\varphi = -3H\rho_\varphi - \Gamma_\varphi \rho_\varphi \tag{4.26a}$$

$$\dot s = -3Hs + \frac{\Gamma_\varphi}{T}\rho_\varphi \tag{4.26b}$$

$$\dot n_B = -3Hn_B + (\epsilon_X \mathcal{N}_X + \epsilon_{\widetilde X}\mathcal{N}_{\widetilde X})\frac{\Gamma_\varphi \rho_\varphi}{m_\varphi}. \tag{4.26c}$$

Here, ρ_φ is the energy density of the modulus field φ, s is the entropy density, and n_B is the visible B charge density (the hidden B asymmetry is $-n_B$). Also, $\mathcal{N}_{X,\widetilde X}$ is the average number of X_1 or its superpartner produced per modulus decay, while $\epsilon_{X,\widetilde X}$ is the CP-asymmetry from $X_1, \widetilde X_1$ decay. In the supersymmetric limit $\epsilon_X = \epsilon_{\widetilde X}$. The modulus decay rate Γ_φ determines the reheat temperature

$$T_{\rm RH} = \left[\frac{45}{4\pi^3 g_*(T_{\rm RH})}\right]^{1/4} \sqrt{\Gamma_\varphi M_{\rm Pl}}. \tag{4.27}$$

The total modulus decay rate is given by [133, 294, 295]

$$\Gamma_\varphi = \frac{m_\varphi^3}{4\pi\Lambda^2}, \tag{4.28}$$

where we take $\Lambda = 2.43 \times 10^{18}$ GeV to be the reduced Planck constant. Along with the Friedmann equation $H^2 = (8\pi G/3)(\rho_\varphi + \rho_r)$, where $\rho_r = (\pi^2/30) g_* T^4$, Eqs. (4.26) form a closed set and can be solved using the method of Refs. [184, 185]. Here g_* is the energy density

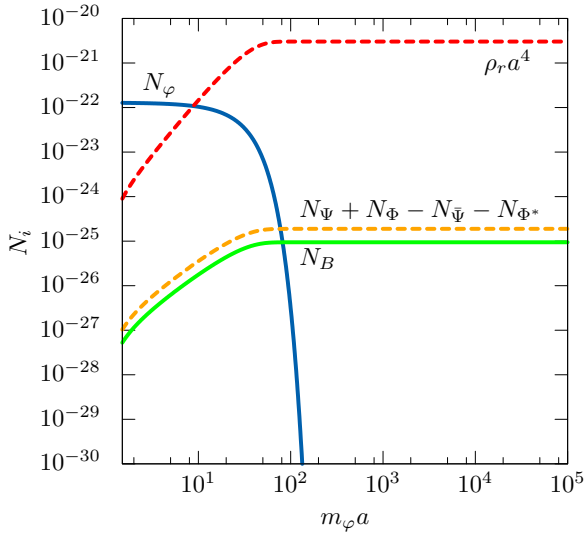

Figure 4.4: Solutions to the reheating Eqs. (4.26a, 4.26b, 4.26c) and DM production, described by Eq. (4.29). Here $N_\varphi = \rho_\varphi a^3/m_\varphi$ and $N_i = n_i a^3$ for $i = B$, Ψ, Φ, $\bar\Psi$, Φ^*.

number of relativistic degrees of freedom. Instead of entropy, one can also solve for radiation density. We take $m_\varphi = 2000$ TeV (corresponding to $T_{\rm RH} \approx 270$ MeV), $\mathcal{N}_X = \mathcal{N}_{\widetilde{X}} = 1$ and $\epsilon_X = \epsilon_{\widetilde{X}} = 3.68\times10^{-4}$. This decay asymmetry can be generated for example by taking $|\lambda_a| \approx 1$, $|\zeta_a| \approx 0.1$,[9] maximal CP-violating phase and $M \approx m_{X_1} \approx m_{X_2}/3 \approx 1$ TeV. These parameters reproduce the observed baryon asymmetry $\eta_B = n_B/s \approx 8.9 \times 10^{-11}$. Numerical solutions to the reheating equations for these parameters are shown in Fig. 4.4. The modulus field φ decays into radiation and the heavy states X, which immediately decay asymmetrically in the visible and hidden sectors, generating the baryon asymmetry and the dark matter abundance.

The production of dark matter and its dynamics are described by a system of four Boltzmann equations for Ψ_1, Φ_1 and their antiparticles[10] which take the form

$$\dot n_i = -3Hn_i + C_i + (\mathcal{N}_{i,X}\mathcal{N}_X + \mathcal{N}_{i,\widetilde{X}}\mathcal{N}_{\widetilde{X}})\frac{\Gamma_\varphi \rho_\varphi}{m_\varphi}, \tag{4.29}$$

for $i = \Psi_1$, $\bar\Psi_1$, Φ_1, Φ_1^*. Here $\mathcal{N}_{i,X}$ is the average number of species i produced per X decay. For $i = \Psi$ (we drop the subscript 1 from hereon) we have

$$\mathcal{N}_\Psi \equiv \mathcal{N}_{\Psi,X} + \mathcal{N}_{\Psi,\widetilde{X}} = \frac{\Gamma(\bar X \to \Psi\Phi) + 2\Gamma(\widetilde{X}^* \to \Psi\Psi)}{\Gamma_X}. \tag{4.30}$$

[9] The magnitude of the coupling constants is chosen to be consistent with hidden sector SUSY-breaking as discussed in Sec. 4.4.

[10] We assume that the heavier dark states Ψ_2 and Φ_i, $i > 1$, decay to Ψ_1 and Φ_1 sufficiently fast.

Similar definitions hold for $\bar{\Psi}$, Φ and Φ^*, so that

$$\mathcal{N}_\Psi + \mathcal{N}_\Phi - \mathcal{N}_{\bar{\Psi}} - \mathcal{N}_{\Phi^*} = 2\epsilon_X + 2\epsilon_{\widetilde{X}}. \tag{4.31}$$

The last term on the right hand side of Eq. (4.29) describes the production of the species i through modulus decay into X which promptly decays into i. The quadratic collision terms C_i describe the particle-antiparticle annihilations as well as the transfer reaction $\Psi\Psi \leftrightarrow \Phi\Phi$, required by supersymmetry. The collision terms for $i = \Psi$, Φ are

$$C_\Psi = -\langle\sigma v\rangle_{\Psi\bar{\Psi}\to Z'Z'}\left[n_\Psi n_{\bar{\Psi}} - (n_\Psi^{\rm eq})^2\right] - \langle\sigma v\rangle_{\Psi\Psi\to\Phi\Phi}\left[n_\Psi^2 - \left(n_\Psi^{\rm eq}/n_\Phi^{\rm eq}\right)^2 n_\Phi^2\right] \tag{4.32}$$

$$C_\Phi = -\langle\sigma v\rangle_{\Phi\Phi^*\to Z'Z'}\left[n_\Phi n_{\Phi^*} - (n_\Phi^{\rm eq})^2\right] - \langle\sigma v\rangle_{\Phi\Phi\to\Psi\Psi}\left[n_\Phi^2 - \left(n_\Phi^{\rm eq}/n_\Psi^{\rm eq}\right)^2 n_\Psi^2\right], \tag{4.33}$$

where

$$n_i^{\rm eq} = \frac{g_i}{2\pi^2} T m_i^2 K_2(m_i/T) \tag{4.34}$$

is the Maxwell-Boltzmann equilibrium number density for a particle of mass m_i with g_i internal degrees of freedom. The collision terms for the antiparticles are identical, with the replacements $\Psi \to \bar{\Psi}$ and $\Phi \to \Phi^*$.

The solutions to the Boltzmann equations for the yields $Y_i = n_i/s$ are shown in Fig. 4.5 for $m_\Psi = 1.9$ GeV, $m_\Phi = 2.2$ GeV, $m_\chi = 5$ GeV, $e' = 0.05$. We consider two cases. In the plot on the left, we show the limit where $\langle\sigma v\rangle_{\Phi\Phi\leftrightarrow\Psi\Psi} = 0$; this can occur when the rate is mixing-suppressed, for a heavy gaugino, or within models with alternative symmetric annihilation mechanisms (see Appendix of Ref. [2]). With the transfer turned off, the scalar and fermion DM sectors are decoupled. The resulting DM abundances are determined by the X and $\widetilde{X}$ decay asymmetries. In this limit, the dark sector reduces to two independent copies of the standard asymmetric DM scenario. We show the case where Ψ and Φ are populated equally by the $\widetilde{X}$ decays, but, in general, the asymmetries can be different for the scalar and fermion DM, as discussed in Sec. 4.3.1.

In the plot on the right we show the result when the transfer is efficient, driving the dark matter population into the lighter state Ψ. Since the asymmetry is also transferred into the lighter state, the $\Psi\bar{\Psi}$ annihilation rate is enhanced, resulting in a highly asymmetric final abundance. The heavier state, on the other hand, freezes out with nearly equal abundances of particle and anti-particle, which are about an order of magnitude smaller than that of Ψ. The transfer reaction does not affect the production of the net hidden sector baryon number $n_\Psi + n_\Phi - n_{\bar{\Psi}} - n_{\Phi^*}$. Its evolution is shown in Fig. 4.4. Note that

$$n_\Psi + n_\Phi - n_{\bar{\Psi}} - n_{\Phi^*} = 2n_B \tag{4.35}$$

as required by B conservation in hylogenesis.

The ratio of the abundances of Ψ to Φ is important for IND. We study the effect of varying

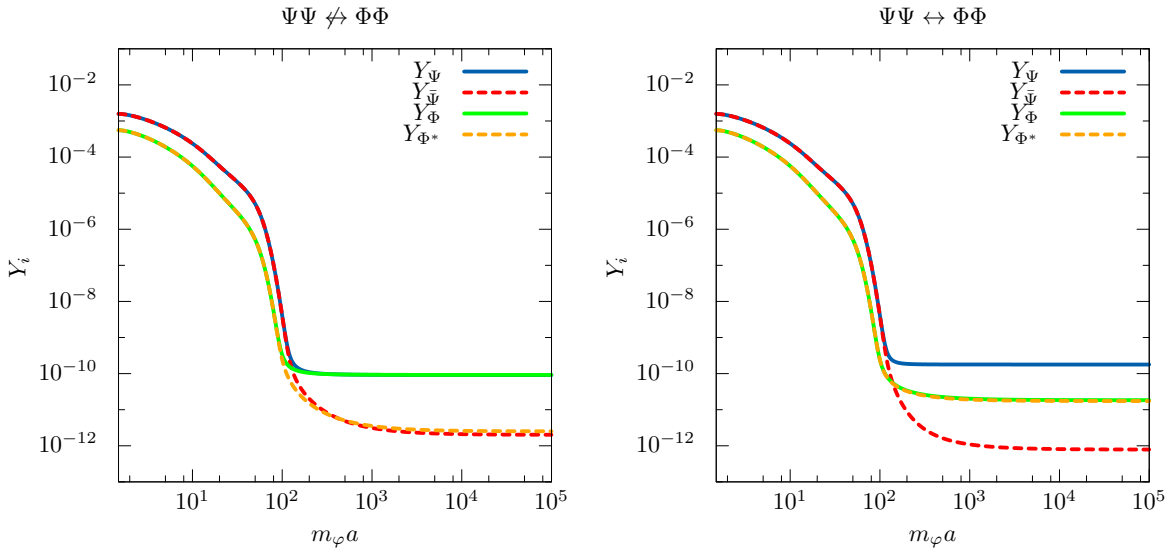

Figure 4.5: Solution to the Boltzmann equations for the yields $Y_i = n_i/s$ as a function of the scale factor a. The plot on the left shows the evolution for the case when the transfer reaction $\Phi\Phi \leftrightarrow \Psi\Psi$ is turned off, while the plot on the right shows the outcome when it is active. The transfer drives the dark matter population into lighter state, Ψ in this case. The DM (anti-DM) abundance is indicated by solid (dashed) lines, with dark (light) lines referring to the fermion (scalar) component. The parameters used are described in the text.

the mass splitting $\Delta m = m_\Phi - m_\Psi$ and the gaugino mass on n_Ψ/n_Φ in Fig. 4.6. For each point in the parameter space, we solve the reheating and DM production equations and plot the final value of n_Ψ/n_Φ. The reheat temperature, asymmetry and gauge coupling strength are the same as for Fig. 4.5. Setting the DM abundance to the observed value fixes m_Ψ. Light gauginos and large DM mass splittings make the transfer more efficient, increasing the abundance of the lighter state relative to the heavier one. For small Δm or heavy m_χ the transfer rate is suppressed.

If the symmetric density does not annihilate efficiently, residual annihilations during the CMB era can inject enough energy to alter the power spectrum. The WMAP7 constraint on the annihilation rate for Dirac fermions or complex scalars is given by [5]

$$2\frac{\Omega_i\Omega_{\bar{i}}}{\Omega_{\rm DM}^2}\frac{f\langle\sigma v\rangle}{m_i} < \frac{2.42\times10^{-27}\,{\rm cm}^3/{\rm s}}{\rm GeV}, \tag{4.36}$$

where $i = \Psi$, Φ and $\Omega_i/\Omega_{\rm DM}$ is the fraction of total DM abundance in species i. This constraint is shown in Fig. 4.6 by the gray line (parameter space to the right is excluded). For the parameters we have chosen, symmetric annihilation is only marginally efficient, and transfer

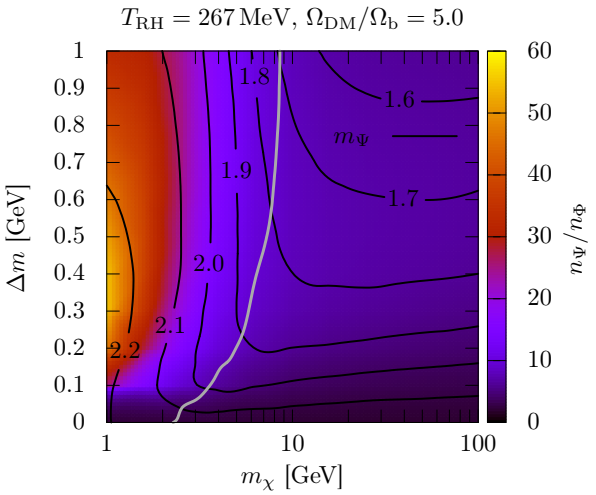

Figure 4.6: The ratio n_Ψ/n_Φ for the allowed range of mass splittings $\Delta m = m_\Phi - m_\Psi$ and relevant values of the hidden gaugino mass m_χ. At each point in the plane the DM abundance is fixed to be $\Omega_{\rm DM}/\Omega_{\rm b} = 5.0$. Contours of constant m_Ψ (in GeV) are also shown. The gray contour shows the CMB constraint for DM annihilations from Ref. [5]. Points to the right of this line are excluded.

processes through the light gaugino help achieve efficient annihilation (hence, the large m_χ region is excluded). For larger gauge coupling $e' = 0.1$, symmetric annihilation is much more efficient, and CMB constraints are evaded in the entire parameter region in Fig. 4.6.

Finally, let us mention that we have not included any baryon washout processes in our Boltzmann equations. For $T_{\rm RH} \ll m_{X_1}, m_{\tilde{q}}$, the only such processes that are allowed kinematically are $\Psi\Phi \leftrightarrow 3\bar{q}$ and the corresponding crossed diagrams. These transitions require the exchanges of massive intermediate P and X states to occur. These processes are therefore well described by effective operators of the kind

$$\mathscr{L} \sim \frac{1}{\Lambda_{\rm IND}^3} uds\Psi\Phi, \tag{4.37}$$

where the scale $\Lambda_{\rm IND}$ is defined in Section 4.5 (see Eq. (4.52)) and the order of fermion contractions depends on which UV completion is used in Eq. (4.12). We find that the corresponding cross sections are safely smaller than the stringent limits found in Ref. [296] provided $m_X, m_P \gtrsim 300$ GeV. For example, we can estimate the cross section for $\Psi\Phi \leftrightarrow 3\bar{q}$ as

$$\langle\sigma v\rangle \sim \left(\frac{1}{4\pi}\right)^3 \frac{m_{\Psi_1}^4}{\Lambda_{\rm IND}^6} = \left(4\times 10^{-21}\ \ {\rm GeV}^{-2}\right)\left(\frac{1\ \ {\rm TeV}}{\Lambda_{\rm IND}}\right)^6\left(\frac{m_{\Psi_1}}{3\ \ {\rm GeV}}\right)^4. \tag{4.38}$$

The authors of Ref. [296] found that washout is negligible for

$$m_{\rm DM}\langle\sigma v\rangle \lesssim 10^{-18}\ \text{GeV}^{-1}, \tag{4.39}$$

which is easily satisfied by Eq. (4.38). Even if these processes were important, the X_1 decay asymmetry can be adjusted to compensate, as long as the couplings satisfy the conditions imposed by SUSY breaking discussed in the next section. Thus, our omission of baryon washout effects is justified.

4.4 Supersymmetry Breaking

Our model for asymmetric antibaryonic dark matter typically requires light hidden scalars with masses of a few GeV to obtain an acceptable dark matter abundance. For such masses to be technically natural, the size of soft supersymmetry breaking felt by the light states should also be near the GeV scale. This is much smaller than the minimal scale of supersymmetry breaking felt in the MSSM sector, which must be close to or above the TeV scale to be consistent with current experimental bounds.

Such a hierarchy between visible and hidden sector soft terms can arise if the hidden sector feels supersymmetry breaking more weakly than the visible. We examine here the necessary conditions for this to be the case based on the interactions required for hylogenesis. We also discuss a few specific mechanisms of supersymmetry breaking that can give rise to the required spectrum. Motivated by the desire for large moduli masses, which are frequently on the same order as the gravitino mass, we pay particular attention to anomaly mediation.

4.4.1 Minimal Transmission of Supersymmetry Breaking

The interactions we have put forward in Section 4.2 will transmit supersymmetry breaking from the MSSM to the hidden sector. Thus, a minimal requirement for small hidden-sector soft terms is that these interactions do not themselves create overly large hidden soft masses. We begin by studying these effects.

The states that we wish to remain light derive from the $Y^{(c)}_{1,2}$ and $H^{(c)}$ chiral multiplets. These multiplets do not couple directly to the MSSM, but they are connected indirectly by their interactions with the $X^{(c)}$ states and $U(1)'-U(1)_Y$ gauge kinetic mixing. Thus, the $X^{(c)}$ multiplets and the gauge kinetic mixing will act as mediators to the hidden states.

Beginning with the X multiplets, they will feel supersymmetry breaking from their direct couplings to the quarks and the triplet $P^{(c)}$ given in Eq. (4.12). The transmission of supersymmetry breaking can be seen in the renormalization group (RG) equations of the soft scalar

squared masses of $X_a^{(c)}$ and $P^{(c)}$ (assuming interactions as in case I):

$$\begin{aligned}
(4\pi)^2\frac{dm^2_{X_a}}{dt} &= 6|\lambda'_a|^2(m^2_{X_a}+m^2_{U^c}+m^2_P+|A_{\lambda'_a}|^2)+4|\zeta_a|^2(m^2_{X_a}+2m^2_Y+|A_{\zeta_a}|^2)\\
(4\pi)^2\frac{dm^2_{X^c_a}}{dt} &= 4|\bar\zeta_a|^2(m^2_{X^c_a}+2m^2_{Y^c}+|A_{\bar\zeta_a}|^2)\\
(4\pi)^2\frac{dm^2_P}{dt} &= \sum_a 2|\lambda'_a|^2(m^2_{X_a}+m^2_{U^c}+m^2_P)-\frac{32}{3}g_3^2|M_3|^2+\ldots\\
(4\pi)^2\frac{dm^2_{P^c}}{dt} &= 4|\lambda''|^2(m^2_{S^c}+m^2_{D^c}+m^2_{P^c})-\frac{32}{3}g_3^2|M_3|^2+\ldots
\end{aligned} \tag{4.40}$$

where the A_i are trilinear soft terms corresponding to superpotential operators, and we have dropped subleading hypercharge contributions for $P^{(c)}$. We see that P and P^c will typically obtain full-strength (TeV) soft masses from their direct coupling to the gluon multiplet, and these will be passed on to X in the course of RG evolution. Recall as well that $\lambda'_{1,2}$ and λ'' must both be reasonably large for hylogenesis to work.

Turning next to the Y multiplets, we find for the Y_1

$$\begin{aligned}
(4\pi)^2\frac{dm^2_{Y_1}}{dt} &= \sum_a 8|\zeta_a|^2\left(m^2_{X_a}+m^2_{Y_1}+|A_{\zeta_a}|^2\right)+2|\gamma|^2\left(m^2_H+m^2_{Y_1}+m^2_{Y_2^c}+|A_\gamma|^2\right)\\
(4\pi)^2\frac{dm^2_{Y_1^c}}{dt} &= \sum_a 8|\bar\zeta_a|^2\left(m^2_{X^c_a}+m^2_{Y_1^c}+|A_{\bar\zeta_a}|^2\right)+2|\bar\gamma|^2\left(m^2_{H^c}+m^2_{Y_1^c}+m^2_{Y_2}+|A_{\bar\gamma}|^2\right)\ .
\end{aligned} \tag{4.41}$$

The Y_2 multiplets are also charged under the $U(1)'$ hidden gauge symmetry, which mixes kinetically with hypercharge with strength κ. This leads to additional contributions to the running [197, 297, 298]. At leading non-trivial order in κ, we have

$$\begin{aligned}
(4\pi)^2\frac{dm^2_{Y_2}}{dt} &= 2|\bar\gamma|^2\left(m^2_{H^c}+m^2_{Y_1^c}+m^2_{Y_2}+|A_{\bar\gamma}|^2\right)\\
&\quad -8e'^2(|M'|^2+\kappa^2|M_1|^2)+2e'^2S_{Z'}-2\kappa\sqrt{\frac{3}{5}}\,g_1e'S_Y\\
(4\pi)^2\frac{dm^2_{Y_2^c}}{dt} &= 2|\gamma|^2\left(m^2_H+m^2_{Y_1}+m^2_{Y_2^c}+|A_\gamma|^2\right)\\
&\quad -8e'^2(|M'|^2+\kappa^2|M_1|^2)-2e'^2S_{Z'}+2\kappa\sqrt{\frac{3}{5}}\,g_1e'S_Y\ ,
\end{aligned} \tag{4.42}$$

where $S_{Z'}=\mathrm{tr}(Q'm^2)$, $S_Y=\mathrm{tr}(Ym^2)$, $g_1=\sqrt{5/3}\,g_Y$, and M_1 is the hypercharge gaugino (Bino) mass. The RG equations for the soft mass of H (H^c) has the same form as for Y_2^c (Y_2) but with signs of the last two "S" terms reversed.

In addition to these RG contributions, there is D-term mixing between hypercharge and $U(1)'$. After electroweak symmetry breaking in the MSSM sector, this generates an effective

Fayet-Iliopoulos [197, 297] term in the hidden sector of the form

$$V \supset \frac{e'^2}{2}\left(|H|^2 + |Y_2|^2 - |H^c|^2 - |Y_2^c|^2 - \xi_{FI}\right)^2 \ , \tag{4.43}$$

with $\xi_{FI} = -\kappa(g_Y/2e')v^2\cos(2\beta)$, where $v \approx 174$ GeV and $\tan\beta$ is the ratio of MSSM Higgs vevs. This term can be absorbed by shifting the hidden-sector soft masses by $m_i^2 \to (m_i^2 - Q_i'\xi_{FI})$.

The RG equations we have presented here are valid down to the scale $m_{\rm soft}$ where the MSSM (and X and $P^{(c)}$ if their supersymmetric masses are near $m_{\rm soft}$) states should be integrated out. This will generate additional threshold corrections to the hidden-sector soft masses. However, these lack the logarithmic enhancement of the RG contributions and are typically subleading. Thus, putting these pieces together we can make estimates for the minimal natural values of the soft terms in the hidden sector. In terms of $m_{\rm soft} \sim M_3 \sim$ TeV and $\Delta t = \ln(\Lambda_*/m_{\rm soft})$ (where Λ_* is the scale of supersymmetry-breaking mediation), we find

$$m_{P^{(c)}} \gtrsim m_{\rm soft} \tag{4.44}$$

$$m_{X^{(c)}} \gtrsim |\lambda'|\, m_{\rm soft}\left(\frac{\sqrt{\Delta t}}{6}\right) \tag{4.45}$$

$$m_{Y_1^{(c)}} \gtrsim |\zeta\,\lambda'|\, m_{\rm soft}\left(\frac{\sqrt{\Delta t}}{6}\right)^2 \tag{4.46}$$

$$m_{Y_2^{(c)}}, m_{H^{(c)}} \gtrsim \max\left\{|\gamma\,\zeta\lambda'|\, m_{\rm soft}\left(\frac{\sqrt{\Delta t}}{6}\right)^{3/2},\ \kappa\, M_1\left(\frac{\sqrt{\Delta t}}{6}\right),\ \sqrt{\frac{\kappa g_Y}{2e'}}\, v\right\} \ . \tag{4.47}$$

Note that $\sqrt{\Delta t} \approx 6$ for $\Lambda_* = M_{\rm Pl}$. We see that the soft masses of the Y_2 and H multiplets can be naturally suppressed relative to the MSSM for relatively small couplings. For example, choosing $\gamma = e' = 0.05$, $\lambda'_1 = 1$, $\kappa \sim 10^{-4}$ and $\zeta = 0.1$ yields soft masses for the $Y_2^{(c)}$ and $H^{(c)}$ multiplets below a few GeV. Therefore the direct coupling of the MSSM to the hidden sector need not induce overly large supersymmetry breaking in the hidden sector.

4.4.2 Mediation Mechanisms

We consider next a few specific mechanisms to mediate supersymmetry breaking to the MSSM and the hidden sector that will produce a mass hierarchy between the two sectors. Motivated by our desire for large moduli masses, which in supergravity constructions are frequently related closely to the gravitino mass [177, 179], the mechanism we will focus on primarily is anomaly mediation. However, we will also describe a second example using gauge mediation with mediators charged only under the SM gauge groups.

With anomaly mediated supersymmetry breaking (AMSB) [102, 135], the leading-order

gaugino mass in the hidden sector is

$$M' = \frac{b' e'^2}{(4\pi)^2} \, m_{3/2} \ , \tag{4.48}$$

where $b' = -4$ is the one-loop $U(1)'$ beta function coefficient. A similar expression applies to the MSSM gaugino soft masses, but with $e'^2 b'$ replaced by the corresponding factor. Based on this comparison, we see that a much lighter hidden gaugino will arise for small values of the hidden gauge coupling [198]. For example, with MSSM gaugino masses in the range of a few hundred GeV, the hidden gaugino mass will be a few GeV for $e'/g_{SM} \sim 0.1$, corresponding to $e' \sim 0.05$.

The hidden-sector scalar soft masses will also be parametrically smaller than those of the MSSM if the corresponding Yukawa couplings are smaller as well. The explicit AMSB expressions for Y_1 and Y_2^c are

$$\begin{aligned} m_{Y_1}^2 &= \frac{m_{3/2}^2}{(4\pi)^4} \left[\gamma^2 (3\gamma^2 - 4e'^2) + 6\gamma^2 \sum_a \zeta_a^2 + 6 \sum_a \zeta_a^2 \lambda'^2_a + 4 \sum_{a,b} \zeta_a^2 \zeta_b^2 (2 + \delta_{ab}) \right] \ , \\ m_{Y_2^c}^2 &= \frac{m_{3/2}^2}{(4\pi)^4} \left[\gamma^2 (3\gamma^2 - 4e'^2) + 2\gamma^2 \sum_a \zeta_a^2 - 16 e'^2 \right] \ . \end{aligned} \tag{4.49}$$

We also have $m_H^2 = m_{Y_2^c}^2$, while $m_{H^c}^2 = m_{Y_2}^2$ are given by the same expressions with $\gamma \to \bar{\gamma}$ and $\zeta_a \to \bar{\zeta}_a$. The latter point also applies to $m_{Y_1^c}^2$ relative to $m_{Y_1}^2$ but with $\lambda'_a \to 0$ as well. Thus, we find GeV-scale soft masses for $Y_2^{(c)}$ and $H^{(c)}$ (and TeV-scale MSSM soft masses) for the fiducial values $\zeta_a \sim 0.1$, $\gamma \sim e' \sim 0.05$, and $m_{3/2} \sim 100$ TeV. Note that in these expressions we have neglected kinetic mixing effects which are negligible for $\kappa < 10^{-3} \ll e'/g_1$, as we assume here.

The result of Eq. (4.49) shows that the AMSB scalar squared masses can be positive or negative, depending on the relative sizes of the gauge and Yukawa couplings. This feature creates a severe problem in the MSSM where minimal AMSB produces tachyonic sleptons. We assume that one of the many proposed solutions to this problem corrects the MSSM soft masses without significantly altering the soft masses in the hidden sector [223, 299]. In contrast to the MSSM, negative scalar soft squared masses need not be a problem in the hidden sector due to the presence of supersymmetric mass terms for all the multiplets. In particular, the supersymmetric mass terms we have included in Eqs. (4.3, 4.12) for the vector-like hidden multiplets can generally be chosen so that only the H and H^c multiplets develop vevs.

Let us mention, however, that supersymmetric mass terms are problematic in AMSB. In particular, a fundamental supersymmetric mass term M_i will give rise to a corresponding holomorphic bilinear soft "b_i" term of size $b_i \sim M_i m_{3/2}$. If $b_i \gg m_{\rm soft}^2, |M_i|^2$, such a term will destabilize the scalar potential. To avoid this, we must assume that the supersymmetric mass

terms we have written in Eqs. (4.3, 4.12) are generated in some other way, such as from the vev of a singlet field.[11] A full construction of such a remedy lies beyond the scope of the present chapter, but we expect that it can be achieved in analogy to the many similar constructions addressing the corresponding $\mu - B\mu$ problem within the MSSM [223, 299] or beyond [198].

A second option for the mediation of supersymmetry breaking that preserves the MSSM-hidden mass hierarchy is gauge mediation by messengers charged only under the SM gauge groups [197, 297]. The soft masses generated in the hidden sector in this case can be deduced from the RG equations, up to boundary terms at the messenger scale on the order of $\kappa\, m_{\rm soft}$, which are safely small. Unfortunately, the $U(1)'$ gaugino mass generated in this scenario only appears at very high loop order, and tends to be unacceptably small [197]. This can be resolved if there are additional gravity-mediated contributions to all the soft masses on the order of a few GeV. The gravitino mass in this case will be on the same order as the hidden states. If it is slightly lighter, it may permit the decay $\Psi_1 \to \psi_{3/2} + \Phi_1$ (for $m_{\Psi_1} > m_{3/2} + m_{\Phi_1}$).

4.5 Phenomenology

4.5.1 Induced Nucleon Decay

Dark matter provides a hidden reservoir of antibaryons. Although baryon transfer interactions are weak enough that visible baryons and hidden antibaryons are kept out of chemical equilibrium today, they are strong enough to give experimentally detectable signatures of DM-induced nucleon destruction. In these events, a DM particle scatters inelastically on a nucleon $N = p, n$, producing a DM antiparticle and mesons. For SUSY models, the simplest IND events are those involving a single kaon,

$$\Psi N \to \Phi^* K\,, \quad \Phi N \to \bar{\Psi} K\,. \tag{4.50}$$

We consider only the lightest DM states $\Psi \equiv \Psi_1$ and $\Phi \equiv \Phi_1$; the heavier states are not kinematically accessible provided their mass gap is larger than $(m_N - m_K) \approx 400$ MeV. Both down-scattering and up-scattering can occur (defined as whether the heavier DM state is in the initial or final state, respectively), but up-scattering is kinematically forbidden for $|m_\Psi - m_\Phi| < m_N - m_K$.

Assuming the hidden states are not observed, IND events mimic standard nucleon decay events $N \to K\nu$, with an unobserved neutrino ν (or antineutrino $\bar{\nu}$). Nucleon decay searches by the Super-Kamiokande experiment have placed strong limits on the N lifetime τ for these modes [281]:

$$\tau(p \to K^+\nu) > 2.3 \times 10^{33}\ \text{years}\,, \quad \tau(n \to K^0_S\nu) > 2.6 \times 10^{32}\ \text{years}. \tag{4.51}$$

[11] Note that we could have $|\mu_P|$, $|\mu_X| \gg m_{3/2}$ without any problems. In this case, the threshold corrections to the light soft masses from integrating out the heavy multiplets precisely cancel their leading contributions from RG, leading to a zero net one-loop AMSB contribution.

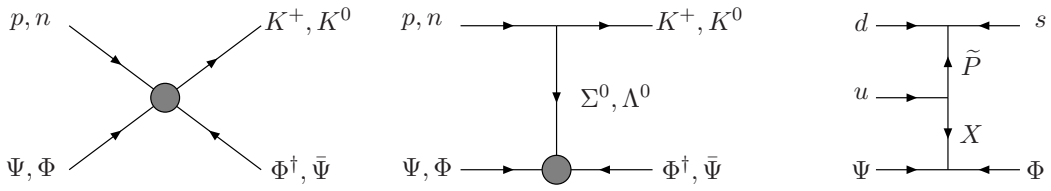

Figure 4.7: IND processes at leading order in chiral effective theory (left, center). Gray dot shows effective B transfer operator, generated by $\widetilde{P}$, X exchange in our model (right).

However, these bounds do not in general apply to IND, due to the different kinematics. For $N \to K\nu$, the K has momentum $p_K \approx 340$ MeV. IND events are typically more energetic: $680 \lesssim p_K \lesssim 1400$ MeV for down-scattering, and $p_K \lesssim 680$ MeV for up-scattering (if allowed).[12] The Super-Kamiokande analysis assumes: for $p \to K^+$, K^+ is emitted below Čerenkov threshold in water, corresponding to $p_K \lesssim 550$ MeV; for $n \to K^0_S$, the K^0_S is emitted with $200 < p_K < 500$ MeV. Therefore, IND is largely unconstrained by standard nucleon decay searches. The limits in Eq. (4.51) only constrain up-scattering IND in a subset of parameter space, whereas down-scattering provides typically the dominant contribution to the total IND rate [279].

Next, we compute the IND rates within our supersymmetric model, starting from the baryon transfer superpotential in Eq. (4.12). The vector-like squarks $\widetilde{P}, \widetilde{P}^c$ mix through the SUSY-breaking term $\mathscr{L}_{\rm soft} \supset b_P \widetilde{P}\widetilde{P}^c$ to generate the mass eigenstates $\widetilde{P}_{1,2}$, with masses $m_{\widetilde{P}_{1,2}}$. The leading contribution to IND arises from tree-level $\widetilde{P}_{1,2}$ exchange, shown in Fig. 4.7, giving (in two-component notation)

$$\mathscr{L}_{\rm eff} = \frac{1}{\Lambda^3_{\rm IND}} \times \begin{cases} \epsilon_{\alpha\beta\gamma}(d^\alpha_R s^\beta_R)(u^\gamma_R \Psi_R)\Phi & \text{(case I)} \\ \epsilon_{\alpha\beta\gamma}(s^\alpha_R u^\beta_R)(d^\gamma_R \Psi_R)\Phi & \text{(case II)} \\ \epsilon_{\alpha\beta\gamma}(u^\alpha_R d^\beta_R)(s^\gamma_R \Psi_R)\Phi & \text{(case III)} \end{cases}, \frac{1}{\Lambda^3_{\rm IND}} \equiv \sum_{a=1,2} \frac{2\bar{\zeta}^*_a Z_{31} V^*_{11} b_P \lambda'_a \lambda'}{m^2_{\widetilde{P}_1} m^2_{\widetilde{P}_2} m_{X_a}}. \quad (4.52)$$

Here, we have neglected higher derivative terms, and $\Lambda_{\rm IND}$ characterizes the IND mass scale. The different cases, corresponding to different baryon transfer interactions in Eq. (4.12), lead to different fermion contractions.

The effective IND rate for nucleon $N = p, n$ is

$$\Gamma(N \to K) = n_\Psi (\sigma v)^{N\Psi \to K\Phi^\dagger}_{\rm IND} + n_\Phi (\sigma v)^{N\Phi \to K\bar{\Psi}}_{\rm IND} \quad (4.53)$$

where $n_{\Psi,\Phi}$ are the local DM number densities and $(\sigma v)_{\rm IND}$ is the IND cross section. The IND

[12] For fixed DM masses, IND is either bichromatic or monochromatic, depending on whether up-scattering is allowed or not; the range in p_K corresponds to the allowed mass range $1.4 \lesssim m_{\Phi,\Psi} \lesssim 3.3$ GeV. If other hidden states $\Psi_{a\geq 2}$ and $\Phi_{b\geq 2}$ are kinematically accessible, the IND spectrum can have additional spectral lines.

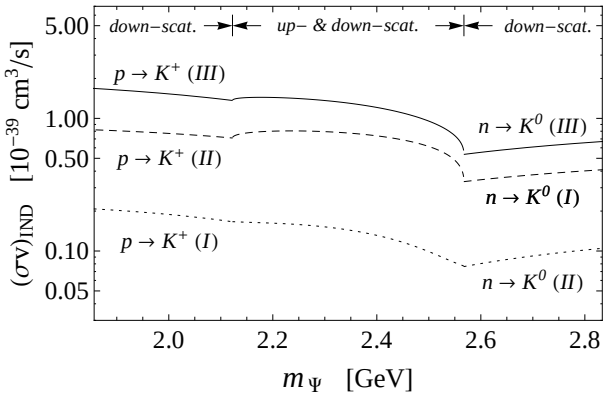

Figure 4.8: Total IND cross section $(\sigma v)_{\rm IND} = (\sigma v)_{\rm IND}^{N\Psi\to K\Phi^*} + (\sigma v)_{\rm IND}^{N\Phi\to K\bar{\Psi}}$ over allowed range for m_Ψ, with $m_\Phi = (\Omega_{\rm DM}/\Omega_{\rm b})m_p - m_\Psi \approx 5m_p - m_\Psi$. The effective baryon transfer mass scale is $\Lambda_{\rm IND} = 1$ TeV. Cases I, II, III correspond to different baryon transfer models considered in Eqs. (4.12,4.52).

lifetime can be expressed as

$$\tau(N \to K) = \frac{1}{\Gamma(N \to K)} = \frac{(1+r)(\Omega_{\rm DM}/\Omega_{\rm b})m_p}{2\rho_{\rm DM}\left[r(\sigma v)_{\rm IND}^{N\Psi\to K\Phi^\dagger} + (\sigma v)_{\rm IND}^{N\Phi\to K\bar{\Psi}}\right]} \tag{4.54}$$

with local DM mass density $\rho_{\rm DM} = m_\Psi n_\Psi + m_\Phi n_\Phi$, and assuming the local ratio $r \equiv n_\Psi/n_\Phi$ is the same as over cosmological scales. The IND cross section is estimated as

$$(\sigma v)_{\rm IND} \approx \frac{m_{\rm QCD}^4}{16\pi\Lambda_{\rm IND}^6} \approx 10^{-39}\,{\rm cm}^3/{\rm s} \times \left(\frac{\Lambda_{\rm IND}}{1\,{\rm TeV}}\right)^{-6}\,, \tag{4.55}$$

with QCD scale $m_{\rm QCD} \approx 1$ GeV.[13] For $r \sim \mathcal{O}(1)$, the IND lifetime is

$$\tau(N \to K) \approx 10^{32}\,{\rm yrs} \times \left(\frac{(\sigma v)_{\rm IND}}{10^{-39}\,{\rm cm/s}}\right)^{-1} \left(\frac{\rho_{\rm DM}}{0.3\,{\rm GeV/cm}^3}\right)^{-1}\,, \tag{4.56}$$

which is exactly in the potential discovery range of existing nucleon decay searches, provided the baryon transfer scale $\Lambda_{\rm IND}$ is set by the weak scale.

More quantitatively, we compute $(\sigma v)_{\rm IND}$ using chiral perturbation theory, which provides an effective theory of baryons and mesons (and DM) from the underlying quark-level interaction in Eq. (4.52), following the same methods applied to standard nucleon decay [300] and with additional input from lattice calculations of hadronic matrix elements [301]. We refer the reader to Ref. [279] for further details. Fig. 4.8 shows numerical results for the total cross section $(\sigma v)_{\rm IND}$, over the allowed mass range m_Ψ for $r = 1$, for the three types of interactions

[13] The cross section $(\sigma v)_{\rm IND}$ also depends on the DM masses $m_{\Psi,\Phi}$, which for the purposes of dimensional analysis are comparable to $m_{\rm QCD}$.

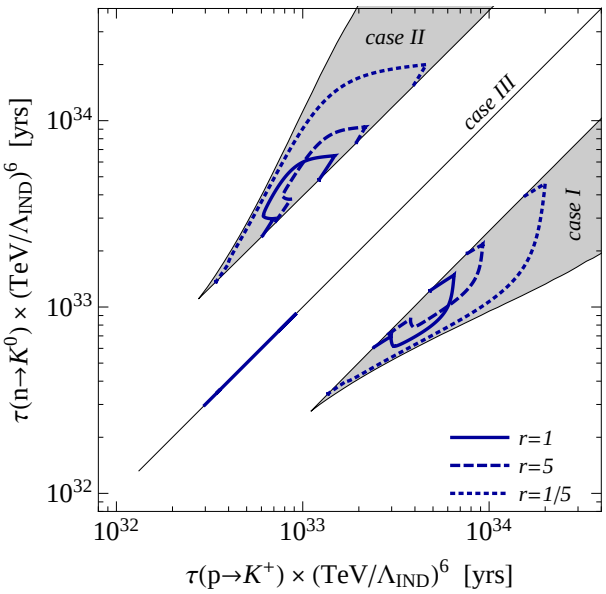

Figure 4.9: Proton and neutron lifetimes for different baryon transfer models (cases I, II, III) considered in Eqs. (4.12) and (4.52). Black line/gray regions show lifetime range for any r, while blue curves correspond to particular r values.

in Eq. (4.52).[14] This calculation agrees well with our previous estimate in Eq. (4.55). However, since the typical IND momentum is comparable to the chiral symmetry breaking scale $\approx 1\,\mathrm{GeV}$ (i.e., where the effective theory breaks down), we regard these results as approximate at best. The different rates for different cases (for fixed Λ_{IND}) satisfy

$$(\sigma v)^{p\to K^+}_{\mathrm{IND,III}} = (\sigma v)^{n\to K^0}_{\mathrm{IND,III}}\,, \quad (\sigma v)^{p\to K^+}_{\mathrm{IND,I}} = (\sigma v)^{n\to K^0}_{\mathrm{IND,II}}\,, \quad (\sigma v)^{p\to K^+}_{\mathrm{IND,II}} = (\sigma v)^{n\to K^0}_{\mathrm{IND,I}} \tag{4.57}$$

as a consequence of strong isospin symmetry [279]. The kinks correspond to up-scatting kinematic thresholds; to the left and right, only down-scatting is allowed, while in the center both up- and down-scattering occur.

More generally, we show in Fig. 4.9 the allowed range for $p \to K^+$ and $n \to K^0$ IND lifetimes. We consider masses $m_{\Psi,\Phi}$ consistent with $\Omega_{\mathrm{DM}}/\Omega_{\mathrm{b}} \approx 5$, for arbitrary r in the range $0 < r < \infty$, and we take $\Lambda_{\mathrm{IND}} = 1$ TeV. For case I (II), the allowed region is shown in gray, with a smaller (larger) lifetime for $n \to K^0$ than $p \to K^+$. For case III, shown by the black line, the p and n IND lifetimes are equal, modulo SUSY radiative corrections and isospin-breaking that we neglect. Specific values for r are shown by blue curves. The solid blue curves show the IND lifetimes for $r = 1$, corresponding to the calculation in Fig. 4.8. For $r \neq 1$, the IND rate can be enhanced if the heavier state is overpopulated (e.g., $r > 1$ for $m_\Psi > m_\Phi$ or $r < 1$ for $m_\Psi < m_\Phi$); on the other hand, the IND rate can be highly suppressed if the heavier state is

[14] The total rate $n \to K^0$ includes both K^0_S and K^0_L final states, and the individual channels $n \to K^0_S$ and $n \to K^0_L$ are (approximately) half the total rate.

depleted and up-scattering is kinematically forbidden. The dashed (dotted) blue curves show the IND lifetimes for $r = 5$ ($r = 1/5$).

We make a number of comments:

- The IND lifetimes scale as $\tau(N \to K) \propto \Lambda_{\rm IND}^6$. Taking $\Lambda_{\rm IND}$ in the range $500\,{\rm GeV} - 5\,{\rm TeV}$ corresponds to lifetimes of $10^{30} - 10^{36}$ years. Lifetimes that can be probed in nucleon decay searches correspond to energy scales accessible in colliders (see below).
- Both channels $p \to K^+$ and $n \to K^0$ provide complementary information, and which one dominates depends on the underlying heavy states mediating baryon transfer.
- The largest IND rates in Fig. 4.9 correspond to Φ-dominated DM ($r \ll 1$) with $m_\Phi > m_\Psi$, and IND is dominated by $\Phi N \to \bar{\Psi} K$ down-scattering.

Lastly, we note that while the observation of IND would be a smoking gun signal for hylogenesis, a nonobservation does not rule out hylogenesis as a baryogenesis mechanism. The IND rate can be suppressed if (i) the effective scale $\Lambda_{\rm IND}$ lies beyond the TeV-scale (due to small couplings or large mass parameters), (ii) baryon transfer in the early Universe involves heavier quark flavours, and/or (iii) the heavier DM state is depleted while up-scattering IND is kinematically blocked.

4.5.2 Precision Probes

At energies well below the weak scale, the light states in the hidden sector interact with the SM primarily through the gauge kinetic mixing interaction. The most important effect of this mixing is an induced coupling of the Z' vector boson to the SM fermions f given by

$$-\mathscr{L} \supset -\kappa c_W Q_f^{em} \bar{f} \gamma^\mu Z'_\mu f \ , \tag{4.58}$$

where Q_f^{em} is the electric charge of the fermion and c_W is the cosine of the weak mixing angle. Direct searches for a light Z' limit $\kappa c_W \lesssim 10^{-3}$ for $m_{Z'} \lesssim 1\,{\rm GeV}$ [202, 292, 302] with significant improvements expected in the coming years [303–305].

The dark matter states in our scenario consist of a Dirac fermion or a complex scalar with a direct coupling to the Z' vector. With the mixing interaction connecting the Z' to SM fermions, this state will efficiently mediate spin-independent elastic scattering of the DM states off nuclei. We estimate the cross section per target nucleon to be [232]

$$\sigma_0^{\rm SI} = (5 \times 10^{-39}\,{\rm cm}^2) \left(\frac{2Z}{A}\right)^2 \left(\frac{\mu_n}{\rm GeV}\right)^2 \left(\frac{e'}{0.05}\right)^2 \left(\frac{\kappa}{10^{-4}}\right)^2 \left(\frac{0.3\ {\rm GeV}}{m_{Z'}}\right)^4 , \tag{4.59}$$

where μ_n is the DM-nucleon reduced mass. While this cross section is quite large, the masses of the DM particles in this scenario lie below the region of sensitivity of most current direct detection DM searches, including the specific low-threshold analyses by COGENT [306], CDMS [307], XENON10 [9], and XENON100 [308]. For a DM mass below 3 GeV, this cross

section lies slightly below the current best limit from CRESST [11]. Proposed low-threshold searches for DM scattering with nuclei or electrons are expected to improve these limits [309].

4.5.3 High-Energy Colliders

The new heavy states required for hylogenesis couple directly to the SM and can potentially be probed in high-energy colliders such as the Tevatron and the LHC. In particular, the effective interactions induced by the vector-like quark multiplets (P, P^c) can generate monojets and modify the kinematic distributions of dijets. We discuss here the approximate limits that existing collider data places on the masses of these multiplets, although we defer a detailed analysis to the future.

Monojet signals arising from the effective four-fermion interaction $(X u_R^c d_R^c s_R^c)/M^2$ present in the minimal hylogenesis model were considered previously in Ref. [279]. More recent searches for monojets by the ATLAS [310] and CMS [311] collaborations limit the corresponding mass scale M to lie above $0.5 - 3$ TeV. Note, however, that in our supersymmetric formulation the corresponding four-fermion operator is only generated once supersymmetry-breaking effects are included. This weakens the correlation between the monojet signal and the operator responsible for hylogenesis, although the limit does typically force the $P^{(c)}$ multiplets to be at least as heavy as a few hundred GeV. On the other hand, this operator is directly related to the IND interaction. An alternative signal that can arise directly from the superpotential interaction is a "monosquark" $\tilde{q}^* \widetilde{X}$ final state, with the squark decaying to a jet and missing energy. In both cases, collider limits may be weakened through cascade decays in the hidden sector, which could produce additional hidden photons or Higgs bosons that decay to SM states.

A second way to probe our supersymmetric UV completion of hylogenesis is through the kinematic distributions of dijets, which can be modified by the direct production of the triplet P scalars (which are R-even). On-shell production of scalar $\tilde{P}$ states via the interactions of Eq. (4.12) can produce a dijet resonance. For heavier masses, the primary effect is described by the non-minimal Kähler potential operator of Eq. (4.13), which gives rise to a four-quark contact operator. Studies of dijet distributions by ATLAS [312] and CMS [313, 314] put limits on the masses of the $P^{(c)}$ scalars of 1-10 TeV, although the specific limits depend on the flavour structure of the quark coupling in Eq. (4.12) present in the underlying theory.

4.6 Conclusions

Through the mechanism of hylogenesis, the cosmological densities of visible and dark matter may share a unified origin. Out-of-equilibrium decays during a low-temperature reheating epoch generate the visible baryon asymmetry, and an equal antibaryon asymmetry among GeV-scale hidden sector states. The hidden antibaryons are weakly coupled to the SM and are the dark matter in the Universe.

We have embedded hylogenesis in a supersymmetric framework. By virtue of its weak couplings to the SM, SUSY-breaking is sequestered from the hidden sector, thereby stabilizing

its GeV mass scale. The DM consists of two states, a quasi-degenerate scalar-fermion pair of superpartners. We studied in detail one particular realization of supersymmetric hylogenesis, considering several aspects:

- We constructed a minimal supersymmetric model for hylogenesis. Hidden sector baryons are chiral superfields X and Y, with $B = 1$ and $-1/2$, respectively. The lightest Y states are DM, while X decays in the early Universe generate the B asymmetries.

- In addition, we introduced a vector-like $SU(3)_C$ triplet to mediate B transfer between visible and hidden sectors, and a hidden Z' gauge boson (with kinetic mixing) to deplete efficiently the symmetric DM densities.

- We showed that hylogenesis can successfully generate the observed B asymmetry during reheating. We computed the CP asymmetry from X decay and solved the coupled Boltzmann equations describing the cosmological dynamics of hylogenesis.

- We studied how SUSY breaking is communicated between the visible and hidden sectors through RG effects. We also examined predictions within an AMSB framework. While anomaly mediation explains the late-time reheating epoch from moduli decay, we have not explicitly addressed the issues of tachyonic slepton masses in the visible sector and the origin of SUSY mass terms in the hidden sector.

- Antibaryonic DM annihilates visible nucleons, causing induced nucleon decay to kaon final states, with effective nucleon lifetime in the range $10^{30} - 10^{36}$ years. DM can be discovered in current nucleon decay searches, and this signal remains unexplored.

- Collider searches for monojets and dijet resonances provide the strongest direct constraints on our model, and these signals are correlated with IND. Lifetimes of $10^{30} - 10^{36}$ years correspond to energy scales $\Lambda_{\rm IND} \sim 0.5 - 5$ TeV that can be probed at the LHC.

- DM direct detection experiments and precision searches for hidden photons constrain the Z' kinetic mixing, although our model remains consistent with current bounds.

We emphasize that our specific model was constructed to illustrate general features of hylogenesis, and certainly there are many other model-building possibilities along these lines. Nevertheless, it is clear that supersymmetric hylogenesis provides a technically natural and viable scenario for the genesis of matter, explaining the cosmic coincidence between the dark and visible matter densities and predicting new experimental signatures to be explored in colliders and nucleon decay searches.

Part III

Tunnelling and First Order Phase Transitions

Chapter 5

Quantum Tunnelling in Field Theory

5.1 Introduction

The present part of the thesis explores two different applications of first-order phase transitions, that is, transitions where an order parameter changes discontinuously. This order parameter is the set of expectation values of some scalar fields. At zero temperature these transitions proceed via quantum tunnelling through a potential barrier. At finite temperature, thermal fluctuations of fields can overcome a free energy barrier in process called "thermal tunnelling". As we will see, these two types of tunnelling are conveniently described using the same formalism.

We will be interested in evaluating the rate of tunnelling events either at zero or at finite temperature. This computation is the field theory analogue of Wentzel-Kramers-Brillouin (WKB) method for evaluating barrier penetration probabilities in ordinary quantum mechanics. In Sec. 5.2 we evaluate the tunnelling rate at zero temperature. Section 5.3 describes the equivalent computation for a thermodynamic system at finite temperature, which is relevant to phase transitions in the early Universe. In Sec. 5.4 we outline the numerical methods useful for the study of such transitions and show examples. These methods are used in the following chapters.

5.2 Tunnelling at Zero Temperature

Quantum tunnelling occurs when a system can minimize its energy by transitioning to a lower energy state through a classically forbidden region in configuration space. The problem of tunnelling in field theory was originally addressed in the seminal papers of Coleman and Callan [315, 316]. In general, the energy of the ground state field configuration $|\phi\rangle$ can be determined from the matrix element

$$\langle\phi|\exp(-H\tau/\hbar)|\phi\rangle = \sum_n \exp(-E_n\tau/\hbar)\langle\phi|n\rangle\langle n|\phi\rangle, \tag{5.1}$$

where $\tau = it$ is the Euclidean time and $\{|n\rangle\}$ is a complete set of eigenstates of the Hamiltonian H. We make $\hbar$ explicit in this section to make use of the semi-classical expansion of the path integral. The eigenvalues of physical Hamiltonians are bounded from below, that is there exists a lowest energy E_0. By considering the large Euclidean time limit $\tau \to \infty$ we can solve for E_0:

$$E_0 = -\hbar \lim_{\tau\to\infty} \frac{1}{\tau} \ln\langle\phi| \exp(-H\tau/\hbar)|\phi\rangle. \tag{5.2}$$

For a stable state, E_0 is real. Now consider the case shown in the left plot of Fig. 5.1: the vacuum at ϕ_+ is not the lowest energy configuration and therefore cannot be the ground state. If the system is found in this configuration, it must somehow evolve into the true vacuum at ϕ_-. This means that $|\phi_+\rangle$ is not an eigenstate of the Hamiltonian, but its energy E_+ can be defined through analytic continuation [317], such that Eq. (5.2) is still valid. E_+ then acquires a non-zero imaginary part, related to the decay rate of the state $|\phi_+\rangle$ through

$$\Gamma = -\frac{2}{\hbar}\mathrm{Im}E_+. \tag{5.3}$$

Our goal is then to compute the leading contribution to this decay rate. The imaginary part of the energy arises due to quantum tunnelling from the false vacuum into the true ground state. Perturbation theory can capture only small deviations from a vacuum state, so this computation is done in the semi-classical limit ($\hbar \to 0$) in the path integral formalism.[1] In ordinary quantum mechanics this reduces to the WKB approximation for tunnelling amplitudes.

First, let us consider the case of a single scalar field ϕ with the Euclidean action

$$S_E = \int d^4x \left[\frac{1}{2}(\partial\phi)^2 + U(\phi)\right], \tag{5.4}$$

where U is a potential function with a false vacuum, such as the one shown in the left plot of Fig. 5.1. The required matrix element can be computed using

$$\langle\phi_+| \exp(-H\tau/\hbar)|\phi_+\rangle = \int [\mathscr{D}\phi] \exp(-S_E[\phi]/\hbar), \tag{5.5}$$

where the path integral on the right hand side is over field configurations such that $\phi(\pm\tau/2) = \phi_+$. In the semi-classical limit $\hbar \to 0$, the dominant contributions to the path integral come from the vicinity of stationary points of the action (via the method of steepest descent - see, e.g., Ref. [318]). In our case, there is a minimum of the action that corresponds to the trivial field configuration that just sits at ϕ_+. It is easy to see that such "motion" does not contribute to the decay rate, since the matrix element is real. Thus, we should look for the leading *imaginary* contribution to the path integral. There is another solution to the classical equation of motion (EOM), called the *bounce*, that is a saddle point of the of the action, which, as we will

[1] The more correct statement of the semi-classical regime is the limit of the *dimensionless* quantity $S/\hbar \to \infty$, where S is the action.

show, gives the desired imaginary part. The idea is to compute the path integral in Eq. (5.5) by expanding the action around this saddle point solution to quadratic order and performing the Gaussian integral. The fact that $\bar{\phi}$ is a saddle configuration means that the operator

$$\frac{\delta^2 S_E}{\delta\phi(x)\delta\phi(y)} = \delta^4(x-y)\left(-\partial^2 + \frac{\delta^2 U}{\delta\phi^2}(\bar{\phi})\right). \tag{5.6}$$

has a negative eigenvalue, i.e., it is not positive definite. As we will emphasize, this is the key feature that generates an imaginary part in E_+.

The bounce $\bar{\phi}$ satisfies the equation of motion

$$\frac{\delta S_E}{\delta\phi} = 0 \;\Rightarrow\; \partial^2\phi = U'(\phi). \tag{5.7}$$

Note the "wrong" sign of the potential gradient, which is due to the fact that we work in Euclidean space. The boundary conditions are

$$\lim_{\tau\to\pm\infty}\phi(\tau,\mathbf{x}) = \phi_+. \tag{5.8}$$

Moreover, for the action to remain finite, the spacial derivatives of ϕ must also vanish at infinity, so, by continuity, we must have

$$\lim_{|\mathbf{x}|\to\infty}\phi(\tau,\mathbf{x}) = \phi_+. \tag{5.9}$$

A theorem due to Coleman, Glaser and Martin [317, 319] states that solutions that are $O(4)$-symmetric have smaller actions than non-symmetric solutions. Here $O(4)$ is just the Euclidean version of the Lorentz group, $O(1,3)$. This means that we can look for solutions that are only a function of the $O(4)$ invariant variable $\rho = (x_\mu x^\mu)^{1/2} = (\tau^2 + \mathbf{x}^2)^{1/2}$. Using the hyperspherical coordinate expression for the four-dimensional Laplacian (and neglecting the angular part), the EOM reduces to

$$\frac{d^2\phi}{d\rho^2} + \frac{3}{\rho}\frac{d\phi}{d\rho} = U'(\phi). \tag{5.10}$$

This has the form of the equation of motion for a particle moving in the *inverted* potential $-U$, subject to a friction force with a time-dependent coefficient $3/\rho$. This observation is useful for understanding the qualitative behaviour of the solutions. Using the definition of ρ, the boundary conditions for an $O(4)$-symmetric solution collapse into a single requirement

$$\lim_{\rho\to\infty}\phi(\rho) = \phi_+. \tag{5.11}$$

Using the particle picture we can discuss the possible solutions. First, we have the trivial solution where the particle just sits at ϕ_+. As mentioned above, this does not contribute to the decay rate. We also have the bounce solution, where the particle starts at ϕ_+ at early times $\tau \to -\infty$ (corresponding to $\rho \to \infty$) rolls off the maximum at ϕ_+, bounces off the potential wall at some finite time, say $\rho = 0$ and position ϕ_* and then returns and comes to rest back at ϕ_+ at

$\tau \to +\infty$ (also corresponding to $\rho \to \infty$).[2] This motion and the inverted potential are shown schematically in the right plot of Fig. 5.1. Therefore to solve for the bounce, we need to find $\phi(\rho = 0) = \phi_*$ such that $\lim_{\rho\to\infty} \phi(\rho) = \phi_+$. This makes the solution of Eq. (5.10) non-trivial, since one of the boundary conditions is unknown. Numerical approaches to this problem are discussed in Sec. 5.4.

With the classical solution in hand, we can expand the action in the path integral of Eq. (5.5) around $\bar{\phi}$:

$$S_E[\phi] = S_E[\bar{\phi}] + \frac{1}{2}\int d^4x d^4y \phi(x) \frac{\delta^2 S_E}{\delta\phi(x)\delta\phi(y)}(\bar{\phi})\phi(y) + \ldots, \tag{5.12}$$

where ϕ represents quantum fluctuations around $\bar{\phi}$ and the ellipsis stands for higher order terms in the expansion of S_E. Using this expansion and Eqs. (5.2, 5.3, 5.5) we can see that the resulting decay rate per unit volume has the form

$$\Gamma/V = A\exp(-B/\hbar), \tag{5.13}$$

where $B = S_E[\bar{\phi}]$ is the Euclidean action evaluated on the classical bounce solution $\bar{\phi}$ and the factor of volume arises from integrating over possible bounce locations [317]. The pre-exponential factor is obtained from the functional Gaussian integral using the second term in Eq. (5.12). It is very difficult to compute because it involves determinants of the differential operator of Eq. (5.6) [320, 321]. Therefore, it is usually estimated on dimensional grounds [322]. For example, for electroweak scale parameters, we will take

$$[A] = M^4 \;\Rightarrow A = (100\ \text{GeV})^4\ . \tag{5.14}$$

In any case, the controlling exponential factor depends on B only. Note that the determinants that appear in A are precisely where the aforementioned imaginary part of the matrix element enters the calculation. Here an analogy with a matrix integral is useful:

$$\int_{-\infty}^{+\infty} \exp\left(-\frac{1}{2}x_i S_{ij} x_j\right) d^n x = \frac{(2\pi)^{n/2}}{\sqrt{\det S}}. \tag{5.15}$$

If the quadratic form S_{ij} is not positive definite, it has a negative eigenvalue, which means that the right hand side can be imaginary. In this case the integral must be defined through analytic continuation. Translating this to field theory, if the operator of Eq. (5.6) has a negative eigenmode, the Gaussian integral will have an imaginary part.[3]

Above we have outlined the computation of the false vacuum decay rate at zero temperature.

[2] The time at the turn-around is a free parameter - this just means that we can translate the solution in space and time to obtain another solution with the same action. This has important consequences for the computation of the path integral.

[3] This depends on how many negative modes there are. It is assumed that there is only one. This has been shown to be the case in a wide range of physical theories [323].

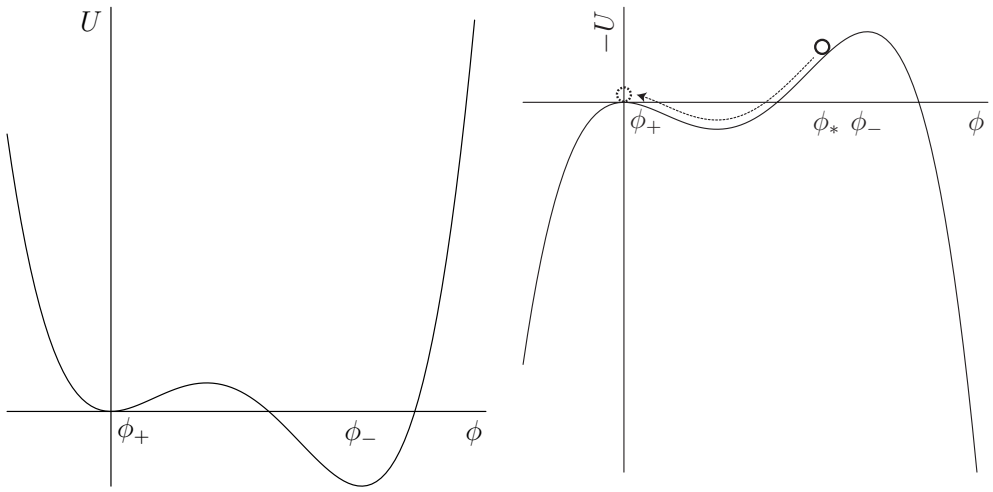

Figure 5.1: (Left) A typical potential with a false vacuum at ϕ_+. (Right) The particle motion interpretation of the bounce equation of motion.

We have ignored many technical details, namely the treatment of the zero mode associated with the translation of the center of the bounce (which we took to be at $\rho = 0$) as well as the computation of the pre-exponential factor. More careful considerations can be found in the original literature (e.g., Refs. [315, 316]), as well as in pedagogical reviews, Refs. [317, 324–326]. Computation of the determinantal prefactors is discussed in Ref. [320, 321]. The $O(4)$/Lorentz invariance of bubbles is considered in [327].

5.3 Tunnelling at Finite Temperature

The early Universe at finite temperature can be described as a closed system in approximate local thermodynamic equilibrium [40]. Thermodynamic properties of this system are then described by the canonical ensemble with the partition function Z

$$Z = \mathrm{Tr} e^{-\beta H} = \sum_a \langle \phi_a | e^{-\beta H} | \phi_a \rangle, \tag{5.16}$$

where $\beta = 1/T$, H is the Hamiltonian and the trace is over a complete set of states $\{|\phi_a\rangle\}$ [328]. This is reminiscent of the amplitude in Eq. (5.5). In fact, the partition function can be written as a path integral:

$$Z = \int \mathscr{D}\phi \exp\left(- \int_0^\beta d\tau \int d^3x \mathscr{L}_E \right), \tag{5.17}$$

where $\mathscr{L}_E$ is the Euclidean (i.e., imaginary time) Lagrangian corresponding to H. The boundary conditions on the fields ϕ follow from Eq. (5.16): we must have $\phi(0, \mathbf{x}) = \phi(\beta, \mathbf{x})$, i.e., the

path integral is over field configurations *periodic* in β.[4] This is completely analogous to the $T = 0$ case, but with a compact Euclidean time interval $\tau \in [0, \beta]$ and periodic (anti-periodic) boundary conditions for the bosonic (fermionic) fields in the theory.

The various phases of the theory at a given temperature T are determined by the minima of the free energy F

$$F = -T \ln Z = E - TS, \tag{5.18}$$

where E and S are the average energy and entropy of the system, respectively. If a phase of lower free energy exists, the system will undergo a transition to that state. In the presence of a barrier between the two phases, this will occur through thermal tunnelling, which was first treated by Affleck and Linde [329, 330]. As before, the false vacuum decay rate can be extracted from the the imaginary part of F via Eq. (5.3) (with $E_+ \to F$).[5] As in the $T = 0$ case, the leading contribution to ImF can be obtained using the semi-classical approximation. It is typically assumed that finite-T bounce solution does not depend on τ and is therefore only $O(3)$ symmetric, that is $\bar{\phi} = \bar{\phi}(r = |\mathbf{x}|)$ [330, 332]. See Ref. [330] for exceptions to this latter assumption. With these caveats in mind, the finite temperature bounce action can be written as

$$S_E[\phi] = S_3/T = \frac{1}{T} \int d^3x \left(\frac{1}{2} (\partial\phi)^2 + U(\phi) \right), \tag{5.19}$$

from which the bounce EOM is found to be

$$\frac{d^2\phi}{dr^2} + \frac{2}{r} \frac{d\phi}{dr} = U'(\phi), \tag{5.20}$$

with boundary conditions given by Eq. (5.11) (with the replacement $\rho \to r$). Formally the only difference between Eq. (5.20) and the $T = 0$ result, Eq. (5.10), is the coefficient of the $\dot{\phi}$ "friction" term. The resulting tunnelling probability per unit volume again has exponential form [332]

$$\Gamma/V = A(T) \exp(-S_3[\bar{\phi}]/T), \tag{5.21}$$

where, as before $A(T)$, is usually estimated using dimensional analysis to be of order $\mathcal{O}(T^4)$ [332].

[4] The corresponding integral for fermionic fields is anti-periodic in β.

[5] There are important subtleties related to the convexity of F and the equivalent quantity at $T = 0$, the effective action. See Ref. [331] for a pedagogical description of these issues.

5.4 Numerical Methods

In Sections 5.2 and 5.3 we saw that the evaluation of tunnelling rates requires the solution of the system of ordinary differential equations

$$\frac{d^2\boldsymbol{\phi}}{d\rho^2} + \frac{\alpha - 1}{\rho}\frac{d\boldsymbol{\phi}}{d\rho} = \nabla U(\boldsymbol{\phi}), \tag{5.22}$$

subject to the boundary conditions

$$\lim_{\rho\to\infty} \boldsymbol{\phi}(\rho) = \boldsymbol{\phi}_+, \quad \frac{d\boldsymbol{\phi}}{d\rho}(\rho = 0) = 0 \tag{5.23}$$

where α is the dimension ($\alpha = 3,\ 4$ for finite and zero temperature tunnelling, respectively). In writing Eqs. (5.22) and (5.23) we have extended the single scalar case to multiple field directions, where $\boldsymbol{\phi}$ is a vector of all relevant scalar fields and $\boldsymbol{\phi}_+$ is the location of the false vacuum. The second boundary condition (BC) ensures that the solution is finite when $\rho \to 0$. This BC is very weak, since it does not fully determine the behaviour at $\rho = 0$. In particular, the bounce point $\boldsymbol{\phi}(\rho = 0) \equiv \boldsymbol{\phi}_*$ must be found. When there is only one field, this can be done using the shooting method used in one-dimensional eigenvalue problems: one simply solves for a ϕ_* such that the first of Eq. (5.23) is satisfied to desired numerical precision, using standard one dimensional root finding algorithms (such as bisection). This becomes intractable with more than one field, since guessing just the right $\boldsymbol{\phi}_*$ in many dimensions is virtually impossible. Several methods of solving the multi-field bounce equation, Eq. (5.22), have been proposed, including Refs. [333–335]. Below we briefly describe two different classes of algorithms.

The algorithm of Ref. [334] (and Ref. [333] on which it is based) exploits the fact the Eq. (5.22) simplifies when $\alpha = 1$. In this limit, there is no damping term in the equation and it takes the form of a Newtonian EOM for a particle moving in an inverted potential $-U$ (see Sec. 5.2). The resulting motion can be obtained by *minimizing*[6] the discretized action

$$S_\alpha[\boldsymbol{\phi}(\rho)] = \Omega_\alpha \sum_{n=0}^{N-1} d\rho (nd\rho)^{\alpha-1} \left[\frac{1}{2}\left(\frac{\boldsymbol{\phi}_{n+1} - \boldsymbol{\phi}_n}{d\rho}\right)^2 + U(\boldsymbol{\phi}_n)\right] \tag{5.24}$$

subject to the constraints

$$U(\boldsymbol{\phi}_0) = U(\boldsymbol{\phi}_+),\ U(\boldsymbol{\phi}_n) \geq U(\boldsymbol{\phi}_+) \ \ \forall\ n < N, \tag{5.25}$$

and

$$\boldsymbol{\phi}_{N-1} = \boldsymbol{\phi}_+. \tag{5.26}$$

In the above equations $\Omega_\alpha = 2\pi^{\alpha/2}/\Gamma(\alpha/2)$, N is the number of lattice sites and $d\rho$ is the

[6] Note that this would not work for the true ($\alpha > 1$) bounce motion since it is a saddle point, not a minimum, of the action.

lattice spacing. The optimization is computationally costly with multiple field directions since one often needs $N \sim \mathcal{O}(100)$ per field direction.

The above procedure yields the $\alpha = 1$ solution that serves as an estimate $\boldsymbol{\phi}_e$ of the true bounce point $\boldsymbol{\phi}_*$. In the second part of the algorithm, deformation from $\alpha = 1$ to a different α is performed in small steps. If the solution does not change much from α to $\alpha + d\alpha$, then the right hand side of Eq. (5.22) can be linearized and the resulting equation discretized and solved using standard numerical linear algebra methods.

The alternative method used in Ref. [335] does not rely on discretization. Instead, the strategy is to make a guess for the tunnelling path $\boldsymbol{\phi}(s)$ parametrized by a arbitrary "time" s. For fixed $\boldsymbol{\phi}(s)$ this reduces the problem to a single differential equation for $s(\rho)$, which can be solved using the shooting method. The initial path $\boldsymbol{\phi}(s)$ is iteratively refined to find the true bounce $\boldsymbol{\phi}(s(\rho))$; the optimal choice of $\boldsymbol{\phi}(s)$ *minimizes* the action (see Appendix A). More quantitatively, we can rewrite Eq. (5.22) as

$$\frac{d^2\boldsymbol{\phi}}{ds^2}\left(\frac{ds}{d\rho}\right)^2 + \left[\frac{d^2 s}{d\rho^2} + \frac{\alpha - 1}{\rho}\frac{ds}{d\rho}\right]\frac{d\boldsymbol{\phi}}{ds} = \nabla U(\boldsymbol{\phi}), \tag{5.27}$$

by applying the chain rule. Since the path parametrization is arbitrary, let us demand that it has unit speed:

$$\left|\frac{d\boldsymbol{\phi}}{ds}\right| = 1. \tag{5.28}$$

We can then use this to show that

$$\frac{d^2\boldsymbol{\phi}}{ds^2} \cdot \frac{d\boldsymbol{\phi}}{ds} = 0. \tag{5.29}$$

Taking the inner products of the EOM with $d\boldsymbol{\phi}/ds$ we get

$$\frac{d^2 s}{d\rho^2} + \frac{\alpha - 1}{\rho}\frac{ds}{d\rho} = \frac{dU}{ds}. \tag{5.30}$$

This is the equation of motion along the parametric path. It has the same form as the equation of a bounce for a single field variable and can be easily solved using the shooting method. There is another equation contained in the EOM associated with deformations of $\boldsymbol{\phi}(s)$, which is obtained by subtracting Eq. (5.30) from Eq. (5.27):

$$\frac{d^2\boldsymbol{\phi}}{ds^2}\left(\frac{ds}{d\rho}\right)^2 = \left(\nabla - \frac{d\boldsymbol{\phi}}{ds}\frac{\partial}{\partial s}\right)U. \tag{5.31}$$

This equation is used to deform the path $\boldsymbol{\phi}(s)$ toward the true bounce. This algorithm has been implemented in the public code `CosmoTransitions` (CT) [335].

In Ch. 6 we make extensive use of CT, so we validated its results by implementing in `C++`

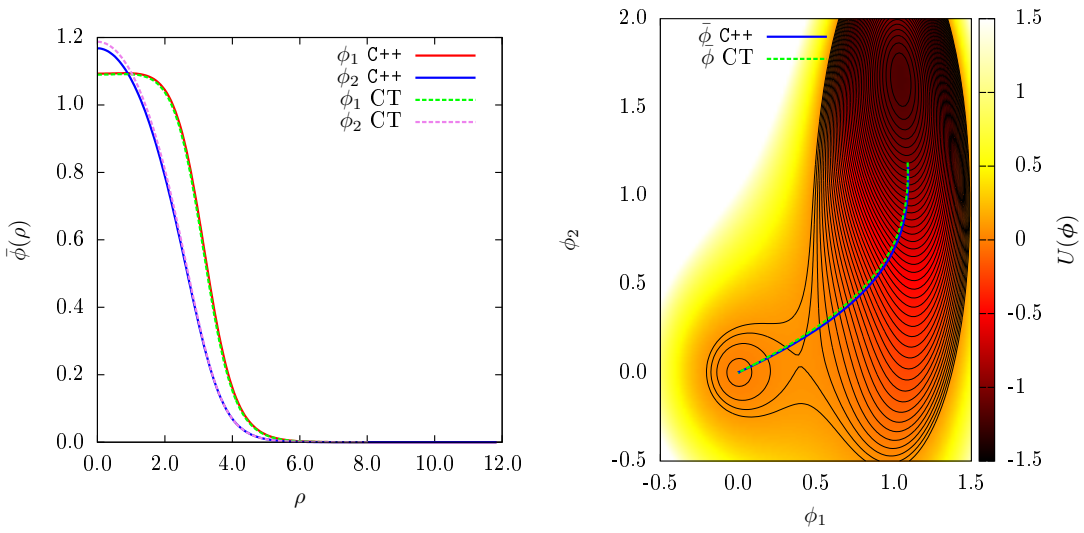

Figure 5.2: The bounce solution for a two dimensional potential evaluated using two different methods. The left plot shows the field profiles as a function of the coordinate ρ, while the right plot shows the tunnelling path in the $\phi_1 - \phi_2$ plane.

the algorithm of Ref. [334] described above. In Fig. 5.2 we show a sample bounce configuration (computed using these different methods) for a toy two dimensional potential

$$U(\boldsymbol{\phi}) = \left(\phi_1^2 + \phi_2^2\right)\left(1.8(\phi_1 - 1)^2 + 0.2(\phi_2 - 1)^2 - \delta\right), \tag{5.32}$$

with $\delta = 0.4$. This potential is used as a test case in Ref. [335]. With this value of δ the true and false minima are at $\boldsymbol{\phi} = (1.04637, 1.66349)$ and $(0, 0)$, respectively. The left plot shows the evolution of each field component with the parameter ρ. The right plot shows the trajectory in field space, which interpolates between the two vacua. We found that the resulting bounce actions differ by less than 10% between the two methods.

Chapter 6

Charge and Colour Breaking in the MSSM

6.1 Introduction

Supersymmetry predicts a scalar superpartner for every fermion in the Standard Model (SM) [80]. While these scalar fields help to protect the scale of electroweak symmetry breaking from large quantum corrections (see Sections 1.3.1 and 2.3), they can also come into conflict with existing experimental bounds. This tension is greatest for the scalar top quarks (stops). On the one hand, the stops must be heavy enough to have avoided detection in collider searches. On the other hand, smaller stop masses maximize the quantum protection of the electroweak scale [336, 337].

In the minimal supersymmetric extension of the Standard Model (MSSM), there is an additional constraint on the stops implied by the discovery of a Higgs boson with mass near $m_h = 125$ GeV [12, 13]. Specifically, the stops must be heavy enough to push the (SM-like) Higgs mass up to the observed value [338, 339]. After electroweak symmetry breaking, the two gauge-eigenstate stops $\tilde{t}_L$ and $\tilde{t}_R$ mix to form two mass eigenstates, $\tilde{t}_1$ and $\tilde{t}_2$ ($m_{\tilde{t}_1} \leq m_{\tilde{t}_2}$). The corresponding mass-squared matrix in the $(\tilde{t}_L\ \tilde{t}_R)^T$ basis is [80]

$$\mathcal{M}^2_{\tilde{t}} = \begin{pmatrix} m^2_{Q_3} + m_t^2 + D_L & m_t X_t \\ m_t X_t^* & m^2_{U_3} + m_t^2 + D_R \end{pmatrix} , \tag{6.1}$$

where $X_t = (A_t^* - \mu \cot\beta)$ is the stop mixing parameter, $m^2_{Q_3,U_3}$ and A_t are soft supersymmetry-breaking parameters, μ is the Higgsino mass parameter, $\tan\beta = v_u/v_d$ is the ratio of the two Higgs expectation values, and $D_{L,R} = (t^3 - Qs^2_W)m^2_Z \cos 2\beta$ are the D-term contributions. The stops generate the most important quantum corrections to the mass of the SM-like Higgs state h^0 in the MSSM. Decoupling the heavier Higgs bosons ($m_A \gg m_Z$), the h^0 mass at one-loop

order is [340–342]

$$m_h^2 \simeq m_Z^2 \cos^2 2\beta + \frac{3}{4\pi^2}\frac{m_t^4}{v^2}\left[\ln\left(\frac{M_S^2}{m_t^2}\right) + \frac{X_t^2}{M_S^2}\left(1 - \frac{X_t^2}{12M_S^2}\right)\right] \ , \tag{6.2}$$

where $M_S = (m_{Q_3} m_{U_3})^{1/2}$. The first term is the tree-level contribution and is bounded above by m_Z^2. The second term in Eq. (6.2) is the sum of one-loop top and stop contributions. This correction is essential to raising the mass of the SM-like MSSM Higgs mass to the observed value.

The contribution of the stops to the h^0 mass depends on both the mass eigenvalues and the mixing angle. Without left-right stop mixing, at least one of the stops must be very heavy, $m_{\tilde{t}} \gtrsim 5$ TeV, to obtain $m_h \simeq 125$ GeV [343]. This leads to a significant tension with the naturalness of the weak scale [336, 337]. This tension can be reduced by stop mixing, with the largest effect seen in the vicinity of the *maximal mixing* scenario of $X_t \simeq \pm\sqrt{6}M_S$ [344]. This is shown in Fig. 6.1, where the maximal mixing scenario corresponds to the maxima of m_h as a function of X_t/M_S. However, such large values of X_t/M_S require a large value of A_t (small μ is needed for naturalness [345]) which can induce new vacua in the scalar field space where the stops develop vacuum expectation values (vevs). The lifetime for tunnelling to these charge- and colour-breaking (CCB) vacua must be longer than the age of the Universe to be consistent with our existence.

The existence of CCB stop vacua in the MSSM has been studied extensively [7, 346–354]. Under the assumption of $SU(3)_C \times SU(2)_L \times U(1)_Y$ D-flatness, an approximate analytic condition for the non-existence of a CCB stop vacuum is [348, 349]

$$A_t^2 < 3(m_{Q_3}^2 + m_{U_3}^2 + m_2^2) \ , \tag{6.3}$$

where $m_2^2 = m_{H_u}^2 + |\mu|^2$ and $m_{H_u}^2$ is the H_u soft mass squared parameter. Generalizations to less restrictive field configurations [349, 352–354] and studies of the thermal evolution of such vacua [355–357] have been performed as well. Relaxing the requirement of absolute stability of our electroweak vacuum and demanding only that the tunnelling rate to the CCB vacua is sufficiently slow provides a weaker bound. The tunnelling rate was computed in Ref. [7], where the net requirement for metastability was expressed in terms of the empirical relation

$$A_t^2 + 3\mu^2 \lesssim 7.5(m_{Q_3}^2 + m_{U_3}^2) \ . \tag{6.4}$$

In this chapter we attempt to update and clarify the stability and metastability bounds on the parameters in the stop sector of the MSSM. We expand upon the previous body of work by investigating the detailed dependence of the limits on the underlying set of stop parameters. Furthermore, we relate our revised limits to recent Higgs and stop search results at the LHC.

The outline of this chapter is as follows. In Sec. 6.2 we specify the ranges of MSSM parameters and field configurations to be considered. Next, in Sec. 6.3 we investigate the necessary

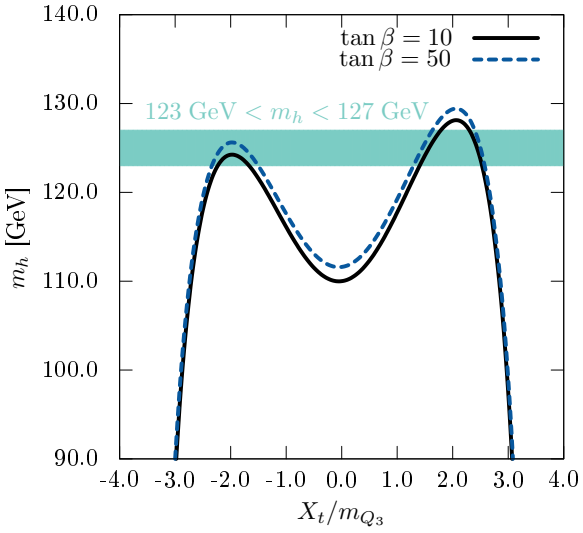

Figure 6.1: The two loop SM-like MSSM Higgs mass as a function of X_t/m_{Q_3} computed using `FeynHiggs` as described in Sec. 6.4. The shaded teal region corresponds to 123 GeV $< m_h <$ 127 GeV, a range that encompasses the approximate theoretical uncertainty in m_h around the measured value $m_h \approx 125\,\text{GeV}$ [6]. Here we have taken $m_A = 1000\,\text{GeV}$, $m_{Q_3} = m_{U_3} = 750\,\text{GeV}$ and $\mu = 250\,\text{GeV}$. These parameters are discussed in Sec. 6.2.

conditions on the underlying stop and Higgs parameters for the scalar potential to be stable or safely metastable. We then compare the constraints from metastability to existing limits on the MSSM stop parameters from the Higgs mass in Sec. 6.4, as well as to direct and indirect stop searches in Sec. 6.5. Finally, we conclude in Sec. 6.6. Some technical details related to our tunnelling calculation are expanded upon in Appendices A and B. This chapter and the aforementioned Appendices are based on work published in Ref. [3] in collaboration with David Morrissey.

6.2 Parameters and Potentials

In our study, we consider only variations in the scalar fields derived from the superfields $Q_3 \to (\tilde{t}_L, \tilde{b}_L)^T$, $U_3^c \to \tilde{t}_R^*$, $H_u \to (H_u^+, H_u^0)$, and $H_d \to (H_d^0, H_d^-)$. To make this multi-dimensional space more tractable, we further restrict ourselves to configurations where $\tilde{b}_L = H_u^+ = H_d^- = 0$ and the remaining fields (and MSSM parameters) are real-valued. Previous studies of CCB vacua in the stop direction suggest that this condition is not overly restrictive [349].

6.2.1 Scalar Potential

Under these assumptions, the tree-level scalar potential becomes

$$V_{\text{tree}} = V_2 + V_3 + V_4 \tag{6.5}$$

where

$$\begin{aligned} V_2 &= (m_{H_u}^2 + |\mu|^2)(H_u^0)^2 + (m_{H_d}^2 + |\mu|^2)(H_d^0)^2 - 2bH_u^0 H_d^0 + m_{Q_3}^2 \tilde{t}_L^2 + m_{U_3}^2 \tilde{t}_R^2 & (6.6)\\ V_3 &= 2y_t(A_t H_u^0 - \mu\, H_d^0)\, \tilde{t}_L \tilde{t}_R & (6.7)\\ V_4 &= y_t^2 \left[\tilde{t}_L^2 \tilde{t}_R^2 + \tilde{t}_L^2 (H_u^0)^2 + \tilde{t}_R^2 (H_u^0)^2\right] + V_D\ , & (6.8) \end{aligned}$$

with

$$V_D = \frac{g'^2}{8}\left[(H_u^0)^2 - (H_d^0)^2 + \frac{1}{3}\tilde{t}_L^2 - \frac{4}{3}\tilde{t}_R^2\right]^2 + \frac{g^2}{8}\left[-(H_u^0)^2 + (H_d^0)^2 + \tilde{t}_L^2\right]^2 + \frac{g_3^2}{6}\left(\tilde{t}_L^2 - \tilde{t}_R^2\right)^2 \ . \tag{6.9}$$

In writing this form, we have implicitly assumed that the stops are aligned (or anti-aligned) in $SU(3)_C$ space, so that $\tilde{t}_L$ and $\tilde{t}_R$ may be regarded as the magnitudes of these colour vectors (up to a possible sign). It is not hard to show that such an alignment maximizes the likelihood of forming a CCB minimum.

In our analysis of metastability, we use the tree-level potential of Eq. (6.5) with the parameters in it taken to be their $\overline{\text{DR}}$ running values defined at the scale M_S. However, we also compare our metastability results to a full two-loop calculation of the Higgs boson mass. While this is a mismatch of orders, we do not expect that including higher order corrections will drastically change our metastability results for two reasons. First and most importantly, the formation of CCB vacua is driven by the trilinear stop coupling A_t, which is already present in the tree-level potential. Second, when a CCB vacuum exists, the large stop Yukawa coupling $y_t \sim 1$ implies that it typically occurs at field values on the order of M_S [349]. Thus we do not expect large logarithmic corrections from higher orders.

Including higher-order corrections in the tunnelling analysis is also challenging for a number of technical reasons. Turning on multiple scalar fields, the mass matrices entering the Coleman-Weinberg corrections to the effective potential become very complicated and multi-dimensional [356]. These corrections can be absorbed into running couplings by an appropriate field-dependent choice of the renormalization scale [347]. In doing so, however, the otherwise field-independent corrections to the vacuum energy (which are not included in the Coleman-Weinberg potential) develop a field dependence. These vacuum energy corrections must be included to ensure the net scale independence of the effective potential [358, 359]. Beyond the effective potential, kinetic corrections (i.e., derivative terms in the effective action) will also be relevant for the non-static tunnelling configurations to be studied. Furthermore, the effective potential and the kinetic corrections are both gauge dependent [360, 361]. The gauge depen-

Parameter	Values
$\lvert m_{Q_3}\rvert$	$[300, 3000]$ GeV
$m^2_{Q_3}/m^2_{U_3}$	$0.3\,, 1,\ 3$
X_t	$[-10, 10] \times \lvert m_{Q_3}\rvert$
μ	150, 300, 500 GeV
m_A	1000 GeV
$\tan\beta$	5, 10, 30

Table 6.1: MSSM scalar potential parameter scan ranges. The values of other parameters to be considered are described in the text.

dence of the effective potential can be shown to cancel on its own for static points [362, 363]. However, to ensure the gauge invariance of the non-static tunnelling configuration and thus the decay rate, kinetic corrections must be included as well [364, 365]. For these various reasons, we defer an investigation of higher-order corrections to metastability to a future work.

6.2.2 Parameter Ranges

Without loss of generality, we may redefine H_u^0 and H_d^0 such that b and H_u^0 are both positive. This ensures that the unique SM-like vacuum (with $\tilde{t}_L = \tilde{t}_R = 0$) has $\tan\beta = \langle H_u^0\rangle/\langle H_d^0\rangle > 0$, and thus $\langle H_d^0\rangle > 0$ as well. By demanding that a local SM-like vacuum exists, b, $m^2_{H_u}$, and $m^2_{H_d}$ can be exchanged in favour of $v = \sqrt{\langle H_u^0\rangle^2 + \langle H_u^0\rangle^2}$, $\tan\beta$, and the pseudoscalar mass m_A:

$$b = \frac{1}{2} m_A^2 \sin(2\beta) \tag{6.10}$$

$$m^2_{H_u} = -\mu^2 + m_A^2 \cos^2\beta + \frac{1}{2} m_Z^2 \cos(2\beta) \tag{6.11}$$

$$m^2_{H_d} = -\mu^2 + m_A^2 \sin^2\beta - \frac{1}{2} m_Z^2 \cos(2\beta)\ . \tag{6.12}$$

Moving out in the stop directions, we may also redefine $\tilde{t}_L$ and $\tilde{t}_R$ such that $\tilde{t}_L$ is positive.

The parameter ranges we investigate are motivated by existing bounds on the MSSM and naturalness. We typically scan over $(m^2_{Q_3}, X_t)$ while holding other potential parameters fixed. We also consider discrete variations in $m^2_{U_3}/m^2_{Q_3}$, $\tan\beta$, μ, and m_A. The corresponding ranges are specified in Table 6.1. For the remaining supersymmetry breaking parameters, we choose $m_{\tilde{f}} = 2$ TeV and $A_f = 0$ for all sfermions other than the stops, as well as $M_1 = 300$ GeV, $M_2 = 600$ GeV, and $M_3 = 2$ TeV. To interface with the Higgs mass calculation, we take these to be running $\overline{\text{DR}}$ values defined at the input scale $M_S = (m_{Q_3} m_{U_3})^{1/2}$. We also use running $\overline{\text{DR}}$ values of y_t, g', g, and g_3 at scale M_S when evaluating the potential.

6.3 Limits from Vacuum Stability

A necessary condition on the viability of any realization of the MSSM is that the lifetime of the SM-like electroweak vacuum at zero temperature be longer than the age of the Universe. This

will certainly be the case if the electroweak vacuum is a global minimum, and it can also be true in the presence of a deeper CCB minimum provided the tunnelling rate is sufficiently small. More stringent conditions can be derived for specific cosmological histories [356]. While colour-broken phases in the early Universe can have interesting cosmological implications, such as for baryogenesis [355–357], we focus exclusively on the history-independent $T = 0$ metastability condition.

6.3.1 Existence of a CCB Vacuum

The first step in a metastability analysis is to determine whether a CCB minimum exists. Such minima are induced by a competition between the trilinear A and quartic couplings λ in the potential, and one generally expects $\langle\phi\rangle_{\rm CCB} \sim A/\lambda$ [349]. We use this expectation as a starting point for a numerical minimization of the potential, Eq. (6.5), employing the minimization routine `Minuit2` [366]. For every MSSM model, we choose the starting point to be $\langle\phi_i\rangle_{\rm CCB} = \xi_i A_t$, where $\xi_i \in [-1, 1]$ is chosen randomly. The global CCB vacua we find are generally unique, up to our restrictions of H_u^0, $\tilde{t}_L \geq 0$. If no global CCB minimum is found, the minimization is repeated several times with new ξ_i values. If the global minimum turns out to be the EW vacuum, the model is considered to be Standard Model-like (SML).

6.3.2 Computing the Tunnelling Rate

When a deeper CCB vacuum is found, the decay rate of the SML vacuum is computed using the Callan-Coleman formalism [315, 316], where the path integral is evaluated in the semi-classical approximation as described in Ch. 5. The decay rate per unit volume is given by

$$\Gamma/V = C \exp(-B/\hbar) \ , \tag{6.13}$$

where $B = S_E[\bar{\boldsymbol{\phi}}]$ is the Euclidean action evaluated on the bounce solution $\bar{\boldsymbol{\phi}}$. The bounce is $O(4)$-symmetric, depending only on $\rho = \sqrt{t^2 + \mathbf{x}^2}$, and satisfies the classical equations of motion subject to the boundary conditions $\partial_\rho \bar{\boldsymbol{\phi}}|_{\rho=0} = 0$ and $\lim_{\rho\to\infty} \bar{\boldsymbol{\phi}} = \boldsymbol{\phi}_+$, where $\boldsymbol{\phi}_+$ is the false-vacuum field configuration. The pre-exponential factor C is obtained from fluctuations around the classical bounce solution. It is notoriously difficult to compute [320, 321], and is therefore usually estimated on dimensional grounds [322]. We use

$$[C] = M^4 \ \Rightarrow C = (100 \ \text{GeV})^4 \ . \tag{6.14}$$

The metastability of the SM-like vacuum then requires

$$\Gamma^{-1} \gtrsim t_0 \ \Rightarrow \ B/\hbar \gtrsim 400, \tag{6.15}$$

where $t_0 = 13.8$ Gyr is the age of the Universe. Our choice of scale for C corresponds to the SM-like vacuum, and provides a reasonable lower bound on C. Larger values of C would

increase the decay rate, implying that the limits we derive are conservative.

Finding the bounce $\bar{\phi}$ is straightforward in one field dimension, since the equation of motion can be solved by the shooting method. This method reduces the problem to a root-finding task for the correct boundary conditions and relies on the unique topology of the one-dimensional field space. Unfortunately, this strategy becomes intractable with more than one field dimension. Several methods of solving the multi-field bounce equation of motion have been proposed [333, 334, 356, 367]. Some of these are described in Sec. 5.4. In the present analysis we use the public code `CosmoTransitions` [335].[1]

`CosmoTransitions` (CT) implements a path deformation method similar to the that suggested in Ref. [356]. Once a pair of local minima are specified, CT fixes a one-dimensional path between them in the field space. Along this path, the one-dimensional bounce solution can be computed using the shooting method. In Appendix A, we show that the action computed from the bounce solution for any such fixed path is necessarily greater than or equal to the unconstrained bounce action. The fixed path in field space is then deformed by minimizing a set of perpendicular gradient terms to be closer to the true bounce path through the field space. This procedure is iterated until convergence is reached. We exclude any points where CT fails to converge.

This path deformation approach has several advantages over other methods. Here, the bounce equation of motion is solved directly, while many other approaches involve minimization of a discretized action as part of the procedure. This is numerically costly, since one needs both a fine lattice spacing to evaluate derivatives accurately, and a large ρ domain to accommodate the boundary condition at infinity. Path deformation involves no discretization or large-scale minimization. As a result `CosmoTransitions` is quite fast for our four-field tunnelling problem.

We also cross check the CT results in two ways. First, we have compared CT to the discretized action methods of Refs. [333, 334] for a set of special cases, and we generally find agreement between these approaches as shown in Sec. 5.4. Second, we also compute the bounce action independently along the optimal path determined by CT, allowing us to estimate the numerical uncertainty on the bounce. Finally, let us emphasize once more that even if the path determined by CT is not the true tunnelling trajectory, our result in Appendix A implies that it still provides an upper bound on the bounce action, and thus a lower bound on the tunnelling rate.

We note that recently a new program, `Vevacious` [369], has been released that can also be used to study metastability in field theories with many scalar fields. While we do not use this code, we share some similarities with their approach in that we both employ Minuit for potential minimization and CT for tunnelling rates. Moreover, as mentioned above, we also carried out extensive independent checks of the tunnelling calculation.

[1] We modify the code slightly, replacing an instance of `scipy.optimize.fmin` by `scipy.optimize.fminbound` in the class `pathDeformation.fullTunneling`. This allows `CosmoTransitions` to better deal with very shallow vacua. The same modification has been used in Ref. [368] (see Footnote 1).

6.3.3 Results and Comparison

We begin by presenting our limits from metastability alone, without imposing any other constraints such as the Higgs mass requirement. This allows for a direct comparison with the results of Ref. [7]. In Fig. 6.2 we show a scan over X_t and $m_{Q_3}^2$ while keeping fixed $m_A = 1000$ GeV, $\tan\beta = 10$, $\mu = 300$ GeV, and $m_{U_3}^2/m_{Q_3}^2 = 1$. Every point shown is a model with a global CCB vacuum. The red points have a tunnelling action $B/\hbar < 400$, and are therefore unstable on cosmological time scales. The blue points have a metastable SM-like vacuum with $B/\hbar > 400$. Also shown in the figure is the analytic bound (green dashed line) of Eq. (6.3), and the empirical result (black dotted line) from Ref. [7] given in Eq. (6.4).

The shape of the regions shown in Fig. 6.2 can be understood simply. As expected, the existence of a CCB vacuum requires a large value of A_t/M_S. The cutoff at the upper-left diagonal edge corresponds to the absence of a CCB vacuum. Above and to the left of this boundary, the SML minimum is a global one and the EW vacuum can be absolutely stable. There is also a lack of points below a lower-right diagonal edge. Here, one of the physical stops becomes tachyonic, and the SML vacuum disappears altogether. At low values of A_t^2, we see that the CCB region is squeezed between the SML region (on the left) and the tachyonic stop region (on the right), giving rise to the cutoff seen in the lower left corner.

It is apparent from Fig. 6.2 that we find much more restrictive metastability bounds on the MSSM than the empirical relation of Eq. (6.4) from Ref. [7]. We also see that the analytic bound of Eq. (6.3) tends to underestimate the existence of CCB vacua, and that it accidentally lines up fairly well with the lower boundary of metastability. It is not clear why our results should be so much more restrictive than those found in Ref. [7], but we are confident that the path deformation method of CT (and our several cross-checks) gives a robust upper bound on the bounce action. We find qualitatively similar results for the other parameters ranges described in Table 6.1. The quantitative results for these ranges will be presented in more detail below in the context of the Higgs mass.

6.4 Implications for the MSSM Higgs Boson

As discussed in the Introduction, there is a significant tension in the MSSM between obtaining the observed Higgs boson mass and keeping the stops relatively light. This tension is reduced when the stops are strongly mixed. To obtain such mixing, large values of X_t are needed. We have just seen that large values of X_t can lead to dangerous CCB minima. In this section we compare the relative conditions imposed by each of these requirements.

To calculate the physical h^0 Higgs boson mass, we use `FeynHiggs 2.9.5` [370]. We also use this program together with `SuSpect 2.43` [371] to compute the mass spectrum of the MSSM superpartners. As inputs, we take $m_t^{\rm pole} = 173.1$ GeV and $\alpha_s(m_Z) = 0.118$ [58]. Our results are exhibited in terms of variations on the fiducial MSSM parameters $\tan\beta = 10$, $\mu = 300$ GeV, $m_A = 1000$ GeV, and $m_{U_3}^2 = m_{Q_3}^2$. The other MSSM parameters are taken as in Section 6.2.2.

In Fig. 6.3 we show points in the X_t-M_S plane (where $M_S = (m_{Q_3} m_{U_3})^{1/2}$) that produce

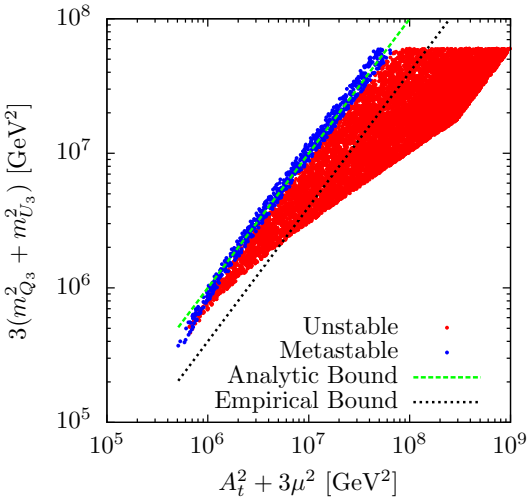

Figure 6.2: Limits from metastability and the existence of a local SM-like (SML) vacuum alone for $\tan\beta = 10$, $\mu = 300$ GeV, $m_A = 1000$ GeV, and $m_{U_3}^2 = m_{Q_3}^2$. All points shown have a global CCB minimum and a local SML minimum. The red points are dangerously unstable, while the blue points are consistent with metastability. The green dashed line is the analytic bound of Eq. (6.3) and the black dotted line corresponds to Eq. (6.4), the empirical bound from Ref. [7]. The values of the other MSSM parameters used here are described in the text.

a Higgs mass in the range 123 GeV $< m_h <$ 127 GeV. All other parameters are set to their fiducial values described above. The pink (blue) region are models with a global SML (CCB) vacuum. The red points are excluded by metastability. The dashed lines show the approximate CCB condition of Eq. (6.3), the empirical limit of Eq. (6.4), and our own attempt at an empirical limit on metastability to be discussed below. The requirement of metastability cuts off a significant portion of the allowed range at very large $|X_t|$. Also shown are contours of constant $m_{\tilde{t}_1}$, the lightest stop mass (grey dot-dashed lines).

In Fig. 6.4 we show the additional dependence of the Higgs mass and the metastability bounds on other relevant MSSM parameters. All parameters are set to their fiducial values except for those we vary one at a time. In the top row we show results for $\tan\beta = 5$ (30) on the left (right). Reducing $\tan\beta$ decreases the tree-level contribution to the MSSM Higgs mass, and so larger values of M_S are needed to raise m_h to the observed range. These larger values also lead to shallower CCB minima and lower tunnelling rates. Larger values of $\tan\beta$ do not appear to differ much from $\tan\beta = 10$.

In the middle row of Fig. 6.4 we show results for $\mu = 150$ (500) , GeV on the left (right). We do not see a large amount of variation in the exclusions from metastability, which is not surprising given that generally have $X_t \simeq A_t \gg \mu$. Setting $\mu = -300$ GeV also produces very similar results.

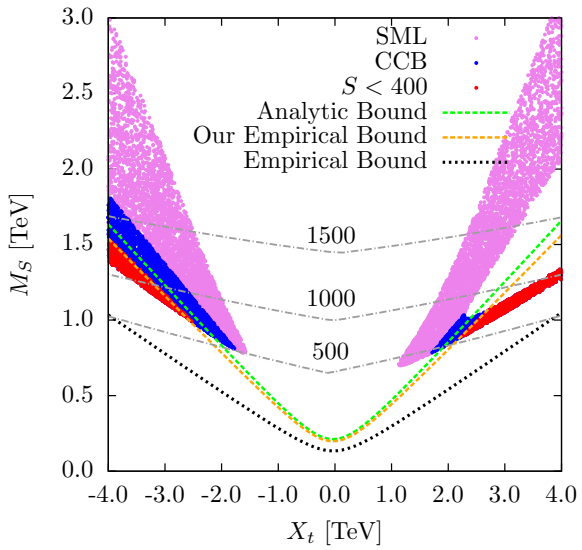

Figure 6.3: Metastability bounds relative to the MSSM Higgs mass. The coloured bands contain models for which 123 GeV $< m_h <$ 127 GeV. Pink models have an absolutely stable SML vacuum, blue points have a global CCB minimum, while red points are unstable on cosmological time scales. The green dashed line is the analytic bound of Eq. (6.3) and the black dotted line is Eq. (6.4). The orange dashed line is an approximate empirical bound discussed in Appendix B. The grey dot-dashed contours are lines of constant lightest stop mass (in GeV). MSSM parameters used here are described in the text.

In the bottom row of Fig. 6.4 we show the same metastability limits for $m_{U_3}^2/m_{Q_3}^2 = 0.3$ (3.0) on the left (right). For these unequal values, there is a tension between minimizing the quadratic terms in the potential and reducing the quartic terms through $SU(3)_C$ D-flatness. Unequal squark vevs also tend to reduce the effective trilinear term. Together, these effects reduce the metastability constraint somewhat, but do not eliminate it.

In summary, the constraint imposed by CCB metastability rules out a significant portion of the MSSM stop parameter space that can produce a Higgs mass near the observed value. The limits are strongest on the outer branches at large $|X_t|$. Varying other MSSM parameters within the restricted ranges we have considered does not drastically alter this result. By comparison, the empirical bound from Ref. [7] does not rule out any of the stop parameter space consistent with the Higgs mass.

As a synthesis of these results, we have attempted to obtain an improved empirical bound on stop-induced metastability. We find the approximate limit

$$A_t^2 \lesssim \left(3.4 + 0.5\frac{|1-r|}{1+r}\right) m_T^2 + 60\, m_2^2 \,, \tag{6.16}$$

where $m_T^2 = (m_{Q_3}^2 + m_{U_3}^2)$, $m_2^2 = (m_{H_u}^2 + \mu^2)$, and $r = m_{U_3}^2/m_{Q_3}^2$. Let us emphasize that this

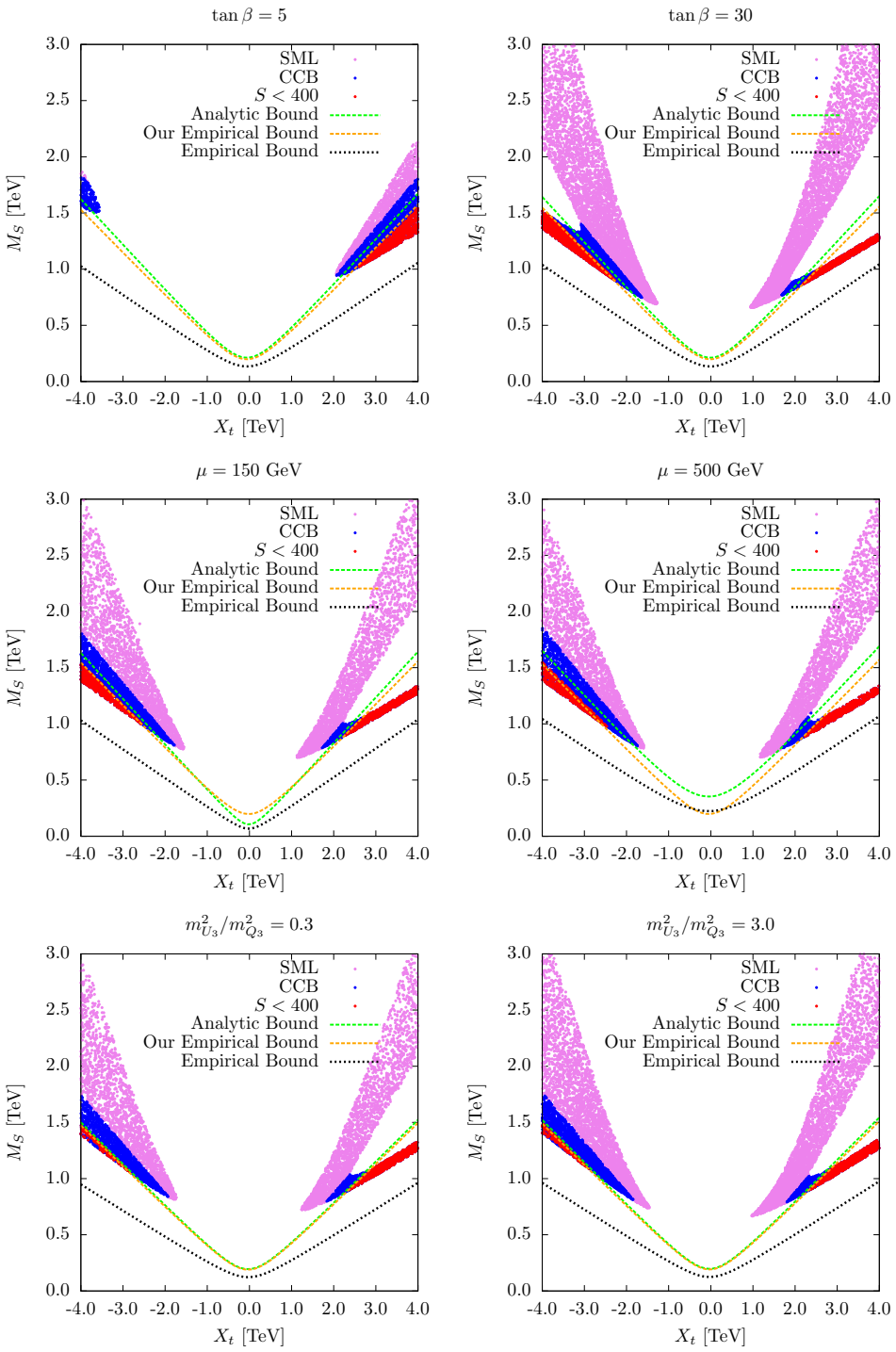

Figure 6.4: Metastability with the correct Higgs mass, $123 < m_h < 127$ GeV. The labelling is the same as in Fig. 6.3, and the relevant MSSM parameter parameters are varied one at a time as summarized in Table 6.1.

limit is very approximate and only applies to smaller values of μ, larger values of m_A, moderate $\tan\beta$, and r not too different from unity. Details on the derivation of this bound are given in

Appendix B.

6.5 Comparison to Other Stop Constraints

The metastability conditions we find exclude parameter regions with large stop mixing. This mixing can produce one relatively light stop mass eigenstate as well as a significant mass splitting between the members of the $\widetilde{Q}_3$ sfermion doublet. These features are constrained indirectly by electroweak and flavour measurements, as well as by direct searches for a light stop. In this section we compare these additional limits to the bounds from metastability.

6.5.1 Precision Electroweak and Flavour

The most important electroweak constraint on light stops comes from $\Delta\rho$, corresponding to the shift in the W mass relative to the Z. In the context of highly mixed stops motivated by the Higgs mass, this effect has been studied in Refs. [372, 373]. We have computed the shift $\Delta\rho$ due to stops and sbottoms using `SuSpect 2.43` [371], which applies the one-loop results contained in Refs. [374, 375]. With a Higgs mass of $m_h \simeq 125$ GeV, the preferred range is $\Delta\rho = (4.2 \pm 2.7) \times 10^{-4}$ [372].

Supersymmetry can also contribute to flavour-mixing. Assuming only super-CKM squark mixing (or even minimal flavour violation [376]), the most constraining flavour observable is frequently the branching ratio $\mathrm{BR}(B \to X_s\gamma)$. It receives contributions in the MSSM from stop-chargino and top-H^+ loops. These contributions tend to cancel each other such that the cancellation would be exact in the supersymmetric limit [377]. With supersymmetry breaking, the result depends on the stop masses and mixings, $\tan\beta$, μ, and the pseudoscalar mass m_A. Constraints on light stops from $\mathrm{BR}(B \to X_s\gamma)$ were considered recently in Refs. [373, 378]. The SM prediction is $\mathrm{BR}(B \to X_s\gamma) = (3.15 \pm 0.23) \times 10^{-4}$ [379], while a recent Heavy Flavour Averaging Group compilation of experimental results finds $\mathrm{BR}(B \to X_s\gamma) = (3.55 \pm 0.24 \pm 0.09) \times 10^{-4}$ [380]. We have investigated the limit from $\mathrm{BR}(B \to X_s\gamma)$ and other flavour observables using `SuperIso 3.3` [381] assuming only super-CKM flavour mixing.

In Fig. 6.5, we show the exclusions from flavour and electroweak bounds for model points with 123 GeV $< m_h <$ 127 GeV for $\tan\beta = 10$, and $m_A = 1000$ GeV, $\mu = 300$ GeV, and $m^2_{Q_3} = m^2_{U_3}$ in the $X_t - m_{Q_3}$ plane. We impose the generous 2σ constraints $\Delta\rho \in [-1.2, 9.4] \times 10^{-4}$ and $\mathrm{BR}(B \to X_s\gamma) \in [2.86, 4.24] \times 10^{-4}$ and show them together with the metastability constraint from the previous Section. The green points show the regions excluded by $\Delta\rho$ while the orange points show those excluded by $\mathrm{BR}(B \to X_s\gamma)$.

The exclusion due to $\Delta\rho$ can be understood in terms of the large stop mixing induced by X_t, which generates a significant splitting between the mass eigenstates derived from the $\widetilde{Q}_3 = (\tilde{t}_L, \tilde{b}_L)^T$ $SU(2)_L$ doublet. This constraint depends primarily on the stop parameters, and is mostly insensitive to variations in μ, m_A, and $\tan\beta$. While this bound overlaps significantly with the limit from metastability, there are regions where only one of the two constraints applies. The limits from $\Delta\rho$ are also weaker for $m^2_{Q_3} > m^2_{U_3}$.

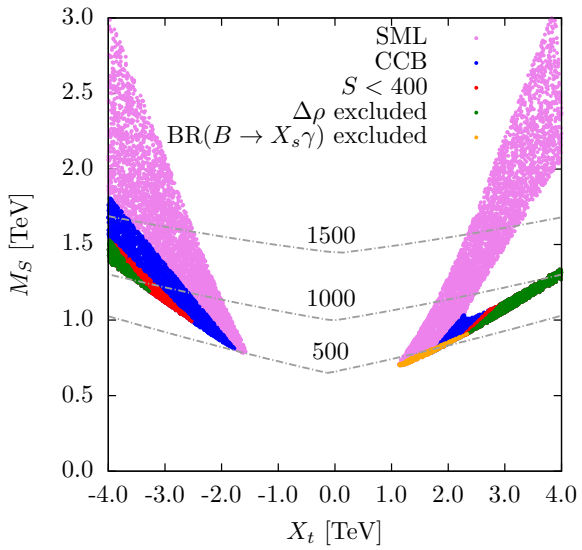

Figure 6.5: Points in the $X_t - m_{Q_3}$ plane with 123 GeV $< m_h <$ 127 GeV as well as exclusions from metastability (red points) from precision electroweak $\Delta\rho$ (green points) and flavour BR($B \to X_s\gamma$) (orange points). The MSSM parameters used are the same as in Fig. 6.3.

Limits from BR($B \to X_s\gamma$) are less significant for this set of fiducial parameters with a moderate value of $\tan\beta$. However, this branching fraction depends significantly on μ, m_A, and $\tan\beta$, and the limit can be much stronger or much weaker depending on the specific values of these parameters. We do not attempt to delineate the acceptable parameter regions, but we do note that the constraint from metastability can rule out an independent region of the parameter space.

6.5.2 Direct Stop Searches

Stops have been searched for at the LHC in a diverse range of final states, and these studies rule out stop masses up to 200-600 GeV, depending on how the stop decays (see, e.g., Refs. [382–385]). While the large stop mixing that occurs in the region excluded by metastability considerations can produce lighter stops, the stop masses in this dangerously metastable region are not necessarily light, as can be seen in Fig. 6.3. Thus, metastability excludes parameter ranges beyond existing direct searches.

Note as well that metastability does not place a lower bound on the mass of the lightest stop. For example, a very light state can be obtained for $m_{U_3}^2 \ll m_{Q_3}^2$ and $X_t = 0$. This scenario is not constrained by metastability, and can generate a SM-like Higgs boson mass consistent with observations for sufficiently large values of $m_{Q_3}^2$ [386].[2]

[2] A lower limit on the light stop mass in this scenario can be obtained from its effect on Higgs production

Our results also have implications for future stop searches and measurements. Should a pair of stops be discovered, a variety of methods can be used to determine the underlying parameters in the stop mass matrix through precision measurements at the LHC [388–391] or a future e^+e^- collider [391–393]. If these stop parameters turn out to lie within the dangerously unstable region, corresponding to larger values of $|X_t|$, we can conclude that new physics beyond the MSSM must be present.

6.5.3 Stop Bound States

An additional phenomenon that can potentially occur in the MSSM when A_t is very large is the formation of a $\tilde{t}_L\tilde{t}_R^*$ bound state through the exchange of light Higgs bosons [394, 395]. Such a state could have the quantum numbers of a Higgs field and mix with the MSSM Higgs fields to participate in electroweak symmetry breaking [394–397]. If this occurs, our results on the metastability of the MSSM may no longer apply. Calculating the critical value of A_t for when a bound state arises is very challenging, but under a set of reasonable approximations Ref. [396] finds that it requires $A_t/M_S \gtrsim 15$. While this lies beyond the region considered in the present chapter, it is conceivable that a full numerical analysis would yield a lower critical value for this ratio.

6.6 Conclusions

In this chapter we have investigated the limits on the stop parameter space imposed by vacuum stability considerations. A SM-like Higgs boson with a mass of ~ 125 GeV in the MSSM points to a particular region of the parameter space if naturalness of the EW scale is desired. In this regime, the two stop gauge eigenstates are highly mixed, and this can induce the appearance of charge- and colour-breaking minima in the scalar potential. Quantum tunnelling to these vacua can destabilize the electroweak ground-state.

We have studied the conditions under which stop mixing can induce CCB vacua and we have computed the corresponding tunnelling rates. We find that metastability provides an important constraint on highly-mixed stops. We have also considered constraints from flavour and precision electroweak observables and direct stop searches, which are sensitive to a similar region of the MSSM parameter space. Metastability provides new and complimentary limits, with a different dependence on the underlying parameter values.

The metastability limits we have derived provide a necessary condition on the MSSM. They apply for both standard and non-standard cosmological histories. Let us emphasize, however, that the MSSM parameter points that we have found to be consistent with stop-induced CCB limits may still be ruled out by more general stability considerations, such as configurations with more non-zero scalar fields. Fortunately, our own SML vacuum appears to be at least safely metastable.

---

and decay rates [387].

Chapter 7

The Electroweak Phase Transition in the Inert Doublet Model

7.1 Electroweak Baryogenesis in the Standard Model and Beyond

The Universe appears to be made entirely of matter, with all observed antimatter consistent with secondary production from, e.g., cosmic ray collisions. It was argued in Sec. 1.3.2 that a dynamical explanation of this baryon asymmetry of the Universe (BAU) necessarily invokes new physics. We also mentioned that SM alone can, *in principle*, generate a small asymmetry. This occurs through the mechanism of electroweak baryogenesis (EWBG) which operates during the electroweak phase transition (EWPT). This transition occurs when the Higgs field spontaneously acquires an expectation value, thereby breaking the electroweak symmetry down to electromagnetism. This mechanism is illustrated in Fig. 7.1, which conveniently captures how each of Sakharov's requirements from Sec. 1.3.2 is satisfied. If the EWPT is first order, it proceeds via the nucleation and subsequent expansion of bubbles of the broken $v \neq 0$ phase. This constitutes a departure from thermal equilibrium. In the symmetric phase baryon (B) and lepton numbers (L) are violated by non-perturbative $SU(2)_L$ processes [326, 398]

$$9q_L \leftrightarrow 3\bar{\ell}_L \tag{7.1}$$

called sphaleron transitions. Note that in these processes $\Delta B = \Delta L$, so $(B - L)$ number is conserved, while $(B + L)$ is violated. The resulting rate of baryon density production can be estimated as [399]

$$\frac{dn_B}{dt} = -3\frac{\Gamma_{\rm sph}(T)}{T}\Delta F, \tag{7.2}$$

where $\Gamma_{\rm sph}$ is the sphaleron rate and ΔF is the difference in free energy between states with $\Delta B = +1$. The sphaleron rate $\Gamma_{\rm sph}$ can be found using semi-classical methods sim-

ilar to those presented in Ch. 5 and depends exponentially on the energy scale $E_{\rm sph}(T) \sim (8\pi m_W/g^2)(v(T)/v_0)$ as $\Gamma_{\rm sph} \propto \exp(-E_{\rm sph}/T)$, where $v(T)$ is the Higgs vev at temperature T and $v_0 = v(0) = 246\,\text{GeV}$ [56]. Note that in the symmetric phase $v = 0$ and $E_{\rm sph} \approx 0$ and there is no exponential suppression for the sphaleron rate. In this phase the sphaleron rate can be estimated from scaling arguments to be $\Gamma_{\rm sph}/V \sim \alpha_W^5 T^4$ [400] and the coefficient of proportionality can be extracted from lattice simulations [401].

Ordinarily, increasing the B charge costs energy so $\Delta F > 0$, meaning that the sphaleron transitions tend to *wash out* any existing baryon number. However, these processes can be biased to produce slightly more baryons than anti-baryons if there is another asymmetry generated by C and CP violating interactions of the plasma particles with the Higgs field [56, 402]. Note that these charge asymmetries can be only created in the vicinity of the bubble wall, where the sphaleron rate is suppressed as discussed below. Thus this asymmetry must diffuse farther into the symmetric phase before it can be "re-processed" by the sphalerons. This scattering and diffusion process is described by a complicated network of quantum transport equations [56]. In the last step, the baryon asymmetry is captured by the expanding bubble.

Electroweak baryogenesis in the SM fails for two reasons. The first problem is that the amount of CP violation available in the SM is insufficient. The second issue is related to the dynamics of the phase transition itself. If the sphaleron transitions are active near the boundary and inside the bubble of true phase, any baryon number that is captured by the bubble will be washed out. The amount of wash out depends on the sphaleron rate in a given phase; integrating Eq. 7.2 over the timescales of the EWPT, $\Delta t_{\rm EW} \sim H^{-1}$, one finds the wash out factor [361]

$$\frac{n_B(\Delta t_{\rm EW})}{n_B(0)} \sim \exp\left(-E_{\rm sph}(T_c)/T_c\right), \tag{7.3}$$

where $E_{\rm sph}$ is defined above and we assumed that the transition occurs at around a temperature T_c (defined below). Requiring that the argument of the exponential is not much bigger than 1 (such that wash out is not so severe) requires [56, 361]

$$\frac{v_c}{T_c} \gtrsim 1, \tag{7.4}$$

where v_c is the Higgs expectation value at $T = T_c$. The quantity v_c/T_c is often referred to as the "strength" of the transition. The phase transition occurs after the symmetric and EW-breaking phases become degenerate, so T_c is defined as the temperature at which this happens. In Fig. 7.2 we show the evolution of the effective potential with temperature for the SM. Above T_c the symmetric phase is energetically favourable; the two phases become degenerate at $T = T_c$. As the Universe cools further, it transitions into the symmetry breaking phase via thermal tunnelling described in Sec. 5.3. The computation of the effective potential is described in detail in Sec. 7.3. For the SM, we find that in this (perturbative) approximation $v_c/T_c \sim 0.17$, so the wash out rate is too great – the transition is not strong enough. This inadequacy of the

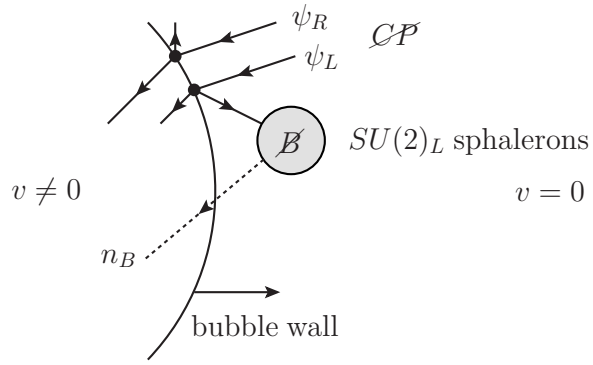

Figure 7.1: Schematic representation of electroweak baryogenesis.

EWPT in the SM is confirmed by non-perturbative lattice simulations, which suggest that the transition is not even first-order, but rather a smooth cross-over for $m_h \gtrsim 75\,\text{GeV}$ [56]. In the following sections we will focus on improving the strength of the transition by considering a particular extension of the SM.

Among the many proposed mechanisms of baryogenesis, EWBG is particularly attractive. Because EWBG is driven by the Higgs field, any new particles that seek to resolve the aforementioned problems in the SM implementation of EWBG must couple strongly to the Higgs; moreover, they must also be abundant in the primordial plasma at the time of the EW phase transition, so they cannot be too heavy.[1] The most salient feature of EWBG is therefore a requirement of new physics close to the EW scale. This aspect of EWBG makes it very predictive and falsifiable. Many simple models of EWBG have already been excluded either by lack of direct discovery of the new light states, or by limits from electric dipole moment searches, which are extremely sensitive to CP violation. However, many well-motivated possibilities still remain. Below we consider an extension of the SM known as the inert doublet model, which in addition to improving the phase transition strength, can also account for the dark matter relic density.

7.2 The Inert Higgs Doublet

The simplest extension of the Standard Model (SM) that includes two $SU(2)_L$ Higgs doublets is known as the Inert Higgs Doublet Model (IDM). In the IDM, the extra doublet has no coupling to SM fermions and is odd under a postulated new $\mathbb{Z}_2$ discrete symmetry, whereas all SM fields are $\mathbb{Z}_2$-even. Such symmetry makes the lightest $\mathbb{Z}_2$-odd particle (LOP) from the extra doublet stable and, thus, a potential weakly interacting massive particle (WIMP) dark matter candidate. The symmetry also eliminates numerous terms in the interaction Lagrangian of the model containing an odd number of extra "inert" scalars.

The IDM was introduced originally as one possible, generic scenario for electroweak symme-

[1] This requirement can be relaxed - see the discussion at the end of Sec. 7.5.

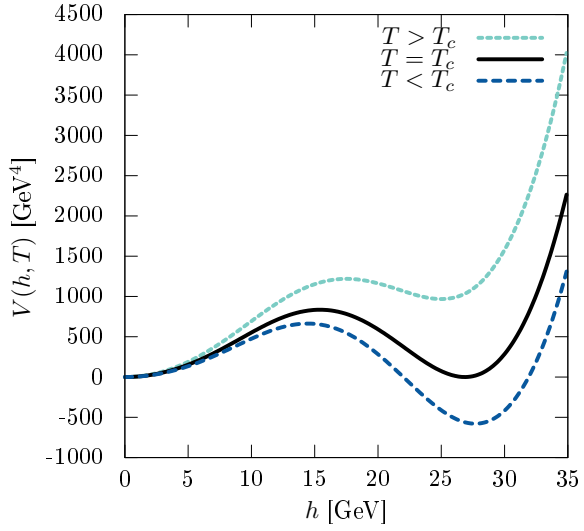

Figure 7.2: Evolution of the temperature-dependent effective potential (free energy) in the Standard Model around the critical temperature T_c.

try breaking (EWSB) [403]. Only subsequently was it realized that the IDM naturally features a WIMP DM candidate [404, 405], possibly providing a thermal relic density compatible with the inferred universal DM abundance. Numerous studies have subsequently investigated the DM and collider phenomenology of the model (see, e.g., Ref. [406–412]).

An additional early motivation to consider the IDM as an appealing augmentation of the SM scalar structure was to allow for a relatively heavy SM-like Higgs while remaining compatible with constraints from electroweak precision observables, and without severe fine tuning [405, 412]. Although this motivation has somewhat faded after the discovery of a SM-like Higgs boson at the LHC with a mass of ~ 125 GeV [12, 13], this important discovery decreases the number of free parameters in the theory by one, and places interesting and stringent constraints on the IDM phenomenology [413].

In the present study we are concerned with the nature of the electroweak phase transition (EWPT) in the IDM, and, specifically, with determining which physical parameters drive the strength of the phase transition, making it more or less strongly first-order, or second-order. This question is intimately related with the possibility to produce the observed baryon-antibaryon asymmetry in the Universe at the electroweak phase transition as discussed in the previous section. A strongly first-order phase transition (in a quantitative sense we shall make clear below) is a necessary ingredient to *(i)* achieve the necessary out-of-equilibrium conditions, occurring on the boundary of broken and unbroken electroweak phase, and to *(ii)* shield a baryon asymmetry captured in the broken electroweak phase region from sphaleron wash-out.

While necessary, a strongly first-order phase transition is not a sufficient condition. The CP violating sources of the SM are known to be insufficient to generate the necessary asymmetry in

the number density of baryons compared to antibaryons during the electroweak phase transition. The unbroken $\mathbb{Z}_2$ symmetry in the IDM precludes any new source of CP violation, and thus this model *per se* cannot accommodate successful electroweak baryogenesis (EWBG). However, the IDM might be in effect a good approximation at low energy of a broader construction that includes such additional CP violating sources at higher energies. Several suggestions of plausible effective higher-dimensional operators have been made in the literature [414, 415]. We will not discuss this aspect any more, as it falls outside the scope of this study.

The nature and strength of the electroweak phase transition in the IDM has been subject of several studies, with increasingly refined treatment of the effective potential [416–420]. For example, Ref. [416] utilized only the high-temperature form of the effective potential without including the zero-temperature Coleman-Weinberg terms. These were then shown to be quantitatively important for the phase transition strength in Ref. [418], where the full one-loop effective potential was used. Alternative $SU(2)_L$ representations of the inert scalar were considered in Ref. [419], where it was argued that in general, higher representations are less successful in satisfying experimental and theoretical constraints, thereby further motivating the study of the doublet case.

With the exception of Ref. [420], the primary focus has been on the Higgs funnel regime (described in more detail in Sec. 7.4). Indeed, we will confirm the findings of Refs. [417, 418] that this is the only region of parameter space that can successfully saturate the DM abundance and provide a strong-enough first-order EWPT. In Ref. [420] it was emphasized that the IDM can be useful for the EWPT even if the LOP provides only a subleading component of DM.

In this work we go beyond previous studies by utilizing a state-of-the-art treatment of the finite-temperature and zero-temperature effective potential including renormalization group, daisy resummation improvements and one-loop model parameter determination. As we discuss in great detail, strongly first-order EWPT in the IDM requires sizable quartic couplings that enhance quantum corrections to masses. This is important in the context of DM phenomenology since DM particle production in the early Universe often relies on resonance and threshold effects [413]. In addition, we also ensure that the phase transition completes by evaluating bubble nucleation rates.

Unlike previous studies which primarily utilized large numerical scans of the parameter space, here we take an orthogonal approach: we restrict our attention to a few, key benchmark models, motivated by the requirement of having a viable dark matter particle candidate and representing different features in the DM phenomenology. Based on these benchmarks, we then discuss how the EWPT depends on the physical model parameters. We identify the key physical inputs that drive the phase transition to the interesting regime where it is strongly enough first-order to accommodate successful electroweak baryogenesis. We will see that in all but one case the demand for a strongly first-order EWPT is in tension with either the relic abundance requirement or with experimental probes.

Our central finding is that the main driver of the strength of the phase transition is the

mass difference between the lightest inert scalar and the heavier scalars. Thus, we extend the results of Refs. [416, 418] to other regions of IDM parameter space. For large enough mass splittings, but for light enough heavy scalars, we find a phase transition strength (as measured by the ratio v_c/T_c, as we discuss in detail below) which increases with the mass splitting.

The remainder of this chapter is organized as follows. In Sec. 7.3 we give a brief introduction to the IDM, thereby clarifying our conventions, discuss quantum and finite-temperature corrections to the effective potential, and outline the computation of the phase transition strength. The essential features of DM phenomenology are reviewed in Sec. 7.4. In Sec. 7.5 we study the electroweak phase transition in several benchmark models motivated by the various DM scenarios available in the IDM. We conclude in Sec. 7.6. This chapter is based on unpublished work in collaboration with Stefano Profumo and Tim Stefaniak [4].

7.3 Phase Transitions in the Inert Doublet Model

7.3.1 IDM at Tree-Level

The IDM is a particular realization of the general type I Two Higgs Doublet Model (2HDM) (see, e.g., Ref. [421] for a review) which features an additional $\mathbb{Z}_2$ symmetry. The SM doublet H is even under $\mathbb{Z}_2$, while the new (inert) doublet Φ is odd. If we take Φ to have hypercharge $+1/2$, the most general renormalizable potential consistent with these symmetries is then given by [413]:

$$V_0 = \mu_1^2|H|^2 + \mu_2^2|\Phi|^2 + \lambda_1|H|^4 + \lambda_2|\Phi|^4 + \lambda_3|H|^2|\Phi|^2 + \lambda_4|H^\dagger\Phi|^2 + \frac{\lambda_5}{2}\left[(H^\dagger\Phi)^2 + \text{h.c.}\right]. \quad (7.5)$$

Conventionally, within CP-conserving Higgs sectors, the physical states are decomposed into CP-even and CP-odd scalars. One should keep in mind, however, that in the IDM there is no observable that can actually distinguish between the CP-even or CP-odd character of the inert Higgs bosons. In the absence of a vacuum expectation value (vev) for Φ, the doublets decompose as

$$H = \begin{pmatrix} G^+ \\ \frac{1}{\sqrt{2}}\left(v + h + \mathrm{i}G^0\right) \end{pmatrix}, \qquad \Phi = \begin{pmatrix} H^+ \\ \frac{1}{\sqrt{2}}\left(H + \mathrm{i}A\right) \end{pmatrix}. \quad (7.6)$$

Below we will consider the thermal evolution of the effective scalar potential in the early Universe. In general, spontaneous breaking of $\mathbb{Z}_2$ can occur, in which case we must also include a vev for the neutral component of Φ which we will indicate with ϕ.

The lightest $\mathbb{Z}_2$-odd particle is stable, and potentially provides a viable particle dark matter candidate. The $\mathbb{Z}_2$ symmetry also forbids Yukawa couplings of Φ to SM fermions (assumed to be even under $\mathbb{Z}_2$), which eliminates tree-level flavor-changing neutral currents. Either H or A can be the LOP, and since gauge interactions with SM states do not distinguish between the two, they are effectively equivalent from the standpoint of phenomenology. Below we will

indicate the LOP as H, but all statements made with respect to DM phenomenology and the electroweak phase transition remain true after the replacements $H \to A$ and $\lambda_L \to \lambda_S$ (the latter determines the coupling of the LOP to the SM Higgs) [417].

In the electroweak vacuum, the tree-level masses of the new states are given by

$$\begin{aligned} m_h^2 &= \mu_1^2 + 3\lambda_1 v^2, \\ m_H^2 &= \mu_2^2 + \lambda_L v^2, \\ m_A^2 &= \mu_2^2 + \lambda_S v^2, \\ m_{H^\pm}^2 &= \mu_2^2 + \frac{1}{2}\lambda_3 v^2, \end{aligned} \tag{7.7}$$

where $\lambda_L = (\lambda_3 + \lambda_4 + \lambda_5)/2$ and $\lambda_S = (\lambda_3 + \lambda_4 - \lambda_5)/2$. In what follows we employ the one-loop effective potential defined in the next section to fix μ_1^2 and λ_1 from the physical values $v = 246.22$ GeV and $m_h \approx 125$ GeV. The remaining parameters of the model are specified using the three physical masses m_H, m_A and $m_{H^\pm}$, along with λ_L and λ_2. The masses are related to potential parameters using the one-loop relations from Ref. [413], while λ_L and λ_2 are given at scale M_Z.

7.3.2 Finite-Temperature Corrections

The effective potential at finite temperature T can be written as

$$V_{\text{eff}} = V_0 + V_1 + V_T, \tag{7.8}$$

where V_0, V_1 and V_T are tree-level, one-loop temperature-independent and -dependent pieces, respectively. The tree-level potential V_0 has been given in Eq. (7.5). The temperature-independent one-loop correction has the Coleman-Weinberg form [317, 331, 332]:

$$V_1 = \sum_i \frac{n_i}{64\pi^2} m_i^4(v,\phi) \left(\ln \frac{m_i^2(v,\phi)}{Q^2} - C_i \right). \tag{7.9}$$

The sum is over all particle species coupling to the doublets; n_i is the number of degrees of freedom (positive for bosons and negative for fermions), C_i are renormalization-scheme-dependent constants ($C_i = 1/2$ for transverse gauge bosons and $3/2$ for everything else in the $\overline{\text{MS}}$ scheme); $m_i^2(v,\phi)$ is the field-dependent squared mass for each species. In writing the above, we have implicitly absorbed the counterterms into V_1; the temperature-dependent part is ultraviolet finite.

The field dependent masses in the IDM for the SM vector bosons and fermions are, respectively,

$$m_W^2 = \frac{1}{4} g^2 (v^2 + \phi^2), \quad m_Z^2 = \frac{1}{4}(g^2 + g'^2)(v^2 + \phi^2), \quad m_\gamma^2 = 0 \tag{7.10}$$

and

$$m_f^2 = \frac{1}{2} y_f^2 v^2, \tag{7.11}$$

with the corresponding bosonic degrees of freedom $n_i = 6,\ 3,\ 2$ for $i = W,\ Z,\ A$, and fermionic degrees of freedom $n_i = -12,\ -12,\ -4$ for $i = t,\ b,\ \tau$.

The field-dependent neutral CP-even, CP-odd and charged scalar mass eigenstates are obtained by diagonalizing

$$M_h^2 = \begin{pmatrix} \mu_1^2 + 3\lambda_1 v^2 + \lambda_L \phi^2 & 2\lambda_L \phi v \\ 2\lambda_L \phi v & \mu_2^2 + 3\lambda_2 \phi^2 + \lambda_L v^2 \end{pmatrix} \tag{7.12}$$

$$M_A^2 = \begin{pmatrix} \mu_1^2 + \lambda_1 v^2 + \lambda_S \phi^2 & \lambda_5 \phi v \\ \lambda_5 \phi v & \mu_2^2 + \lambda_2 \phi^2 + \lambda_S v^2 \end{pmatrix} \tag{7.13}$$

$$M_\pm^2 = \begin{pmatrix} \mu_1^2 + \lambda_1 v^2 + \frac{1}{2}\lambda_3 \phi^2 & \frac{1}{2}(\lambda_5 + \lambda_4)\phi v \\ \frac{1}{2}(\lambda_5 + \lambda_4)\phi v & \mu_2^2 + \lambda_2 \phi^2 + \frac{1}{2}\lambda_3 v^2 \end{pmatrix}. \tag{7.14}$$

Notice that for $\phi = 0$ the (22) components reduce to the expressions in Eq. (7.7).

The leading order quantum corrections give rise to a renormalization scale-dependent potential. One can choose the renormalization scale Q to minimize the size of higher order k-loop corrections which scale with $(\ln m^2/Q^2)^k$. The scale choice can be important when a parameter in the potential is very different from the electroweak vev ~ 246 GeV. We thus choose to use the renormalization group (RG) improved effective potential to minimize the scale dependence. The potential parameters are replaced by their running values, evaluated at the scale Q. The relevant one-loop β functions are given in Appendix C.

The leading order temperature-dependent corrections to the effective potential take the form [332]

$$V_T = \frac{T^4}{2\pi^2}\left(\sum_{i=\text{bosons}} n_i J_B\left[m_i^2(v,\phi)/T^2\right] + \sum_{i=\text{fermions}} n_i J_F\left[m_i^2(v,\phi)/T^2\right] \right), \tag{7.15}$$

where the J functions are defined as

$$J_B(x) = \int_0^\infty dt\ t^2 \ln\left[1 - \exp\left(-\sqrt{t^2 + x}\right)\right], \tag{7.16}$$

$$J_F(x) = \int_0^\infty dt\ t^2 \ln\left[1 + \exp\left(-\sqrt{t^2 + x}\right)\right]. \tag{7.17}$$

These functions admit useful high-temperature expansions which allow us to study the phase

structure as a function of T analytically (as long as the expansion is justified):

$$T^4 J_B\left[m^2/T^2\right] = -\frac{\pi^4 T^4}{45} + \frac{\pi^2}{12} T^2 m^2 - \frac{\pi}{6} T\left(m^2\right)^{3/2} - \frac{1}{32} m^4 \ln \frac{m^2}{a_b T^2} + \mathcal{O}\left(m^2/T^2\right) \tag{7.18}$$

$$T^4 J_F\left[m^2/T^2\right] = \frac{7\pi^4 T^4}{360} - \frac{\pi^2}{24} T^2 m^2 - \frac{1}{32} m^4 \ln \frac{m^2}{a_f T^2} + \mathcal{O}\left(m^2/T^2\right), \tag{7.19}$$

where $a_b = 16 a_f = 16\pi^2 \exp(3/2 - 2\gamma_E)$. The T^2 terms in the expressions above illustrate symmetry restoration at high temperatures. The non-analytic m^3 term in Eq. (7.18) can be responsible for the barrier between the high T phase (at the field origin) and low T phase that breaks $SU(2)_L \times U(1)_Y$.

Note that symmetry restoration signals the breakdown of perturbation theory — higher order diagrams become important. This can be accounted for by performing a resummation of daisy diagrams [422–424]. The resummation is performed by adding finite-temperature corrections to the boson masses in Eq. (7.16):

$$m^2 \to m^2 + cT^2, \tag{7.20}$$

where c is computed from the infrared limit of the corresponding two-point function. For the SM Higgs doublet we find

$$c_1 = \frac{1}{8} g^2 + \frac{1}{16}(g^2 + g'^2) + \frac{1}{2}\lambda_1 + \frac{1}{12}\lambda_L + \frac{1}{12}\lambda_S + \frac{1}{12}\lambda_3 + \frac{1}{4} y_t^2 + \frac{1}{4} y_b^2 + \frac{1}{12} y_\tau^2. \tag{7.21}$$

The various components of the inert doublet receive similar contributions (but without contributions from the fermions):

$$c_2 = \frac{1}{8} g^2 + \frac{1}{16}(g^2 + g'^2) + \frac{1}{2}\lambda_2 + \frac{1}{12}\lambda_L + \frac{1}{12}\lambda_S + \frac{1}{12}\lambda_3. \tag{7.22}$$

These expressions are in agreement with those in Refs. [418, 425, 426]. We implement these corrections by replacing $\mu_i^2 \to \mu_i^2 + c_i T^2$ in the scalar mass matrices, Eqs. (7.12, 7.13, 7.14).[2]

The thermal masses of the gauge bosons are more complicated. Only the longitudinal components receive corrections. The expressions for these in the SM can be found in Ref. [425], but it is easy to modify them to include the contribution of an extra Higgs doublet. For the longitudinally polarized W boson, the result is

$$m_{W_L}^2 = m_W^2 + 2 g^2 T^2. \tag{7.23}$$

This includes contributions from gauge boson self-interactions, two Higgs doublets and all three fermion families. The masses of the longitudinal Z and A are determined by diagonalizing the

[2]There are subleading thermal corrections to off-diagonal self-energies suppressed by additional powers of coupling constants and vevs which are usually neglected.

matrix

$$\frac{1}{4}(v^2+\phi^2)\begin{pmatrix} g^2 & -gg' \\ -gg' & g'^2 \end{pmatrix} + \begin{pmatrix} 2g^2T^2 & 0 \\ 0 & 2g'^2T^2 \end{pmatrix}. \tag{7.24}$$

The eigenvalues can be written as

$$m^2_{Z_L,A_L} = \frac{1}{2}m_Z^2 + (g^2+g'^2)T^2 \pm \Delta, \tag{7.25}$$

where

$$\Delta^2 = \left(\frac{1}{2}m_Z^2 + (g^2+g'^2)T^2\right)^2 - g^2g'^2T^2(v^2+\phi^2+4T^2). \tag{7.26}$$

7.3.3 Electroweak Phase Transition

Armed with the finite-temperature effective potential, we can now study the structure of the EWPT. The key property we intend to investigate is the transition strength, which sets the baryon number wash-out rate inside a bubble of broken phase (for a recent review of electroweak baryogenesis, see, e.g., Ref. [56]). In order to suppress sphaleron wash-out in the regions of broken electroweak phase, the relevant condition is typically quantified by requiring that [398]

$$\frac{v_c}{T_c} \gtrsim 1, \tag{7.27}$$

where v_c is the Higgs vev at the critical temperature T_c, defined as the temperature at which the origin is degenerate with the electroweak-breaking vacuum.

Note that it has been shown that this baryon number preservation condition (BNPC) is a quantity which is manifestly not gauge-invariant [361]. A gauge invariant BNPC can be however derived from the high-T expansion of the dimensionally reduced effective action and the critical temperature T_c must be obtained using the gauge invariant prescription of Ref. [361], which employs expansions in powers of $\hbar$ of the potential and vev. Near the critical temperature, $\mathcal{O}(\hbar)$ contributions to the potential are as important as the tree-level terms, so the $\hbar$ expansion fails. This is also why an all-orders ring diagram resummation discussed in Sec. 7.3.2 is needed. A consistent gauge-invariant method for implementing the ring resummation for the effective potential evaluated at the minimum was also demonstrated in Ref. [361]. We will be interested in studying tunnelling and nucleation temperatures, which require the evaluation of the potential away from the minima. For this reason, below we employ the standard BNPC of Eq. (7.27) and use the full one-loop effective potential to study IDM phases. We will argue that our results do not depend strongly on the issues of gauge invariance. We leave the full gauge-invariant treatment of the IDM to future work.

Finally let us note that the physical phase transition does not begin at T_c, but rather at a lower *nucleation* temperature T_n, at which the bubble formation rate exceeds the Hubble

expansion rate. Equivalently, the probability of nucleating a bubble of broken phase within one Hubble volume is close to 1 [332]. The nucleation rate per unit volume is evaluated in Sec. 5.3. If this rate is too slow, the false vacuum is metastable and the transition does not complete. The above conditions translate into a requirement on the bounce action $S_3(T_n)/T_n \lesssim 140$, which defines T_n [332]. We evaluate the nucleation temperature for a given model with a first-order phase transition using the `CosmoTransitions` package [335].

7.4 Dark Matter

The requirement of a thermal relic abundance for the LOP matching the observed DM density in the Universe of $\Omega_{\rm cdm}h^2 = 0.1199 \pm 0.0022$ [17], or at least of not over-producing such density via thermal production ("subdominant IDM", see, e.g., Ref. [420]) naturally selects four distinct sectors of the model's parameter space:

1. a *low* mass regime, with a LOP mass, m_H, well below half the observed SM-like Higgs mass, $m_H \lesssim m_h/2$;
2. a *resonant* or *funnel* region, $m_H \sim m_h/2$, i.e., a mass range where LOP annihilation proceeds predominantly through quasi on-shell Higgs s-channel exchange;
3. an *intermediate* mass regime, with a LOP mass of $m_h/2 \ll m_H \lesssim 500\,\text{GeV}$;
4. a *heavy* mass regime, with a LOP mass between 500 GeV a few TeV.

In the first case, the *low* mass regime, the DM pair-annihilation predominantly proceeds via the pair production of the heaviest kinematically accessible fermion (τ leptons, b quarks) through h exchange. The lower the LOP mass, the larger the $\lambda_{L,S}$ couplings need to be in order to produce a large enough pair-annihilation cross section. The allowed mass values range down to values close to the classical Lee-Weinberg lower mass limit for WIMPs [427], for this class of models somewhere in between 3 and 4 GeV. Direct detection limits from XENON10 [9] probe such combinations of masses and couplings quite tightly, such that only a small mass window below $5 - 7\,\text{GeV}$ remains.[3]

As the mass of the LOP approaches the resonant condition $m_H \sim m_h/2$, the resonant Higgs exchange allows for much smaller values of the $\lambda_{L,S}$ couplings, and direct detection constraints can be readily evaded. The relevant mass window left unconstrained by XENON100 [429] and LUX [8] has a width of approximately $10 - 15\,\text{GeV}$ centered around $m_h/2$ [430].

The mass regions above and below the resonance $m_H = m_h/2$ are actually slightly different from each other: Above the resonance, the pair production of WW^* in the final state of DM pair annihilation processes becomes increasingly important, even if $\lambda_{L,S} = 0$, because the four-point interaction through gauge couplings, independent of $\lambda_{L,S}$, starts contributing significantly. As

[3] The exact limit depends on the different possible choices of nucleon matrix elements, especially those connected with the strange quark content of nucleons [428].

	M_H	M_A	$M_{H^\pm}$	λ_L	λ_2	T_c	T_n	v_c/T_c	$\mu_{\gamma\gamma}$
BM1	66	300	300	1.07×10^{-2}	0.01	113.3	110.3	1.5	0.90
BM2	200	400	400	0.01	0.01	116.1	113.7	1.5	0.93
BM3	5	265	265	-6×10^{-3}	0.01	118.2	116.3	1.3	0.90

Table 7.1: Input parameters for the three benchmark scenarios discussed in the text along with critical and nucleation temperatures, the transition strength and the signal strength for $h \to \gamma\gamma$. The masses, given in GeV, are pole masses and the couplings λ_i are specified at $Q = M_Z$. Temperatures are also given in GeV.

a result the values of $\lambda_{L,S}$ giving the "correct" relic density are pushed to increasingly (with LOP mass) large, negative values.

For larger and larger LOP masses, the cross section for LOP pair annihilation to gauge bosons becomes very large, such that the thermal relic density is systematically below the universal dark matter density for any combination of model parameters. Barring non-thermal production mechanisms, in this intermediate mass region the LOP cannot be the dominant dark matter constituent [413, 420].

Finally, at about $m_H \simeq 500$ GeV, for $\lambda_{L,S} \simeq 0$ cancellations between scalar t- and u-channel exchange diagrams and the four-point interaction diagram alluded to above allow, again, for a sufficiently large thermal relic density. Such cancellations are suppressed by driving $\lambda_{L,S}$ away from zero. Thus, tuning $\lambda_{L,S}$ for increasing values of m_H generally allows one to achieve the correct relic density for mass values from $m_H \gtrsim 500\,\text{GeV}$ up into the multi-TeV range.

7.5 Benchmark Models

The benchmark models specified in Ref. [413] demonstrated various aspects of DM phenomenology and the possibility for the IDM to influence the $h \to \gamma\gamma$ rate. Unfortunately, none of the suggested scenarios exhibits a strongly first-order EW phase transition. In this Section, we identify alternate benchmark models which can potentially yield a strongly first-order EW phase transition, while having disparate properties for the lightest $\mathbb{Z}_2$-odd particle. All our benchmark models are compatible with constraints from Higgs collider bounds and rate measurements, which has been explicitly checked using the tools `HiggsBounds` [431–433] and `HiggsSignals` [434], where the model predictions have been calculated using a `SARAH`-generated `SPheno` version [435–438]. In the following discussion we mostly focus on the interplay between the dark matter phenomenology and the strengths of the EWPT.

Our key finding is that the requirement of a strongly first-order phase transition generally leads to a large mass splitting between the LOP and the other scalars in the IDM. Our benchmark models are summarized in Tab. 7.1, along with the corresponding critical and nucleation temperatures, as well as phase transition strengths, as parametrized by the ratio v_c/T_c. In each case the masses of the A and $H^\pm$ are chosen to ensure a strongly first-order phase transition. In Fig. 7.3 we show the dependence of the transition strength on these parameters. The lines

corresponding to BM1 and BM3 terminate where the potential develops a non-inert ($\phi \neq 0$) vacuum first during thermal evolution. This vacuum can then either continuously evolve into the SM/inert ($\phi = 0$) vacuum at $T = 0$ or it can persist to low temperatures. In the latter case, the EWPT can occur in two steps. Such models are viable if the inert vacuum is deeper than the new one at $T = 0$ and both transitions complete (i.e., nucleation rate(s) are large enough). Two step electroweak phase transitions have been investigated in detail in Refs. [439, 440]. In this work we consider only simple one step transitions, hence the truncation. Notice that in Ref. [418] the strength of the EW phase transition in models with multiple phase transition steps was always weaker, see Fig. 3 and 4 in Ref. [418].

First, let us consider model BM1, where LOP production in the early Universe is predominantly set by near-resonant s-channel Higgs exchange. This scenario has been recently examined in the context of phase transitions in Ref. [418]. Even more recently, it has also been suggested as a possible explanation [441] of the Fermi-LAT gamma-ray excess (see Ref. [442] and references therein). As discussed above, the on-resonance requirement forces $m_H \sim m_h/2$, but allows λ_L to be small enough to be consistent with direct detection constraints. Here DM production does not rely on interactions with A or $H^\pm$, so their masses can be essentially chosen freely, as long as the resulting quartic couplings λ_i (through Eq. (7.7)) satisfy perturbativity and constraints from electroweak precision observables (EWPO), which we check with `2HDMC` [443]. In order to satisfy the BNPC of Eq. (7.27), one needs to increase the coupling of the new scalars to h, which, in turn increases the splitting of A and $H^\pm$ relative to H. For this and the following models we choose $m_A = m_{H^\pm}$ to minimize the impact of splitting these states from H on the Peskin-Takeuchi T function [405] and to reduce the number of parameters. This assumption can be somewhat relaxed, but the results are qualitatively similar. This benchmark represents the only class of scenarios where the thermal LOP relic density (which we calculated with the `micrOMEGAs` code [444]) matches the observed DM universal density, and where the EW phase transition is strong enough.

When $m_A,\ m_{H^\pm} \gtrsim 340$ GeV, the corresponding loop corrections to m_H are large and require $\mu_2^2 < 0$. This causes a second minimum to appear in the potential at $T = 0$. As $m_A = m_{H^\pm}$ is increased further, this minimum quickly becomes deeper than the SM one, corresponding to the termination of the blue curve in Fig. 7.3 at $m_A \sim 350\,\text{GeV}$. This behaviour was also observed in Ref. [418].

In this scenario, the LOP mass m_H has been chosen slightly above the kinematic threshold of the decay $h \to HH$ in order to evade constraints from direct searches for invisible Higgs decays and Higgs rate measurements. These however become important for our benchmark scenario BM3 (see below).

The second benchmark BM2 in Tab. 7.1 represents the intermediate mass regime. Here annihilation into gauge bosons is efficient and DM is generally underabundant, unless there is a cancellation among different amplitudes [413]. The cancellation depends, as indicated above, on how close $\lambda_{L,S} \to 0$, i.e., on how degenerate the IDM Higgs sector is. In our benchmark,

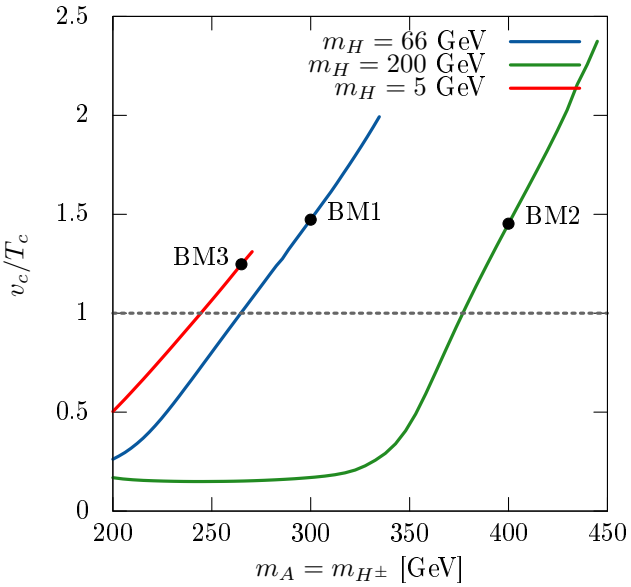

Figure 7.3: Phase transition strength as a function of the heavier IDM scalar masses, taking $m_A = m_{H^\pm}$. The remaining parameters are chosen as in the benchmark models of Table 7.1, which are shown by black dots. The lines for BM1 and BM3 terminate where the inert doublet develops a non-zero vev, $\phi \neq 0$, as described in the text.

such a cancellation requires $m_H \approx m_A \approx m_{H^\pm}$ with a maximum splitting of ~ 10 GeV. These small splittings lead to small couplings of the new states to h and therefore an insufficiently strong phase transition. Thus the phase transition requirement forces *thermal relic* DM to be underabundant. The observed DM density can be explained here, however, by invoking non-thermal production mechanisms (e.g., the decay of a heavy particle) or with the existence of additional DM particles (e.g., axions). The multitude of "non-standard" production mechanisms has been recently reviewed in Ref. [74].

The final benchmark model, BM3, belongs to the light-mass regime, and is another example that requires further ingredients to be fully consistent with the phenomenology of the DM sector. For $m_H < m_h/2$, decays of the SM Higgs to invisible final states become possible, with a decay rate [405]

$$\Gamma(h \to HH) = \frac{v^2 \lambda_L^2}{8\pi m_h} \left(1 - \frac{4m_H^2}{m_h^2}\right)^{1/2}. \tag{7.28}$$

Requiring consistency with the observed 95% C.L. upper limit on the branching fraction, $\mathrm{BR}(h \to HH) \leq 17\%$ [445], provides a strong constraint on the coupling λ_L of $|\lambda_L| \lesssim 0.007$, while a large value $|\lambda_L| \gtrsim 0.4$ is required to sufficiently deplete the DM abundance [413]. These problems can be remedied by softly breaking the $\mathbb{Z}_2$, which would allow H to decay [446, 447].

As in the previous example, another explanation for DM is then needed. An alternative possibility is to provide the LOP with new annihilation modes, e.g., to new light vector bosons [448], or a mechanism to dilute the thermal relic density, such as an episode of late entropy injection [449, 450].

DM phenomenology aside, it is again easy to get a strongly first-order phase transition with a large mass splitting between H and A, $H^\pm$. We note that this scenario requires a significant tuning of parameters, because a small LOP mass requires near cancellation of tree-level and loop contributions. For $\lambda_L > 0$, this leads to negative values of μ_2^2 which can result in the appearance of a new $\phi \neq 0$ minimum.

In all three cases, the first-order transition is driven by the non-analytic $(m^2)^{3/2}$ terms (see Eq. 7.18) due to A and $H^\pm$, while the gauge boson contributions are not as important. This explains the common feature of large splittings between H and A, $H^\pm$ among the benchmark scenarios. These lead to large couplings between h and the new states, enhancing the size of thermal corrections. This appears to be a generic requirement for increasing the strength of the phase transition in the IDM. It is also important to emphasize that thermal corrections to the crucial $(m^2)^{3/2}$ terms from A and $H^\pm$ are not subject to gauge invariance issues that affect the gauge sector contributions. As a result, we expect these arguments to remain valid in the context of a fully gauge invariant treatment. This can be further tested in a toy model with all gauge coupling constants set to 0, thereby completely eliminating gauge dependence from the effective potential.[4] We checked that such a simplified analysis gives quantitatively similar results for critical temperatures and transition strengths when the scalar couplings are large.

The high T expansion of the effective potential also provides a simple explanation for the shape of the curves in Fig. 7.3. In this limit the transition strength is proportional to the coefficient of the v^3 term [332]. For the IDM scalars such terms arise from the non-analytic contributions proportional to $(\mu_2^2+\lambda_S v_c^2)^{3/2}$ (assuming $m_A = m_{H^\pm}$, as above, and ignoring daisy contributions for simplicity), which behaves as v^3 only when $\lambda_S v_c^2 \gg \mu_2^2$. Thus when $\lambda_S v_c^2 \ll \mu_2^2$, the transition strength is independent of IDM parameters, corresponding to the plateau of the green curve in Fig. 7.3. In the opposite limit, the IDM gives an additional contribution to the cubic coefficient, so the transition strength scales as $\lambda_S^{3/2} \sim m_A^3$, as illustrated by the monotonically increasing sections of the curves in Fig. 7.3.[5]

For heavy masses $m^2/T^2 \gg 1$ (with $T \sim 100$ GeV), the IDM states thermally decouple, but this does not mean that they have no impact on the phase transition. When $\mu_2^2 \gg |\mu_1|^2$, the heavy doublet can be integrated out to yield a SM effective theory with the potential

$$V_0 = \mu^2|H|^2 + \lambda|H|^4 + \kappa|H|^6 + \dots \tag{7.29}$$

where the dots stand for higher mass dimension operators. The parameters μ^2, λ and κ can be

[4] We thank Michael Ramsey-Musolf for pointing this out to us.

[5] The precise scaling is modified by Daisy corrections, $\mathcal{O}(\mu_2^2/\lambda_S v_c^2)$ terms, finite-T and renormalization group effects.

related to those in the fundamental IDM by equating the effective potentials for the two models at a *matching* scale $Q \sim \mu_2$. For example, one-loop matching yields

$$\kappa = \frac{1}{24\pi^2\mu_2^2}(\lambda_L^3 + \lambda_S^3 + \lambda_3^3/4), \tag{7.30}$$

while μ^2 and λ are determined below the matching scale by fixing the vev and the Higgs mass. With the presence of a dimension-six term in the potential, the barrier required for a strongly first-order transition can be generated if $\lambda \lesssim 0$ and $\mu^2 + cT^2 > 0$ for $T \sim T_c$, where c encodes thermal corrections from SM states only [425]. Scenarios of this type have been considered, e.g., in Refs. [451–454]. One immediate difficulty is that in the IDM κ is generated only at one-loop, so in order for this operator to be significant for field values of around the electroweak vev, one must overcome the loop suppression, suggesting that the combination $\lambda_L^3 + \lambda_S^3 + \lambda_3^3/4$ cannot be too small. This again forces a large splitting between the IDM states, meaning that the heavy DM scenario described in Section 7.4 cannot be realized together with a strongly first-order phase transition. Such large couplings can run into perturbativity problems and invalidate the expansion used to generate the effective field theory.

We briefly comment on the discovery prospects of the new IDM states at the LHC. Due to the $\mathbb{Z}_2$ symmetry, the IDM states can only be produced pairwise at colliders. Successive decays of the heavier IDM states A and $H^\pm$ into the LOP and a Z or W boson, respectively, can give rise to multilepton signatures [412, 455, 456]. In a recent analysis [456] of LHC searches for supersymmetric particles with two leptons plus missing transverse energy in the final state in the context of the IDM, mass limits of up to $m_A \lesssim 140$ GeV for LOP masses $m_H \lesssim 55$ GeV and charged Higgs masses around $85 - 150$ GeV have been derived. While these limits partly exceed previous limits from the LEP collider, they are not yet sensitive to the parameter regions that yield a strongly first-order phase transition as required for successful electroweak baryogenesis, see Fig. 7.3.

The new IDM states can also have an indirect effect on precision Higgs measurements. In particular, the new charged state $H^\pm$ provides an additional contribution to the loop-induced $h \to \gamma\gamma$ and γZ rates. These effects have been recently studied in Refs. [457, 458] in the context of the 125 GeV Higgs boson. Modifications of these branching fractions by $\mathcal{O}(10\%)$ are a *generic* feature of our benchmark scenarios, as we show below. The $h \to \gamma\gamma$ rate has the form [421, 457–461]

$$\Gamma(h \to \gamma\gamma) = \frac{\alpha^2 G_F m_h^3}{128\sqrt{2}\pi^3} \left| \mathcal{A}_{\rm SM} + \frac{\lambda_3 v^2}{2m_{H^\pm}^2} A_0\left(\frac{m_h^2}{4m_{H^\pm}^2}\right) \right|^2 , \tag{7.31}$$

where the leading contributions to the SM amplitude $\mathcal{A}_{\rm SM} \approx -6.56 + 0.08i$ come from W bosons and top quarks. The second term is the new contribution from $H^\pm$, where A_0 is a loop function with the property $\lim_{x\to 0} A_0(x) = 1/3$ [461]. For our benchmarks we have $\lambda_3 > 0$, so

one expects a suppression of $h \to \gamma\gamma$ relative to the SM.[6] Note that for fixed μ_2^2, the amplitude for the $H^\pm$ contribution tends to a constant value $1/3$ as λ_3 is increased. This means that in the limit of a large mass splitting between H and $H^\pm$, which is required for a strongly first order phase transition, the branching fraction is reduced by $\sim 10\%$. This effect was also noticed in Refs. [417, 420] for models similar to our BM1 and BM2, respectively. The deviations to $\mathrm{BR}(h \to \gamma\gamma)$ induced by $H^\pm$ are shown in Tab. 7.1 in terms of the SM normalized signal strength $\mu_{\gamma\gamma} = (\sigma\ \mathrm{BR})/(\sigma\ \mathrm{BR})_{\mathrm{SM}}$. While they are still consistent with the present measurements from ATLAS [462] and CMS [463], the LHC should reach a precision of 4–8% for $\mu_{\gamma\gamma}$ [113, 445], thereby definitively testing the benchmark scenarios in Tab. 7.1.

While our benchmarks feature sizable deviations of $\mathrm{BR}(h \to \gamma\gamma)$ from the SM expectation, we note that it *is* possible to avoid this by taking $H^\pm$ to be nearly degenerate with H, and using A alone to drive the phase transition to be strongly first order. However, in this case, efficient coannihilation of H with $H^\pm$ during freeze-out generally results in a very small relic abundance [464]. The near degeneracy is also required by constraints on the oblique T parameter when $m_A \gg m_{H^\pm}$ [405]. For example, taking $m_{H^\pm} = 70\,\mathrm{GeV}$, $m_A = 370\,\mathrm{GeV}$ and other parameters as in BM1 results in a strongly first order phase transition, an order of magnitude smaller relic abundance and only a $\sim 3\%$ depression of $\mu_{\gamma\gamma}$ relative to the SM.

7.6 Discussion and Conclusions

We studied the structure of the electroweak phase transition in the inert Higgs doublet model, utilizing a set of three benchmark scenarios that feature a potentially viable dark matter particle. Our choices for the three benchmark models essentially exhaust all possible prototypical setups for particle dark matter in the inert doublet model. While only one of the benchmarks has a dark matter particle with a thermal relic density matching the observed dark matter density, the other two (under- and over-abundant) can be made viable by invoking additional production mechanisms or a scenario where the thermal relic density is diluted away, respectively.

The key finding of our study is that in all cases where the model possesses a reasonable particle dark matter candidate, the inert scalar spectrum can be arranged in such a way so as to produce a strongly first-order electroweak phase transition. Central to achieving such a phase transition is to postulate a large enough splitting between the dark matter candidate and the heavier inert scalars. The physics driving this result is simple: Large mass splittings generically correspond to large couplings between the inert scalars and the Standard Model Higgs; These, in turn, increase the magnitude of non-analytic $\sim (m^2)^{3/2}$ terms in the temperature-dependent effective potential and thus the potential barrier between the field origin and the $SU(2)_L \times U(1)_Y$-breaking phase.

[6] Various limits on LOP-Higgs coupling discussed above force $|\lambda_L|$ to be small, such that the H mass is primarily determined by μ_2^2 (at tree level, see Eq. (7.7)). If the charged Higgs $H^\pm$ is heavier than H then this forces $\lambda_3 > 0$.

The mass splitting under consideration cannot be arbitrarily large. For large enough values, for example, the phase structure of the model becomes more complicated, with possible non-zero vacuum expectation values for the inert doublet and multiple-step phase transitions. While, based upon the results of Ref. [418] the latter possibility is not expected to yield stronger electroweak phase transitions than in the single-step case, this is an interesting possibility which we leave for future studies.

The question of how to embed large-enough CP violating sources in detail was also left unanswered here. It will be interesting to study whether such a source (for example an additional gauge-singlet complex scalar, see Ref. [465]) significantly impacts the electroweak phase transition and dark matter phenomenology, and, with this, the conclusions reached in the present study.

Part IV

Conclusions

Chapter 8

Conclusion and Outlook

In this thesis we have investigated extensions of the Standard Model of particle physics that seek to address one or more of the problems outlined in Ch. 1. These included theoretical issues, such as the hierarchy problem, as well as observational questions of dark matter and the baryon asymmetry of the Universe. We classified our discussion in terms of phase transitions – events in the history of the Universe, when an order parameter, such as an energy density of a cosmological species (Part II) or the expectation value of a scalar field (Part III), changes abruptly, modifying subsequent evolution. To conclude, below we summarize the main results and outline prospects for experimental tests of these ideas.

In Chapters 3 and 4 we considered string theory motivated cosmological scenarios with late-time reheating. In many realistic string compactifications long lived scalar fields called moduli dominate the energy density of the Universe until their decay just before the onset of primordial nucleosynthesis. This relatively late phase transition from matter to radiation domination can be responsible for dark matter and baryon asymmetry genesis.

Chapter 3 was dedicated to the production of massive supersymmetric particles during the era of moduli reheating. Such states can account for the observed dark matter relic abundance. However, due to the low reheating temperature, $T_{\rm RH} \gtrsim 5\,{\rm MeV}$, DM generation is *non-thermal* and the lightest supersymmetric particle (LSP) must rely on large annihilation cross sections to deplete its number density to acceptable levels. In the Minimal Supersymmetric Standard Model (MSSM) with a sub-TeV wino LSP, this generally leads to a conflict with gamma ray observations of the Galactic Center. In an attempt to preserve the string-motivated moduli cosmology, we considered three extensions of the MSSM gauge structure. These share the common feature that the additional gauge sector contains the true LSP of the theory, allowing the wino to decay. The first two models discussed were based on an additional $U(1)_x$, kinetically mixed with the MSSM hypercharge. We explored the possibility of (symmetric) self-conjugate and (asymmetric) $U(1)_x$-charged DM, finding that the former case still suffers from a large indirect detection rate, generally inconsistent with observations (except for extreme choices of parameters). The asymmetric DM model is compatible with experiment. However, both cases require light scalar particles, which is puzzling in the context of the MSSM itself, where

LHC bounds suggest that the scalar superpartners are heavy. This issue was addressed in the third example, which relied on a pure $SU(N)_x$ gauge theory and therefore did not require any unnaturally light scalars. While this case provided a solution to the moduli-induced LSP problem in the MSSM, we found that this model can only account for a small fraction of DM in order to be consistent with structure formation in our Universe. Thus, none of the three models discussed provided a fully satisfactory (theoretically and/or experimentally) solution to the moduli problem. These conclusions hold for generic moduli parameters, relatively low scale of SUSY breaking and R-parity conserving supersymmetry. The results of our study can therefore be interpreted in two ways. First, they may be taken as hint that moduli properties, such as the relation of the modulus mass to the SUSY breaking scale and its coupling to ordinary matter, are *not* generic in our string vacuum. The second interpretation suggests that R-parity is violated, such that supersymmetry does not give rise to a stable dark matter candidate. Alternatively, the scale of SUSY breaking (and therefore the modulus mass) can be much larger than expected, leading to a higher reheating temperature.

The late-time moduli decays discussed above occur far out of equilibrium and therefore provide a viable setting for generating the baryon asymmetry of the Universe. This idea was developed in Ch. 4, where we considered a unified origin for the matter-antimatter asymmetry and dark matter, through the mechanism of hylogenesis. In this scenario the moduli decay products give rise to an excess of visible baryons over antibaryons, and an equal asymmetry in *hidden antibaryons* (such that total baryon number is conserved) that populate a "dark sector". The hidden antibaryons are the dark matter. The structure of the dark sector is very similar to the asymmetric $U(1)_x$ extension used in Ch. 3. The operator that mediates baryon transfer between the visible and hidden sectors also gives rise to a novel direct detection signature – induced nucleon decay (IND). This arises when a DM particle (which carries antibaryon number) scatters inelastically off a nucleon, destroying it and producing another hidden state and a meson. In a nucleon decay detector, this looks like a standard nucleon decay event (spontaneous emission of a meson, together with missing momentum), but with different kinematics for the outgoing meson. The resulting effective nucleon lifetime is accessible by present and future nucleon decay searches. The strongest limits at present come from the Super-Kamiokande experiment [466]. However, these limits are not directly applicable due different kinematics of standard and induced nucleon decay. Because the experiments optimize their event selection for standard nucleon decay, the resulting efficiency for IND events can be as small as 5% [467] – the effective constraints on IND rates and the underlying parameters in the model are weak. These limits can be improved by relaxing event selection (so that more IND events pass the cuts), tailoring analyses specifically for IND and by the next generation of experiments, such as Hyper-Kamiokande [468].

The operators needed for hylogenesis can also be probed at colliders. For example, the effective baryon transfer operator $(X u_R^c d_R^c d_R^c)/M^2$ contributes to the LHC production of jets and missing energy (via the decay $X \to \overline{\Psi}\Phi^*$). The resulting limits from the 8 TeV run constrain

$M \gtrsim 2.6{-}3.5\,\mathrm{TeV}$, depending on the flavour structure [469]. An ultraviolet-complete model that generates the above operator also gives rise to dijet resonances, which modify QCD predictions of dijet mass and angular distributions. The latest results from ATLAS [470, 471] and CMS [472, 473] are consistent with SM predictions and set lower limits on the scale suppressing contact operators (roughly corresponding to the mass of the P scalars discussed in Sec. 4.2.2) that in some cases reach $\sim 12\,\mathrm{TeV}$.[1] These limits depend on the flavour structure of the complete theory. However, note that the effective scale enters the CP asymmetry parameter defined in Sec. 4.3.1 and for large enough values the baryon asymmetry produced during hylogenesis will be insufficient to explain the observed value. As this thesis is being completed, the LHC is preparing to begin Run 2 at near design energy of 13 TeV. Stronger limits from this new energy frontier will be instrumental in testing hylogenesis.

The baryon transfer operator is only one of two portals between the visible and dark sectors. The implementation of hylogenesis presented in Ch. 4, as well as two models in Ch. 3 also feature a kinetic mixing interaction that can be probed from multiple directions. First, irrespective of whether or not the hidden sector contains a DM candidate that saturates the relic abundance, the hidden vector can be produced in fixed target/beam dump experiments and at the flavour factories (see Ref. [203] for a review). This search strategy has the advantage of being relatively model independent. Indeed, if the vector decays back to SM particles, the signal is a function only of the vector mass and the kinetic mixing parameter. As discussed in Sections 3.3.2 and 4.3.2, there exist certain minimal values of this mixing parameter in the range $10^{-5} - 10^{-4}$ from the requirement of sufficiently fast decays of certain hidden sector states. While this parameter range is not probed by current measurements for hidden photons (for GeV-scale vector masses), the next generation of experiments such as HPS and Belle II *will* be sensitive to the interesting parameter region [203, 474]. If no signal is found, our implementation of hylogenesis and the related models of Ch. 3 will be in tension with bounds on energy injection during primordial nucleosynthesis.

A complementary set of probes of the $U(1)_x$ hidden sector paradigm is available when the hidden sector contains a viable dark matter candidate. For example, the kinetic mixing interaction gives a direct detection rate that is very sensitive to the hidden photon mass – see Eqs. (3.53) and (4.59). These rates also depend on the kinetic mixing parameter and the hidden gauge coupling. However, these quantities are bounded from below as discussed above, suggesting that there is a also a minimum rate for scattering on nucleons. This roughly corresponds to the lower dashed line in Fig. 8.1, where we also demonstrate the best constraints in the low mass regime from various experiments. Models with scattering rates far below the lower dashed line will generally overclose the Universe or have problematic late-decaying particles in the hidden sector. We note, however, that predictions of direct detection signals are subject to astrophysical uncertainties such as the local DM density and velocity distributions. Another disadvantage is that these searches are very model dependent. For example, when the

[1] The numbers cited in Sec. 4.5.3 hold for older LHC results with a partial Run 1 data set.

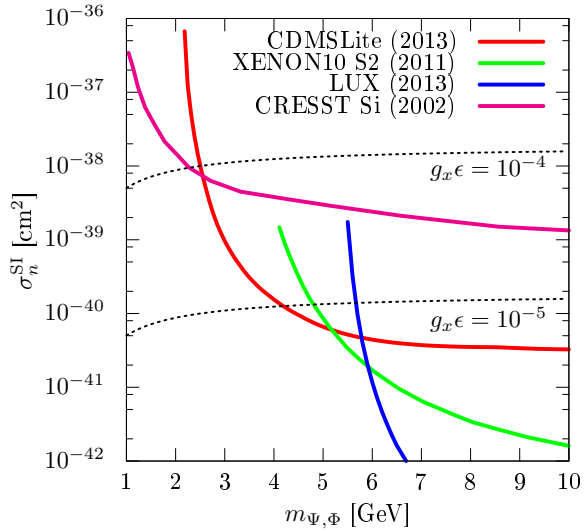

Figure 8.1: Constraints on the spin-independent scattering cross section as a function of DM mass (for the model of Sec. 3.4) from LUX [8], XENON10 S2 only analysis [9], CDMSLite [10] and CRESST-Si [11]. The dashed lines show the expected cross section for various combinations of $g_x\epsilon$ (see Eq. (3.53)).

DM candidate is a Majorana fermion, as in Sec. 3.3, the resulting interactions only allow for spin-dependent scattering for which experimental limits are much weaker than for the spin-dependent case. With these caveats in mind, the next 5–10 years should bring improvements in experimental sensitivity of an order of magnitude or better in the light mass regime [76]. From Fig. 8.1 it is clear that this will probe a significant portion of viable parameter space.

A second important probe of cosmological dark matter, indirect detection, was discussed in detail in Ch. 3. It was shown, despite significant astrophysical uncertainties, that continuum gamma ray observations provide a sensitive test of models with non-thermal dark matter. This is because the large annihilation rates needed to produce the correct relic density also lead to significant annihilation at late times. These limits, in particular those coming from Fermi-LAT will continue to improve, as more data is collected. With an expected mission lifetime of 10 years, it is plausible that the Fermi-LAT sensitivity will improve by an order of magnitude, translating to more stringent constraints of models of light non-thermal DM, even if it is a subdominant component [475].

In the above discussion we emphasized the fact that the models considered in Part II are testable at readily available energies, despite the fact that some of the core dynamics originates from speculative high scale physics. In contrast, Part III studies phase transitions associated with electroweak scales. In Ch. 6 we studied the implications of naturalness of the Higgs mass, m_h, and its observed value on the vacuum structure of the MSSM. Supersymmetry introduces many new field directions in the scalar potential. Minima of the potential in these directions

generally break charge and colour symmetries. If such a minimum is deeper than the one we live in, our vacuum can be destabilized by quantum tunnelling, corresponding to a phase transition from colour preserving to a colour broken phase. Interestingly, the appearance of these minima is correlated with m_h through quantum corrections due to stops, superpartners of the top quark. We computed the tunnelling rates to various charge and colour-breaking minima and placed new constraints on the MSSM parameter space. These limits are complementary to experimental results described in Sec. 2.5, since they reach a different region of the stop parameter space and are independent of the nature of the LSP. The experimental limits on stops, on the other hand, are quite sensitive to the mass of the LSP. If stops are discovered, our results will useful in determining whether the electroweak vacuum is stable, as discussed in Sec. 6.5.2.

The transitions studied above occur late in the evolution of the Universe, when the temperature is effectively zero. At finite temperature, however, a similar phase transition occurs even in the Standard Model, when the electroweak symmetry is broken down to electromagnetism when the Higgs field acquires an expectation value. If this transition proceeds through bubble nucleation and is sufficiently strong, it can potentially explain the production of the observed baryon asymmetry in the Universe. In the SM, this process produces too little baryon number for reasons explained in Sec. 7.1. This can be remedied by including additional matter that couples strongly to the Higgs field. In Ch. 7 we investigated this possibility within one of the simplest possible extensions of the SM: the inert doublet model (IDM). Despite its simplicity, the IDM is able to produce an electroweak phase transition appropriate for baryogenesis, and even account for DM for certain choices of parameters. Motivated by different classes of DM phenomenology, we presented three benchmark scenarios that generated a strongly first order phase transition. In all but one case, we found that the requirement of a good DM candidate and a strong electroweak transition are mutually exclusive. This is because appropriate levels of DM annihilation often rely on precise relationships among the IDM particle masses or values of parameters that are inconsistent with precision SM Higgs measurements. In contrast, a sufficiently strong electroweak transition requires large couplings of the Higgs to the new states, which in turn translates into large mass splittings in the IDM sector. This has important implications for collider limits on IDM, which are typically obtained by recasting SUSY searches for neutralinos and charginos for the IDM H, A, and $H^{\pm}$ states (see, e.g., Ref. [456] for recent results). For example, in dilepton searches, larger splittings between the IDM states give rise to highly boosted lepton pairs. Interestingly, this can actually *reduce* the sensitivity of current searches due to a veto on leptons from on-shell Z decays [456]. As a result, at present the limits on the interesting region of IDM parameter space are weak. In particular, the Higgs funnel regime, which accounts for both DM and a strongly first order electroweak phase transition (see Sec. 7.5), is completely unconstrained at the moment. Fortunately, Run 2 should begin to probe this regime [456]. Note that the above comments apply only to recasting of existing searches; dedicated IDM analyses should yield more stringent results. The existence of a charged scalar also alters loop-induced Higgs decay rates. In particular, the $h \to \gamma\gamma$ signal strength is modified

by $\mathcal{O}(10\%)$ for our benchmark scenarios. While this is consistent within error bars with current measurements [462, 463], the LHC is expected to reach a precision of 4–8% for this branching ratio, thereby definitively testing our benchmark models [113].

The inert doublet model addresses only one of Sakharov's conditions for successful baryogenesis. The IDM does not introduce any new sources of CP violation. A more complete theory of EWBG will also address this shortcoming of the SM as well. In this case, new sources of CP violation can be probed by measurements of electric dipole moments of electrons, neutrons, atoms and molecules as described in Sec. 2.5.

The imminent restart of the LHC promises to resolve several fundamental issues in particle physics. As discussed above, the new collider data will be crucial for testing theories of dark matter and baryogenesis; direct and indirect detection, along with precision measurements will provide complementary probes of these models. Perhaps even more importantly, Run 2 will determine the ultimate fate of naturalness, which has been a major motivator for physics beyond the Standard Model not far from the electroweak scale. The hierarchy and the closely related naturalness issues are problems of low scale phenomena being extremely sensitive to high scale, ultraviolet physics. A century ago theoretical physics was also afflicted by an ultraviolet catastrophe in the classical black body radiation spectrum. The solution to that small problem initiated the quantum revolution. The hierarchy problem may be the UV catastrophe of the twenty first century. Its resolution will either lead to another revolution (supersymmetry, little Higgs or something completely unexpected!) or to a fundamental realization that nature *is* fine-tuned, perhaps hinting at modification of naturalness or even environmental selection.

Bibliography

[1] N. Blinov, J. Kozaczuk, A. Menon, and D. E. Morrissey, *Confronting the moduli-induced lightest-superpartner problem*, *Phys.Rev.* **D91** (2015), no. 3 035026, [arXiv:1409.1222].

[2] N. Blinov, D. E. Morrissey, K. Sigurdson, and S. Tulin, *Dark Matter Antibaryons from a Supersymmetric Hidden Sector*, *Phys.Rev.* **D86** (2012) 095021, [arXiv:1206.3304].

[3] N. Blinov and D. E. Morrissey, *Vacuum Stability and the MSSM Higgs Mass*, *JHEP* **1403** (2014) 106, [arXiv:1310.4174].

[4] N. Blinov, S. Profumo, and T. Stefaniak, *The Electroweak Phase Transition in the Inert Doublet Model*, *JCAP* **2015** (2015), no. 07 028, [arXiv:1504.05949].

[5] T. Lin, H.-B. Yu, and K. M. Zurek, *On Symmetric and Asymmetric Light Dark Matter*, *Phys.Rev.* **D85** (2012) 063503, [arXiv:1111.0293].

[6] **ATLAS, CMS**, G. Aad et al., *Combined Measurement of the Higgs Boson Mass in pp Collisions at $\sqrt{s} = 7$ and 8 TeV with the ATLAS and CMS Experiments*, 2015, [arXiv:1503.07589].

[7] A. Kusenko, P. Langacker, and G. Segre, *Phase transitions and vacuum tunneling into charge and color breaking minima in the MSSM*, *Phys.Rev.* **D54** (1996) 5824–5834, [hep-ph/9602414].

[8] **LUX Collaboration**, D. Akerib et al., *First results from the LUX dark matter experiment at the Sanford Underground Research Facility*, *Phys.Rev.Lett.* **112** (2014) 091303, [arXiv:1310.8214].

[9] **XENON10 Collaboration**, J. Angle et al., *A search for light dark matter in XENON10 data*, *Phys.Rev.Lett.* **107** (2011) 051301, [arXiv:1104.3088].

[10] **SuperCDMS Collaboration**, R. Agnese et al., *Search for Low-Mass Weakly Interacting Massive Particles Using Voltage-Assisted Calorimetric Ionization Detection in the SuperCDMS Experiment*, *Phys.Rev.Lett.* **112** (2014), no. 4 041302, [arXiv:1309.3259].

[11] G. Angloher, S. Cooper, R. Keeling, H. Kraus, J. Marchese, et al., *Limits on WIMP dark matter using sapphire cryogenic detectors*, *Astropart.Phys.* **18** (2002) 43–55.

[12] **ATLAS Collaboration**, G. Aad et al., *Observation of a new particle in the search for the Standard Model Higgs boson with the ATLAS detector at the LHC*, *Phys.Lett.* **B716** (2012) 1–29, [arXiv:1207.7214].

[13] **CMS Collaboration**, S. Chatrchyan et al., *Observation of a new boson at a mass of 125 GeV with the CMS experiment at the LHC*, *Phys.Lett.* **B716** (2012) 30–61, [arXiv:1207.7235].

[14] P. W. Higgs, *Broken Symmetries and the Masses of Gauge Bosons*, *Phys.Rev.Lett.* **13** (1964) 508–509.

[15] F. Englert and R. Brout, *Broken Symmetry and the Mass of Gauge Vector Mesons*, *Phys.Rev.Lett.* **13** (1964) 321–323.

[16] G. Guralnik, C. Hagen, and T. Kibble, *Global Conservation Laws and Massless Particles*, *Phys.Rev.Lett.* **13** (1964) 585–587.

[17] **Planck Collaboration**, P. Ade et al., *Planck 2015 results. XIII. Cosmological parameters*, 2015, [arXiv:1502.01589].

[18] H. K. Dreiner, H. E. Haber, and S. P. Martin, *Two-component spinor techniques and Feynman rules for quantum field theory and supersymmetry*, *Phys.Rept.* **494** (2010) 1–196, [arXiv:0812.1594].

[19] C. Wu, E. Ambler, R. Hayward, D. Hoppes, and R. Hudson, *Experimental Test of Parity Conservation in Beta Decay*, *Phys.Rev.* **105** (1957) 1413–1414.

[20] M. E. Peskin and D. V. Schroeder, *An Introduction to Quantum Field Theory*. Westview Press, 1995.

[21] J. E. Kim and G. Carosi, *Axions and the Strong CP Problem*, *Rev.Mod.Phys.* **82** (2010) 557–602, [arXiv:0807.3125].

[22] P. Fileviez Perez and H. H. Patel, *The Electroweak Vacuum Angle*, *Phys.Lett.* **B732** (2014) 241–243, [arXiv:1402.6340].

[23] S. Pokorski, *Gauge Field Theories, Second Edition*. Cambridge University Press, 2003.

[24] M. D. Schwartz, *Quantum Field Theory and the Standard Model*. Cambridge University Press, 2014.

[25] T.-P. Cheng and L.-F. Li, *Gauge Theory of Elementary Particle Physics*. Oxford, 2000.

[26] C. Burgess and G. Moore, *The Standard Model: A Primer*. Cambridge University Press, 2007.

[27] **Particle Data Group**, K. Olive et al., *Review of Particle Physics*, *Chin.Phys.* **C38** (2014) 090001.

[28] I. J. R. Aitchison and A. J. G. Hey, *Gauge Theories in Particle Physics*. Taylor & Francis, 2004.

[29] H. Georgi, *Weak Interactions and Modern Particle Theory*. Dover Publications, 2009.

[30] E. G. John F. Donoghue and B. R. Holstein, *Dynamics of the Standard Model*. Cambridge University Press, 1992.

[31] T. Muta, *Foundations of Quantum Chromodynamics*. World Scientific, 1987.

[32] L. H. Ryder, *Quantum Field Theory*. Cambridge University Press, 1985.

[33] A. Pais, *Inward Bound: of Matter and Forces in the Physical World*. Clarendon Press, 1986.

[34] D. Gross, *Asymptotic freedom and QCD: A historical perspective*, *Nucl.Phys.Proc.Suppl.* **135** (2004) 193–211.

[35] C. Quigg, *Electroweak Symmetry Breaking in Historical Perspective*, *Ann.Rev.Nucl.Part.Sci.* (2015) [arXiv:1503.01756].

[36] S. Weinberg, *Cosmology*. Oxford, 2008.

[37] S. Carroll, *Spacetime and Geometry: An Introduction to General Relativity*. Addison-Wesley, 2003.

[38] **Planck Collaboration**, P. Ade et al., *Planck 2013 results. XVI. Cosmological parameters*, *Astron.Astrophys.* **571** (2014) A16, [arXiv:1303.5076].

[39] G. Efstathiou, *Preliminary 2014 results from planck*, in *PLANCK 2014*, 2014.

[40] E. W. Kolb and M. S. Turner, *The Early Universe*. Westview Press, 1994.

[41] J. Bernstein, *Kinetic Theory in the Expanding Universe*. Cambridge University Press, 2004.

[42] P. Gondolo and G. Gelmini, *Cosmic abundances of stable particles: Improved analysis*, *Nucl.Phys.* **B360** (1991) 145–179.

[43] K. Griest and D. Seckel, *Three exceptions in the calculation of relic abundances*, *Phys.Rev.* **D43** (1991) 3191–3203.

[44] D. Baumann, *TASI Lectures on Inflation*, in *TASI 2009: The Dawn of the LHC Era*, 2009. arXiv:0907.5424.

[45] A. Riotto, *Theories of baryogenesis*, in *Summer School in High Energy Physics and Cosmology*, pp. 326–436, 1998. hep-ph/9807454.

[46] R. Mohapatra and A. Smirnov, *Neutrino Mass and New Physics*, *Ann.Rev.Nucl.Part.Sci.* **56** (2006) 569–628, [hep-ph/0603118].

[47] C. Quigg, *Particle Physics in a Season of Change*, *EPJ Web Conf.* **28** (2012) 01001, [arXiv:1202.4391].

[48] M. Schmaltz and D. Tucker-Smith, *Little Higgs review*, *Ann.Rev.Nucl.Part.Sci.* **55** (2005) 229–270, [hep-ph/0502182].

[49] D. Marzocca, M. Serone, and J. Shu, *General Composite Higgs Models*, *JHEP* **1208** (2012) 013, [arXiv:1205.0770].

[50] C. Csaki, *TASI lectures on extra dimensions and branes*, *TASI 2002: Particle Physics and Cosmology: The Quest for Physics Beyond the Standard Model(s)* (2004) 605–698, [hep-ph/0404096].

[51] E. Ponton, *TASI 2011: Four Lectures on TeV Scale Extra Dimensions*, in *TASI 2011: The Dark Secrets of the Terascale*, 2012. arXiv:1207.3827.

[52] R. Harnik, G. D. Kribs, and G. Perez, *A Universe without weak interactions*, *Phys.Rev.* **D74** (2006) 035006, [hep-ph/0604027].

[53] A. Schellekens, *Life at the Interface of Particle Physics and String Theory*, *Rev.Mod.Phys.* **85** (2013), no. 4 1491–1540, [arXiv:1306.5083].

[54] A. De Rujula, *Avatars of a matter - antimatter universe*, in *32nd Rencontres de Moriond: High-Energy Phenomena in Astrophysics*, 1997. astro-ph/9705045.

[55] A. Sakharov, *Violation of CP Invariance, c Asymmetry, and Baryon Asymmetry of the Universe*, *Pisma Zh.Eksp.Teor.Fiz.* **5** (1967) 32–35.

[56] D. E. Morrissey and M. J. Ramsey-Musolf, *Electroweak baryogenesis*, *New J.Phys.* **14** (2012) 125003, [arXiv:1206.2942].

[57] F. Zwicky, *Die Rotverschiebung von extragalaktischen Nebeln*, *Helv.Phys.Acta* **6** (1933) 110–127.

[58] **Particle Data Group**, J. Beringer et al., *Review of Particle Physics (RPP)*, *Phys.Rev.* **D86** (2012) 010001.

[59] A. Del Popolo, *Nonbaryonic Dark Matter in Cosmology*, *Int.J.Mod.Phys.* **D23** (2014) 1430005, [arXiv:1305.0456].

[60] V. C. Rubin and J. Ford, W. Kent, *Rotation of the Andromeda Nebula from a Spectroscopic Survey of Emission Regions*, *Astrophys.J.* **159** (1970) 379–403.

[61] G. Bertone, D. Hooper, and J. Silk, *Particle dark matter: Evidence, candidates and constraints*, *Phys.Rept.* **405** (2005) 279–390, [hep-ph/0404175].

[62] L. Bergstrom, *Nonbaryonic dark matter: Observational evidence and detection methods*, *Rept.Prog.Phys.* **63** (2000) 793, [hep-ph/0002126].

[63] D. N. Schramm and M. S. Turner, *Big bang nucleosynthesis enters the precision era*, *Rev.Mod.Phys.* **70** (1998) 303–318, [astro-ph/9706069].

[64] K. Nakamura and P. D. Group, *Review of particle physics*, *Journal of Physics G: Nuclear and Particle Physics* **37** (2010), no. 7A 075021.

[65] B. D. Fields, *The primordial lithium problem*, *Ann.Rev.Nucl.Part.Sci.* **61** (2011) 47–68, [arXiv:1203.3551].

[66] K. Lawson and A. R. Zhitnitsky, *Quark (Anti) Nugget Dark Matter*, in *Cosmic Frontier Workshop : Snowmass 2013*, 2013. arXiv:1305.6318.

[67] W. Hu and S. Dodelson, *Cosmic microwave background anisotropies*, *Ann.Rev.Astron.Astrophys.* **40** (2002) 171–216, [astro-ph/0110414].

[68] A. Brooks, *Re-Examining Astrophysical Constraints on the Dark Matter Model*, *Annalen Phys.* **526** (2014), no. 7-8 294–308, [arXiv:1407.7544].

[69] S. Dodelson, *Modern Cosmology*. Academic Press, 2003.

[70] **SDSS Collaboration**, M. Tegmark et al., *The 3-D power spectrum of galaxies from the SDSS*, *Astrophys.J.* **606** (2004) 702–740, [astro-ph/0310725].

[71] M. Kuhlen, M. Vogelsberger, and R. Angulo, *Numerical simulations of the dark universe: State of the art and the next decade*, *Physics of the Dark Universe* **1** (Nov., 2012) 50–93, [arXiv:1209.5745].

[72] D. H. Weinberg, J. S. Bullock, F. Governato, R. K. de Naray, and A. H. G. Peter, *Cold dark matter: controversies on small scales*, in *Sackler Colloquium 2012: Dark Matter Universe : On the Threshhold of Discovery*, 2013. arXiv:1306.0913.

[73] S. Dodelson, *The Real Problem with MOND*, *Int.J.Mod.Phys.* **D20** (2011) 2749–2753, [arXiv:1112.1320].

[74] H. Baer, K.-Y. Choi, J. E. Kim, and L. Roszkowski, *Dark matter production in the early Universe: beyond the thermal WIMP paradigm*, *Phys.Rept.* **555** (2014) 1–60, [arXiv:1407.0017].

[75] G. Jungman, M. Kamionkowski, and K. Griest, *Supersymmetric dark matter*, *Phys.Rept.* **267** (1996) 195–373, [hep-ph/9506380].

[76] P. Cushman, C. Galbiati, D. McKinsey, H. Robertson, T. Tait, et al., *Working Group Report: WIMP Dark Matter Direct Detection*, in *Community Summer Study 2013 : Snowmass on the Mississippi*, 2013. arXiv:1310.8327.

[77] M. Cirelli, *Indirect Searches for Dark Matter: a status review*, *Pramana* **79** (2012) 1021–1043, [arXiv:1202.1454].

[78] J. Conrad, *Indirect Detection of WIMP Dark Matter: a compact review*, in *IPA 2014: Interplay between Particle and Astroparticle physics*, 2014. arXiv:1411.1925.

[79] D. Bauer, J. Buckley, M. Cahill-Rowley, R. Cotta, A. Drlica-Wagner, et al., *Dark Matter in the Coming Decade: Complementary Paths to Discovery and Beyond*, in *Community Summer Study 2013 : Snowmass on the Mississippi*, 2013. arXiv:1305.1605.

[80] S. P. Martin, *A Supersymmetry primer*, *Adv.Ser.Direct.High Energy Phys.* **21** (2010) 1–153, [hep-ph/9709356].

[81] J. Terning, *Modern Supersymmetry: Dynamics and Duality*. Oxford University Press, 2009.

[82] N. Seiberg and E. Witten, *Electric - magnetic duality, monopole condensation, and confinement in N=2 supersymmetric Yang-Mills theory*, *Nucl.Phys.* **B426** (1994) 19–52, [hep-th/9407087].

[83] S. R. Coleman and J. Mandula, *All Possible Symmetries of the S Matrix*, *Phys.Rev.* **159** (1967) 1251–1256.

[84] R. Haag, J. T. Lopuszanski, and M. Sohnius, *All Possible Generators of Supersymmetries of the s Matrix*, *Nucl.Phys.* **B88** (1975) 257.

[85] J. Wess and J. Bagger, *Supersymmetry and Supergravity*. Princeton University Press, 1992.

[86] D. Bertolini, J. Thaler, and Z. Thomas, *TASI 2012: Super-Tricks for Superspace*, in *TASI 2012: Searching for New Physics at Small and Large Scales*, 2013. arXiv:1302.6229.

[87] I. J. R. Aitchison, *Supersymmetry in Particle Physics*. Cambridge University Press, 2007.

[88] S. Ferrara, L. Girardello, and F. Palumbo, *A General Mass Formula in Broken Supersymmetry*, *Phys.Rev.* **D20** (1979) 403.

[89] S. Dimopoulos and D. W. Sutter, *The Supersymmetric flavor problem*, *Nucl.Phys.* **B452** (1995) 496–512, [hep-ph/9504415].

[90] D. Bailin and A. Love, *Supersymmetric Gauge Field Theory and String Theory*. Institute of Physics Publishing, 1994.

[91] L. O'Raifeartaigh, *Spontaneous Symmetry Breaking for Chiral Scalar Superfields*, *Nucl.Phys.* **B96** (1975) 331.

[92] Y. Shadmi and Y. Shirman, *Dynamical supersymmetry breaking*, *Rev.Mod.Phys.* **72** (2000) 25–64, [hep-th/9907225].

[93] K. A. Intriligator and N. Seiberg, *Lectures on Supersymmetry Breaking*, *Class.Quant.Grav.* **24** (2007) S741–S772, [hep-ph/0702069].

[94] M. Dine and J. D. Mason, *Supersymmetry and Its Dynamical Breaking*, *Rept.Prog.Phys.* **74** (2011) 056201, [arXiv:1012.2836].

[95] E. Poppitz and S. P. Trivedi, *Dynamical supersymmetry breaking*, *Ann.Rev.Nucl.Part.Sci.* **48** (1998) 307–350, [hep-th/9803107].

[96] M. Dine, *Supersymmetry and String Theory: Beyong the Standard Model*. Cambridge University Press, 2007.

[97] H. P. Nilles, *Supersymmetry, Supergravity and Particle Physics*, *Phys.Rept.* **110** (1984) 1–162.

[98] D. Cerdeno and C. Munoz, *An introduction to supergravity*, *PoS* **CORFU98** (1998) 011.

[99] S. Weinberg, *The Quantum Theory of Fields: Volume III. Supersymmetry*. Cambridge University Press, 2000.

[100] M. A. Luty, *2004 TASI lectures on supersymmetry breaking*, in *TASI 2004: Physics in D greater than or equal to 4*, pp. 495–582, 2005. hep-th/0509029.

[101] G. Giudice and R. Rattazzi, *Extracting supersymmetry breaking effects from wave function renormalization*, *Nucl.Phys.* **B511** (1998) 25–44, [hep-ph/9706540].

[102] L. Randall and R. Sundrum, *Out of this world supersymmetry breaking*, *Nucl.Phys.* **B557** (1999) 79–118, [hep-th/9810155].

[103] J. A. Bagger, T. Moroi, and E. Poppitz, *Anomaly mediation in supergravity theories*, *JHEP* **0004** (2000) 009, [hep-th/9911029].

[104] **ATLAS Collaboration**, G. Aad et al., *Search for direct pair production of the top squark in all-hadronic final states in proton-proton collisions at $\sqrt{s} = 8$ TeV with the ATLAS detector*, *JHEP* **1409** (2014) 015, [arXiv:1406.1122].

[105] **CMS Collaboration**, *Exclusion limits on gluino and top-squark pair production in natural SUSY scenarios with inclusive razor and exclusive single-lepton searches at 8 TeV*, tech. rep. CMS-PAS-SUS-14-011, 2014.

[106] **CMS Collaboration**, S. Chatrchyan et al., *Search for new physics in the multijet and missing transverse momentum final state in proton-proton collisions at $\sqrt{s}$= 8 TeV*, *JHEP* **1406** (2014) 055, [arXiv:1402.4770].

[107] **ATLAS Collaboration**, G. Aad et al., *Search for squarks and gluinos with the ATLAS detector in final states with jets and missing transverse momentum using $\sqrt{s} = 8$ TeV proton–proton collision data*, *JHEP* **1409** (2014) 176, [arXiv:1405.7875].

[108] **CMS Collaboration**, V. Khachatryan et al., *Searches for electroweak production of charginos, neutralinos, and sleptons decaying to leptons and W, Z, and Higgs bosons in pp collisions at 8 TeV*, *Eur.Phys.J.* **C74** (2014), no. 9 3036, [arXiv:1405.7570].

[109] **ATLAS Collaboration**, G. Aad et al., *Search for direct production of charginos and neutralinos in events with three leptons and missing transverse momentum in $\sqrt{s} =$ 8TeV pp collisions with the ATLAS detector*, *JHEP* **1404** (2014) 169, [arXiv:1402.7029].

[110] M. Carena, H. E. Haber, I. Low, N. R. Shah, and C. E. M. Wagner, *Complementarity between nonstandard Higgs boson searches and precision Higgs boson measurements in the MSSM*, *Phys.Rev.* **D91** (2015), no. 3 035003, [arXiv:1410.4969].

[111] T. Cohen, D. E. Morrissey, and A. Pierce, *Electroweak Baryogenesis and Higgs Signatures*, *Phys.Rev.* **D86** (2012) 013009, [arXiv:1203.2924].

[112] A. Hammad, S. Khalil, and S. Moretti, *Higgs boson decays into $\gamma\gamma$ and $Z\gamma$ in the MSSM and BLSSM*, 2015, [arXiv:1503.05408].

[113] S. Dawson, A. Gritsan, H. Logan, J. Qian, C. Tully, et al., *Working Group Report: Higgs Boson*, in *Community Summer Study 2013 : Snowmass on the Mississippi*, 2013. arXiv:1310.8361.

[114] M. Cahill-Rowley, J. Hewett, A. Ismail, and T. Rizzo, *Higgs boson coupling measurements and direct searches as complementary probes of the phenomenological MSSM*, *Phys.Rev.* **D90** (2014), no. 9 095017, [arXiv:1407.7021].

[115] G. Isidori, Y. Nir, and G. Perez, *Flavor Physics Constraints for Physics Beyond the Standard Model*, *Ann.Rev.Nucl.Part.Sci.* **60** (2010) 355, [arXiv:1002.0900].

[116] W. Altmannshofer, M. Carena, N. R. Shah, and F. Yu, *Indirect Probes of the MSSM after the Higgs Discovery*, *JHEP* **1301** (2013) 160, [arXiv:1211.1976].

[117] **LHCb Collaboration**, R. Aaij et al., *First Evidence for the Decay $B_s^0 \to \mu^+\mu^-$*, *Phys.Rev.Lett.* **110** (2013), no. 2 021801, [arXiv:1211.2674].

[118] M. Ramsey-Musolf and S. Su, *Low Energy Precision Test of Supersymmetry*, *Phys.Rept.* **456** (2008) 1–88, [hep-ph/0612057].

[119] **ACME Collaboration**, J. Baron et al., *Order of Magnitude Smaller Limit on the Electric Dipole Moment of the Electron*, *Science* **343** (2014) 269–272, [arXiv:1310.7534].

[120] M. Cahill-Rowley, R. Cotta, A. Drlica-Wagner, S. Funk, J. Hewett, et al., *Complementarity of dark matter searches in the phenomenological MSSM*, *Phys.Rev.* **D91** (2015), no. 5 055011, [arXiv:1405.6716].

[121] J. Polchinski, *String theory. Vol. 1: An introduction to the bosonic string*. Cambridge University Press, 1998.

[122] J. Polchinski, *String theory. Vol. 2: Superstring theory and beyond*. Cambridge University Press, 1998.

[123] B. de Carlos, J. Casas, F. Quevedo, and E. Roulet, *Model independent properties and cosmological implications of the dilaton and moduli sectors of 4-d strings*, *Phys.Lett.* **B318** (1993) 447–456, [hep-ph/9308325].

[124] B. S. Acharya, G. Kane, and P. Kumar, *Compactified String Theories – Generic Predictions for Particle Physics*, *Int.J.Mod.Phys.* **A27** (2012) 1230012, [arXiv:1204.2795].

[125] F. Quevedo, *Lectures on string/brane cosmology*, *Class.Quant.Grav.* **19** (2002) 5721–5779, [hep-th/0210292].

[126] B. S. Acharya, P. Kumar, K. Bobkov, G. Kane, J. Shao, et al., *Non-thermal Dark Matter and the Moduli Problem in String Frameworks*, *JHEP* **0806** (2008) 064, [arXiv:0804.0863].

[127] M. Dine, L. Randall, and S. D. Thomas, *Supersymmetry breaking in the early universe*, *Phys.Rev.Lett.* **75** (1995) 398–401, [hep-ph/9503303].

[128] R. Durrer and J. Hasenkamp, *Testing Superstring Theories with Gravitational Waves*, *Phys.Rev.* **D84** (2011) 064027, [arXiv:1105.5283].

[129] A. L. Erickcek and K. Sigurdson, *Reheating Effects in the Matter Power Spectrum and Implications for Substructure*, *Phys.Rev.* **D84** (2011) 083503, [arXiv:1106.0536].

[130] R. Easther, R. Galvez, O. Ozsoy, and S. Watson, *Supersymmetry, Nonthermal Dark Matter and Precision Cosmology*, *Phys.Rev.* **D89** (2014), no. 2 023522, [arXiv:1307.2453].

[131] L. Iliesiu, D. J. Marsh, K. Moodley, and S. Watson, *Constraining supersymmetry with heavy scalars: Using the CMB*, *Phys.Rev.* **D89** (2014), no. 10 103513, [arXiv:1312.3636].

[132] J. Fan, O. Özsoy, and S. Watson, *Nonthermal histories and implications for structure formation*, *Phys.Rev.* **D90** (2014), no. 4 043536, [arXiv:1405.7373].

[133] T. Moroi and L. Randall, *Wino cold dark matter from anomaly mediated SUSY breaking*, *Nucl.Phys.* **B570** (2000) 455–472, [hep-ph/9906527].

[134] S. Hannestad, *What is the lowest possible reheating temperature?*, *Phys.Rev.* **D70** (2004) 043506, [astro-ph/0403291].

[135] G. F. Giudice, M. A. Luty, H. Murayama, and R. Rattazzi, *Gaugino mass without singlets*, *JHEP* **9812** (1998) 027, [hep-ph/9810442].

[136] K. Choi, A. Falkowski, H. P. Nilles, M. Olechowski, and S. Pokorski, *Stability of flux compactifications and the pattern of supersymmetry breaking*, *JHEP* **0411** (2004) 076, [hep-th/0411066].

[137] K. Choi, A. Falkowski, H. P. Nilles, and M. Olechowski, *Soft supersymmetry breaking in KKLT flux compactification*, *Nucl.Phys.* **B718** (2005) 113–133, [hep-th/0503216].

[138] A. E. Nelson and N. J. Weiner, *Extended anomaly mediation and new physics at 10-TeV*, 2002, [hep-ph/0210288].

[139] R. Sundrum, *'Gaugomaly' mediated SUSY breaking and conformal sequestering*, *Phys.Rev.* **D71** (2005) 085003, [hep-th/0406012].

[140] K. Hsieh and M. A. Luty, *Mixed gauge and anomaly mediation from new physics at 10-TeV*, *JHEP* **0706** (2007) 062, [hep-ph/0604256].

[141] L. L. Everett, I.-W. Kim, P. Ouyang, and K. M. Zurek, *Moduli Stabilization and Supersymmetry Breaking in Deflected Mirage Mediation*, *JHEP* **0808** (2008) 102, [arXiv:0806.2330].

[142] M. Luty and R. Sundrum, *Anomaly mediated supersymmetry breaking in four-dimensions, naturally*, *Phys.Rev.* **D67** (2003) 045007, [hep-th/0111231].

[143] M. Schmaltz and R. Sundrum, *Conformal Sequestering Simplified*, *JHEP* **0611** (2006) 011, [hep-th/0608051].

[144] A. Anisimov, M. Dine, M. Graesser, and S. D. Thomas, *Brane world SUSY breaking from string / M theory*, *JHEP* **0203** (2002) 036, [hep-th/0201256].

[145] S. Kachru, J. McGreevy, and P. Svrcek, *Bounds on masses of bulk fields in string compactifications*, *JHEP* **0604** (2006) 023, [hep-th/0601111].

[146] S. Kachru, L. McAllister, and R. Sundrum, *Sequestering in String Theory*, *JHEP* **0710** (2007) 013, [hep-th/0703105].

[147] J. D. Wells, *PeV-scale supersymmetry*, *Phys.Rev.* **D71** (2005) 015013, [hep-ph/0411041].

[148] L. J. Hall and Y. Nomura, *Spread Supersymmetry*, *JHEP* **1201** (2012) 082, [arXiv:1111.4519].

[149] A. Arvanitaki, N. Craig, S. Dimopoulos, and G. Villadoro, *Mini-Split*, *JHEP* **1302** (2013) 126, [arXiv:1210.0555].

[150] N. Arkani-Hamed, A. Gupta, D. E. Kaplan, N. Weiner, and T. Zorawski, *Simply Unnatural Supersymmetry*, 2012, [arXiv:1212.6971].

[151] M. Ibe and T. T. Yanagida, *The Lightest Higgs Boson Mass in Pure Gravity Mediation Model*, *Phys.Lett.* **B709** (2012) 374–380, [arXiv:1112.2462].

[152] M. Ibe, S. Matsumoto, and T. T. Yanagida, *Pure Gravity Mediation with $m_{3/2} = 10 - 100$ TeV*, *Phys.Rev.* **D85** (2012) 095011, [arXiv:1202.2253].

[153] G. B. Gelmini and P. Gondolo, *Neutralino with the right cold dark matter abundance in (almost) any supersymmetric model*, *Phys.Rev.* **D74** (2006) 023510, [hep-ph/0602230].

[154] B. S. Acharya, G. Kane, S. Watson, and P. Kumar, *A Non-thermal WIMP Miracle*, *Phys.Rev.* **D80** (2009) 083529, [arXiv:0908.2430].

[155] G. Arcadi and P. Ullio, *Accurate estimate of the relic density and the kinetic decoupling in non-thermal dark matter models*, *Phys.Rev.* **D84** (2011) 043520, [arXiv:1104.3591].

[156] T. Moroi, M. Nagai, and M. Takimoto, *Non-Thermal Production of Wino Dark Matter via the Decay of Long-Lived Particles*, *JHEP* **1307** (2013) 066, [arXiv:1303.0948].

[157] N. Arkani-Hamed, A. Delgado, and G. Giudice, *The Well-tempered neutralino*, *Nucl.Phys.* **B741** (2006) 108–130, [hep-ph/0601041].

[158] T. Cohen, M. Lisanti, A. Pierce, and T. R. Slatyer, *Wino Dark Matter Under Siege*, *JCAP* **1310** (2013) 061, [arXiv:1307.4082].

[159] J. Fan and M. Reece, *In Wino Veritas? Indirect Searches Shed Light on Neutralino Dark Matter*, *JHEP* **1310** (2013) 124, [arXiv:1307.4400].

[160] M. Endo, K. Hamaguchi, and F. Takahashi, *Moduli-induced gravitino problem*, *Phys.Rev.Lett.* **96** (2006) 211301, [hep-ph/0602061].

[161] S. Nakamura and M. Yamaguchi, *Gravitino production from heavy moduli decay and cosmological moduli problem revived*, *Phys.Lett.* **B638** (2006) 389–395, [hep-ph/0602081].

[162] T. Asaka, S. Nakamura, and M. Yamaguchi, *Gravitinos from heavy scalar decay*, *Phys.Rev.* **D74** (2006) 023520, [hep-ph/0604132].

[163] M. Dine, R. Kitano, A. Morisse, and Y. Shirman, *Moduli decays and gravitinos*, *Phys.Rev.* **D73** (2006) 123518, [hep-ph/0604140].

[164] A. Linde, Y. Mambrini, and K. A. Olive, *Supersymmetry Breaking due to Moduli Stabilization in String Theory*, *Phys.Rev.* **D85** (2012) 066005, [arXiv:1111.1465].

[165] J. L. Evans, M. A. Garcia, and K. A. Olive, *The Moduli and Gravitino (non)-Problems in Models with Strongly Stabilized Moduli*, *JCAP* **1403** (2014) 022, [arXiv:1311.0052].

[166] R. Allahverdi, M. Cicoli, B. Dutta, and K. Sinha, *Nonthermal dark matter in string compactifications*, *Phys.Rev.* **D88** (2013), no. 9 095015, [arXiv:1307.5086].

[167] R. Slansky, *Group Theory for Unified Model Building*, *Phys.Rept.* **79** (1981) 1–128.

[168] R. Blumenhagen, M. Cvetic, P. Langacker, and G. Shiu, *Toward realistic intersecting D-brane models*, *Ann.Rev.Nucl.Part.Sci.* **55** (2005) 71–139, [hep-th/0502005].

[169] R. Blumenhagen, B. Kors, D. Lust, and S. Stieberger, *Four-dimensional String Compactifications with D-Branes, Orientifolds and Fluxes*, *Phys.Rept.* **445** (2007) 1–193, [hep-th/0610327].

[170] J. L. Feng and J. Kumar, *The WIMPless Miracle: Dark-Matter Particles without Weak-Scale Masses or Weak Interactions*, *Phys.Rev.Lett.* **101** (2008) 231301, [arXiv:0803.4196].

[171] D. Hooper and K. M. Zurek, *A Natural Supersymmetric Model with MeV Dark Matter*, *Phys.Rev.* **D77** (2008) 087302, [arXiv:0801.3686].

[172] N. Arkani-Hamed and N. Weiner, *LHC Signals for a SuperUnified Theory of Dark Matter*, *JHEP* **0812** (2008) 104, [arXiv:0810.0714].

[173] T. Kaluza, *On the Problem of Unity in Physics*, *Sitzungsber.Preuss.Akad.Wiss.Berlin (Math.Phys.)* **1921** (1921) 966–972.

[174] O. Klein, *Quantum Theory and Five-Dimensional Theory of Relativity. (In German and English)*, *Z.Phys.* **37** (1926) 895–906.

[175] M. R. Douglas and S. Kachru, *Flux compactification*, *Rev.Mod.Phys.* **79** (2007) 733–796, [hep-th/0610102].

[176] D. Bailin and A. Love, *Cosmology in Gauge Field Theory and String Theory*. Institute of Physics Publishing, 2004.

[177] J. Fan, M. Reece, and L.-T. Wang, *Mitigating Moduli Messes in Low-Scale SUSY Breaking*, *JHEP* **1109** (2011) 126, [arXiv:1106.6044].

[178] M. Bose, M. Dine, and P. Draper, *Moduli or Not*, *Phys.Rev.* **D88** (2013) 023533, [arXiv:1305.1066].

[179] S. Kachru, R. Kallosh, A. D. Linde, and S. P. Trivedi, *De Sitter vacua in string theory*, *Phys.Rev.* **D68** (2003) 046005, [hep-th/0301240].

[180] G. Coughlan, W. Fischler, E. W. Kolb, S. Raby, and G. G. Ross, *Cosmological Problems for the Polonyi Potential*, *Phys.Lett.* **B131** (1983) 59.

[181] E. W. Kolb and M. S. Turner, *The Early Universe*, *Front.Phys.* **69** (1990) 1–547.

[182] K. Harigaya, M. Kawasaki, K. Mukaida, and M. Yamada, *Dark Matter Production in Late Time Reheating*, *Phys.Rev.* **D89** (2014), no. 8 083532, [arXiv:1402.2846].

[183] J. Kaplan, *Dark matter generation and split supersymmetry*, *JHEP* **0610** (2006) 065, [hep-ph/0601262].

[184] D. J. Chung, E. W. Kolb, and A. Riotto, *Production of massive particles during reheating*, *Phys.Rev.* **D60** (1999) 063504, [hep-ph/9809453].

[185] G. F. Giudice, E. W. Kolb, and A. Riotto, *Largest temperature of the radiation era and its cosmological implications*, *Phys.Rev.* **D64** (2001) 023508, [hep-ph/0005123].

[186] T. Moroi, *Effects of the gravitino on the inflationary universe*. PhD thesis, Tohoku University, 1995. hep-ph/9503210.

[187] R. Allahverdi, B. Dutta, and K. Sinha, *Non-thermal Higgsino Dark Matter: Cosmological Motivations and Implications for a 125 GeV Higgs*, *Phys.Rev.* **D86** (2012) 095016, [arXiv:1208.0115].

[188] L. Roszkowski, S. Trojanowski, and K. Turzyński, *Neutralino and gravitino dark matter with low reheating temperature*, *JHEP* **1411** (2014) 146, [arXiv:1406.0012].

[189] **ATLAS Collaboration**, G. Aad et al., *Search for charginos nearly mass degenerate with the lightest neutralino based on a disappearing-track signature in pp collisions at $\sqrt{s}$=8 TeV with the ATLAS detector*, *Phys.Rev.* **D88** (2013), no. 11 112006, [arXiv:1310.3675].

[190] N. de Filippis *et al.*, "Combined LEP Chargino Results, up to 208 GeV for low DM.", http://lepsusy.web.cern.ch/lepsusy/www/inoslowdmsummer02/charginolowdm_pub.html (2002).

[191] T. Gherghetta, G. F. Giudice, and J. D. Wells, *Phenomenological consequences of supersymmetry with anomaly induced masses*, *Nucl.Phys.* **B559** (1999) 27–47, [hep-ph/9904378].

[192] A. Gupta, D. E. Kaplan, and T. Zorawski, *Gaugomaly Mediation Revisited*, *JHEP* **1311** (2013) 149, [arXiv:1212.6969].

[193] P. Gondolo, J. Edsjo, P. Ullio, L. Bergstrom, M. Schelke, et al., *DarkSUSY: Computing supersymmetric dark matter properties numerically*, *JCAP* **0407** (2004) 008, [astro-ph/0406204].

[194] P. Gondolo, J. Edsjö, P. Ullio, L. Bergström, M. Schelke, E. Baltz, T. Bringmann, and G. Duda, *DarkSUSY*, 2014.

[195] T. Falk, K. A. Olive, and M. Srednicki, *Heavy sneutrinos as dark matter*, *Phys.Lett.* **B339** (1994) 248–251, [hep-ph/9409270].

[196] M. Srednicki, K. A. Olive, and J. Silk, *High-Energy Neutrinos from the Sun and Cold Dark Matter*, *Nucl.Phys.* **B279** (1987) 804.

[197] D. E. Morrissey, D. Poland, and K. M. Zurek, *Abelian Hidden Sectors at a GeV*, *JHEP* **0907** (2009) 050, [arXiv:0904.2567].

[198] J. L. Feng, V. Rentala, and Z. Surujon, *WIMPless Dark Matter in Anomaly-Mediated Supersymmetry Breaking with Hidden QED*, *Phys.Rev.* **D84** (2011) 095033, [arXiv:1108.4689].

[199] J. L. Feng, V. Rentala, and Z. Surujon, *WIMPless Dark Matter from an AMSB Hidden Sector with No New Mass Parameters*, *Phys.Rev.* **D85** (2012) 055003, [arXiv:1111.4479].

[200] Y. F. Chan, M. Low, D. E. Morrissey, and A. P. Spray, *LHC Signatures of a Minimal Supersymmetric Hidden Valley*, *JHEP* **1205** (2012) 155, [arXiv:1112.2705].

[201] D. E. Morrissey and A. P. Spray, *New Limits on Light Hidden Sectors from Fixed-Target Experiments*, *JHEP* **1406** (2014) 083, [arXiv:1402.4817].

[202] J. D. Bjorken, R. Essig, P. Schuster, and N. Toro, *New Fixed-Target Experiments to Search for Dark Gauge Forces*, *Phys.Rev.* **D80** (2009) 075018, [arXiv:0906.0580].

[203] R. Essig, J. A. Jaros, W. Wester, P. H. Adrian, S. Andreas, et al., *Working Group Report: New Light Weakly Coupled Particles*, in *Community Summer Study 2013 : Snowmass on the Mississippi*, 2013. arXiv:1311.0029.

[204] **BaBar Collaboration**, J. Lees et al., *Search for a Dark Photon in e^+e^- Collisions at BaBar*, *Phys.Rev.Lett.* **113** (2014), no. 20 201801, [arXiv:1406.2980].

[205] **Fermi-LAT Collaboration**, http://fermi.gsfc.nasa.gov/ssc/data/access/ (2014).

[206] L. Bouchet, E. Jourdain, J. Roques, A. Strong, R. Diehl, et al., *INTEGRAL SPI All-Sky View in Soft Gamma Rays: Study of Point Source and Galactic Diffuse Emissions*, *Astrophys.J.* **679** (2008) 1315, [arXiv:0801.2086].

[207] S. C. Kappadath, *Measurement of the Cosmic Diffuse Gamma-Ray Spectrum from 800 keV to 30 MeV*. PhD thesis, University of New Hampshire, 1998.

[208] A. W. Strong, I. V. Moskalenko, and O. Reimer, *Evaluation of models for diffuse continuum gamma-rays in EGRET range*, 2003, [astro-ph/0306346].

[209] A. W. Strong, I. V. Moskalenko, and O. Reimer, *Diffuse galactic continuum gamma rays. A Model compatible with EGRET data and cosmic-ray measurements*, *Astrophys.J.* **613** (2004) 962–976, [astro-ph/0406254].

[210] **Fermi-LAT Collaboration**, M. Ackermann, M. Ajello, W. B. Atwood, L. Baldini, J. Ballet, G. Barbiellini, D. Bastieri, et al., *Fermi-LAT Observations of the Diffuse Gamma-Ray Emission: Implications for Cosmic Rays and the Interstellar Medium*, *Astrophys.J.* **750** (2012) 3, [arXiv:1202.4039].

[211] D. Hooper, C. Kelso, and F. S. Queiroz, *Stringent and Robust Constraints on the Dark Matter Annihilation Cross Section From the Region of the Galactic Center*, *Astropart.Phys.* **46** (2013) 55–70, [arXiv:1209.3015].

[212] R. Essig, E. Kuflik, S. D. McDermott, T. Volansky, and K. M. Zurek, *Constraining Light Dark Matter with Diffuse X-Ray and Gamma-Ray Observations*, *JHEP* **1311** (2013) 193, [arXiv:1309.4091].

[213] N. Padmanabhan and D. P. Finkbeiner, *Detecting dark matter annihilation with CMB polarization: Signatures and experimental prospects*, *Phys.Rev.* **D72** (2005) 023508, [astro-ph/0503486].

[214] T. R. Slatyer, N. Padmanabhan, and D. P. Finkbeiner, *CMB Constraints on WIMP Annihilation: Energy Absorption During the Recombination Epoch*, *Phys.Rev.* **D80** (2009) 043526, [arXiv:0906.1197].

[215] P. Meade, M. Papucci, and T. Volansky, *Dark Matter Sees The Light*, *JHEP* **0912** (2009) 052, [arXiv:0901.2925].

[216] D. Hooper, N. Weiner, and W. Xue, *Dark Forces and Light Dark Matter*, *Phys.Rev.* **D86** (2012) 056009, [arXiv:1206.2929].

[217] J. F. Navarro, C. S. Frenk, and S. D. White, *The Structure of cold dark matter halos*, *Astrophys.J.* **462** (1996) 563–575, [astro-ph/9508025].

[218] J. F. Navarro, E. Hayashi, C. Power, A. Jenkins, C. S. Frenk, et al., *The Inner structure of Lambda-CDM halos 3: Universality and asymptotic slopes*, *Mon.Not.Roy.Astron.Soc.* **349** (2004) 1039, [astro-ph/0311231].

[219] V. Springel, J. Wang, M. Vogelsberger, A. Ludlow, A. Jenkins, et al., *The Aquarius Project: the subhalos of galactic halos*, *Mon.Not.Roy.Astron.Soc.* **391** (2008) 1685–1711, [arXiv:0809.0898].

[220] G. Hutsi, J. Chluba, A. Hektor, and M. Raidal, *WMAP7 and future CMB constraints on annihilating dark matter: implications on GeV-scale WIMPs*, *Astron.Astrophys.* **535** (2011) A26, [arXiv:1103.2766].

[221] S. Galli, F. Iocco, G. Bertone, and A. Melchiorri, *Updated CMB constraints on Dark Matter annihilation cross-sections*, *Phys.Rev.* **D84** (2011) 027302, [arXiv:1106.1528].

[222] D. P. Finkbeiner, S. Galli, T. Lin, and T. R. Slatyer, *Searching for Dark Matter in the CMB: A Compact Parameterization of Energy Injection from New Physics*, *Phys.Rev.* **D85** (2012) 043522, [arXiv:1109.6322].

[223] A. Pomarol and R. Rattazzi, *Sparticle masses from the superconformal anomaly*, *JHEP* **9905** (1999) 013, [hep-ph/9903448].

[224] E. Katz, Y. Shadmi, and Y. Shirman, *Heavy thresholds, slepton masses and the mu term in anomaly mediated supersymmetry breaking*, *JHEP* **9908** (1999) 015, [hep-ph/9906296].

[225] S. Nussinov, *Technocosmology: Could a Technibaryon Excess Provide a 'natural' Missing Mass Candidate?*, *Phys.Lett.* **B165** (1985) 55.

[226] S. M. Barr, *Baryogenesis, sphalerons and the cogeneration of dark matter*, *Phys.Rev.* **D44** (1991) 3062–3066.

[227] D. B. Kaplan, *A Single explanation for both the baryon and dark matter densities*, *Phys.Rev.Lett.* **68** (1992) 741–743.

[228] D. E. Kaplan, M. A. Luty, and K. M. Zurek, *Asymmetric Dark Matter*, *Phys.Rev.* **D79** (2009) 115016, [arXiv:0901.4117].

[229] M. L. Graesser, I. M. Shoemaker, and L. Vecchi, *Asymmetric WIMP dark matter*, *JHEP* **1110** (2011) 110, [arXiv:1103.2771].

[230] H. Iminniyaz, M. Drees, and X. Chen, *Relic Abundance of Asymmetric Dark Matter*, *JCAP* **1107** (2011) 003, [arXiv:1104.5548].

[231] N. F. Bell, S. Horiuchi, and I. M. Shoemaker, *Annihilating Asymmetric Dark Matter*, *Phys.Rev.* **D91** (2015) 023505, [arXiv:1408.5142].

[232] H. Davoudiasl, D. E. Morrissey, K. Sigurdson, and S. Tulin, *Hylogenesis: A Unified Origin for Baryonic Visible Matter and Antibaryonic Dark Matter*, *Phys.Rev.Lett.* **105** (2010) 211304, [arXiv:1008.2399].

[233] R. Allahverdi, B. Dutta, and K. Sinha, *Cladogenesis: Baryon-Dark Matter Coincidence from Branchings in Moduli Decay*, *Phys.Rev.* **D83** (2011) 083502, [arXiv:1011.1286].

[234] N. F. Bell, K. Petraki, I. M. Shoemaker, and R. R. Volkas, *Pangenesis in a Baryon-Symmetric Universe: Dark and Visible Matter via the Affleck-Dine Mechanism*, *Phys.Rev.* **D84** (2011) 123505, [arXiv:1105.3730].

[235] C. Cheung and K. M. Zurek, *Affleck-Dine Cogenesis*, *Phys.Rev.* **D84** (2011) 035007, [arXiv:1105.4612].

[236] G. Kane, J. Shao, S. Watson, and H.-B. Yu, *The Baryon-Dark Matter Ratio Via Moduli Decay After Affleck-Dine Baryogenesis*, *JCAP* **1111** (2011) 012, [arXiv:1108.5178].

[237] K. M. Zurek, *Asymmetric Dark Matter: Theories, Signatures, and Constraints*, *Phys.Rept.* **537** (2014) 91–121, [arXiv:1308.0338].

[238] W. Fischler, D. Lorshbough, and W. Tangarife, *Supersymmetric Partially Interacting Dark Matter*, *Phys.Rev.* **D91** (2015), no. 2 025010, [arXiv:1405.7708].

[239] J. L. Feng and Y. Shadmi, *WIMPless Dark Matter from Non-Abelian Hidden Sectors with Anomaly-Mediated Supersymmetry Breaking*, *Phys.Rev.* **D83** (2011) 095011, [arXiv:1102.0282].

[240] K. K. Boddy, J. L. Feng, M. Kaplinghat, and T. M. P. Tait, *Self-Interacting Dark Matter from a Non-Abelian Hidden Sector*, *Phys.Rev.* **D89** (2014) 115017, [arXiv:1402.3629].

[241] T. Appelquist and H. D. Politzer, *Orthocharmonium and e^+e^- Annihilation*, *Phys.Rev.Lett.* **34** (1975) 43.

[242] S. J. Brodsky, J. Gunion, and D. E. Soper, *The Physics of Heavy Quark Production in Quantum Chromodynamics*, *Phys.Rev.* **D36** (1987) 2710.

[243] H. Baer, K.-m. Cheung, and J. F. Gunion, *A Heavy gluino as the lightest supersymmetric particle*, *Phys.Rev.* **D59** (1999) 075002, [hep-ph/9806361].

[244] R. H. Cyburt, B. D. Fields, K. A. Olive, and E. Skillman, *New BBN limits on physics beyond the standard model from He-4*, *Astropart.Phys.* **23** (2005) 313–323, [astro-ph/0408033].

[245] G. Mangano and P. D. Serpico, *A robust upper limit on $N_{\rm eff}$ from BBN, circa 2011*, *Phys.Lett.* **B701** (2011) 296–299, [arXiv:1103.1261].

[246] E. Di Valentino, A. Melchiorri, and O. Mena, *Dark radiation sterile neutrino candidates after Planck data*, *JCAP* **1311** (2013) 018, [arXiv:1304.5981].

[247] L. Ackerman, M. R. Buckley, S. M. Carroll, and M. Kamionkowski, *Dark Matter and Dark Radiation*, *Phys.Rev.* **D79** (2009) 023519, [arXiv:0810.5126].

[248] J. L. Feng, M. Kaplinghat, H. Tu, and H.-B. Yu, *Hidden Charged Dark Matter*, *JCAP* **0907** (2009) 004, [arXiv:0905.3039].

[249] M. R. Buckley and P. J. Fox, *Dark Matter Self-Interactions and Light Force Carriers*, *Phys.Rev.* **D81** (2010) 083522, [arXiv:0911.3898].

[250] M. Rocha, A. H. Peter, J. S. Bullock, M. Kaplinghat, S. Garrison-Kimmel, et al., *Cosmological Simulations with Self-Interacting Dark Matter I: Constant Density Cores and Substructure*, *Mon.Not.Roy.Astron.Soc.* **430** (2013) 81–104, [arXiv:1208.3025].

[251] A. H. Peter, M. Rocha, J. S. Bullock, and M. Kaplinghat, *Cosmological Simulations with Self-Interacting Dark Matter II: Halo Shapes vs. Observations*, *Mon.Not.Roy.Astron.Soc.* **430** (2013) 105, [arXiv:1208.3026].

[252] M. Vogelsberger, J. Zavala, and A. Loeb, *Subhaloes in Self-Interacting Galactic Dark Matter Haloes*, *Mon.Not.Roy.Astron.Soc.* **423** (2012) 3740, [arXiv:1201.5892].

[253] J. Zavala, M. Vogelsberger, and M. G. Walker, *Constraining Self-Interacting Dark Matter with the Milky Way's dwarf spheroidals*, *Monthly Notices of the Royal Astronomical Society: Letters* **431** (2013) L20–L24, [arXiv:1211.6426].

[254] D. J. Gross, R. D. Pisarski, and L. G. Yaffe, *QCD and Instantons at Finite Temperature*, *Rev.Mod.Phys.* **53** (1981) 43.

[255] L. D. McLerran, *The Physics of the Quark - Gluon Plasma*, *Rev.Mod.Phys.* **58** (1986) 1021–1064.

[256] P. B. Arnold and L. G. Yaffe, *The NonAbelian Debye screening length beyond leading order*, *Phys.Rev.* **D52** (1995) 7208–7219, [hep-ph/9508280].

[257] S. Tulin, H.-B. Yu, and K. M. Zurek, *Beyond Collisionless Dark Matter: Particle Physics Dynamics for Dark Matter Halo Structure*, *Phys.Rev.* **D87** (2013), no. 11 115007, [arXiv:1302.3898].

[258] D. V. Nanopoulos, S. Ono, and T. Yanagida, *How Would the World Look if There Were Supersymmetric Particles?*, *Phys.Lett.* **B137** (1984) 363.

[259] J. H. Kuhn and S. Ono, *Production and Decay of Gluino - Gluino Bound States*, *Phys.Lett.* **B142** (1984) 436.

[260] J. T. Goldman and H. Haber, *Gluinonium: The Hydrogen Atom of Supersymmetry*, *Physica* **15D** (1985) 181–196.

[261] F.-Y. Cyr-Racine, R. de Putter, A. Raccanelli, and K. Sigurdson, *Constraints on Large-Scale Dark Acoustic Oscillations from Cosmology*, *Phys.Rev.* **D89** (2014) 063517, [arXiv:1310.3278].

[262] S. Dubovsky, D. Gorbunov, and G. Rubtsov, *Narrowing the window for millicharged particles by CMB anisotropy*, *JETP Lett.* **79** (2004) 1–5, [hep-ph/0311189].

[263] A. Dolgov, S. Dubovsky, G. Rubtsov, and I. Tkachev, *Constraints on millicharged particles from Planck data*, *Phys.Rev.* **D88** (2013), no. 11 117701, [arXiv:1310.2376].

[264] J. Fan, A. Katz, L. Randall, and M. Reece, *Double-Disk Dark Matter*, *Phys.Dark Univ.* **2** (2013) 139–156, [arXiv:1303.1521].

[265] M. Kawasaki, K. Kohri, and T. Moroi, *Big-Bang nucleosynthesis and hadronic decay of long-lived massive particles*, *Phys.Rev.* **D71** (2005) 083502, [astro-ph/0408426].

[266] K. Jedamzik, *Big bang nucleosynthesis constraints on hadronically and electromagnetically decaying relic neutral particles*, *Phys.Rev.* **D74** (2006) 103509, [hep-ph/0604251].

[267] D. Hooper, J. March-Russell, and S. M. West, *Asymmetric sneutrino dark matter and the Ω_b/Ω_{DM} puzzle*, *Phys.Lett.* **B605** (2005) 228–236, [hep-ph/0410114].

[268] R. Kitano and I. Low, *Dark matter from baryon asymmetry*, *Phys.Rev.* **D71** (2005) 023510, [hep-ph/0411133].

[269] K. Agashe and G. Servant, *Baryon number in warped GUTs: Model building and (dark matter related) phenomenology*, *JCAP* **0502** (2005) 002, [hep-ph/0411254].

[270] G. R. Farrar and G. Zaharijas, *Dark matter and the baryon asymmetry*, *Phys.Rev.Lett.* **96** (2006) 041302, [hep-ph/0510079].

[271] K. Kohri, A. Mazumdar, N. Sahu, and P. Stephens, *Probing Unified Origin of Dark Matter and Baryon Asymmetry at PAMELA/Fermi*, *Phys.Rev.* **D80** (2009) 061302, [arXiv:0907.0622].

[272] J. Shelton and K. M. Zurek, *Darkogenesis: A baryon asymmetry from the dark matter sector*, *Phys.Rev.* **D82** (2010) 123512, [arXiv:1008.1997].

[273] P. Hut and K. A. Olive, *A COSMOLOGICAL UPPER LIMIT ON THE MASS OF HEAVY NEUTRINOS*, *Phys.Lett.* **B87** (1979) 144–146.

[274] S. Dodelson and L. M. Widrow, *Baryogenesis in a Baryon Symmetric Universe*, *Phys.Rev.* **D42** (1990) 326–342.

[275] V. A. Kuzmin, *A Simultaneous solution to baryogenesis and dark matter problems*, *Phys.Part.Nucl.* **29** (1998) 257–265, [hep-ph/9701269].

[276] P.-H. Gu, *Origin of matter in the universe*, *Phys.Lett.* **B657** (2007) 103–106, [arXiv:0706.1946].

[277] H. An, S.-L. Chen, R. N. Mohapatra, and Y. Zhang, *Leptogenesis as a Common Origin for Matter and Dark Matter*, *JHEP* **1003** (2010) 124, [arXiv:0911.4463].

[278] H. Davoudiasl and R. N. Mohapatra, *On Relating the Genesis of Cosmic Baryons and Dark Matter*, *New J.Phys.* **14** (2012) 095011, [arXiv:1203.1247].

[279] H. Davoudiasl, D. E. Morrissey, K. Sigurdson, and S. Tulin, *Baryon Destruction by Asymmetric Dark Matter*, *Phys.Rev.* **D84** (2011) 096008, [arXiv:1106.4320].

[280] S. Dimopoulos and L. J. Hall, *Baryogenesis at the MeV Era*, *Phys.Lett.* **B196** (1987) 135.

[281] **Super-Kamiokande Collaboration**, K. Kobayashi et al., *Search for nucleon decay via modes favored by supersymmetric grand unification models in Super-Kamiokande-I*, *Phys.Rev.* **D72** (2005) 052007, [hep-ex/0502026].

[282] **LBNE Collaboration**, T. Akiri et al., *The 2010 Interim Report of the Long-Baseline Neutrino Experiment Collaboration Physics Working Groups*, 2011, [arXiv:1110.6249].

[283] **IceCube Collaboration**, R. Abbasi et al., *The IceCube Neutrino Observatory V: Future Developments*, 2011, [arXiv:1111.2742].

[284] J. Hewett, H. Weerts, R. Brock, J. Butler, B. Casey, et al., *Fundamental Physics at the Intensity Frontier*, 2012, [arXiv:1205.2671].

[285] T. Cohen and K. M. Zurek, *Leptophilic Dark Matter from the Lepton Asymmetry*, *Phys.Rev.Lett.* **104** (2010) 101301, [arXiv:0909.2035].

[286] M. R. Buckley and S. Profumo, *Regenerating a Symmetry in Asymmetric Dark Matter*, *Phys.Rev.Lett.* **108** (2012) 011301, [arXiv:1109.2164].

[287] M. Cirelli, P. Panci, G. Servant, and G. Zaharijas, *Consequences of DM/antiDM Oscillations for Asymmetric WIMP Dark Matter*, *JCAP* **1203** (2012) 015, [arXiv:1110.3809].

[288] S. Tulin, H.-B. Yu, and K. M. Zurek, *Oscillating Asymmetric Dark Matter*, *JCAP* **1205** (2012) 013, [arXiv:1202.0283].

[289] L. E. Ibanez and G. G. Ross, *Discrete gauge symmetry anomalies*, *Phys.Lett.* **B260** (1991) 291–295.

[290] L. M. Krauss and F. Wilczek, *Discrete Gauge Symmetry in Continuum Theories*, *Phys.Rev.Lett.* **62** (1989) 1221.

[291] M. Pospelov, A. Ritz, and M. B. Voloshin, *Secluded WIMP Dark Matter*, *Phys.Lett.* **B662** (2008) 53–61, [arXiv:0711.4866].

[292] M. Pospelov, *Secluded U(1) below the weak scale*, *Phys.Rev.* **D80** (2009) 095002, [arXiv:0811.1030].

[293] B. Batell, M. Pospelov, and A. Ritz, *Probing a Secluded U(1) at B-factories*, *Phys.Rev.* **D79** (2009) 115008, [arXiv:0903.0363].

[294] R. Allahverdi, B. Dutta, and K. Sinha, *Baryogenesis and Late-Decaying Moduli*, *Phys.Rev.* **D82** (2010) 035004, [arXiv:1005.2804].

[295] B. S. Acharya, G. Kane, and E. Kuflik, *String Theories with Moduli Stabilization Imply Non-Thermal Cosmological History, and Particular Dark Matter*, 2010, [arXiv:1006.3272].

[296] U. Ellwanger and P. Mitropoulos, *Upper Bounds on Asymmetric Dark Matter Self Annihilation Cross Sections*, *JCAP* **1207** (2012) 024, [arXiv:1205.0673].

[297] M. Baumgart, C. Cheung, J. T. Ruderman, L.-T. Wang, and I. Yavin, *Non-Abelian Dark Sectors and Their Collider Signatures*, *JHEP* **0904** (2009) 014, [arXiv:0901.0283].

[298] A. Kumar, D. E. Morrissey, and A. Spray, *Kinetically-Enhanced Anomaly Mediation*, *JHEP* **1112** (2011) 013, [arXiv:1109.1565].

[299] Z. Chacko, M. A. Luty, I. Maksymyk, and E. Ponton, *Realistic anomaly mediated supersymmetry breaking*, *JHEP* **0004** (2000) 001, [hep-ph/9905390].

[300] M. Claudson, M. B. Wise, and L. J. Hall, *Chiral Lagrangian for Deep Mine Physics*, *Nucl.Phys.* **B195** (1982) 297.

[301] **RBC-UKQCD Collaboration**, Y. Aoki et al., *Proton lifetime bounds from chirally symmetric lattice QCD*, *Phys.Rev.* **D78** (2008) 054505, [arXiv:0806.1031].

[302] M. Reece and L.-T. Wang, *Searching for the light dark gauge boson in GeV-scale experiments*, *JHEP* **0907** (2009) 051, [arXiv:0904.1743].

[303] **A1 Collaboration**, H. Merkel et al., *Search for Light Gauge Bosons of the Dark Sector at the Mainz Microtron*, *Phys.Rev.Lett.* **106** (2011) 251802, [arXiv:1101.4091].

[304] **APEX Collaboration**, S. Abrahamyan et al., *Search for a New Gauge Boson in Electron-Nucleus Fixed-Target Scattering by the APEX Experiment*, *Phys.Rev.Lett.* **107** (2011) 191804, [arXiv:1108.2750].

[305] S. Andreas and A. Ringwald, *Status of sub-GeV Hidden Particle Searches*, in *6th Patras Workshop on Axions, WIMPs and WISPs*, 2010. arXiv:1008.4519.

[306] **CoGeNT collaboration**, C. Aalseth et al., *Results from a Search for Light-Mass Dark Matter with a P-type Point Contact Germanium Detector*, *Phys.Rev.Lett.* **106** (2011) 131301, [arXiv:1002.4703].

[307] **CDMS Collaboration**, D. Akerib et al., *A low-threshold analysis of CDMS shallow-site data*, *Phys.Rev.* **D82** (2010) 122004, [arXiv:1010.4290].

[308] **XENON100 Collaboration**, E. Aprile et al., *Dark Matter Results from 100 Live Days of XENON100 Data*, *Phys.Rev.Lett.* **107** (2011) 131302, [arXiv:1104.2549].

[309] R. Essig, J. Mardon, and T. Volansky, *Direct Detection of Sub-GeV Dark Matter*, *Phys.Rev.* **D85** (2012) 076007, [arXiv:1108.5383].

[310] **ATLAS Collaboration**, *Search for New Phenomena in Monojet plus Missing Transverse Momentum Final States using 1 fb^{-1} of pp Collisions at $\sqrt{s} = 7$ TeV with the ATLAS Detector*, tech. rep. ATLAS-CONF-2011-096, 2011.

[311] **CDF Collaboration**, T. Aaltonen et al., *A Search for dark matter in events with one jet and missing transverse energy in $p\bar{p}$ collisions at $\sqrt{s} = 1.96$ TeV*, *Phys.Rev.Lett.* **108** (2012) 211804, [arXiv:1203.0742].

[312] **ATLAS Collaboration**, *Search for New Physics in Dijet Mass and Angular Distributions using 4.8/fb of pp Collisions at $\sqrt{s} = 7$ TeV collected by the ATLAS Detector*, tech. rep. ATLAS-CONF-2012-038, ATLAS-COM-CONF-2012-027, 2012.

[313] **CMS Collaboration**, S. Chatrchyan et al., *Search for Resonances in the Dijet Mass Spectrum from 7 TeV pp Collisions at CMS*, *Phys.Lett.* **B704** (2011) 123–142, [arXiv:1107.4771].

[314] **CMS Collaboration**, S. Chatrchyan et al., *Search for quark compositeness in dijet angular distributions from pp collisions at $\sqrt{s} = 7$ TeV*, *JHEP* **1205** (2012) 055, [arXiv:1202.5535].

[315] S. R. Coleman, *The Fate of the False Vacuum. 1. Semiclassical Theory*, *Phys.Rev.* **D15** (1977) 2929–2936.

[316] J. Callan, Curtis G. and S. R. Coleman, *The Fate of the False Vacuum. 2. First Quantum Corrections*, *Phys.Rev.* **D16** (1977) 1762–1768.

[317] R. H. Brandenberger, *Quantum Field Theory Methods and Inflationary Universe Models*, *Rev.Mod.Phys.* **57** (1985) 1.

[318] C. M. Bender and S. A. Orszag, *Advanced Mathematical Methods for Scientists and Engineers: Asymptotic Methods and Perturbation Theory*. Springer, 1999.

[319] S. R. Coleman, *Aspects of Symmetry*. Cambridge University Press, 1985.

[320] G. V. Dunne and H. Min, *Beyond the thin-wall approximation: Precise numerical computation of prefactors in false vacuum decay*, *Phys.Rev.* **D72** (2005) 125004, [hep-th/0511156].

[321] H. Min, *On the prefactor in false vacuum decay*, *J.Phys.* **A39** (2006) 6551–6557.

[322] E. J. Weinberg, *Vacuum decay in theories with symmetry breaking by radiative corrections*, *Phys.Rev.* **D47** (1993) 4614–4627, [hep-ph/9211314].

[323] S. R. Coleman, *Quantum Tunneling and Negative Eigenvalues*, *Nucl.Phys.* **B298** (1988) 178.

[324] R. Rajaraman, *Solitons and Instantons*. North Holland, 1987.

[325] V. Rubakov, *Classical Theory of Gauge Fields*. Princeton University Press, 2002.

[326] M. A. Shifman, *Advanced Topics in Quantum Field Theory*. Cambridge University Press, 2012.

[327] M. Dine, P. Draper, and C.-S. Park, *Deformed Bubbles and Lorentz Invariance in Vacuum Decay*, *Phys.Rev.* **D86** (2012) 065033, [arXiv:1206.5880].

[328] J. Kapusta and C. Gale, *Finite Temperature Field Theory: Principles and Applications*. Cambridge University Press, 2006.

[329] I. Affleck, *Quantum Statistical Metastability*, *Phys.Rev.Lett.* **46** (1981) 388.

[330] A. D. Linde, *Decay of the False Vacuum at Finite Temperature*, *Nucl.Phys.* **B216** (1983) 421.

[331] M. Sher, *Electroweak Higgs Potentials and Vacuum Stability*, *Phys.Rept.* **179** (1989) 273–418.

[332] M. Quiros, *Finite temperature field theory and phase transitions*, in *ICTP Summer School in High Energy Physics and Cosmology*, pp. 187–259, 1999. hep-ph/9901312.

[333] T. Konstandin and S. J. Huber, *Numerical approach to multi dimensional phase transitions*, *JCAP* **0606** (2006) 021, [hep-ph/0603081].

[334] J.-h. Park, *Constrained potential method for false vacuum decays*, *JCAP* **1102** (2011) 023, [arXiv:1011.4936].

[335] C. L. Wainwright, *CosmoTransitions: Computing Cosmological Phase Transition Temperatures and Bubble Profiles with Multiple Fields*, *Comput.Phys.Commun.* **183** (2012) 2006–2013, [arXiv:1109.4189].

[336] R. Barbieri and G. Giudice, *Upper Bounds on Supersymmetric Particle Masses*, *Nucl.Phys.* **B306** (1988) 63.

[337] C. Wymant, *Optimising Stop Naturalness*, *Phys.Rev.* **D86** (2012) 115023, [arXiv:1208.1737].

[338] L. J. Hall, D. Pinner, and J. T. Ruderman, *A Natural SUSY Higgs Near 126 GeV*, *JHEP* **1204** (2012) 131, [arXiv:1112.2703].

[339] J.-J. Cao, Z.-X. Heng, J. M. Yang, Y.-M. Zhang, and J.-Y. Zhu, *A SM-like Higgs near 125 GeV in low energy SUSY: a comparative study for MSSM and NMSSM*, *JHEP* **1203** (2012) 086, [arXiv:1202.5821].

[340] J. R. Ellis, G. Ridolfi, and F. Zwirner, *Radiative corrections to the masses of supersymmetric Higgs bosons*, *Phys.Lett.* **B257** (1991) 83–91.

[341] H. E. Haber and R. Hempfling, *Can the mass of the lightest Higgs boson of the minimal supersymmetric model be larger than m_Z?*, *Phys.Rev.Lett.* **66** (1991) 1815–1818.

[342] M. S. Carena, H. Haber, S. Heinemeyer, W. Hollik, C. Wagner, et al., *Reconciling the two loop diagrammatic and effective field theory computations of the mass of the lightest CP - even Higgs boson in the MSSM*, *Nucl.Phys.* **B580** (2000) 29–57, [hep-ph/0001002].

[343] P. Draper, P. Meade, M. Reece, and D. Shih, *Implications of a 125 GeV Higgs for the MSSM and Low-Scale SUSY Breaking*, *Phys.Rev.* **D85** (2012) 095007, [arXiv:1112.3068].

[344] J. Casas, J. Espinosa, M. Quiros, and A. Riotto, *The Lightest Higgs boson mass in the minimal supersymmetric standard model*, *Nucl.Phys.* **B436** (1995) 3–29, [hep-ph/9407389].

[345] R. Kitano and Y. Nomura, *Supersymmetry, naturalness, and signatures at the LHC*, *Phys.Rev.* **D73** (2006) 095004, [hep-ph/0602096].

[346] J. Frere, D. Jones, and S. Raby, *Fermion Masses and Induction of the Weak Scale by Supergravity*, *Nucl.Phys.* **B222** (1983) 11.

[347] G. Gamberini, G. Ridolfi, and F. Zwirner, *On Radiative Gauge Symmetry Breaking in the Minimal Supersymmetric Model*, *Nucl.Phys.* **B331** (1990) 331–349.

[348] M. Claudson, L. J. Hall, and I. Hinchliffe, *Low-Energy Supergravity: False Vacua and Vacuous Predictions*, *Nucl.Phys.* **B228** (1983) 501.

[349] J. Casas, A. Lleyda, and C. Munoz, *Strong constraints on the parameter space of the MSSM from charge and color breaking minima*, *Nucl.Phys.* **B471** (1996) 3–58, [hep-ph/9507294].

[350] T. Falk, K. A. Olive, L. Roszkowski, and M. Srednicki, *New constraints on superpartner masses*, *Phys.Lett.* **B367** (1996) 183–187, [hep-ph/9510308].

[351] A. Riotto and E. Roulet, *Vacuum decay along supersymmetric flat directions*, *Phys.Lett.* **B377** (1996) 60–66, [hep-ph/9512401].

[352] J. Casas, A. Lleyda, and C. Munoz, *Some implications of charge and color breaking in the MSSM*, *Phys.Lett.* **B389** (1996) 305–311, [hep-ph/9606212].

[353] C. Le Mouel, *Optimal charge and color breaking conditions in the MSSM*, *Nucl.Phys.* **B607** (2001) 38–76, [hep-ph/0101351].

[354] C. Le Mouel, *Charge and color breaking conditions associated to the top quark Yukawa coupling*, *Phys.Rev.* **D64** (2001) 075009, [hep-ph/0103341].

[355] M. S. Carena, M. Quiros, and C. Wagner, *Opening the window for electroweak baryogenesis*, *Phys.Lett.* **B380** (1996) 81–91, [hep-ph/9603420].

[356] J. M. Cline, G. D. Moore, and G. Servant, *Was the electroweak phase transition preceded by a color broken phase?*, *Phys.Rev.* **D60** (1999) 105035, [hep-ph/9902220].

[357] H. H. Patel, M. J. Ramsey-Musolf, and M. B. Wise, *Color Breaking in the Early Universe*, *Phys.Rev.* **D88** (2013) 015003, [arXiv:1303.1140].

[358] B. M. Kastening, *Renormalization group improvement of the effective potential in massive ϕ^4 theory*, *Phys.Lett.* **B283** (1992) 287–292.

[359] C. Ford, D. Jones, P. Stephenson, and M. Einhorn, *The Effective potential and the renormalization group*, *Nucl.Phys.* **B395** (1993) 17–34, [hep-lat/9210033].

[360] R. Jackiw, *Functional evaluation of the effective potential*, *Phys.Rev.* **D9** (1974) 1686.

[361] H. H. Patel and M. J. Ramsey-Musolf, *Baryon Washout, Electroweak Phase Transition, and Perturbation Theory*, *JHEP* **1107** (2011) 029, [arXiv:1101.4665].

[362] N. Nielsen, *On the Gauge Dependence of Spontaneous Symmetry Breaking in Gauge Theories*, *Nucl.Phys.* **B101** (1975) 173.

[363] R. Fukuda and T. Kugo, *Gauge Invariance in the Effective Action and Potential*, *Phys.Rev.* **D13** (1976) 3469.

[364] D. Metaxas and E. J. Weinberg, *Gauge independence of the bubble nucleation rate in theories with radiative symmetry breaking*, *Phys.Rev.* **D53** (1996) 836–843, [hep-ph/9507381].

[365] M. Garny and T. Konstandin, *On the gauge dependence of vacuum transitions at finite temperature*, *JHEP* **1207** (2012) 189, [arXiv:1205.3392].

[366] F. James and M. Roos, *Minuit: A System for Function Minimization and Analysis of the Parameter Errors and Correlations*, *Comput.Phys.Commun.* **10** (1975) 343–367.

[367] A. Kusenko, *Improved action method for analyzing tunneling in quantum field theory*, *Phys.Lett.* **B358** (1995) 51–55, [hep-ph/9504418].

[368] M. Reece, *Vacuum Instabilities with a Wrong-Sign Higgs-Gluon-Gluon Amplitude*, *New J.Phys.* **15** (2013) 043003, [arXiv:1208.1765].

[369] J. Camargo-Molina, B. O'Leary, W. Porod, and F. Staub, **Vevacious***: A Tool For Finding The Global Minima Of One-Loop Effective Potentials With Many Scalars*, *Eur.Phys.J.* **C73** (2013) 2588, [arXiv:1307.1477].

[370] S. Heinemeyer, W. Hollik, and G. Weiglein, *FeynHiggs: A Program for the calculation of the masses of the neutral CP even Higgs bosons in the MSSM*, *Comput.Phys.Commun.* **124** (2000) 76–89, [hep-ph/9812320].

[371] A. Djouadi, J.-L. Kneur, and G. Moultaka, *SuSpect: A Fortran code for the supersymmetric and Higgs particle spectrum in the MSSM*, *Comput.Phys.Commun.* **176** (2007) 426–455, [hep-ph/0211331].

[372] V. Barger, P. Huang, M. Ishida, and W.-Y. Keung, *Scalar-Top Masses from SUSY Loops with 125 GeV mh and Precise Mw*, *Phys.Lett.* **B718** (2013) 1024–1030, [arXiv:1206.1777].

[373] J. R. Espinosa, C. Grojean, V. Sanz, and M. Trott, *NSUSY fits*, *JHEP* **1212** (2012) 077, [arXiv:1207.7355].

[374] M. Drees and K. Hagiwara, *Supersymmetric Contribution to the Electroweak ρ Parameter*, *Phys.Rev.* **D42** (1990) 1709–1725.

[375] S. Heinemeyer, W. Hollik, and G. Weiglein, *Electroweak precision observables in the minimal supersymmetric standard model*, *Phys.Rept.* **425** (2006) 265–368, [hep-ph/0412214].

[376] G. D'Ambrosio, G. Giudice, G. Isidori, and A. Strumia, *Minimal flavor violation: An Effective field theory approach*, *Nucl.Phys.* **B645** (2002) 155–187, [hep-ph/0207036].

[377] M. Ciuchini, G. Degrassi, P. Gambino, and G. Giudice, *Next-to-leading QCD corrections to $B \to X_s\gamma$ in Supersymmetry*, *Nucl.Phys.* **B534** (1998) 3–20, [hep-ph/9806308].

[378] S. Heinemeyer, O. Stal, and G. Weiglein, *Interpreting the LHC Higgs Search Results in the MSSM*, *Phys.Lett.* **B710** (2012) 201–206, [arXiv:1112.3026].

[379] B. Grzadkowski and M. Misiak, *Anomalous Wtb coupling effects in the weak radiative B-meson decay*, *Phys.Rev.* **D78** (2008) 077501, [arXiv:0802.1413].

[380] **Heavy Flavor Averaging Group**, Y. Amhis et al., *Averages of B-Hadron, C-Hadron, and tau-lepton properties as of early 2012*, 2012, [arXiv:1207.1158].

[381] A. Arbey and F. Mahmoudi, *SuperIso Relic: A Program for calculating relic density and flavor physics observables in Supersymmetry*, *Comput.Phys.Commun.* **181** (2010) 1277–1292, [arXiv:0906.0369].

[382] **ATLAS Collaboration**, G. Aad et al., *Search for direct third-generation squark pair production in final states with missing transverse momentum and two b-jets in $\sqrt{s} = 8$ TeV pp collisions with the ATLAS detector*, *JHEP* **1310** (2013) 189, [arXiv:1308.2631].

[383] **ATLAS Collaboration**, *Search for Supersymmetry in Events with Large Missing Transverse Momentum, Jets, and at Least One Tau Lepton in 21 fb^{-1} of $\sqrt{s} = 8$ TeV Proton-Proton Collision Data with the ATLAS Detector*, tech. rep. ATLAS-CONF-2013-026, ATLAS-COM-CONF-2013-012, 2013.

[384] **CMS Collaboration**, S. Chatrchyan et al., *Search for top-squark pair production in the single-lepton final state in pp collisions at $\sqrt{s}$ = 8 TeV*, *Eur.Phys.J.* **C73** (2013) 2677, [arXiv:1308.1586].

[385] **CMS Collaboration**, *Search for supersymmetry using razor variables in events with b-jets in pp collisions at 8 TeV*, tech. rep. CMS-PAS-SUS-13-004, 2013.

[386] M. Carena, G. Nardini, M. Quiros, and C. E. Wagner, *The Effective Theory of the Light Stop Scenario*, *JHEP* **0810** (2008) 062, [arXiv:0806.4297].

[387] J. Fan and M. Reece, *A New Look at Higgs Constraints on Stops*, *JHEP* **1406** (2014) 031, [arXiv:1401.7671].

[388] J. Hisano, K. Kawagoe, R. Kitano, and M. M. Nojiri, *Scenery from the top: Study of the third generation squarks at CERN LHC*, *Phys.Rev.* **D66** (2002) 115004, [hep-ph/0204078].

[389] K. Rolbiecki, J. Tattersall, and G. Moortgat-Pick, *Towards Measuring the Stop Mixing Angle at the LHC*, *Eur.Phys.J.* **C71** (2011) 1517, [arXiv:0909.3196].

[390] M. Blanke, D. Curtin, and M. Perelstein, *SUSY-Yukawa Sum Rule at the LHC*, *Phys.Rev.* **D82** (2010) 035020, [arXiv:1004.5350].

[391] M. Perelstein and M. Saelim, *SUSY-Yukawa Sum Rule at the LHC and the ILC*, 2012, [arXiv:1201.5839].

[392] M. Berggren, R. Keranen, H. Kluge, and A. Sopczak, *Study of scalar top quarks at a future e^+e^- linear collider*, 1999, [hep-ph/9911345].

[393] E. Boos, H. Martyn, G. A. Moortgat-Pick, M. Sachwitz, A. Sherstnev, et al., *Polarization in sfermion decays: Determining tan beta and trilinear couplings*, *Eur.Phys.J.* **C30** (2003) 395–407, [hep-ph/0303110].

[394] G. F. Giudice and A. Kusenko, *A Strongly interacting phase of the minimal supersymmetric model*, *Phys.Lett.* **B439** (1998) 55, [hep-ph/9805379].

[395] P. Hernandez, N. Rius, and V. Sanz, *Trilinear couplings and scalar bound states in supersymmetric extensions of the standard model*, *Nucl.Phys.Proc.Suppl.* **95** (2001) 272–275.

[396] J. M. Cornwall, A. Kusenko, L. Pearce, and R. Peccei, *Can supersymmetry breaking lead to electroweak symmetry breaking via formation of scalar bound states?*, *Phys.Lett.* **B718** (2013) 951–956, [arXiv:1210.6433].

[397] L. Pearce, A. Kusenko, and R. Peccei, *Phenomenology of Supersymmetric Models with a Symmetry-Breaking Seesaw Mechanism*, *Phys.Rev.* **D88** (2013) 075011, [arXiv:1307.6157].

[398] V. Kuzmin, V. Rubakov, and M. Shaposhnikov, *On the Anomalous Electroweak Baryon Number Nonconservation in the Early Universe*, *Phys.Lett.* **B155** (1985) 36.

[399] A. G. Cohen, D. Kaplan, and A. Nelson, *Progress in electroweak baryogenesis*, *Ann.Rev.Nucl.Part.Sci.* **43** (1993) 27–70, [hep-ph/9302210].

[400] P. B. Arnold, D. Son, and L. G. Yaffe, *The Hot Baryon Violation Rate is $\mathcal{O}(\alpha_W^5 T^4)$*, *Phys.Rev.* **D55** (1997) 6264–6273, [hep-ph/9609481].

[401] D. Bodeker, G. D. Moore, and K. Rummukainen, *Chern-Simons number diffusion and hard thermal loops on the lattice*, *Phys.Rev.* **D61** (2000) 056003, [hep-ph/9907545].

[402] M. Trodden, *Electroweak baryogenesis*, *Rev.Mod.Phys.* **71** (1999) 1463–1500, [hep-ph/9803479].

[403] N. G. Deshpande and E. Ma, *Pattern of Symmetry Breaking with Two Higgs Doublets*, *Phys.Rev.* **D18** (1978) 2574.

[404] E. Ma, *Verifiable radiative seesaw mechanism of neutrino mass and dark matter*, *Phys.Rev.* **D73** (2006) 077301, [hep-ph/0601225].

[405] R. Barbieri, L. J. Hall, and V. S. Rychkov, *Improved naturalness with a heavy Higgs: An Alternative road to LHC physics*, *Phys.Rev.* **D74** (2006) 015007, [hep-ph/0603188].

[406] M. Gustafsson, E. Lundstrom, L. Bergstrom, and J. Edsjo, *Significant Gamma Lines from Inert Higgs Dark Matter*, *Phys.Rev.Lett.* **99** (2007) 041301, [astro-ph/0703512].

[407] P. Agrawal, E. M. Dolle, and C. A. Krenke, *Signals of Inert Doublet Dark Matter in Neutrino Telescopes*, *Phys.Rev.* **D79** (2009) 015015, [arXiv:0811.1798].

[408] S. Andreas, M. H. Tytgat, and Q. Swillens, *Neutrinos from Inert Doublet Dark Matter*, *JCAP* **0904** (2009) 004, [arXiv:0901.1750].

[409] E. Nezri, M. H. Tytgat, and G. Vertongen, *e^+ and anti-p from inert doublet model dark matter*, *JCAP* **0904** (2009) 014, [arXiv:0901.2556].

[410] C. Arina, F.-S. Ling, and M. H. Tytgat, *IDM and iDM or The Inert Doublet Model and Inelastic Dark Matter*, *JCAP* **0910** (2009) 018, [arXiv:0907.0430].

[411] J.-O. Gong, H. M. Lee, and S. K. Kang, *Inflation and dark matter in two Higgs doublet models*, *JHEP* **1204** (2012) 128, [arXiv:1202.0288].

[412] M. Gustafsson, S. Rydbeck, L. Lopez-Honorez, and E. Lundstrom, *Status of the Inert Doublet Model and the Role of multileptons at the LHC*, *Phys.Rev.* **D86** (2012) 075019, [arXiv:1206.6316].

[413] A. Goudelis, B. Herrmann, and O. Stål, *Dark matter in the Inert Doublet Model after the discovery of a Higgs-like boson at the LHC*, *JHEP* **1309** (2013) 106, [arXiv:1303.3010].

[414] M. Dine, P. Huet, J. Singleton, Robert L., and L. Susskind, *Creating the baryon asymmetry at the electroweak phase transition*, *Phys.Lett.* **B257** (1991) 351–356.

[415] M. Dine, P. Huet, and J. Singleton, Robert L., *Baryogenesis at the electroweak scale*, *Nucl.Phys.* **B375** (1992) 625–648.

[416] T. A. Chowdhury, M. Nemevsek, G. Senjanovic, and Y. Zhang, *Dark Matter as the Trigger of Strong Electroweak Phase Transition*, *JCAP* **1202** (2012) 029, [arXiv:1110.5334].

[417] D. Borah and J. M. Cline, *Inert Doublet Dark Matter with Strong Electroweak Phase Transition*, *Phys.Rev.* **D86** (2012) 055001, [arXiv:1204.4722].

[418] G. Gil, P. Chankowski, and M. Krawczyk, *Inert Dark Matter and Strong Electroweak Phase Transition*, *Phys.Lett.* **B717** (2012) 396–402, [arXiv:1207.0084].

[419] S. S. AbdusSalam and T. A. Chowdhury, *Scalar Representations in the Light of Electroweak Phase Transition and Cold Dark Matter Phenomenology*, *JCAP* **1405** (2014) 026, [arXiv:1310.8152].

[420] J. M. Cline and K. Kainulainen, *Improved Electroweak Phase Transition with Subdominant Inert Doublet Dark Matter*, *Phys.Rev.* **D87** (2013), no. 7 071701, [arXiv:1302.2614].

[421] G. Branco, P. Ferreira, L. Lavoura, M. Rebelo, M. Sher, et al., *Theory and phenomenology of two-Higgs-doublet models*, *Phys.Rept.* **516** (2012) 1–102, [arXiv:1106.0034].

[422] R. R. Parwani, *Resummation in a hot scalar field theory*, *Phys.Rev.* **D45** (1992) 4695, [hep-ph/9204216].

[423] P. B. Arnold and O. Espinosa, *The Effective potential and first order phase transitions: Beyond leading-order*, *Phys.Rev.* **D47** (1993) 3546, [hep-ph/9212235].

[424] J. Espinosa and M. Quiros, *Improved metastability bounds on the standard model Higgs mass*, *Phys.Lett.* **B353** (1995) 257–266, [hep-ph/9504241].

[425] M. Carrington, *The Effective potential at finite temperature in the Standard Model*, *Phys.Rev.* **D45** (1992) 2933–2944.

[426] J. M. Cline, K. Kainulainen, and A. P. Vischer, *Dynamics of two Higgs doublet CP violation and baryogenesis at the electroweak phase transition*, *Phys.Rev.* **D54** (1996) 2451–2472, [hep-ph/9506284].

[427] B. W. Lee and S. Weinberg, *Cosmological Lower Bound on Heavy Neutrino Masses*, *Phys.Rev.Lett.* **39** (1977) 165–168.

[428] R. Young, *Strange quark content of the nucleon and dark matter searches*, *PoS* **LATTICE2012** (2012) 014, [arXiv:1301.1765].

[429] **XENON100 Collaboration**, E. Aprile et al., *Dark Matter Results from 225 Live Days of XENON100 Data*, *Phys.Rev.Lett.* **109** (2012) 181301, [arXiv:1207.5988].

[430] A. Arhrib, Y.-L. S. Tsai, Q. Yuan, and T.-C. Yuan, *An Updated Analysis of Inert Higgs Doublet Model in light of the Recent Results from LUX, PLANCK, AMS-02 and LHC*, *JCAP* **1406** (2014) 030, [arXiv:1310.0358].

[431] P. Bechtle, O. Brein, S. Heinemeyer, G. Weiglein, and K. E. Williams, *HiggsBounds: Confronting Arbitrary Higgs Sectors with Exclusion Bounds from LEP and the Tevatron*, *Comput.Phys.Commun.* **181** (2010) 138–167, [arXiv:0811.4169].

[432] P. Bechtle, O. Brein, S. Heinemeyer, G. Weiglein, and K. E. Williams, *HiggsBounds 2.0.0: Confronting Neutral and Charged Higgs Sector Predictions with Exclusion Bounds from LEP and the Tevatron*, *Comput.Phys.Commun.* **182** (2011) 2605–2631, [arXiv:1102.1898].

[433] P. Bechtle, O. Brein, S. Heinemeyer, O. Stål, T. Stefaniak, et al., *HiggsBounds-4: Improved Tests of Extended Higgs Sectors against Exclusion Bounds from LEP, the Tevatron and the LHC*, *Eur.Phys.J.* **C74** (2014), no. 3 2693, [arXiv:1311.0055].

[434] P. Bechtle, S. Heinemeyer, O. Stål, T. Stefaniak, and G. Weiglein, *HiggsSignals: Confronting arbitrary Higgs sectors with measurements at the Tevatron and the LHC*, *Eur.Phys.J.* **C74** (2014), no. 2 2711, [arXiv:1305.1933].

[435] W. Porod, *SPheno, a program for calculating supersymmetric spectra, SUSY particle decays and SUSY particle production at e^+e^- colliders*, *Comput.Phys.Commun.* **153** (2003) 275–315, [hep-ph/0301101].

[436] W. Porod and F. Staub, *SPheno 3.1: Extensions including flavour, CP-phases and models beyond the MSSM*, *Comput.Phys.Commun.* **183** (2012) 2458–2469, [arXiv:1104.1573].

[437] F. Staub, *SARAH*, [arXiv:0806.0538], 2008.

[438] F. Staub, *SARAH 4: A tool for (not only SUSY) model builders*, *Comput.Phys.Commun.* **185** (2014) 1773–1790, [arXiv:1309.7223].

[439] H. H. Patel and M. J. Ramsey-Musolf, *Stepping Into Electroweak Symmetry Breaking: Phase Transitions and Higgs Phenomenology*, *Phys.Rev.* **D88** (2013) 035013, [arXiv:1212.5652].

[440] N. Blinov, J. Kozaczuk, D. E. Morrissey, and C. Tamarit, *Electroweak Baryogenesis from Exotic Electroweak Symmetry Breaking*, 2015, [arXiv:1504.05195].

[441] K. P. Modak and D. Majumdar, *Confronting Galactic and Extragalactic γ-ray observed by Fermi-LAT with Annihilating Dark Matter in Inert Higgs Doublet Model*, 2015, [arXiv:1502.05682].

[442] T. Daylan, D. P. Finkbeiner, D. Hooper, T. Linden, S. K. N. Portillo, et al., *The Characterization of the Gamma-Ray Signal from the Central Milky Way: A Compelling Case for Annihilating Dark Matter*, 2014, [arXiv:1402.6703].

[443] D. Eriksson, J. Rathsman, and O. Stal, *2HDMC: Two-Higgs-Doublet Model Calculator Physics and Manual*, *Comput.Phys.Commun.* **181** (2010) 189–205, [arXiv:0902.0851].

[444] G. Belanger, F. Boudjema, A. Pukhov, and A. Semenov, *micrOMEGAs3: A program for calculating dark matter observables*, *Comput.Phys.Commun.* **185** (2014) 960–985, [arXiv:1305.0237].

[445] P. Bechtle, S. Heinemeyer, O. Stål, T. Stefaniak, and G. Weiglein, *Probing the Standard Model with Higgs signal rates from the Tevatron, the LHC and a future ILC*, *JHEP* **1411** (2014) 039, [arXiv:1403.1582].

[446] R. Enberg, J. Rathsman, and G. Wouda, *Higgs phenomenology in the Stealth Doublet Model*, 2013, [arXiv:1311.4367].

[447] R. Enberg, J. Rathsman, and G. Wouda, *Higgs properties in a broken Inert Doublet Model*, *JHEP* **1308** (2013) 079, [arXiv:1304.1714].

[448] P. Ko, Y. Omura, and C. Yu, *Dark matter and dark force in the type-I inert 2HDM with local U(1)$_H$ gauge symmetry*, *JHEP* **1411** (2014) 054, [arXiv:1405.2138].

[449] G. Gelmini, P. Gondolo, A. Soldatenko, and C. E. Yaguna, *The Effect of a late decaying scalar on the neutralino relic density*, *Phys.Rev.* **D74** (2006) 083514, [hep-ph/0605016].

[450] C. Wainwright and S. Profumo, *The Impact of a strongly first-order phase transition on the abundance of thermal relics*, *Phys.Rev.* **D80** (2009) 103517, [arXiv:0909.1317].

[451] C. Grojean, G. Servant, and J. D. Wells, *First-order electroweak phase transition in the standard model with a low cutoff*, *Phys.Rev.* **D71** (2005) 036001, [hep-ph/0407019].

[452] C. Delaunay, C. Grojean, and J. D. Wells, *Dynamics of Non-renormalizable Electroweak Symmetry Breaking*, *JHEP* **0804** (2008) 029, [arXiv:0711.2511].

[453] B. Grinstein and M. Trott, *Electroweak Baryogenesis with a Pseudo-Goldstone Higgs*, *Phys.Rev.* **D78** (2008) 075022, [arXiv:0806.1971].

[454] D. J. Chung, A. J. Long, and L.-T. Wang, *125 GeV Higgs boson and electroweak phase transition model classes*, *Phys.Rev.* **D87** (2013), no. 2 023509, [arXiv:1209.1819].

[455] X. Miao, S. Su, and B. Thomas, *Trilepton Signals in the Inert Doublet Model*, *Phys.Rev.* **D82** (2010) 035009, [arXiv:1005.0090].

[456] G. Belanger, B. Dumont, A. Goudelis, B. Herrmann, S. Kraml, et al., *Dilepton constraints in the Inert Doublet Model from Run 1 of the LHC*, 2015, [arXiv:1503.07367].

[457] B. Swiezewska and M. Krawczyk, *Diphoton rate in the inert doublet model with a 125 GeV Higgs boson*, *Phys.Rev.* **D88** (2013), no. 3 035019, [arXiv:1212.4100].

[458] A. Arhrib, R. Benbrik, and N. Gaur, *$H \to \gamma\gamma$ in Inert Higgs Doublet Model*, *Phys.Rev.* **D85** (2012) 095021, [arXiv:1201.2644].

[459] G. K. John F. Gunion, Howard E. Haber and S. Dawson, *The Higgs Hunter's Guide*. Perseus Publishing, 1990.

[460] A. Djouadi, *The Anatomy of electro-weak symmetry breaking. II. The Higgs bosons in the minimal supersymmetric model*, *Phys.Rept.* **459** (2008) 1–241, [hep-ph/0503173].

[461] M. Spira, A. Djouadi, D. Graudenz, and P. Zerwas, *Higgs boson production at the LHC*, *Nucl.Phys.* **B453** (1995) 17–82, [hep-ph/9504378].

[462] **ATLAS Collaboration**, G. Aad et al., *Measurement of Higgs boson production in the diphoton decay channel in pp collisions at center-of-mass energies of 7 and 8 TeV with the ATLAS detector*, *Phys.Rev.* **D90** (2014), no. 11 112015, [arXiv:1408.7084].

[463] **CMS Collaboration**, V. Khachatryan et al., *Observation of the diphoton decay of the Higgs boson and measurement of its properties*, *Eur.Phys.J.* **C74** (2014), no. 10 3076, [arXiv:1407.0558].

[464] A. Pierce and J. Thaler, *Natural Dark Matter from an Unnatural Higgs Boson and New Colored Particles at the TeV Scale*, *JHEP* **0708** (2007) 026, [hep-ph/0703056].

[465] C. Bonilla, D. Sokolowska, J. L. Diaz-Cruz, M. Krawczyk, and N. Darvishi, *IDMS: Inert Dark Matter Model with a complex singlet*, 2014, [arXiv:1412.8730].

[466] **Super-Kamiokande**, K. Abe et al., *Search for proton decay via $p \to \nu K^+$ using 260 kiloton $\cdot$ year data of Super-Kamiokande*, *Phys.Rev.* **D90** (2014), no. 7 072005, [arXiv:1408.1195].

[467] J. Huang and Y. Zhao, *Dark Matter Induced Nucleon Decay: Model and Signatures*, *JHEP* **1402** (2014) 077, [arXiv:1312.0011].

[468] K. Abe, T. Abe, H. Aihara, Y. Fukuda, Y. Hayato, et al., *Letter of Intent: The Hyper-Kamiokande Experiment — Detector Design and Physics Potential —*, 2011, [arXiv:1109.3262].

[469] S. Demidov, D. Gorbunov, and D. Kirpichnikov, *Collider signatures of Hylogenesis*, *Phys.Rev.* **D91** (2015), no. 3 035005, [arXiv:1411.6171].

[470] **ATLAS Collaboration**, G. Aad et al., *Search for new phenomena in the dijet mass distribution using $p-p$ collision data at $\sqrt{s} = 8$ TeV with the ATLAS detector*, *Phys.Rev.* **D91** (2015), no. 5 052007, [arXiv:1407.1376].

[471] **ATLAS Collaboration**, G. Aad et al., *Search for New Phenomena in Dijet Angular Distributions in Proton-Proton Collisions at $\sqrt{s} = 8$ TeV Measured with the ATLAS Detector*, 2015, [arXiv:1504.00357].

[472] **CMS Collaboration**, V. Khachatryan et al., *Search for resonances and quantum black holes using dijet mass spectra in proton-proton collisions at $\sqrt{s} = 8$ TeV*, *Phys.Rev.* **D91** (2015), no. 5 052009, [arXiv:1501.04198].

[473] **CMS Collaboration**, V. Khachatryan et al., *Search for quark contact interactions and extra spatial dimensions using dijet angular distributions in proton-proton collisions at $\sqrt{s} = 8$ TeV*, 2014, [arXiv:1411.2646].

[474] O. Moreno, *The Heavy Photon Search Experiment at Jefferson Lab*, in *Meeting of the American Physical Society Division of Particles and Fields*, 2013. arXiv:1310.2060.

[475] J. Buckley, D. Cowen, S. Profumo, A. Archer, M. Cahill-Rowley, et al., *Working Group Report: WIMP Dark Matter Indirect Detection*, in *Community Summer Study 2013 : Snowmass on the Mississippi*, 2013. arXiv:1310.7040.

[476] P. Ferreira and D. Jones, *Bounds on scalar masses in two Higgs doublet models*, *JHEP* **0908** (2009) 069, [arXiv:0903.2856].

Appendix A

Minimality of the Action Under Path Deformations

In this appendix we show that fixing a path in field space connecting two vacua and computing the one-dimensional bounce action along that path provides on upper bound on the bounce action for tunnelling between those vacua. Equivalently, the bounce solution of the Euclidean action is a minimum of the action with respect to deformations of fixed, one-dimensional paths in the field space. The implication of this result is that the path deformation method of `CosmoTransitions` (CT) [335] is guaranteed to provide at least an upper bound on the tunnelling lifetime.

Recall that the multi-field bounce solution $\bar{\boldsymbol{\phi}}(\rho)$, $\rho = \sqrt{t^2 + \mathbf{x}^2}$, of the Euclidean action is an $O(4)$-symmetric solution of the classical equations of motion subject to the boundary conditions

$$\partial_\rho \bar{\boldsymbol{\phi}}(\rho = 0) = 0 \ , \qquad \lim_{\rho \to \infty} \bar{\boldsymbol{\phi}} = \boldsymbol{\phi}_+ \ , \tag{A.1}$$

where $\boldsymbol{\phi}_+$ is the metastable vacuum configuration. The bounce action is just the Euclidean action evaluated on the bounce solution.

Let us now restate our claim more precisely. The bounce solution is an element of the set of parametric curves on $\mathbb{R}^F$, where F is the number of scalar fields. Any path $\boldsymbol{\phi}(\rho)$ in this set can be written in terms of a unit speed curve $\boldsymbol{\gamma}(s)$:

$$\boldsymbol{\phi}(\rho) = \boldsymbol{\gamma}(s(\rho)) \ , \quad \text{where} \quad |\dot{\boldsymbol{\gamma}}(s)| = 1 \ . \tag{A.2}$$

The function $s(\rho)$ is the solution of

$$\frac{ds}{d\rho} = \left| \frac{d\boldsymbol{\phi}}{d\rho} \right| \ , \tag{A.3}$$

and $\boldsymbol{\gamma}(s) = \boldsymbol{\phi}(\rho(s))$. The Euclidean action in α spacetime dimensions becomes

$$S_E[\boldsymbol{\gamma}, s] = \Omega_\alpha \int d\rho \rho^{\alpha-1} \left[\frac{1}{2} \left(\frac{ds}{d\rho} \right)^2 + V(\boldsymbol{\gamma}(s(\rho))) \right], \tag{A.4}$$

where $\Omega_\alpha = 2\pi^{\alpha/2}/\Gamma(\frac{\alpha}{2})$ is the surface area of a unit $(\alpha-1)$-sphere. Suppose we fix a path in field space $\boldsymbol{\gamma}$ connecting two vacua and extremize the action with respect to $s(\rho)$ subject to the boundary conditions of the bounce along this one-dimensional trajectory. The corresponding solution can then be used to obtain a restricted bounce action along the fixed trajectory. This is the procedure used by CT at each intermediate step of its deformation procedure. We claim that the action obtained for any such fixed path is greater than or equal to the unconstrained bounce action.

To prove this claim, we use the fact that the bounce is a stationary point of the action. For tunnelling configurations, however, it is not an extremum of the action. This coincides with the fact that the second variation of the action with respect to the fields has a negative eigenvalue. The corresponding operator is

$$-\delta_{ij}\partial^2 + \frac{\delta V}{\delta\phi_i \delta\phi_j}(\bar{\boldsymbol{\phi}}) \ . \tag{A.5}$$

We assume that this operator has only a single negative mode [316, 348]. This has been proved for a single field in the thin wall limit [316, 323]. If this assumption is false, the entire Callan-Coleman formalism does not apply. We show that this negative eigenvalue is associated exclusively with the variation of $s(\rho)$ using the argument of Ref. [348]. As a result, the bounce action is an extremum with respect to variations in the orthogonal parameter $\boldsymbol{\gamma}$, and can easily be shown to be a minimum by explicit construction.

Consider the scaling transformation

$$s(\rho) \to s(\rho/\lambda). \tag{A.6}$$

The action of Eq. (A.4) transforms as

$$S[\boldsymbol{\gamma}, s] \to \lambda^{\alpha-2} S_T[\boldsymbol{\gamma}, s] + \lambda^\alpha S_V[\boldsymbol{\gamma}, s], \tag{A.7}$$

where

$$S_T[\boldsymbol{\gamma}, s] = \Omega_\alpha \int d\rho \rho^{\alpha-1} \frac{1}{2} \left(\frac{ds}{d\rho} \right)^2 \tag{A.8}$$

and

$$S_V[\boldsymbol{\gamma}, s] = \Omega_\alpha \int d\rho \rho^{\alpha-1} V(\boldsymbol{\gamma}(s(\rho))). \tag{A.9}$$

Requiring that S is stationary with respect to these scale variations yields

$$\frac{\delta S}{\delta \lambda} = 0 \Rightarrow S_T = -\frac{\alpha}{\alpha - 2} S_V > 0. \tag{A.10}$$

We can also evaluate the second variation of S

$$\frac{\delta^2 S}{\delta \lambda^2} = \begin{cases} -S_T & \alpha = 3 \\ -2(\alpha - 2) S_T & \alpha > 3 \end{cases} < 0. \tag{A.11}$$

This means that the bounce is a maximum of the action with respect to the scaling transformation of Eq. (A.6). Thus the crucial negative eigenmode is due to scaling, and, since this transformation does not involve the normalized path $\boldsymbol{\gamma}$, it is due entirely to the functional variation of $s(\rho)$. The tunnelling action obtained by computing the bounce solution along a fixed one-dimensional path is therefore an upper bound on the true bounce action. This justifies the procedure of using a fixed normalized field path and computing $s(\rho)$ as a way to check the `CosmoTransitions` results.

Appendix B

An Approximate Empirical Bound for Charge and Colour-Breaking Vacua in the MSSM

In this second appendix we describe an approximate empirical bound on metastability valid in the parameter region $r \equiv m_{U_3}^2/m_{Q_3}^2 \sim 1$, moderate $\tan\beta$, smaller μ, and larger m_A. We begin by deriving a condition on *absolute* stability to motivate the functional form of the empirical formula. Let us emphasize that our empirical bound is only an approximation, and is not guaranteed to work outside the limited regime we consider.

To derive an improved bound on absolute stability of the SM-like (SML) vacuum, we impose only $SU(3)_C$ D-flatness and $H_d^0 = 0$. Similar existing formulae typically also assume $SU(2)_L$ and $U(1)_Y$ flatness, which precludes the existence of a SML vacuum. For $m_{U_3}^2/m_{Q_3}^2 \sim 1$, $SU(3)_C$ D-flatness should be a good approximation since the strong gauge coupling is larger than the others [353]. Setting $H_d^0 = 0$ is also well-justified for large $\tan\beta$ near the SML vacuum; at the CCB minimum one typically finds $|H_d^0| < |H_u^0|$ as well.

Applying the $SU(3)_C$ D-flatness condition, we have

$$T \equiv \tilde{t}_L = |\tilde{t}_R| \ , \tag{B.1}$$

and the potential becomes

$$V \ = \ m_T^2 T^2 + m_2^2 (H_u^0)^2 \pm 2 y_t A_t H_u^0 T^2 + y_t^2 \left[T^4 + 2T^2 (H_u^0)^2\right] + \frac{\bar{g}^2}{8}\left[(H_u^0)^2 - T^2\right]^2 \ ,$$

where $m_T^2 = m_{Q_3}^2 + m_{U_3}^2$, $\bar{g} = \sqrt{g^2 + g'^2}$ and $m_2^2 = m_{H_u}^2 + |\mu|^2$.

Minimizing, we have

$$0 = \frac{\partial V}{\partial T} = T\left[2m_T^2 \pm 4 y_t A_t H_u + 4 y_t^2 H_u^2 - \frac{\bar{g}^2}{2}((H_u^0)^2 - T^2) + 4 y_t^2 T^2\right] \ . \tag{B.2}$$

The solutions are evidently $T = 0$ and

$$T^2 = \left[\mp 2 y_t A_t H_u^0 - m_T^2 - 2(y_t^2 - \bar{g}^2/8)(H_u^0)^2\right] \Big/ 2(y_t^2 + \bar{g}^2/8) \ . \tag{B.3}$$

Since we are restricting ourselves to $H_u^0 \geq 0$, the relative orientation of the stops in any potential CCB minimum must be such that $\mp y_t A_t = |y_t A_t|$. Note as well that the A-term must overpower the others to make $T^2 > 0$. Under our given assumptions, this already provides a necessary condition on the existence of a CCB vacuum,

$$A_t^2 > 2 m_T^2 (1 - \bar{g}^2/8 y_t^2) \ . \tag{B.4}$$

This is a somewhat weaker requirement than the analytical formula Eq. (6.3).

Minimizing with respect to H_u (and choosing the relative stop alignment as above) gives

$$0 = \frac{\partial V}{\partial H_u} = 2 m_2^2 H_u^0 + 4(\bar{g}^2/8)(H_u^0)^3 + \left[(2(y_t^2 - \bar{g}^2/8) H_u^0 - y_t A_t\right] \ (2T^2) \ . \tag{B.5}$$

For $T^2 = 0$, this reproduces the SM-like minimum. On the other hand, we can also plug in our non-zero solution for T^2, which is quadratic in H_u^0. This generates a cubic equation for H_u^0 that can be solved analytically. A cubic equation has three roots, with at least one of them real. The other two roots are either real, or complex conjugates of each other. We need at least three real roots to have both a SML vacuum and a CCB vacuum since there must also be at least a saddle point between them.

In this approximation, we can check for CCB vacua by simply scanning over stop parameters and computing cube roots, for which there exist analytical formulae. The EW vacuum is trivial to find, and corresponds to $T = 0$. The $T^2 \neq 0$ solutions may correspond to CCB vacua. A necessary condition for this is that all the roots are real, and that at least two of them are positive. With the roots in hand, it is then straightforward to use them in the potential to compare the relative depths of the minima. Fixing $m_2^2 = -m_Z^2/2$ to get the correct SML vacuum expectation value, we find numerically that $A_t^2 \gtrsim (2.4)(m_T^2 + m_2^2)$ gives a very good estimate of the condition for a CCB vacuum to be deeper than the SML vacuum for this simplified potential.

In our analysis of metastability, we find that the boundary between metastable and dangerously unstable regions tends to track the boundary between SML and CCB regions. Motivated by this and our previous result for CCB vacua, we will attempt to fit the boundary between metastable and unstable regions by an expression of the form

$$A_t^2 = \alpha m_T^2 + \beta |m_{Q_3}^2 - m_{U_3}^2| + \gamma m_2^2 = \left(\alpha + \beta \frac{|1 - r|}{1 + r}\right) m_T^2 + \gamma m_2^2 \tag{B.6}$$

The second term in the above expression is included to model the effect of small deviations from $SU(3)_C$ D-flatness.

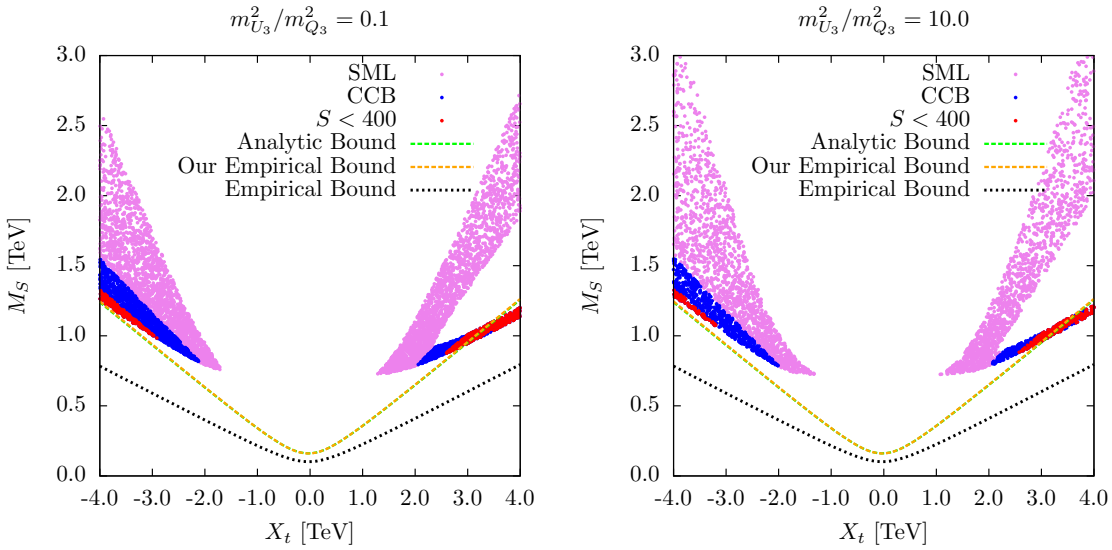

Figure B.1: The deterioration of the empirical bound of Eq. (B.6) for $m^2_{U_3}/m^2_{Q_3} \gg 1$ or $m^2_{U_3}/m^2_{Q_3} \ll 1$. For these parameter ranges the assumption of $SU(3)_C$ D-flatness that motivated Eq. (B.6) breaks down and it cannot be used to reliably model the boundary between the metastable and unstable parameter regions.

We estimate the parameters α and γ by using a least-squares fit to the lower boundary of the metastable region in Fig. 6.2, without imposing the Higgs mass constraint. This is an arbitrary choice to fit to; different choices in Tab. 6.1 lead to variations in α on the order of 15% and 100% in γ. The large variation in γ is not a big problem since it is multiplied by $|m_2^2| \sim m_Z^2 \ll m_T^2$. We obtain $\alpha \simeq 3.4$ and $\gamma \simeq 60$. With α and γ fixed, we fit β to models with $r \neq 1$. We again see that there is a significant variation $\mathcal{O}(20\%)$ depending on what r is, indicating that the functional form of Eq. (B.6) is an oversimplification. With this in mind, we find an average value of $\beta \simeq -0.5$ for $r \in [0.3, 3]$. We show the resulting bound in the results of Section 6.3.3. For $r \simeq 1$, Eq. (B.6) approximates the true boundary between metastable and unstable models well. However, we expect this constraint to deteriorate as one moves away from the assumption of $SU(3)_C$ D-flatness by choosing soft masses with $r \gg 1$ or $r \ll 1$. We show an explicit example of this in Fig. B.1.

We emphasize that this bound is a *very* rough guideline for metastability in the MSSM in a specific corner of the parameter space and should only be used as a first order approximation. A full numerical analysis is required when any of the above assumptions are violated or better precision is required.

Appendix C

Renormalization Group Equations in the Inert Doublet Model

Here we list the beta functions for the inert 2HDM at one-loop order. The general form of the RG equations is

$$\frac{d\lambda}{dt} = \frac{1}{16\pi^2}\beta_\lambda, \tag{C.1}$$

where $t = \ln Q/Q_0$ and Q_0 is a reference scale. We take $Q_0 = M_Z$. The $U(1)_Y$ gauge coupling has the GUT normalization: $g_1 = \sqrt{5/3}g'$. The beta functions below have been checked with `SARAH` [438]. Partial one loop results can be found in Refs. [413, 421, 476] for dimensionless parameters only. These agree with the formulae below.

The gauge coupling evolution is determined by

$$\beta_{g_1} = \frac{21}{5}g_1^3 \tag{C.2}$$

$$\beta_{g_2} = -3g_2^3 \tag{C.3}$$

$$\beta_{g_3} = -7g_3^3. \tag{C.4}$$

For the third generation Yukawas we have

$$\beta_{y_t} = -\frac{17}{20}g_1^2 y_t - \frac{9}{4}g_2^2 y_t - 8g_3^2 y_t + \frac{9}{2}y_t^3 + \frac{3}{2}y_b^2 y_t + y_t y_\tau^2 \tag{C.5}$$

$$\beta_{y_b} = -\frac{1}{4}g_1^2 y_b - \frac{9}{4}g_2^2 y_b - 8g_3^2 y_b + \frac{3}{2}y_b y_t^2 + y_b y_\tau^2 + \frac{9}{2}y_b^3 \tag{C.6}$$

$$\beta_{y_\tau} = -\frac{9}{4}g_1^2 y_\tau - \frac{9}{4}g_2^2 y_\tau + 3y_t^2 y_\tau + 3y_b^2 y_\tau + \frac{5}{2}y_\tau^3. \tag{C.7}$$

Next we consider the scalar potential parameters. The evolution of the dimensionless quartic couplings λ_i is governed by

$$\beta_{\lambda_1} = -\frac{9}{5}g_1^2\lambda_1 - 9g_2^2\lambda_1 + \frac{27}{200}g_1^4 + \frac{9}{20}g_2^2g_1^2 \tag{C.8}$$
$$+ \frac{9}{8}g_2^4 + 24\lambda_1^2 + 2\lambda_3^2 + \lambda_4^2 + \lambda_5^2 + 2\lambda_3\lambda_4$$
$$+ 12\lambda_1 y_t^2 - 6y_t^4 + 12\lambda_1 y_b^2 - 6y_b^4 + 4\lambda_1 y_\tau^2 - 2y_\tau^4$$
$$\beta_{\lambda_2} = -\frac{9}{5}g_1^2\lambda_2 - 9g_2^2\lambda_2 + \frac{27}{200}g_1^4 + \frac{9}{20}g_2^2g_1^2 + \frac{9}{8}g_2^4 + 24\lambda_2^2 \tag{C.9}$$
$$+ 2\lambda_3^2 + \lambda_4^2 + \lambda_5^2 + 2\lambda_3\lambda_4$$
$$\beta_{\lambda_3} = -\frac{9}{5}g_1^2\lambda_3 - 9g_2^2\lambda_3 + \frac{27}{100}g_1^4 - \frac{9}{10}g_2^2g_1^2 + \frac{9}{4}g_2^4 \tag{C.10}$$
$$+ 4\lambda_3^2 + 2\lambda_4^2 + 2\lambda_5^2 + 12\lambda_1\lambda_3 + 12\lambda_2\lambda_3 + 4\lambda_1\lambda_4$$
$$+ 4\lambda_2\lambda_4 + 6\lambda_3 y_t^2 + 6\lambda_3 y_b^2 + 2\lambda_3 y_\tau^2$$
$$\beta_{\lambda_4} = -\frac{9}{5}g_1^2\lambda_4 - 9g_2^2\lambda_4 + \frac{9}{5}g_2^2g_1^2 + 4\lambda_4^2 + 8\lambda_5^2 \tag{C.11}$$
$$+ 4\lambda_1\lambda_4 + 4\lambda_2\lambda_4 + 8\lambda_3\lambda_4 + 6\lambda_4 y_t^2 + 6\lambda_4 y_b^2 + 2\lambda_4 y_\tau^2$$
$$\beta_{\lambda_5} = -\frac{9}{5}g_1^2\lambda_5 - 9g_2^2\lambda_5 + 4\lambda_1\lambda_5 + 4\lambda_2\lambda_5 + 8\lambda_3\lambda_5 \tag{C.12}$$
$$+ 12\lambda_4\lambda_5 + 6\lambda_5 y_t^2 + 6\lambda_5 y_b^2 + 2\lambda_5 y_\tau^2$$

The beta functions for the mass parameters are given by

$$\beta_{\mu_1^2} = -\frac{9}{10}g_1^2\mu_1^2 - \frac{9}{2}g_2^2\mu_1^2 + 12\lambda_1\mu_1^2 + 4\lambda_3\mu_2^2 + 2\lambda_4\mu_2^2 \tag{C.13}$$
$$+ 6\mu_1^2 y_t^2 + 6\mu_1^2 y_b^2 + 2\mu_1^2 y_\tau^2$$
$$\beta_{\mu_2^2} = -\frac{9}{10}g_1^2\mu_2^2 - \frac{9}{2}g_2^2\mu_2^2 + 12\lambda_2\mu_2^2 + 4\lambda_3\mu_1^2 + 2\lambda_4\mu_1^2. \tag{C.14}$$

Finally, the anomalous dimensions for the Higgs and the inert scalar are

$$\gamma_h = -\frac{9}{20}g_1^2 - \frac{9}{4}g_2^2 + 3y_t^2 + 3y_b^2 + y_\tau^2 \tag{C.15}$$
$$\gamma_\phi = -\frac{9}{20}g_1^2 - \frac{9}{4}g_2^2. \tag{C.16}$$